Evaluation of Aluminum-Boron Carbide Neutron Absorbing Materials for Interim Storage of Used Nuclear Fuel

by

Jonathan Brett Wierschke

A dissertation submitted in partial fulfillment
of the requirements for the degree of
Doctor of Philosophy
(Nuclear Engineering and Radiological Sciences)
in the University of Michigan
2015

Doctoral Committee:

Professor Lumin Wang, Chair
Associate Professor Samantha H. Daly
Professor Fei Gao
Brady D. Hanson, Pacific Northwest National Lab

Dedication

To my family: Kathlen, Brett, Katherine, Emma, and the one still yet to be named.

Acknowledgements

I would like to recognize and thank Brady Hanson for all his guidance and support at PNNL. Without Brady's help I would not have been able to work at PNNL and gain the experiences that I have. He has worked hard to make sure that I was able to receive all of the help and support that I needed to carry out my work. He has also been instrumental in helping me design my experiments and has provided guidance when I needed it.

I would also like to thank Lumin Wang for accepting me into his group at the University of Michigan and for teaching me and advising me. He has opened my eyes to the world of microscopy and helped ignite my interest in the microscopic world. I would like to thank Lumin and Brady for all the time that they have taken to support me and for all of their encouragement.

I would be remiss if I did not acknowledge all of the staff at PNNL that has provided support and technical expertise on this project. I would like to thank Monty Telander for all of his help in setting up and maintaining the autoclave systems and for his support in sample preparation and control. I would like to thank Shelley Carlson and Clyde Chamberlin for lending their experience and expertise to solving the problem of sample preparation. I would also like to thank Paul MacFarlan for putting up with me and teaching me how to get things done at PNNL. I would also like to acknowledge the expertise and dedication of Alan Schemer-Kohrn who has spent countless hours with me on the SEM. I would also like to thank Jarrod Jones for his administrative support in helping me sort out all of the paperwork associated with government work.

A portion of this work was performed at NIST. This work would not have been completed without the excellent help of Greg Downing. I would like to thank Greg for going above and beyond all expectations to help me while I was there. I would like to thank him for taking the time to explain the details of the NDP system to me and for all of the late nights that he stayed around so that I could collect the data that I needed. I would also like to thank him for the hospitality that he showed me and for helping make the trip a memorable and productive experience.

I would also like to recognize all of the staff that helped me during my time at the University of Michigan. I would like to thank Alex Flick for his support in the design and construction of a static autoclave system. I would also like to thank Kai Sun and Haiping Sun for their support in training me on how to use an electron microscope.

I would be ungrateful if I didn't give special acknowledgement to Peggy Jo Gramer at the University of Michigan. I would like to thank her for stepping in to advocate for me whenever I had a need. She was instrumental in providing a way for me to go to PNNL as well as making sure that I was always taken care of. I would like to thank Peggy for always being there when I needed help and for being an advocate for me.

Finally, I would like to thank my family and recognize them for all the sacrifices that they have made to support me through this work. I would like to thank my wife Kathlen for taking a chance on me and standing beside through the good and bad times. I would like to thank her for listening through my problems and complaints, even if she had no clue what I was talking about. I would also like to thank my kids Brett, Kate, and Emma. They have known nothing but a dad in school their whole lives but have never complained about the time that it has required of me. I would also like to thank my parents, Brett and Shelley, for their close support

while we were in Michigan and for their continued moral support as we have been away. I would also like to acknowledge my mother and father-in-law, Bob and Nila Hodgson, for the many hours given and miles driven to support my family when I could not be there for them. I would also like to thank my sister-in-law Mikaela Hodgson for the many hours that she has spent taking care of my kids while my wife has been ill.

This work was supported by the U.S. Department of Energy Nuclear Energy University Partnership Grant DE-AC07-05ID14517.

Table of Contents

List of Tables

List of Figures

List of Appendices

List of Abbreviations

ADF	Annular Dark Field
BF	Bright Field
BWR	Boiling Water Reactor
DI	De-ionized
EBSD	Electron Backscatter Diffraction
EDS	Energy Dispersive (X-ray) Spectroscopy
EELS	Electron Energy Loss Spectroscopy
EPRI	Electric Power Research Institute
FCC	Face-centered Cubic
FEG	Field Emission Gun
FIB	Focused Ion Beam
FOM	Figure of Merit
HCP	Hexagonal Close-packed
MMC	Metal Matrix Composite
NDP	Neutron Depth Profile
NIST	National Institute for Standards and Technology
NWPA	Nuclear Waste Policy Act
PNNL	Pacific Northwest National Laboratory
PWR	Pressurized Water Reactor
SCCM	Standard Cubic Centimeter per Minute
SCFM	Standard Cubic Foot per Minute
SE	Secondary Electrons
SEM	Scanning Electron Microscope
TEM	Transmission Electron Microscope
TGA	Thermogravimetric Analyzer
UM	University of Michigan
XRD	X-ray Diffraction
XRF	X-ray Fluorescence

Abstract

The objective of this work was to understand the long-term corrosion behavior of Boral® and Bortec® neutron absorbers during deployment in a used nuclear fuel dry cask storage environment for several hundred years. Corrosion effects were accelerated by flowing humidified argon through an autoclave at temperatures between 300 and 570°C. Humidity levels ranged from 0.028 to 0.58 mass fraction with flow rates ranging from approximately 0.2 scfh to 1.5 scfh.

Results from corrosion testing at temperatures between 300 and 570°C with varying humidity have shown that both Boral® and Bortec® develop new aluminum-boron-carbon phases. The phases formed are consistent at 300 and 400°C. Different formations were observed at 570°C. The samples also showed boron depletion at all temperatures.

It is predicted that two mechanisms control the changes in Boral® and Bortec®. The phase changes observed result from the interaction of boron carbide with aluminum. These interactions result in boron and carbon diffusing into the aluminum matrix. The other series of interactions occurring between the sample and the water in the humidified argon. Boron on the surface rapidly reacts with the water to form B_2O_3 which can be volatilized. The loss of boron at the surface creates a concentration profile that can result in the continued diffusion of boron to the surface. The water will also react with the aluminum to form Al_2O_3. Aluminum oxide formed in humid conditions has some porosity and can degrade away and allow for continued oxidation of aluminum.

Additional research is required to determine the suitability of these materials for use in dry cask storage. The new phase formation may affect mechanical properties and adversely affect the fuel baskets structural integrity. Boron redistribution may cause localized areas of boron depletion, additional testing needs to be conducted to determine boron diffusion in these materials in the absence of humidity. In the presence of humidity the boron will leach from the samples. Cask humidity levels need to be determined to be able to predict how much boron may be lost.

Chapter 1 Storage of Used Nuclear Fuel

1.1 Used Fuel Storage

In the United States used fuel from commercial nuclear power plants is primarily stored in used fuel pools. However, these pools have limited capacity, a fact which is being accentuated by the operating license extensions that many power plants have applied for and many have been granted. In addition, the events at Fukushima Daiichi have raised public concerns about the safety of storing large quantities of spent fuel in these pools. The result has been an initiative to move more of the used fuel inventory into dry cask storage.

1.1.1 Used Fuel Pools

Upon removal from a reactor, used fuel is moved into a large pool for storage. Storage in a pool is essential for heat removal from the used fuel assemblies and to provide radiation shielding. Water quality and temperature in the pool are closely monitored and controlled. The water quality, or impurity levels, are especially important since even small amounts of impurity compounds can have pronounced effects on any materials stored in the water system [1].

Due to the large amount of used fuel stored in pools they have received the attention of policy makers and the public. Pool crowding and safety concerns have driven the deployment of dry cask storage of used fuel assemblies that have cooled. Even though these dry casks operate outside of the pool they are still affected by the fuel pools. The water from the pools is chemisorbed and physisorbed onto the assemblies, including the aluminum of the neutron absorbing materials[2, 3]. In addition, residual pool water can be left behind in the casks as a result of incomplete drying after loading. In order to understand the drive for cask storage as

well as corrosion potential in cask storage it is important to have an understanding of used fuel pools.

1.1.1.1 A Brief History of Used Fuel Legislation

During the early years of nuclear power in the United States power plant designers expected that the spent fuel pools would only need to accommodate 1 1/3 cores before the oldest assemblies were removed and taken to a reprocessing plant [4]. The U.S. pursued reprocessing and in 1966 the first privately owned reprocessing plant went online in West Valley, New York. Although the West Valley plant was privately owned, it reprocessed spent fuel from the defense weapons program. West Valley continued to reprocess defense waste until 1972, when stricter regulatory requirements forced the plant to shut down.

West Valley was the first and only commercial reprocessing plant to operate in the United States. In 1976 President Ford announced that work on reprocessing would be suspended. Then, in 1977, President Carter placed an indefinite ban on all reprocessing. The ban was lifted in 1981 by President Regan but subsequent administrations have failed to aggressively pursue reprocessing [5].

With the reliance placed on reprocessing, Congress had not enacted any legislation regarding the disposal of spent nuclear fuel. The reprocessing ban placed by President Carter created a need for regulation; the result was the Nuclear Waste Policy Act of 1982 (NWPA). The NWPA specified that the federal government would take responsibility for all commercial spent fuel by 1998. The NWPA called for construction of a geologic repository, and specified that civilian nuclear power reactors have the primary responsibility for providing interim storage of the spent fuel until the repository was completed [6]. The NWPA indicated that waste collection would begin in 1998 [6].

As directed by the NWPA, three sites were identified as potential candidates for the long-term repository. The NWPA was amended in 1987 to designate Yucca Mountain, Nevada as the only site to be characterized [6]. Characterization of Yucca Mountain continued until 2010 when President Obama cut funding to the Office of Civilian Waste Management which was in charge of Yucca Mountain. Obama took the funding cut a step further in his 2011 budget proposal where he proposed that all funding be zeroed out for the next 10 years and the Office of Civilian Waste management be dissolved. These budget cuts stopped work on the only repository candidate in the United States [7].

1.1.1.2 Increasing the Capacity of Spent Fuel Pools

The size and location of spent fuel pools differ from site to site (Figure 1). The pools are all typically around 12 meters deep and extend around 12 meters or more in each horizontal direction [8]. The pool depth allows for approximately 8 meters of water above the top of the fuel assemblies. This allows the water to provide adequate shielding, even during fuel assembly transfers. Pools are typically constructed with 1.2-2.4 meter thick concrete walls. Pools also contain a 6 to 13 centimeter thick stainless steel liner [8].

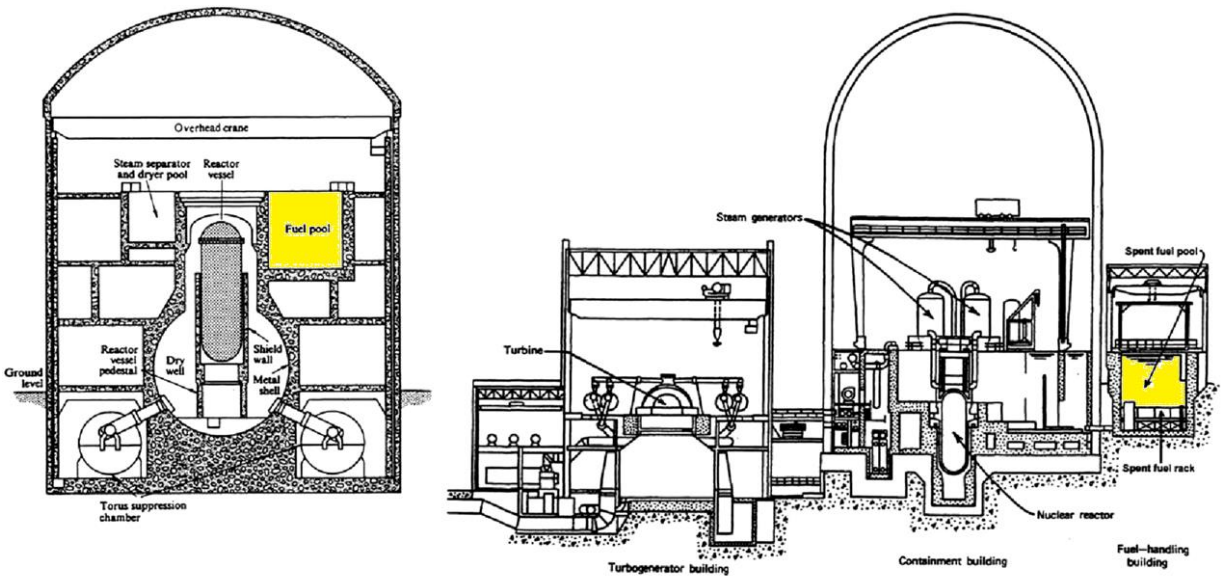

Figure 1. Locations of spent fuel pools in a typical BWR reactor (left) and a PWR reactor (right)

As delays crept into the development of a repository it became apparent that the original designs for the spent fuel pools would not be sufficient to hold all of the spent fuel that was being generated. To be able to safely store spent fuel, utilities began to find ways to increase their pool's capacity. One method that was used was the addition of approximately 2000ppm of boron to pool water [9]. To use the boron, utilities had to show that they could maintain k_{eff} less than or equal to 0.95 with 95% probability at 95% confidence at operating chemistries and less than 1 if all the boron in the water were lost [10]. This allowed some increase in packing density but it still wasn't sufficient.

To further increase the pool's capacity, utility companies began using free-standing high-density rack configurations [4]. These racks incorporate neutron absorbing materials into their structure to help maintain criticality control, shown as Boraflex in (Figure 2). Virtually all of the spent fuel pools in the U.S. have been re-racked using these high density casks that allow the pools to pack spent fuel assemblies in near reactor-core densities [11]. Currently fuel pools are

in use at all 65 operating reactor sites in the U.S. along with 8 former reactor sites and one additional site not associated with a power reactor [8]. It is estimated that of these sites with active reactors up to three or four will reach full capacity in their pools each year until at least 2019 [8].

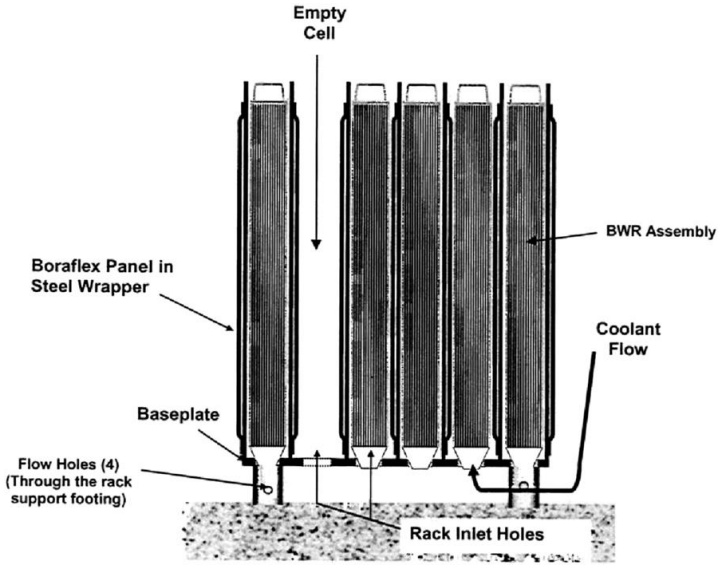

Figure 2. Cross section of a storage rack used for dense packing of BWR fuel in a used fuel storage pool.

1.1.1.3 Hazards Associated With Dense Packing in Spent Fuel Pools

When spent fuel is discharged from a reactor it is both thermally and radiologically hot. The water in the pool acts as radiation shielding in addition to keeping the fuel assemblies cool. The pools use large pumps and heat exchangers to remove the decay heat and prevent the water from boiling. If the cooling systems are lost then the temperature of the water will rise until the pool beings to boil. If no action is taken then, over time, the water will boil away until the fuel assemblies are uncovered. The amount of time that it takes for the fuel to become uncovered depends on how full the pool is and the age of the assemblies in the pool.

Loss of water in the fuel pool can also occur through other means. Although the pools themselves are very robust it is possible that a well-directed terrorist attack could cause the pool to completely drain [12]. There is also concern that significant seismic activity could cause the fuel pools to rupture. Heightened fears of seismic damage arose as a result of the March 11, 2011 earthquake in Japan. Particular concern was given to the spent fuel pool at Fukushima Daiichi Unit 4 since it had a fresh core off-load in it. However, subsequent investigations and calculations indicate that the fuel pool remained intact and that the water levels never dropped sufficiently to uncover any of the assemblies [13].

Loss of cooling in a spent fuel pool can result in the self-sustained oxidation of the zirconium fuel cladding. Self-sustained oxidation of zirconium occurs around a temperature of 1173K in air and 1473K in steam [14]. The result is the failure of cladding and release of a significant amount of volatile fission products such as Cs-137 along with potential release of additional fission products if the temperatures increase sufficiently. The use of high-density racks in the pool further exacerbates these problems.

As the fuel is packed tighter and tighter into the pools the ability for natural convection to cool the assemblies in the event of an accident has decreased [15]. This loss of cooling allows for temperatures between elements to greatly increase. Eventually it is possibly that the Zircaloy fire could propagate from recently discharged assemblies to lower power assemblies [16]. In any given assembly the heat flux from the fuel inside combined with the heat flux from the outside could result in cladding within 100-400 seconds from the time that water is lost and could result in between 5 and 20 percent of the fuel being dissolved [17]. The resulting release of radionuclides could result in widespread contamination [11].

1.1.1.4 Removing Spent Fuel from the Pools

Reducing the amount of spent fuel in the pools will reduce the total heat generation in the pool, allow for improved natural convection during an accident, and reduce the total radionuclide inventory. Upon removal from the reactor the thermal power of a fuel assembly decreases rapidly. Within a year of discharge from the reactor, decay-heat production in spent nuclear fuel is dominated by four radionuclides: Ruthenium-106 (372.6-day half-life) cerium-144(284.4-day half-life), cesium-137(30.2-year half-life), and cesium-134 (2.1-year half-life) and their short-lived decay products contribute nearly 90 percent of the decay heat from a spent fuel assembly[8]. The short half-life of these nuclides results in continued rapid decrease of decay heat for a period in excess of 100 years (Figure 3)[18]. Spent fuel that has been out of the reactor for more than 5 years can safely be removed from the pool and cooled using natural convection in dry cask storage.

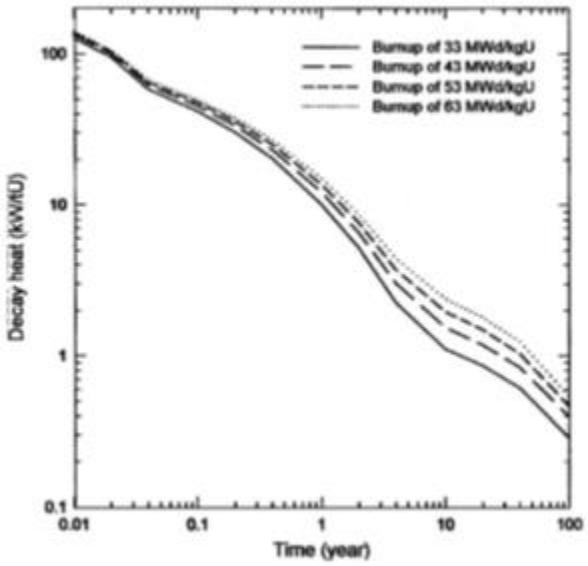

Figure 3 Decay heat in spent fuel for various burnups as a function of time since discharge

1.1.2 Dry Cask Storage

1.1.2.1 General Cask Information

Dry cask storage gets its name from the dry environment in which spent fuel is stored as opposed to the wet storage of spent fuel pools. They are passively cooled and rely on natural conduction and convection to keep the fuel cool [8]. These casks are designed to meet four safety objectives: (1) ensure that doses from used fuel in storage systems are less than limits prescribed in the regulations, (2) maintain subcriticality under all credible conditions, (3) ensure that there is adequate confinement and containment of the used fuel under all credible conditions of storage and even "redundant sealing of confinement systems," and (4) allow the ready retrieval of the used fuel from the storage systems[19] [20]. Part of the ready retrieval requirement includes the stipulation that the fuel must be able to be recovered in wet or dry spent fuel loading and unloading facilities [21].

Each cask is designed to hold up to 10-15 tonnes of spent fuel. This is equivalent to about 32 Pressurized Water Reactor (PWR) assemblies or 68 Boiling Water Reactor (BWR) assemblies. Typically they used concrete, steel, and/or lead to shield from gamma radiation and polyethylene, concrete, water, and/or boron-impregnated metal or resins to shield neutrons [8]. These casks help to minimize potential release of radioactive material by dividing up the spent fuel among multiple canisters and by the robustness of these canisters.

There are primarily two different types of casks that have been designed: bare fuel and canister based (Figure 4). In bare-fuel casks the assemblies are placed directly into a basket that is integrated into the cask. In canister-based casks the assemblies are placed in a basket that is integrated into a thin-walled cask. The thin-walled cask is then placed into a thick-walled overpack [8]. These casks are then subdivided into horizontal or vertical storage applications.

Each cask is also classified according to its use: single-, dual-, or multi-purpose [8]. Single-purpose casks are licensed for storage only and dual-purpose casks are licensed for storage and transportation. Multi-purpose casks are licensed for storage, transport, and disposal but since a long-term repository solution has not been developed no casks have received a multi-purpose license.

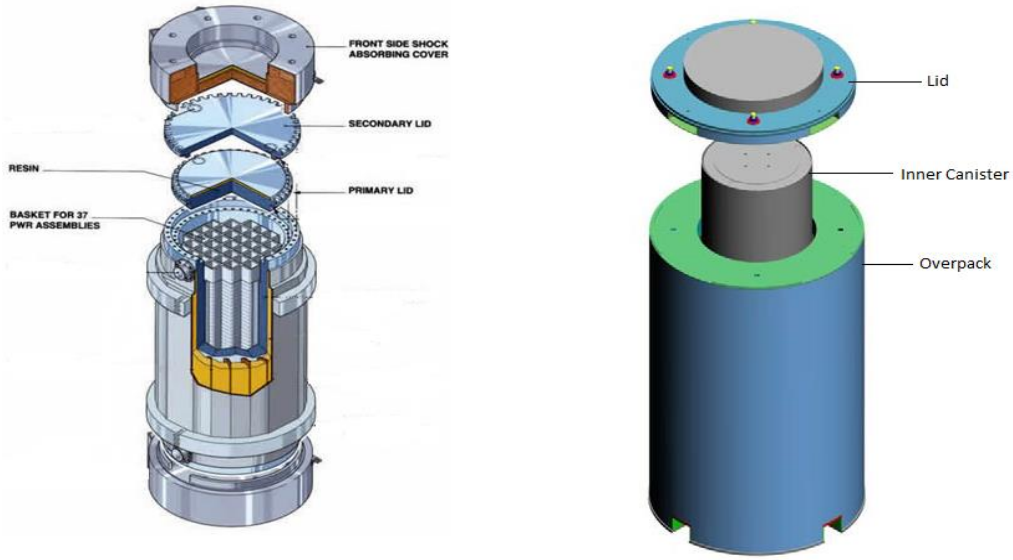

Figure 4. Representations of a typical bare-fuel cask (left) and canister-based cask (right)

1.1.2.2 Dry Cask Loading and Drying

Although the casks are intended for dry storage they are loaded wet. Loading begins with the cask being filled with water and subsequently submerged in the fuel pool. Only intact fuel elements are loaded into the fuel basket in the storage container. Any damaged fuel rods are first loaded into special containers before they are loaded into the cask [18]. After loading, the cask is removed from the pool. It is then decontaminated and the lid is sealed on. After the cask has been sealed the water is drained out and the cask is dried, typically by vacuum drying or forced helium dehydration. After drying, which can take up to one week, the cask is backfilled with

helium and all vents and drains are sealed. The integrity of the seals is checked and the cask is then moved to a concrete storage pad. If the cask is properly sealed then helium loss over 1000 years of storage is expected to be negligible [18].

Drying is the longest part of the cask loading process but is also one of the most critical. Drying prevents internal damage to the canister from over-pressurization or corrosion; it also helps minimize hydrogen generation that may occur as internal materials corrode [22]. Even after drying some water may continue to reside in a variety of forms on the fuel, cladding, or internal cask components. The forms that have been found to exist include unbound water, ice, physisorbed water, and chemisorbed water [22]. The residual water often comes from CRUD and sludge along with defects in fuel rods. Water can also get trapped in guide tubes if a dashpot drain hole is blocked [22].

Residual water is especially concerning for aluminum-clad spent nuclear fuel and any aluminum components that may exist inside the cask. The concern comes from the large quantities of stainless steel that are typically present in storage containers. Galvanic coupling between the stainless steel and aluminum can occur and accelerate corrosion of the aluminum [22]. Corrosion of all components is further accelerated by the potential for radiolysis of the water by the radiation given off from the spent fuel. Gamma radiolysis has resulted in hydrogen pressure increases of up to 10 psi in an enclosed system [22]. This is especially a concern during loading and unloading operations where the radiolysis of water can create sufficient hydrogen gas that it achieves combustible concentrations [23].

If correct drying procedures are used most of the water can be successfully removed from the system. One of the limits placed on casks during drying is temperature limits. The recommended temperature limit for short-term loading operations is 400°C. In addition thermal

cycling should be limited to less than 10 cycles with cladding temperature variations less than 65°C per cycle [19]. To prevent exceeding the temperature limit casks with high decay heat are dried using forced helium dehydration [23]. In forced helium dehydration helium gas is circulated through the canister to evaporate and removed any moisture. The gas exiting the demoisturizer is held below 21°F for at least 30 minutes to ensure that the system is dry [24].

If a system does not have high decay heat then a vacuum drying system is commonly employed. A stepped evacuation process is used to ensure that there is no ice formation during the drying process. The internal pressure is slowly reduced to about 3 torr and held there for at least 30 minutes to ensure that all the water is gone [24].

1.1.2.3 Dry Cask Internal Environment

1.1.2.3.1 Humidity

There are three major factors inside a dry cask storage canister that affect a materials performance: humidity, temperature, and radiation. The humidity levels are kept low through proper application of the correct drying process. As discussed earlier though, water can become trapped in various geometries as well as being chemisorbed and physisorbed to various materials. In addition, cracks and pores in a surface can hinder the drying of physisorbed water and be a source of water that is slowly released during the storage period.

Even though great care is taken in drying the cask, assessing long-term performance of a dry cask storage canister's incomplete drying must be taken into account since currently the casks are not monitored for humidity levels. Oxidation due to air ingress is not suspected to be a problem since the casks are backfilled with helium and slightly pressurized. The casks are then monitored for helium leakage and for pressure loss. Thus any ingress of air is expected to be caught quickly.

1.1.2.3.2 Radiation

Since the fuel to be stored in the casks is contained either in its cladding or some other containment the total alpha and beta radiation doses on the neutron absorbing material is expected to be negligible. The gamma and neutron dose received depends on a number of factors including fuel burnup, storage time in the pool, and the self-shielding of the fuel assemblies. Estimates of the total neutron and gamma fluence from the spent fuel during 300 year storage can be obtained through use of the ORIGEN code.

For calculations of the neutron fluence, ORIGEN includes the neutrons generated by spontaneous fission along with neutrons from other sources such as alpha,n reactions. Likewise for the total photon (gamma) fluence ORIGEN includes gamma from radioactive decay as well as gammas generated due to interaction of radiation with other materials present in the storage cask. Table 1 shows the simulation parameters and the results returned from ORIGEN. Note that the values given for areal fluences are calculated from dimensions and loadings from typical fuel assemblies and are the fluences that would be incident on the neutron absorbing material assuming no self-shielding from the fuel assemblies.

Table 1 - Results of ORIGEN fluence calculations for 300 year dry cask storage

Scenario Parameters	
BWR Fuel Type	GE 8x8 BWR
PWR Fuel Type	w17x17 PWR
Enrichment	5 wt%
Burnup	60000 MWd/MTU
Power History	100% up
Average Power	25 MW/MTU
Cooling Time in Spent Fuel Pool	3 years
Cumulative Fluence for 300 year storage	
BWR Neutron Fluence	1.21×10^{18}/MTU (1.32×10^{13}/cm^2)
BWR Photon Fluence	1.92×10^{25}/MTU (2.1×10^{20}/cm^2)
PWR Neutron Fluence	1.77×10^{18}/MTU (1.94×10^{13}/cm^2)
PWR Photon Fluence	1.96×10^{25}/MTU (2.15×10^{20}/cm^2)

1.1.2.3.3 Temperature

Although spent fuel is initially allowed to cool in the pool, significant decay heat is still generated during dry cask storage. Figure 3 shows the rapid decrease in decay heat during the first 100 years of storage. An EPRI numerical simulation of cladding temperatures at the hottest axial position in the fuel rod decreases from 400°C to 300°C after the first 10 years and will drop to 260°C after 20 years, 235°C after 30 years, and 220°C after 40 years [18]. The maximum cladding temperature occurs around 14 meters up from the bottom of the casks. Figure 5 shows how the temperature varies with height inside the cask.

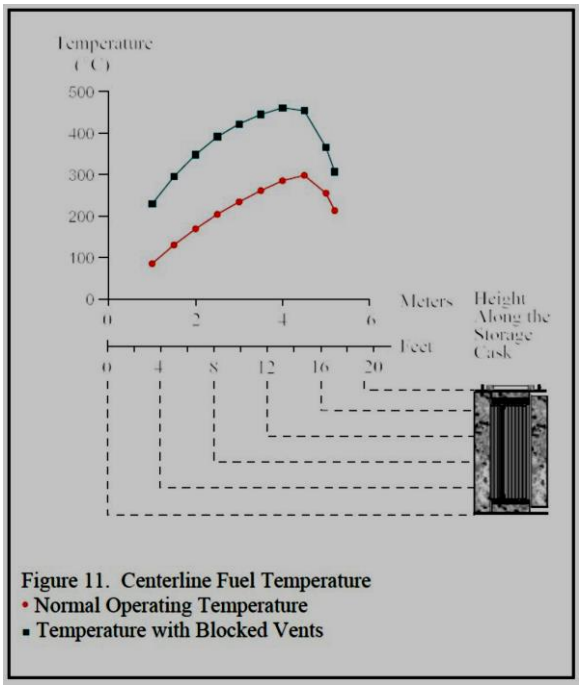

Figure 5: Cladding temperature as a function of vertical position in a typical cask

Temperature is one of the most critical parameters in considering the safety and reliability of dry cask storage. The design and operation of the casks is based around the need to keep the spent fuel cool. According to the NRC the maximum calculated fuel cladding

temperature should not exceed 400°C for normal conditions of storage and short-term loading operations. During loading operations, repeated thermal cycling may occur but should be limited to less than 10 cycles, with cladding temperature variations that are less than 65°C each. For off-normal and accident conditions, the maximum cladding temperature should not exceed 570°C [19].

1.1.2.4 Short-term Licensing

Currently, licensing of casks is for a period of no more than 40 years [25]. Given the original hope of the development of a permanent repository this time period seemed reasonable. However, given the uncertainty surrounding a permanent waste solution it is becoming apparent that dry casks may have to be used for a much longer duration. In preparation for extended use of dry cask storage the Nuclear Waste Technical Review Board (NWTRB) evaluated the technical basis for extending the use of dry cask storage and issued their report in 2010.

Among the findings of the NWTRB was that "The technical information currently available, together with the experience gained to date in the dry storage of spent fuel, demonstrates that used fuel can be safely stored in the short term and then transported for additional storage, processing, or repository disposal without concern. However, additional information is required to demonstrate with similarly high confidence that used fuel can be stored in dry-storage facilities for extended periods without the fuel degrading to the extent that it may not perform satisfactorily during continued storage and subsequent transportation" [18]. This critique of research pertaining to fuel performance also held true for the performance of various materials in use as part of the dry cask system.

1.2 Neutron Poison Materials Used in Spent Fuel Storage

This study focuses on two materials that are in use as neutron poisons in spent fuel storage: Boral® and Bortec®. Both of these materials are aluminum/boron carbide composites that are typically manufactured in plate form and incorporated into the fuel baskets housing spent fuel assemblies in both spent fuel pool and dry cask storage. Both of these materials are produced by Ceradyne, Inc, now a subsidiary of 3M.

The major difference between the Boral® and Bortec® is that Boral® is classified as a cermet while the Bortec® is considered a metal matrix composite (MMC). The difference between a cermet and an MMC is in the manufacturing process. An aluminum cermet like Boral® is produced from an ingot that is an aluminum clad container filled with a homogeneous mixture of boron carbide powder and atomized aluminum powder. The ingot is heated and then hot-rolled into plate form, sintering the powder in the process. However, the sintering process is not complete in that the core contains some porosity [26]. Alternately, an MMC ingot is formed by casting or a power metallurgical process under high pressure. The final rolled plate is void of internal porosity [26].

1.2.1 Boral®

1.2.1.1 Boral® Manufacturing Process

The manufacturing of Boral® starts with an 1100 alloy aluminum box that holds the aluminum/boron carbide powder blend. The box is between 12 and 15 inches on a side. The height of the box depends on the desired thickness of the finished core. The walls of the box are typically around 1 inch thick. The powder used is prepared in a mixing mill using 1100 series aluminum and up to 65% nuclear grade boron. The boron carbide particle sizes range from 75 to 250 microns with the average particle size being 85 microns [26].

After the aluminum box is filled with the aluminum/boron carbide powder a top is welded on and vent holes are added to provide a pathway for air to escape during heating and rolling. In 2004 the manufacturing process changed to incorporate a preheating of the powder-filled aluminum box. The box is heated to 1000F and held at temperature for 6-7 hours followed by a slow cool to 700F. This process help facilitate the sintering of the powder, thus reducing the porosity [26].

The result is a flat sheet consisting of a core of uniformly mixed and distributed boron carbide and 1100 aluminum particles sandwiched between two sheets of solid 1100 aluminum that acts as a surface cladding. Figure 6 shows a cross-sectional image of Boral® in which the cladding and core regions are clearly visible [26].

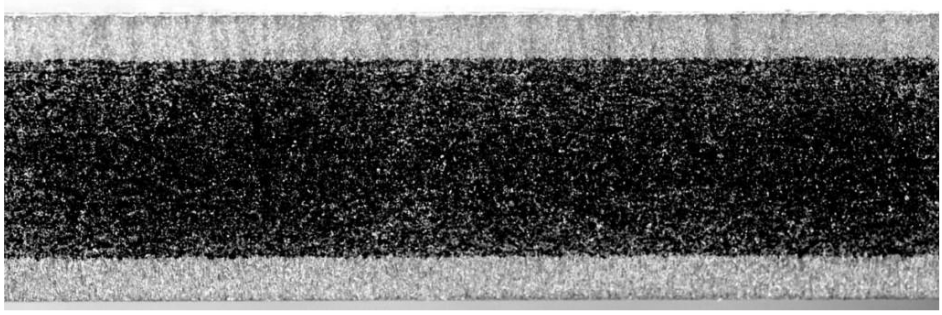

Figure 6 - Cross section of Boral® showing the porous core region (dark) that contains the boron carbide and the two outer aluminum clad layers (light) that sandwich and support the core

1.2.1.2 Boral® Properties

During the manufacturing of Boral® care is taken to limit the amount of impurities allowed. These impurities can affect the corrosion resistance and mechanical properties of Boral®.

Table 2 contains the impurity limits that are allowed in Boral®[26].

Table 2 - Maximum impurity levels in Boral®

Element	Limit
Fe	≤0.5%
Si	≤0.1%
Ti	≤0.1%
Cu	≤0.1%
Zn	≤0.1%

The density of Boral® is dependent upon the core thickness and boron carbide loading. Typical densities reported for just the clad layer are 2.713 g/cm^3 which compares well to the standard density of aluminum at 2.7 g/cm^3. The typical core density is reported at 2.481 g/cm^3. The maximum theoretical core density with 50% boron carbide loading by volume is 2.61 g/cm^3. Accordingly, the standard core has approximately 5% porosity [26]. Total Boral® densities (cladding plus core) as a function of core thickness are given in Table 3.

Table 3 – Boral® density as a function of core thickness. Given densities are based on a clad thickness of 12.5 mils

Core Thickness (in)	Density (g/cm^3)
0.05	2.557
0.06	2.548
0.07	2.541
0.08	2.536
0.09	2.531
0.10	2.527
0.11	2.523
0.12	2.520

Although 1100 alloy aluminum is extremely corrosion resistant it is not very strong and therefore generally not used as a structural material. It has most of the same properties as pure aluminum since total impurities and alloying agents are maintained less than 1%. Like aluminum it can be work hardened, though work hardening does make the material more brittle.

1.2.1.3 Issues with Boral®

Boral® has been continuously employed since it was first added to the Yankee Rowe spent fuel pool storage racks in 1964 [26]. Since that time it has been deployed in over 100 spent fuel pools and dry cask storage sites around the world. In that time it has performed functioned properly, though concerns have been raised with regards to blistering that has been noticed.

Since Boral® is not a structural material any loss to mechanical integrity due to the blistering has been ignored. The blisters have not been noticed to cause changes to Boral®'s neutron absorbing properties but the blisters do cause two potential problems. First, the blisters can reduce the free clearance in the cells that hold the fuel assemblies. This reduced clearance could impede recovery of the fuel assemblies from the storage rack. Secondly, the blisters cause water to be displaced from the flux trap region between storage cells. This reduces the amount of water in the flux trap, reducing its ability to thermalize neutrons[26].

The extent to which the Boral® blisters depends on when it was manufactured. Boral® manufactured in the 1970s develops series of small blisters that typically do not extend more than 1 inch in from the edge of the material. Boral® manufactured in the 1990s has been seen to blister along the edge as well as in the center of the coupons [26].

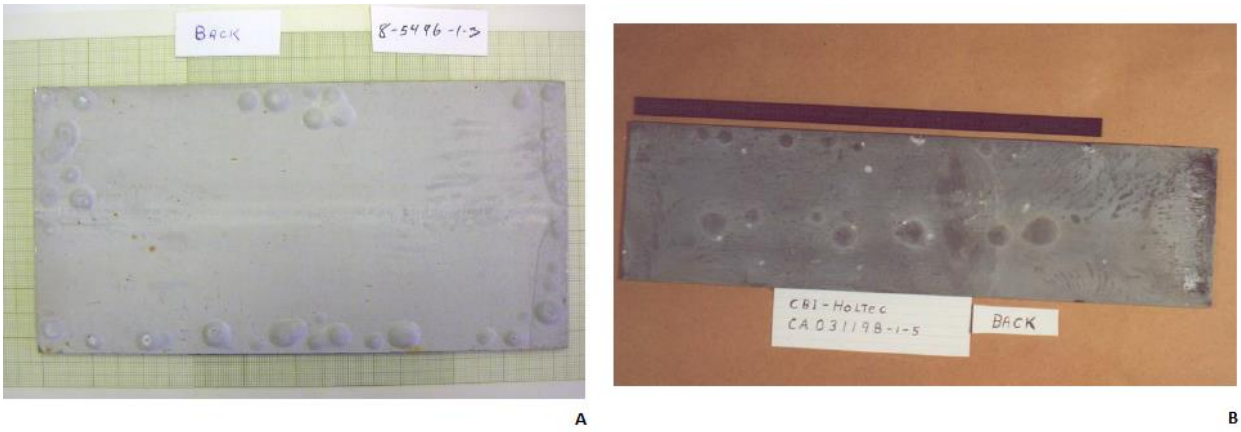

Figure 7 - Blistering in Boral®. Figure A is a sample of Boral® produced in the 1970s and Figure B is a sample manufactured in the 1990s. Both samples came from the same BWR pool [27]

Blistering of Boral® in spent fuel pool racks has generally been minimal due to rack designs that sandwiched the Boral® within seal-welded stainless steel cover plates. Water ingress into these cover plates had led to corrosion of the Boral® and bulging of the cover plates due to gas buildup. The bulging was sufficiently severe to cause a problem with interference with the fuel assemblies [28].

The blistering of Boral® has not been limited just to the plates that were used in spent fuel storage. Boral® used in dry cask storage at the AECL Chalk River Laboratory was observed to have blistered during the vacuum drying process. This blistering led to deformations of the basket wall. Equipos Nuclear S.A. in Spain performed drying tests on full sized baskets and canisters to further study this problem. In their tests, several cells failed during the drying tests due to the Boral® clad becoming delaminated from the cores and forming blisters [26]. One of the concerns with blistering and general corrosion in dry cask storage applications is that the corrosion process produces hydrogen. In some instances, sufficient hydrogen has been generated to raise the lid on a storage cask [28]. This creates an explosion concern during the cask lid welding process.

According to a test by EPRI, ENRESA, and NAC, the most important parameter influencing blister formation in Boral® is the amount (and nature) of core porosity inherent in the Boral®. Samples of Boral® with greater as-fabricated core porosity had more corrosion but was less likely to experience blistering. This is most likely due to the pores providing pathways for the corrosion gasses generated to escape. Boral® samples with less porosity had increased blistering. This is likely due to the pores allowing water to ingress into the sample but the volume expansion that accompanies the aluminum-to-aluminum oxide transformation seals off the pores and traps the gasses inside the sample. Improvements made to the Boral® manufacturing process have greatly reduced blistering, though the presence of corrosion-induced pits on the aluminum cladding provide a pathway for water ingress that has led to blister formation [26].

1.2.2 Bortec®

Bortec® is an aluminum/boron carbide MMC. It is produced using the powder metallurgy technique of hot vacuum pressing. As such it is considered fully dense and does not show much porosity [27]. The matrix material is an aluminum 6090 alloy with the purity requirements given in Table 4. Bortec® also uses Type 3 of ASTM C-750 89 (re-approved 1997) nuclear graded boron carbide along with additional requirements that are given in Table 5.

Table 4 - Specifications for Al 6090 [27]

Element	Weight%
Silicon	0.4-0.8
Iron	0.5 Max
Copper	0.15-1.0
Manganese	0.15 Max
Magnesium	0.8-1.2
Chromium	0.15 Max
Zinc	0.25 Max
Titanium	0.15 Max
Oxygen	0.05-0.50

Others, Each	0.05 Max
Others, Total	0.15 Max
Aluminum	Remainder

Table 5 - Boron requirements for Bortec® [27]

Item	**Requirement**
Total boron	76.0 wt% min
HNO_3 soluble boron	0.9 wt% max
Water soluble boron	0.3 wt % max
Iron	0.5 wt% max
Total (boron + carbon)	97.0 wt% min.
B-10	19.90 ± 0.3 atom%

The field performance of Bortec® is not well known since Bortec® is a relatively new material and has not been as widely implemented as Boral®. Given the past performance of Boral® along with the high density it is expected that Boral® will be able to perform without complication. Additionally, since Bortec® is nearly fully dense and made using a 6000 series aluminum alloy it is anticipated to see use as a structural material. This makes Bortec® testing critical.

Some initial testing of Bortec® has been performed by EPRI. EPRI performed a short duration, high temperature test over 48 hours at 900°F (482°C). Two long-term tests were also performed; the first was carried out at 750°F (399°C) for 4623 hours, and a second was carried out at 195°F (90.6°C) for 4560 hours in boric acid and demineralized water. Upon completion of the testing it was noted that insignificant to minimal changes were noticed in the categories of mass, dimension, hardness, tensile strength, or boron-10 areal density. No accelerated corrosion effects were noticed around scratched regions nor around welds [27].

1.3 Properties and Behavior of Aluminum and Boron Carbide

To be able to predict how these neutron poison materials will behave during dry cask storage it is important to have an understanding of the structure and behavior of aluminum and boron carbide. Aluminum is a very important material in manufacturing and its use has been consistently increasing. Much of its attractiveness in manufacturing comes from its light weight as well as its corrosion resistance. Boron carbide is also widely used in a variety of applications including armor plating, automotive brakes, abrasives, cutting tools, and even as fuel for ramjets. Aluminum/boron carbide MMCs have also been deployed across industries in applications such as high performance drive shafts in cars. Yet with all of this attention, very little is known about how these materials perform in the environment that is found inside a dry cask storage canister.

1.3.1 Physical Properties

1.3.1.1 Aluminum

Aluminum is a silvery metal that is highly ductile and malleable. Though not as strong as many steels it's low density has made it a popular material choice in applications where weight is a factor. Table 6 compares the strength and density of various steel, titanium, and aluminum alloys. Though the aluminum alloys are not able to match the upper end of the steel alloys or the titanium alloy for strength the density is 40% lower than titanium and almost one third that of steel. Aluminum is also a very soft metal with a hardness rating of 2.75 on the Mohs hardness scale.

Table 6 – Strength and density of various materials

Material	Yield Strength (MPa)	Ultimate Strength (MPa)	Density (g/cm^3)
A36 Structural Steel	250	400	7.8
1090 Carbon Steel	250	841	7.58
A514 Steel	690	760	7.8
AISI 4130 Steel	951	1110	7.85

AISI A11 Tool Steel	5171	5205	7.45
Titanium 11	940	1040	4.5
2014 Aluminum	414	483	2.8
6063-T6 Aluminum		248	2.63

Like most metals, aluminum is at solid a room temperature and does not melt until it reaches a temperature of 660°C. It remains a liquid until it reaches its boiling point of 2467°C. As a solid, aluminum organizes into a face centered cubic crystal structure. Solid aluminum is also both thermally and electrically conductive and has moderate heat capacity and thermal expansion.

Aluminum atoms are organized into a face-centered cubic (FCC) lattice structure, identified by the Fm-3m space group. The characteristic cell parameter for the aluminum lattice is a=4.04963Å. Since aluminum is a metal, bonding between atoms is a metallic bond with strong overlap of the external electron shells.

1.3.1.2 Boron Carbide

Boron carbide has many unique characteristics that have resulted in it gaining a lot of attention for use in a variety of applications. Boron carbide is also one of the hardest materials known (just below diamond and cubic boron nitride) and so it is often used as an abrasive and cutting material along with use as a coating on materials to prevent wear. Boron carbide is thermally stable and at temperatures above 1200°C it has been reported that its hardness exceeds that of diamond [29]. Due to its thermal stability and high melt temperature of 2763°C it has seen use in many high temperature applications. Boron carbide excels in ballistic performance and has seen widespread use in bullet-proofing. Boron carbide is also chemically inert and can thus be used in many chemically aggressive environments. In addition boron carbide is a high temperature semi-conductor and can be used to create electronic devices suited for use in high temperature situations. [30, 31]. Along with its impressive capabilities on its own, it is also

often used as an alloying element, particularly for use in metal matrix composites such as high performance drive-shafts in automobiles. These properties, along with its ease of synthesis and low cost make it a very practical material.

Along with its unique properties, boron carbide has a fairly unique crystal structure. The basic crystal structure is rhombohedral with the $R\bar{3}m$ space group. The rhombohedrum consists of 12-atom icosahedra that lie on the vertices and a 3-atom chain that links the icosahedra along the (111) rhombohedral axis [32]. The crystal structure of boron carbide can also be described using hcp coordinates in which the chains lie along the <c> axis as seen in Figure 8 [31]. The presence of icosahedra within the boron carbide structure is a consequence of the ability of boron to form caged structures. The icosahedra are essentially two pentagonal pyramids that are bonded together. This shape results in the icosahedra having two chemically unique sites located at the polar and equatorial positions. The polar sites are identified as those that link the icosahedra together. The equatorial positions are those sites that the 3-atom chains bond to, resulting in a hexagonal chair within the icosahedra [31].

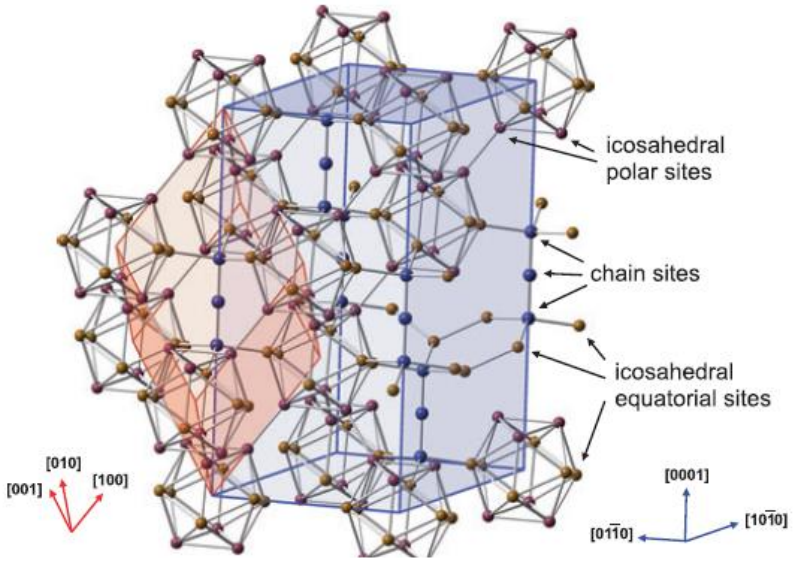

Figure 8 – Ball and stick model representing the boron carbide structure and showing the boron icosahedra that occupy the lattice sites [31]

Although the structure of boron carbide is known, there is still uncertainty about the location of the carbon atoms [29, 31, 33]. The difficulty in determining the position of the carbon arises because the x-ray form factors of boron and carbon are too close to allow certain distinction. Neutrons have also been used to attempt to discern the structure of boron carbide but the scattering length of boron-11 and carbon-12 are too close to allow differentiation. To help overcome the limitations of experimental methods, much effort has been but into modeling the boron carbide and determining which models best match up with the experimental data.

Part of the difficulty with accurately modeling the boron carbide structure is the disagreement about the relative strengths of inter-icosahedra and inter-icosahedra bonding, along with trying to identify the nature of the bonding in the three-carbon chain. The evidence suggests that inter-icosahedral bonds are strong than the intra-icosahedral bonds, making boron carbide an "inverted molecular solid" [29]. Based on the current evidence, the generally accepted structure of B4C boron carbide consists of $B_{11}C$ icosahedra with the carbon atom occupying a polar site and the icosahedra interconnected by a C-B-C chain [31].

One of the unique characteristics of boron carbide is its ability to adapt to a wide range of compositions without changing it basic structure. The stable range of carbon solubility in boron carbide is well agreed to be between ~8 at% and ~20 at%. This corresponds to a compositional range between $B_{12}C_3$ and $B_{14}C$. This wide diversity of compositions adds difficulty in determining the location of the carbon atoms and it is not precisely known how the site occupancy changes with composition.

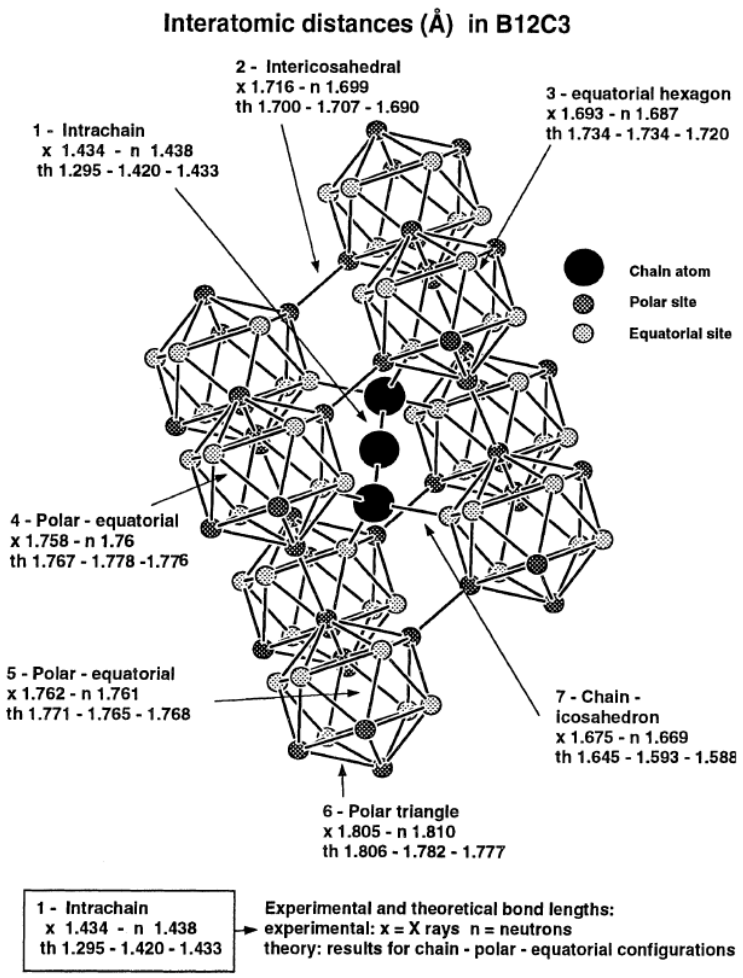

Figure 9 - Atomic positions and interatomic distances in $B_{12}C_3$ boron carbide. Note that the distances will change as the composition changes [33]

One theory for the site loading of carbon suggests that, with increasing boron concentration, the boron is preferentially substituted along the C-B-C chain, resulting in the formation of CBB chains. As the boron content increases the number of C-B-B chains increases until all chains have been substituted. This corresponds to the $B_{6.5}C$ stoichiometry or a composition of 13.3 at% C. As the carbon concentration continues to decrease, the substitution of boron for carbon will occur within the icosahedra until the stoichiometry decreases to 6.7 at% C with a (B_{12})CBB configuration [31].

An alternative theory proposes that carbon is preferably replaced by boron at the icosahedra site. Thus, as the carbon concentration decreases down toward the stoichiometric B6.5C phase the structure is given to be (B_{12})CBC. As the carbon concentration continues to decreases from 13 at% down to 8 at%, the boron begins to occupy chain sites resulting in the (B_{12})CBB configuration [31]. Other theories include the possibility of displaced central atoms and vacancies in the chain at boron-rich compositions [31, 32].

Of additional interest is the presence and effect of defects and impurities. One common property of boron-rich compounds is disordered atomic arrangements in the ground-state. These defects are not due to entropic effects at high temperatures but result in macroscopic residual entropy, allowing for these materials to be classified as frustrated. In addition to natural disorder, all poly-crystalline boron carbides contain free-carbon impurities in the form of either amorphous carbon or intra-granular graphitic inclusions [31]. Differences in carbon content and the presence of impurities (especially Al, and Si) cause variations in mechanical properties that make comparisons between different samples of boron carbide difficult [34].

1.3.2 Irradiation Behavior

Since materials used in dry cask storage are exposed to a radiation environment it is important to understand the effects that irradiation can have on the materials. Since aluminum and boron carbide have such different physical properties we can expect that they will both behave differently in a radiation environment. Thus we will look at each separately.

1.3.2.1 Aluminum

Research regarding the irradiation effects in aluminum mainly stems from the use of aluminum as a cladding material in research reactors. As radiation effects in aluminum have been studied there are two striking differences that set aluminum apart from other materials.

First is that the radiation damage is affected strongly by solid silicon which develops as a transmutation product. The second feature is that Al seems to be much more tolerant of radiation effects than most other metals, at least at ambient temperatures [35].

1.3.2.1.1 Activation Products and Impurities

One advantage of using aluminum for nuclear applications is the absence of long-lived radioisotopes produced as a consequence of neutron activation. Most of the activity produced by neutron irradiation of aluminum comes from the ^{24}Na produced by the ^{27}Al(n,α)^{24}Na reaction. The ^{24}Na decays by γ-emission with a half-life of 15 hours. Additionally, ^{27}Al can react with thermal neutrons and produce ^{28}Si by the following two-step reaction:

$$^{27}Al + n_{th} \rightarrow {}^{28}Al + \gamma;\ {}^{28}Al \rightarrow {}^{28}Si + \beta^{-}.$$

The Si is insoluble in aluminum at temperatures below ~350°C and typically precipitates out in its elemental form. The Si precipitates make a substantial contribution to radiation damage in Al and is the dominant hardening agent at high thermal neutron fluences [35].

In addition to activation of the aluminum, some of the alloying elements can also become activated during neutron irradiation. The three alloy elements that contribute the most to the activity of neutron irradiated aluminum are iron, zinc, and chromium. Table 7 lists the neutron activation products for the major alloying elements in aluminum. Upon removal from a neutron source one of the major sources of activity will be from the copper, though after 5 days the copper will be decayed away. Of the rest of the isotopes, only Fe-54 has a half-life measured in years but Fe-54 only makes up 5.8% of the iron in the aluminum, thus minimizing its impact.

Table 7 - Neutron activation products in aluminum

Isotopic Composition (mole fraction)	Isotope	Reaction	Daughter	Half-life
0.043	Cr-50	(n,γ)	Cr-51	27.70 d
0.69	Cu-63	(n,γ)	Cu-64	12.70 h
0.31	Cu-65	(n,γ)	Cu-66	5.100 m
0.058	Fe-54	(n,γ)	Fe-55	2.700 a
0.0028	Fe-58	(n,γ)	Fe-59	44.53 d
0.48	Zn-64	(n,γ)	Zn-65	243.9 d
0.19	Zn-68	(n,γ)	Zn-69	57.00 m

Another potential trace inclusion in aluminum is boron carbide. Natural boron contains 19.8% boron-10 which has a neutron capture cross section of 3835 barns. Upon neutron capture the B-10 produces helium and lithium daughter products. In aluminum, the recoiled He atom has a range of ~5μm and can segregate in a well-defined halo around the parent particle. The Li daughter nuclide has a smaller range than the He and produces a halo around the parent particle with a radius smaller than that of the He halo. Where a halo intercepts a grain boundary the voids seem to disappear, but they become visible as bubbles upon annealing [35]. Figure 10 shows these halos around a suspected B4C particle.

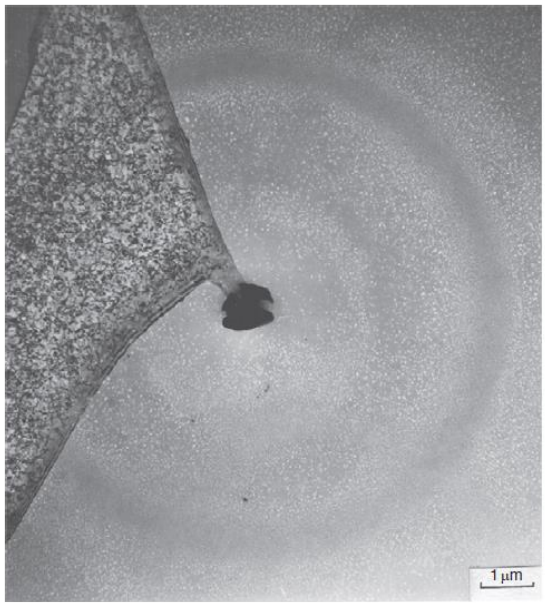

Figure 10 - Halos around a suspected B_4C particle irradiated to $2.9x10^{26}$ n/m^2 at about 55°C. The dark region of the outer halo is filled with small cavities [35]

Hydrogen and helium are also produced as a result of fast neutron irradiation of the aluminum at a rate of 615 and 140 appm/dpa respectively [36]. The helium and hydrogen have a considerable effect on the radiation damage structure by encouraging the nucleation of voids, dislocation loops, and bubbles. He is insoluble in Al; it binds strongly with vacancies and has limited mobility. Hydrogen is also nearly insoluble at room temperature but solubility increases with temperature. The degree of promotion of voids and loops by the gases decreases with increasing irradiation temperature, and the promotion of bubbles increases [35].

1.3.2.1.2 Effect on Microstructure

The nature of irradiation damage in aluminum depends strongly on irradiation temperature and dose. To determine the dose effect, high purity aluminum samples were irradiated at <60°C. The samples consisted of foils 100, 76.2, and 12.7 nm thick. None of the 100nm foils showed damage structure for exposure up to $5x10^{18}$ n/cm^2. At a fluence of $3x10^{19}$ n/cm^2 the 12.7 and 76.2 mm thick films showed many small loops about 25 nm in diameter with

spotty distribution. After a dose of $1.6x10^{20}$ n/cm^2 the loop concentration was higher, though the size remained approximately the same [35].

Comparing the damage caused by the same radiation dose received at different temperatures reveals that irradiation at higher temperature causes a coarsening of the damage microstructure and a decrease in the degree of radiation hardening. At 150°C the dislocation structure mostly disappears and the number of voids is reduced, although the voids at 150°C are larger, facetted, and more elongated than the voids present at 50°C [35]. In general it appears that there is an inverse relationship between both void and bubble number densities and irradiation temperature [37].

Annealed aluminum samples that were then irradiated at temperatures over 150°C exhibited neither dislocation-type irradiation damage nor voids but did show coarse Si particles. Aluminum samples that had been cold-rolled still retained some large cavities after the sample had been irradiated at 220°C [35]. High purity aluminum that had been irradiated with 600MeV protons showed no voids if the irradiation temperature exceeded 160°C [37]. However, as temperatures reached and exceeded 320°C clear evidence of irradiation induced precipitation was noted [37].

The presence of certain solutes in the aluminum has been demonstrated to reduce the radiation damage structure. Chromium, copper, manganese, titanium, and vanadium have all been observed to reduce radiation damage structure at concentrations of 100 appm [35]. In addition, silicon, copper, iron, and vanadium have all been reported to reduce radiation induced swelling [38].

Post-irradiation annealing also has influence on the microstructure of irradiated aluminum. Aluminum that has been irradiated by fast neutrons at temperatures between ~30-

40% of the melt temperature readily has voids annealed out by post-irradiation annealing at temperatures up to 300°C. For samples that were irradiated to a higher fluence, higher annealing temperatures were required to remove the voids [39]. Table 8 shows the effect of annealing temperature on swelling for ultra-pure aluminum. For aluminum alloys, damage recovery was slowed by impurity content as well as higher doses. For 1100Al, recovery of void swelling began after 1 hour at 200°C and was almost complete at 300°C. At 300°C gas bubble swelling began to dominate void swelling effects [35].

Table 8 - Influence of post-irradiation annealing on swelling in 99.9999% aluminum, as determined by TEM. All annealing was performed for 1 hour [39]

Annealing Treatment	Swelling (%)	
	$1.6x10^{21}$ n/cm^2	$1.6x10^{22}$ n/cm^2
As-irradiated	0.85	8.5
100°C	0.91	-
150°C	0.68	-
200°C	0.94	6.2
250°C	0.40	5.3
300°C	0	5.1
350°C	-	5.5
400°C	-	2.7
500°C	0	0

Much of the irradiation behavior exhibited by aluminum can be explained by the development of side and conspicuous denuded zones. Incoherent interfaces are comprised of structural dislocation networks and high equilibrium concentrations of vacancies that make the boundaries deep sinks for absorption and recombination of freely migrating point defects. They are pulled in from the near regions of the butting grains, leaving a volume of matrix straddling the boundary that is diminished in radiation-produced point defects. Due to the greater mobility of the interstitials and the bias of dislocations for absorption of interstitials the zone deprived of interstitials is wider than that for the vacancies. This creates an unbalanced concentration of vacancies at the rim of the denuded zone. Therefore, vacancy clusters are encouraged to form in

that rim and they become more numerous and/or larger than those in the grain matrix. Impurities and transmutation products are also drawn into the grain boundary, but they are not annihilated there; they accumulate. If they are largely insoluble, as H, He, and Si are in Al, they will precipitate and grow there, the gases as bubbles and the Si as particles or films. Within the grains, the gases will stabilize embryo clusters of vacancies and facilitate their growth into voids as long as there is an excess of vacancies. Some of the Si will attach itself to the voids. Grown-in dislocations in the grain interiors are also sinks for point defects [35].

1.3.2.1.3 Effect on Corrosion and Mechanical Properties

The effects of irradiation on corrosion and mechanical properties of aluminum are controversial. There is limited data on the effect of neutron irradiation on the corrosion of aluminum alloys. What data does exist is often contradicting. Some experiments show little difference between experiments performed in water loops and fuel cladding from test reactors [35]. Other data indicates that irradiation enhances corrosion while yet other data seems to indicate that irradiation reduces corrosion rates. There seems to be a general feeling, especially among the Russians, that irradiation does indeed decrease corrosion rates [40].

One of the major controversies with regard to the effects of neutron irradiation on aluminum is in regards to irradiation softening. Some research has found evidence of neutron irradiation induced hardening, typically as a result of the formation of Si precipitates. However, other studies have found the exact opposite. One study in particular noticed that a fluence of 8.7×10^{17} n/cm^2 in a cold-rolled Al-Mg alloy resulted in a 75% decrease in yield strength, a 35% decrease in hardness and a 500% increase in ductility [41]. Much of the reason for the discrepancy may be due to the manufacturing process (i.e. annealing, cold working) and the particular alloys used.

1.3.2.2 Boron Carbide

One of the many unusual properties of boron carbide is its extreme resistance to radiation damage. Boron carbide subjected to high energy electron fluences in a Transmission Electron Microscope (TEM) failed to show evidence of damage of any sort (dislocation loops, bubbles) after two hours of irradiation at temperatures between 20 and 800°C. Even regions containing faults and/or dislocations failed to show agglomerations of interstitials formed due to irradiation damage that should preferentially migrate to those regions. Even samples that had been previously neutron irradiated failed to show any relaxation of the strain fields or any additional damage after electron bombardment for 2 hours [42].

Irradiation tests have also been performed using heavy ions. Post-irradiation investigation using high-resolution TEM failed to detect clustering of defects or amorphization even for irradiations carried out at temperatures as low as ~12K. The only change observed was moderate swelling that was attributed to trapping of ions inside the sample. The fluences tested were estimated by TRIM to have been sufficient to cause 36 dpa damage [43].

One theory for the stability of the icosahedra during irradiation is that an electron from a departing boron atom is retained by the icosahedron from which it is knocked. Thus, Coulomb attraction will foster recombination between a departing boron cation and an icosahedron possessing an extra negative charge. In addition, the small size of a boron cation should aid diffusion and help facilitate recombination. This view is supported by the observation that icosahedra which are "degraded" by the loss of an atom do indeed garner an extra negative charge [43].

Although boron carbide is generally resistant to knock-on radiation damage, the vast majority of radiation damage comes as a result of recoil atoms created during the $^{10}B(n,\alpha)^{7}Li$ nuclear reaction [44]. Upon capture of a thermal neutron boron has two interaction pathways.

$$^{10}_{5}B + ^{1}_{0}n \rightarrow \begin{cases} ^{4}_{2}He + ^{7}_{3}Li + 2.8MeV\ kinetic\ energy\ (6\%) \\ ^{4}_{2}He + ^{7}_{3}Li + \gamma + 2.3MeV\ kinetic\ energy\ (94\%) \end{cases}$$

The most common interaction results in the release of a 0.48MeV gamma ray along with a 0.84 MeV Li-7 atom and a 1.47 MeV alpha particle. It is through the generation of, and interaction with, these particles that boron carbide receives the most damage. Of course, the actual distribution of damage relies heavily on the energy spectrum of the neutrons. In a fast spectrum, only about 18% of the total displacement damage is due to the $^{10}B(n,\alpha)$ reaction. Yet in a thermal reactor, displacements caused by the products of the $^{10}B(n,\alpha)$ reaction are dominant and can exceed primary knock-on displacements by a factor of about 380 [42]

Table 9 - Comparison of damage induced by recoils and neutron scattering in a boron carbide pellet during PWR irradiation[44]

Fluence ($x10^{20}$ n/cm^2)	0	13	250
Damage per 1020 n/cm2 due to recoils (%)	82	77	72
Damage per 1020 n/cm2 due to neutron scattering (%)	18	23	28

The production of lithium causes little concern for either the boron carbide or the aluminum. Little work has been done with lithium in boron carbide and researchers have concluded that Li is sufficiently soluble that even implantation of less than ~20 at% Li into boron carbide has little effect on the structure [45]. There have also not been lithium-bearing precipitates discovered despite a wide range of boron-10 burnups and temperatures being investigated [42]. Recoil and diffusion of the lithium into the aluminum matrix is also expected to have little effect due to the high solubility of lithium in aluminum. The use of lithium in

aluminum is well documented and lithium is one of the characteristic alloying elements in 2xxx series aluminum alloys.

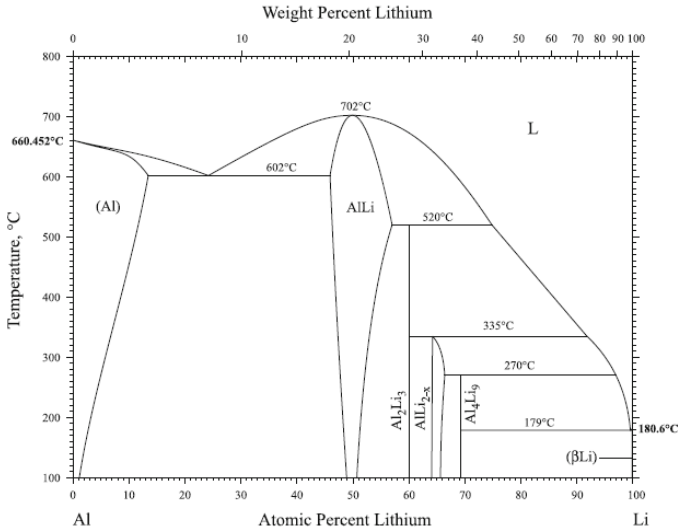

Figure 11 - Aluminum-Lithium Phase Diagram [46]

One of the major features formed during neutron irradiation of boron carbide is the growth of helium bubbles. In fact some researchers have noted that the helium bubbles formed due to the $^{10}B(n,\alpha)$ reaction create the sole form of radiation damage visible in the electron microscope and that dislocation loops nor precipitates had been noticed [42]. Even though the helium will coalesce into bubble, the formation of bubbles only occurs during high temperature (>1000°C) annealing [42, 47].The bubbles are generally small and surrounded by large strain fields as seen in Figure 12.

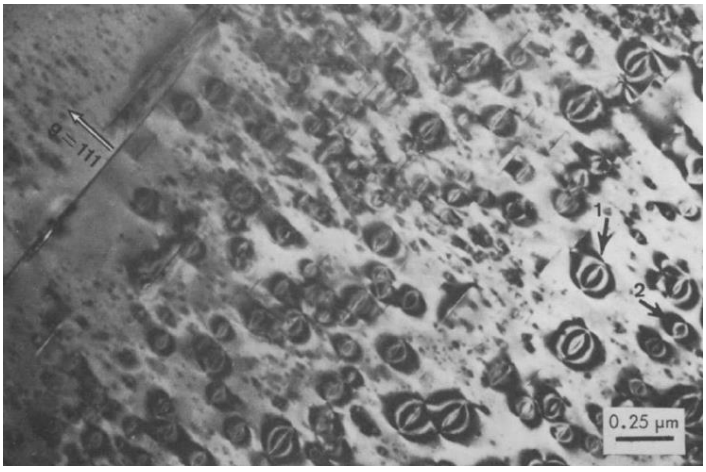

Figure 12 - Strain fields around He bubbles in neutron irradiated boron carbide [42]

The predominant microstructural change induced by irradiation is the formation of microcracks in the boron carbide pellets. The formation of these cracks has been attributed to the presence of free graphite in the un-irradiated pellet. During irradiation, a pellet my swell by 0.85-1.35% though the volume of a crystal unit cell only increases by 0.23-0.24%. The remainder of the swelling can be attributed to the formation of these microcracks. The formation of these microcracks can help facilitate the release of helium gas from the interior of the boron carbide pellet [48].

1.3.3 Corrosion Behavior

Understanding the corrosion behavior of Boral® and Bortec® is essential to understanding the long-term performance capabilities of these materials. Both aluminum and boron carbide are extremely popular commercial materials that have been deployed in a wide range of applications. As such, the corrosion mechanisms of both of these materials have been extensively studied across a wide variety of environments. Yet, even though the corrosion mechanisms of both boron carbide and aluminum are well known, what is not well known is how both of these materials influence the other's corrosion behavior.

1.3.3.1 Aluminum Oxidation

The corrosion behavior of aluminum is controlled by the formation of a protective oxide barrier. The nature of this oxide barrier is controlled by a number of factors including temperature, moisture levels, air/water flow rates, and electrochemistry. Understanding the nature of aluminum oxide is difficult due to the diverse factors that influence oxide growth as well as the diversity of methods used to conduct corrosion tests and to measure parameters. Corrosion tests have been carried out in open cups, closed autoclaves, vented autoclaves, closed

loops, bypass loops, or used fuel plates. Evaporation or consumption of water may cause moisture levels to vary during the test. Tests with static water may experience a change in water chemistry over the duration of the test [35].

Post-test examinations are conducted by different methods too. Six common methods have been employed to measure oxide growth: (1) direct measurement by optical or electron microscopy; (2) physical measurement using micrometers; (3) weight gain of the material with oxide film in place; (4) weight loss of coupon after removal of the oxide film; (5) acoustic and eddy current measurements; and (6) thermal resistivity changes [35]. One of the problems suffered by all techniques is that the specimens were, either inadvertently or deliberately, dried prior to measurement. Very little work has been done to determine if the cooling and drying of the specimen affects tests. Some tests procedures have included removal and drying of the sample for measurement and then returning the sample to the test apparatus. It is possible that cooling and drying will change the bulk film and thus alter the results of a test or measurement. One test showed loss of oxide thickness in species that had been previously measured and then let sit at room temperature for as little as 48 hours [49].

1.3.3.1.1 Dry Oxidation

In dry air, the oxidation of aluminum proceeds through two different mechanisms dependent on the oxidation temperature. At low temperatures ($T \leq 300°C$) an amorphous oxide layer forms quickly and attains a uniform thickness of about 1 nm in less than a minute. For oxidation temperatures below 77°C no further oxidation is detected. For temperatures above 77°C the thickness slowly increases after the initial fast oxidation step. The amorphous oxide that forms is deficient in Al cations when compared to γ-Al_2O_3 and can be described as a close packing of oxygen atoms with the Al cations distributed over the octahedral and tetrahedral

interstices [50]. At high temperatures, the amorphous oxide follows the same form but is enriched in Al cations in comparison to γ-Al_2O_3.

The rate of oxidation in dry air is strongly influenced by the sticking probability of O_2 onto the bare and oxidized aluminum surface. The sticking probability increases from -30°C to ~327°C. Above ~327°C the sticking probability decreases. This explains the observation that at higher temperatures the formation of the amorphous oxide layer proceeds through formation of oxide "islands" and complete surface oxidation takes longer than at lower temperatures [50, 51]. Across all temperatures the thickness of the formed oxide layer is fairly uniform for a given temperature. However, at higher temperatures regions of "necking" or thinning in the oxide have been observed [52]. It is supposed that these necks are remnants of the oxide islands that initially formed.

In the high temperature oxidation regime, the amorphous oxide film composition progresses toward the Al_2O_3 stoichiometry and gradually undergoes transformation into a crystalline oxide structure. Aluminum oxide, or alumina, can exist in many forms. The stable form of alumina is the corundum or α-Al_2O_3 form that is seen in nature as sapphires or rubies. The other forms of alumina are metastable and can be divided into two categories based on crystal structure face-centered cubic (fcc) or hexagonal close-packed (hcp). The fcc polymorphs of alumina includes γ, η (cubic), θ (monoclinic), and δ (either tetragonal or orthorhombic), whereas the Al_2O_3 structures based on hcp packing are represented by the α (trigonal), κ (orthorhombic), and χ (hexagonal) phases [53].

Table 10 - Common processing routs resulting in formation of different metastable Al_20_3 structures and the sequences of phase transformations toward the stable α- Al_20_3 phase [53]

hcp

$$\alpha\text{-AlOOH (diaspore)} \xrightarrow{700°–800°C} \alpha\text{-}Al_2O_3$$

$$\gamma\text{-Al(OH)}_3\text{(gibbsite)} \xrightarrow{150°–300°C} \chi \xrightarrow{650°–750°C} \kappa \xrightarrow{1000°C} \alpha\text{-}Al_2O_3$$

$$5Al_2O_3\cdot H_2O\text{ (tohdite)} \xrightarrow{700°–800°C} \kappa' \xrightarrow{750°C} \kappa \xrightarrow{900°C} \alpha\text{-}Al_2O_3$$

$$\text{Vapor (CVD)} \rightarrow \kappa \rightarrow \alpha\text{-}Al_2O_3$$

fcc

$$\gamma\text{AlOOH (boehmite)} \xrightarrow{300°–500°C} \gamma \xrightarrow{700°–800°C} \delta \xrightarrow{900°–1000°C} \theta \xrightarrow{1000°–1100°C} \alpha\text{-}Al_2O_3$$

$$\alpha\text{-Al(OH)}_3\text{ (bayerite)} \xrightarrow{200°–300°C} \eta \xrightarrow{600°–800°C} \theta \xrightarrow{1000°–1100°C} \alpha\text{-}Al_2O_3$$

$$\text{Amorphous (anodic film)} \rightarrow \gamma \rightarrow \delta \rightarrow \theta \rightarrow \alpha\text{-}Al_2O_3$$

$$\text{Melt} \rightarrow \gamma \rightarrow \delta,\theta \rightarrow \alpha\text{-}Al_2O_3$$

The temperatures of operation of aluminum and its alloys preclude the formation of oxides other than γ-Al_2O_3. The growth of γ-Al_2O_3 begins in the region between the amorphous thermal oxide layer and the aluminum substrate [54]. As the crystalline oxide begins to form oxidation kinetics change from being governed by the outward transport of Al cations due to the concentration gradient to being governed by the inward chemical diffusion of oxygen along grain boundaries, cracks, and other "easy paths" [50, 54].

The preferential sites for the nucleation of the γ-Al_2O_3 occur along naturally occurring ridges that arise from imperfections in the surface of the aluminum. These ridges produce points of higher stress in the amorphous oxide film that forms. Cracking in the amorphous film provides diffusion pathways for the oxygen. As the subsurface aluminum oxidizes and transforms into γ-Al_2O_3 it also undergoes a volume expansion of about 19%, further stressing the amorphous oxide layer and providing additional pathways for oxygen diffusion [54]. Figure 13 and Figure 14 show micrographs of the growth of γ-Al_2O_3 crystals.

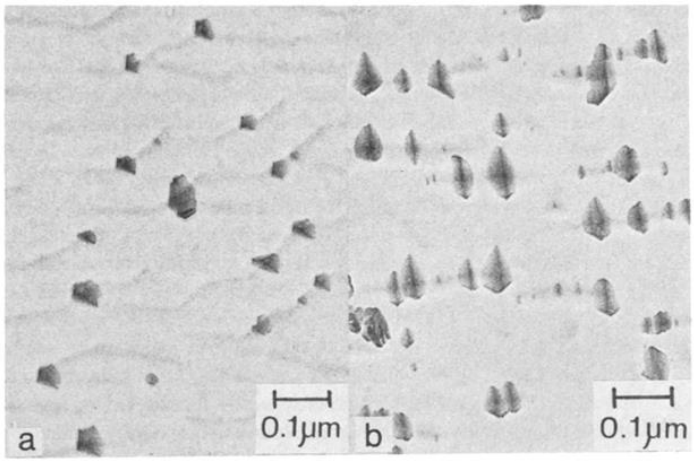

Figure 13 - TEM micrograph of the stripped thermal oxide films grown on grains of non (100) orientations, showing preferential nucleation of γ-Al_2O_3 crystals along the darker corrugation patterns [54]

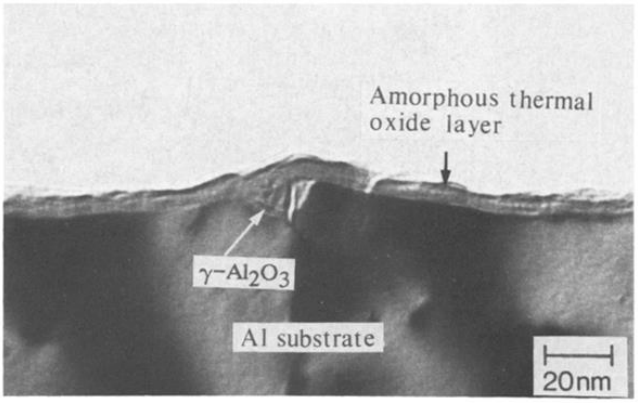

Figure 14 - TEM micrograph of an ultramicrotomed section of the aluminum substrate and the thermal oxide film, showing the nucleation of a γ-Al_2O_3 crystal at the metal ridge beneath the amorphous oxide layer

1.3.3.1.2 Wet Oxidation

During oxidation of aluminum, the introduction of water vapor into O_2 unambiguously modifies the kinetics and structure of aluminum film oxidation. The "wet" aluminum oxide layers that form are less effective passivants than oxide layers formed in dry conditions [55]. Much of the loss of effectiveness of the hydrated oxide layers comes from the more open structures of the oxides formed [56].

Measurements of the hydrated oxide layer indicate that this barrier grows on the outside of the amorphous barrier oxide layer and forms by the hydration of the barrier layer itself [49].

These hydrated oxide layers are quite thick compared to the barriers formed in dry air, often reaching thicknesses of 1μm or more [35]. The continued growth of these layers is influenced and accelerated by increasing temperature and humidity [57]. The oxide layer will quickly grow until it reaches some limiting thickness. When a steady-state thickness is reached the oxide layer will not grow but oxidation may still be occurring. In these instances a balance is reached between formation of the oxide from the barrier layer and breakdown of the hydrated oxide in the wet air [49]. Tests performed in flowing water showed no difference in corrosion rates for water velocities in the range of 0.305-5.58 m/s [35].

Oxide layers formed at elevated temperatures tend not to be stable in moist air at lower temperatures. A sample that had been heated at 200°C for sufficient time for the barrier layer to reach its ultimate thickness was stored at room temperature in a moist environment. After 48 hours the thickness of the barrier layer had been reduced by ~30%. Additional samples that had been heated at various temperatures up to 538°C were stored at room temperature for extended time. After storage they were investigated and all of the samples had the same room temperature barrier oxide layer thickness [49].

In a wet environment the most common oxide forms are boehmite, ($Al_2O_3 \cdot H_2O$), and bayerite ($Al_2O_3 \cdot 3H_2O$). Below ~77°C, the boehmite phase is formed preferentially but may transform to bayerite with continued immersion. At temperatures between ~77°C and ~100°C, a pseudoboehmite structure grows. Aging of the pseudoboehmite structure may lead to the formation of other hydrated oxide forms or it may retain is pseudoboehmite structure. Between ~100 and ~400°C, crystalline boehmite will form. A gelatinous boehmite is the chemical precursor of both of the crystalline hydroxides [35].

Modeling corrosion of aluminum in water during transient temperature conditions is difficult due to the number of different corrosion domains that control the corrosion of aluminum. The common temperature domains of corrosion in water are:

1. <70°C – pitting corrosion dominates
2. 60-100°C – tendency to pitting decreases, general corrosion
3. 100-150°C – general corrosion
4. 150-250°C general corrosion and intercrystalline corrosion
5. >250°C – change to linear rate law, highly destructive inter-crystalline corrosion with rapid destruction of the metal [58].

Even though these trends generally hold true there are other complex interactions that can influence corrosion rates. For example, sintered aluminum powders have relatively good resistance to steam at 500°C but at temperatures around 300°C rapid disintegration is noted unless the aluminum is alloyed with 1% nickel [57]. In addition, if a crevice is formed between two aluminum surfaces or between the aluminum and a non-metallic material, localized corrosion can, and most often will, occur within the crevice in the presence of an electrolyte [59].

1.3.3.1.3 Porous Oxide Growth

The presence of electrolytes during aqueous corrosion of aluminum can lead to the growth of unique porous oxide structures. From a commercial standpoint, one of the most important properties of anodic alumina is the capability for self-organized formation of hexagonal oxide structures in various acids [60]. These structures are formed from the barrier oxide film and are characterized by a pore diameter and a cell diameter. Figure 15 shows a schematic of these porous structures and Figure 16 shows an SEM image of these pores.

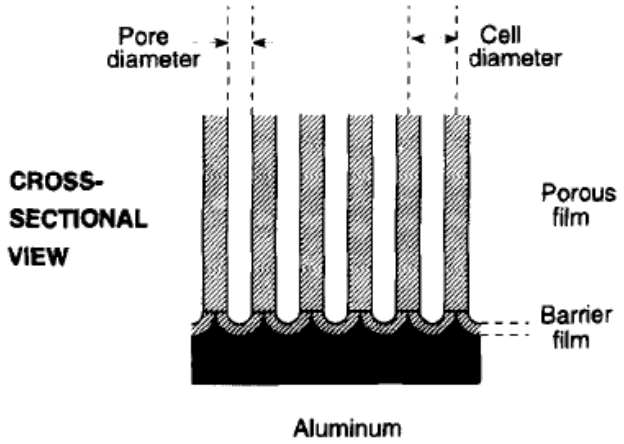

Figure 15 - Cross-sectional schematic of a porous oxide film formed electrochemically above a barrier film on aluminum [61]

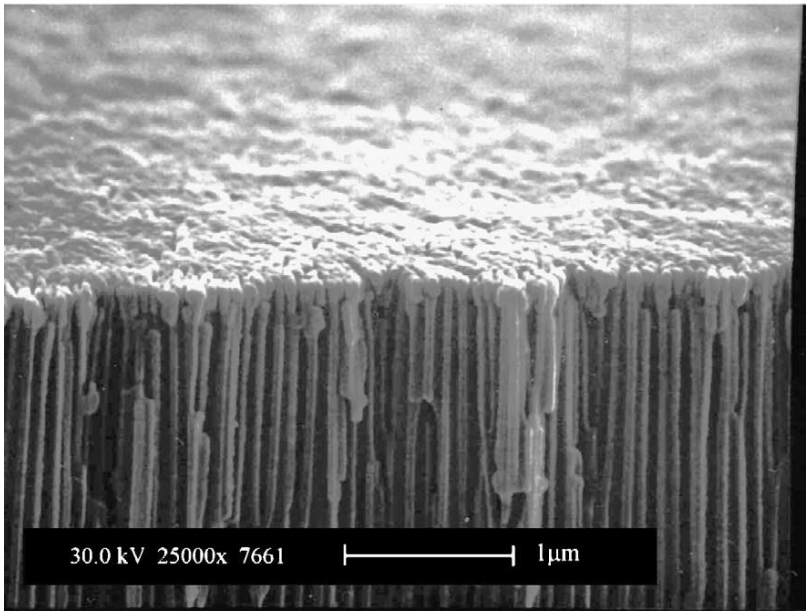

Figure 16 - SEM image of a fracture section of anodic alumina film formed in oxalic acid at current-density of 10 mA/cm^2 at 20°C [60].

There are three essential factors that help explain the formation of these porous oxide structures:

1. The Faraday law is valid for the aluminum ionization reaction (current efficiency 99.8-99.9%) $Al \rightarrow Al^{3-} + 3e$
2. A thin compact barrier oxide layer always exists between the metal and the porous oxide.

3. Porous oxide layer growth occurs at the bottom of the pores through the formation-transformation of the barrier layer [62].

The nature of the porous oxide that forms is dependent largely upon the nature of the electrolyte. In particular, boric acid solutions produce a barrier-type oxide film that is completely insoluble [63]. An investigation of the formation of porous aluminum oxides in boric acid has noted the formation of three different types of oxides at the barrier: (1) a hydrated oxide at the oxide-electrolyte interface, (2) occurrences of irregular patches of crystalline γ-Al_2O_3, and (3) the amorphous oxide that constitutes the majority of the barrier oxide film [63].

Growth of the porous oxide layer occurs through the generation of new material in the barrier layer due to the migration of charged aluminum and oxygen ions. The growth of the barrier layer is extremely efficient with 60% of the oxide being generated close to the metal/oxide interface and the remaining 40% being generated at the oxide/electrolyte interface. The rate of formation of the oxide layer is determined by the ionic transport rate through the barrier oxide layer [64]. Although much research indicates that these porous oxides grow from an amorphous barrier layer it has been shown that, just as in air, the porous oxide layer will form crystallites of γ-Al_2O_3 at higher temperatures [63].

1.3.3.2 Boron Carbide

As with aluminum, boron carbide will also form a protective oxide layer when exposed to an oxidizing environment. In the presence of air or steam boron carbide can react along a number of pathways:

$$B_4C(s) + 4O_2(g) = 2B_2O_3(l) + CO_2(g) \quad (1)$$

$$B_4C(s) + \frac{7}{2}O_2(g) = 2B_2O_3(l) + CO(g) \quad (2)$$

$$B_4C(s) + 8H_2O(g) = 2B_2O_3(l) + CO_2(g) + 8H_2(g) \quad (3)$$

$$B_4C(s) + 7H_2O(g) = 2B_2O_3(l) + CO(g) + 7H_2(g) \quad (4)$$

$$B_4C(s) + 6H_2O(g) = 2B_2O_3(l) + C(s) + 6H_2(g) \quad (5)$$

$$B_4C(s) + 6H_2O(g) = 2B_2O_3(l) + CH_4(g) + 4H_2(g) \quad (6)$$

Each of these reactions has a negative Gibbs free energy, indicating that they are all thermodynamically favorable [65]. Figure 17 shows the Gibbs energy of the above reactions as a function of temperature.

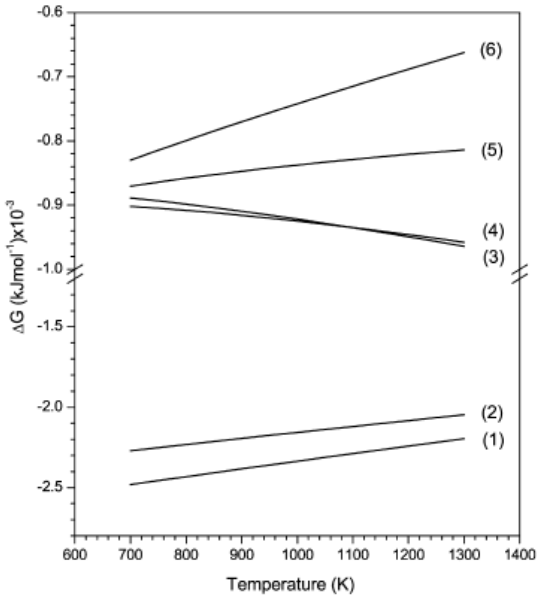

Figure 17 - Gibbs free energy of boron carbide oxidation reactions [65]

In addition to being thermodynamically favorable the oxidation of boron carbide is exothermic, highly so in steam. The heat released by steam oxidation is around 800 kJ/mol [66]. Some tests have indicated that this heat release has negligible effect on oxidation, though the exact extant in different conditions is not known [67].

In addition to oxidizing the boron carbide, steam can further oxidize the boron oxide to produce boric acids, or if the temperature is high enough the boron oxide can also be vaporized directly as shown in the following reactions:

$$B_2O_3(l) = B_2O_3(g)$$

$$B_2O_3(l) + 3H_2O(g) = 2H_3BO_3(g) \text{ (orthoboric acid)}$$
$$B_2O_3(l) + H_2O = 2HBO_2(g) \text{ (metaboric acid) [67].}$$

The interplay between the oxidation reactions and the formation of the boric acids determines the nature and rate of the oxidation of a boron carbide particle in a humid environment. If the rate of transport of boric acid exceeds the rate of formation of B_2O_3 the weight loss curves directly depict the oxidation rate. If, however, the rate of oxidation exceeds the formation and removal of the boric acid then an oxide film will build up and an initial mass increase may be noticed. The oxide film will inhibit further oxidation of the boron carbide and the oxidation rate will decrease until an equilibrium is achieved between oxide formation and B_2O_3 transport [68].

The kinetics of oxidation are heavily dependent on temperature, but are also affected by particle size and atmosphere. Comparison testing of oxidation of coarse (D_{50} ~59.6 µm), medium (D_{50} ~22.5 µm), and fine (D_{50} ~1.52 µm) boron carbide powders in dry air showed distinct behaviors. In Figure 18 the effect of particle size on degree of oxidation can be seen. The small, medium, and large particle sizes all reach a steady-state oxidation at which point the protective nature of the oxide inhibits further oxidation. For all particles, oxidation below 450°C is negligible. For small particle sizes, oxidation above 650°C is nearly instantaneous.

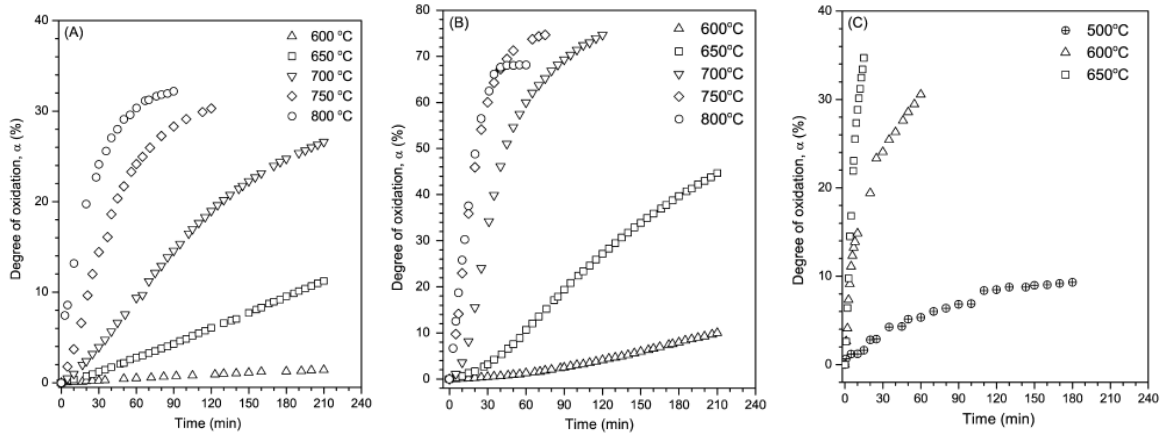

Figure 18 - Isothermal oxidation for: (A) coarse (D_{50} ~59.6 µm), (B) medium (D_{50} ~22.5 µm), and (C) fine (D_{50} ~1.52 µm) B4C powders [65].

In dry air, the mostly linear kinetics of oxidation indicates that the B_2O_3 does not impede oxidation until some threshold limit is reached. However, in humid air the formation of the boron oxide does impede oxidation. At first glance this may seem counterintuitive since in air boron carbide doesn't oxidize below ~450°C whereas in humid air submicron boron carbide powders have been found to be oxidized slowly at room temperature [65] and large boron carbide particles have been noted to oxidize at temperatures as low as 250-300°C [68, 69]. In steam, oxidation progresses in a couple of stages. The first stage lasts only about 15 minutes and accounts for ~70% of the hydrogen that is released. The last stage progresses slowly and can continue until the boron carbide is completely oxidized [70].

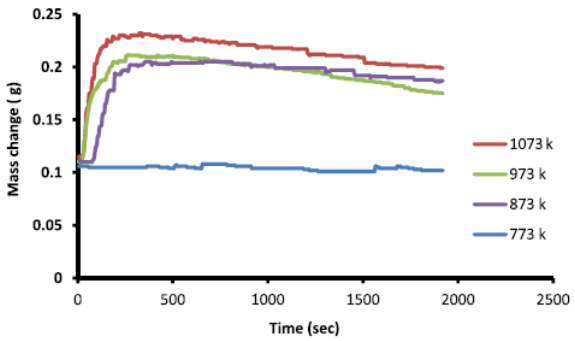

Figure 19 - Temperature effect on mass conversion and gasification rate at 773, 873, 973, and 1073K and water flow rate of 0.5mL/min [70]

To understand the oxidation behavior of boron carbide it is important to understand the nature of the B_2O_3 that forms. Boron oxide grown at ambient pressures forms in a vitreous state and the crystal state of B_2O_3 was not discovered until it was formed in a laboratory in 1938 [71]. There is discrepancy about the nature of the vitreous form of B_2O_3, but there appears to be general consensus that between 60-80% of the boron atoms are bound in boroxol rings [72]. The vitreous structures of boron oxide are seen in Figure 20.

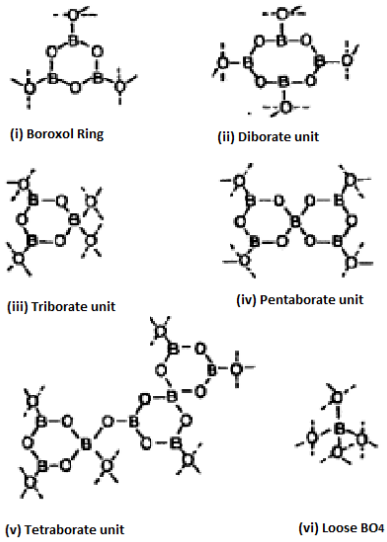

Figure 20 - Vitreous structures of boron oxide [73]

The glass transition temperatures that have been identified range from 227°C [74] and 267°C [75]. The melt temperatures given for the vitreous oxide range between 450°C [75] and 577°C [76], though most reports indicate that melt happens around 450°C. One suggestion for the lack of crystallization at ambient pressures is that the boroxol ring doesn't open up until above the glass transition temperature [75] [71]. This theory fits nicely with the supposition of the existence of boroxol groups existing in the melt [72]

The relatively low melt temperature of the B_2O_3 seems to control much of the behavior of the oxidation. In dry air, appreciable oxidation doesn't occur until 450°C, corresponding with the start of the melt. In both wet and dry environments the oxide layer grows through a diffusive process through the oxide layer, though in wet atmospheres this oxide layer itself may react [77]. The melt allows mobility of oxygen though in dry environments, thus enabling oxidation whereas in wet environments the oxide layer is reacting with the oxygen before it can diffuse through.

1.3.3.3 Aluminum/Boron Carbide

Both aluminum and boron carbide have complex oxidation behaviors. However, in considering the oxidation and corrosion of an aluminum/boron carbide cermet it is critical to consider the potential interactions between the boron carbide and the aluminum. With the interest in development of aluminum/boron carbide MMCs some research has been done to identify potential phases that could form during manufacturing. It was found that aluminum, boron, and carbon can react to form the following compounds: Al_4C_3, B_4C, AlB_2, AlB_{12}, $Al_3B_{48}C_2$ (high temperature form, decomposes near 2300K to $\beta - AlB_{12}$), $AlB_{24}C_4$ (decomposes at 2110 K to AlB_{10}), $Al_8B_4C_7$ (Decomposes at 2110K to $Al_8B_xC_6$ with $2<x<4$), and Al_3BC (stable up to at least 1273K). It was also found that most of these don't form below 900K [78].

The reactions between aluminum and boron carbide typically show an incubation period. It is assumed that this incubation period corresponds to a time period required to break through the initial oxide layers on both the aluminum and the boron carbide. The reactions can also be inhibited by the formation of Al_3BC. In places where the Al_3BC crystals form and start to grow, the boron carbide is protected against further attack. On the other hand, any place where liquid aluminum is in direct contact with the surface of boron carbide particles, dissolution continues. This dissolution gives rise to the formation of deep craters on the boron carbide surface [78].

Limited research has also been done concerning the corrosion of aluminum/boron carbide composites. Most corrosion work has been performed at low temperatures and in chloride solutions, but it does provide a starting point for consideration.

One test performed looked at both pure aluminum and aluminum alloys that were reinforced with boron carbide fibers. These samples were then exposed to an aqueous chloride solution. After exposure it was found that the samples with the fibers suffered greater localized

corrosion, both in stressed and unstressed samples. The increased corrosion occurred on the surfaces that contained exposed fibers [79].

Corrosion tests on samples of boron carbide containing 6061 aluminum alloy at 25°C in salt water showed that 10 wt% boron carbide loading led to increased non-uniformity of the passive oxide layer. The non-uniformity creates points of high stress that lead to small pores and cracks forming in the oxide layer. In addition, large hemispherical pits were noticed on the surface of the alloys. The researchers assume that the pits formed by detachment of the precipitates due to gravity. At 10 wt% boron carbide the pits were noticed both in proximity to and separate from boron carbide particles. At 20 wt% boron carbide, the pits were only noticed near the boron carbide particles [80]. Figure 21 shows an elemental map of the pits that were formed during cyclic testing.

The presence of these pits is thought to arise from the cathodic nature of the B_4C particles in an aluminum matrix. This results in the production of hydroxyl groups, resulting in a pH increase near the B_4C-Al interface. This enhanced crevice corrosion results in circular pits around the inclusion. In addition the high donor density values and low flat band potential for boron carbide bearing composites attributes to the highly disordered amorphous nature of the passive films. This disordered state reduces the stability of the film and results in increasing susceptibility to pitting corrosion [80].

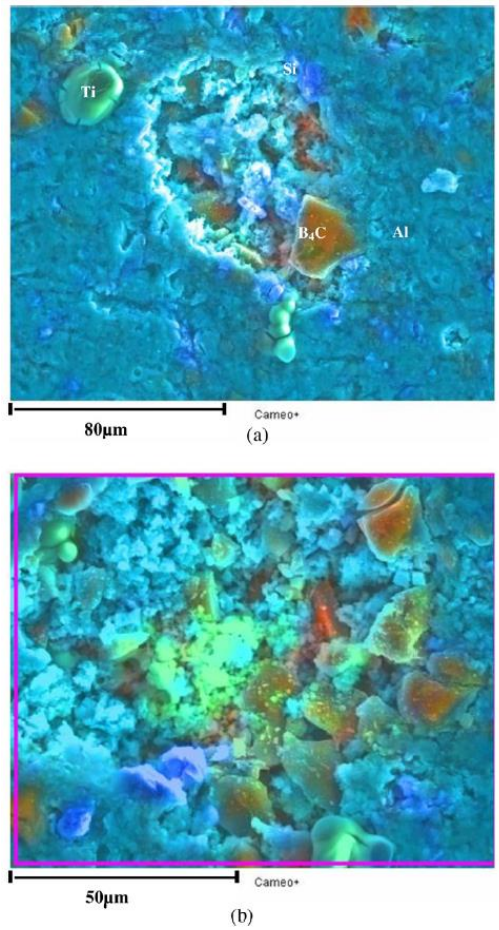

Figure 21 - SEM elemental mapping of pores formed in (a) 10 wt% and (b) 20wt% boron carbide loaded aluminum/boron carbide composites [80]

In addition to interactions between aluminum and boron carbide some research has also shown that Al_2O_3/B_2O_3 can interact to form $Al_{18}B_4O_{33}$ at temperatures above 1000°C[81]. Other interactions in the Al-B-C system have been studied but there have not been any studies published in open literature about long-term behavior at temperatures below the melt temperature of aluminum [82]. The complex interactions possible between aluminum, boron, carbon, and their oxides need to be understood to be able to predict long-term behavior.

Chapter 2 Experimental Procedures

Experiments for this project have been carried out at a number of different facilities associated with a number of different organizations. Most of the work for this project has been performed at the Pacific Northwest National Lab (PNNL) in Richland, Washington. Some of the work on this project has also been performed at the University of Michigan (UM) in Ann Arbor, Michigan and at the National Institute for Standards and Technology (NIST) in Gaithersburg, Maryland

2.1 Sample Preparation

The material used for this project has been supplied by Ceradyne Canada, the manufacturer of Boral® and Bortec®. The material provided meets all the specifications of their production material but contains natural boron as opposed to being enriched in boron-10. The material provided came in the form of 2"x3" plates that were then cut down to 1" x 2". Cutting of the samples was performed on a Buehler IsoMet Low Speed Saw with a 4" diamond wafering blade. To control heating the saw was water cooled. The thin blade of the saw combined with the hardness of the boron carbide necessitated the use of low weight and slow speeds to obtain a clean cut with minimal damage to the sample or the blade.

Following cutting the samples were drilled through the top with a 4.5mm carbide drill bit to allow mounting on sample racks. After the hole was drilled an identification number was engraved on the sample surface. Following drilling the samples were cleaned with 18 mega ohm deionized (DI) water and then sonicated in ethanol. After air drying the samples were weighed

using a Sartorius BP210S balance calibrated for accuracy to 0.1 mg. The samples were then measured across their length, width, thickness, and hole diameter using calipers. Length measurements were taken 3 times across the sample, along both edges and in the middle. Width measurements were also taken 3 times, across the bottom, middle, and top of the sample.

Specimens prepared for any investigative work were always taken from points away from the edge of the sample. A minimum of 5mm was trimmed off the end of a sample coupon and set aside, typically using the slow speed saw used to cut the coupons. A second cut was then taken out of the coupon on the newly formed piece was used for analysis.

2.2 Corrosion Testing

One of the principle goals of this work is to determine the fate of Boral® and Bortec® during lifetime operation in a used fuel storage cask. Initial assumptions at the start of the project were that corrosion of the aluminum would be the limiting factor that would set the service life of these materials. As such, corrosion testing was the major focus of this work.

2.2.1 Initial Corrosion Testing

Qualification work for Boral® and Bortec® has been performed to determine performance over its service life [26, 27]. However, this testing has not taken into account the possibility of long-term storage at elevated temperature in a dry cask environment. One of the major reasons that aluminum is used in construction is that it has a strong resistance to corrosion. Aluminum will oxidize quickly and form a protective alumina layer that will passivate the surface against further corrosion. The lack of corrosion data in literature regarding the corrosion of aluminum in high temperature steam lead to doubts if the samples would show any signs of corrosion.

In an effort to determine if corrosion would be a factor an exploratory test was performed. The test was carried out using (3) 22 mL Parr non-stirred general purpose pressure

vessels. The vessel is stainless steel and rated to operate at temperatures up to 300°C and/or 1700 psi. Each vessel was to be filled with differing amounts of water to correspond to different humidity levels. It was desirable to prevent free water from remaining in the bottom of the vessel so a quick calculation was performed using the Van der Waals equation for gasses.

The first step was to calculate the vapor pressure for water. The vapor pressure for water is a function of the temperature and can be calculated by using the Antoine equation:

$$\log_{10} P = A - \frac{B}{C+T} \qquad 2.1$$

where A, B, and C are empirical parameters based on fluid and temperature range and T is the temperature. Given the operating limits of the pressure vessels it was determined that the test would run at 275°C to allow for a safety margin. To convert this pressure into a water volume the Van der Waals equation was used:

$$\left(P + \frac{n^2 a}{V^2}\right)(V - nb) = nRT \qquad 2.2$$

In the Van der Waals equation *a* is a measure of the attraction between particles and *b* is the volume excited by a mole of particles. Values for *a* and *b* have been tabulated for a wide range of substances. The value used for pressure (P) came from the value calculated using the Antoine equation and the volume of the container (V) was the full volume and did not account for the volume of the samples since the sample value is small compared to the volume of the pressure vessel.

After solving Equation 2.2 for the number of moles (n) then the number of moles was converted to volume using the molecular weight of water and the density of water at room temperature. To ensure that there was no free standing water the actual volume added to each vessel was less than the calculated value for the higher degrees of saturation. Table 11 shows the calculated volumes as well as the actual volumes used.

Table 11 Water volumes used to approximate various humidity levels for initial corrosion test

Degree of saturation	Required water volume (calculated)	Required water volume (used)
100%	1.10 mL	1 mL
66%	0.687 mL	0.66 mL
33%	0.33 mL	0.33 mL

The pressure vessels were filled with the correct amount of water and the samples were placed directly into the vessel. The vessels were then placed in a bucket and argon was allowed to flow through the bucket for 5 minutes, replacing all of the air. The lids were then screwed on in the bucket. After removing the vessels from the bucket the lids were tightened on and placed in a bench-top furnace. The furnace was set to 275°C and let run for 3700 hours.

After the test was completed the vessels were cooled for 24 hours and then opened. Upon opening the vessels it was noted that they were all dry, there was no residual water. Initial speculation was that the gaskets had failed and that the water had seeped out. However, optical investigation of the samples revealed a corrosion layer on the sample, indicating that the water had all reacted with the sample and not escaped. However, the possibility still existed that the systems had air ingress and that the air had corroded the samples.

The initial corrosion test was not able to provide any quantitative results due the complete loss of water and the potential of galvanic corrosion between the sample and the stainless steel vessel. The loss of water indicates that the humidity level of the environment changed over time and it is unknown how long the samples sat in a dry environment.

Galvanic corrosion between the aluminum and the stainless steel will cause a different corrosion mechanism with different rate constants than if the sample had been insulated. The potential of galvanic corrosion was not a serious concern since, in a dry cask environment, the samples of Boral® will be in stainless steel sleeves and both materials will be in contact with

stainless steel in the bottom of the cask. Even though the test was not successful at providing any quantitative data it did show that the samples will corrode in a dry cask environment. Confirmation of corrosion meant that further corrosion testing could progress.

2.2.2 Autoclave Corrosion Testing

The results of the initial corrosion test showed that a sealed system would not work for corrosion testing. The variable humidity levels would make it difficult to maintain a humid environment for the entire duration of testing. The presence of a large volume of water in the autoclave would also result in high pressures in the system, contrary to what is in the dry cask environment. Elevated test temperatures would also result in further increased pressure and the potential to push the water past its critical point. High pressures and supercritical water would invalidate the results for application to the dry cask storage environment.

A constant level of moisture in the autoclave can be achieved by flowing a humidified gas through the system. During storage the inside of the cask is filled with helium. For testing purposes it was decided that argon would be used. One of the major reasons for the choice to use argon is that it is denser than air. Since all the outlets on the autoclave are through the lid on top the presence of a leak would not result in the ingress of air as the argon would continue to cover the samples.

Humidification of the argon was accomplished by passing the argon through water. 2 L Nalgene bottles were fitted with Swagelock fittings to allow 1/4” steel tubing to be connected to the bottles. The inlet tube was run down to the bottom of the bottle where it was fitted with a diffuser. The outlet tube extended 1 inch from the top of the lid to ensure that it would stay out of the water. The inlet gas was bubbled through the water and the vapor head above the water

was forced out through the outlet tube. To ensure that water-based contaminants would not be introduced into the system the bottles were only filled with 18 mega ohm DI water.

The humidity level of the gas was controlled by the temperature of the water. The Nalgene bottles placed in a large oven to maintain an even temperature environment around the bottle. A refill bottle was kept inside the furnace so that there was not a temperature spike in the system when a bottle had to be refilled. The outlet lines coming out of the furnace were wrapped in heat tape to prevent condensation inside the lines. The outlet was then connected to the inlet of the autoclave.

Figure 22 Humidification system for autoclave corrosion

Just as with the Nalgene bottles in the humidification system, the inlet from the autoclave was run down to the bottom of the autoclave while the outlet just barely extended down from the

lid. The outlet from the autoclave was run into a condensate trap. The purpose of the condensate trap was to allow some of the humidity to condense out of the gas before the rest of the gas was sent up the building exhaust stack.

Initial setup used 1/4" steel tubing for all piping in the system. Two autoclaves were set up in parallel to allow for the simultaneous running of tests at two different temperatures. The testing originally started with 24 samples being loaded into each autoclave, 6 samples of each material and thickness. One of the autoclaves was set to run at 570°C and the second autoclave was set to run at 400°C. The argon flow rate was set to 1 standard cubic foot per minute (SCFM) and the temperature of the humidification system was set to 90°C. Water consumption averages approximately 5.5L per week per autoclave.

After 10 days of running it was noticed that there was nothing coming out of the outlet. Upon opening the autoclaves it was noticed that the outlet lines were plugged with a white substance. Standard operating procedure for the autoclaves were written for tests up to 300°C and called for the use of Teflon to coat the gaskets. Since the temperature of the tests was far in excess of the melt temperature of Teflon it was assumed that it was Teflon that had plugged up the autoclave.

To confirm that Teflon was the cause of the plug the outlet lines were scraped and the deposits were analyzed by X-ray Fluorescence (XRF). XRF signals are generated by bombarding a sample with high energy X-rays and the detecting the emission of characteristic x-rays, similar to EDS. The results of the XRF test can be seen in Table 12. The high concentration of gold is due to the presence of gold in the sample holder. Additionally, the Sn, Sb, and Te peaks are close together so not all of those elements may be present. The high concentration of nitrogen along with carbon and fluorine lent credence to the suspicion of Teflon

contamination. The wide variety of other elements listed raised concern for the potential of other sources of contamination.

Table 12 Results of XRF analysis of deposts in the outlet line of the autoclaved used for 570°C corrosion test

Element	Wt%	Element	Wt%
C	7.02	Zr	0.81
N	15.5	Mo	1.18
F	1.11	Ag	0.39
Na	0.21	Cd	0.73
Mg	0.08	In	0.55
Si	0.2	Sn	5.12
P	0	Sb	3.17
Cl	0.12	Te	4.17
Ca	0.11	I	5.66
Ti	0.1	Cs	0.14
Cr	0.14	Ba	0.32
Mn	0.13	La	0.31
Fe	0.65	Ce	0.41
Co	0.14	Nd	0.24
Ni	0.19	Ta	0.34
Cu	0.22	W	0.41
Zn	0.21	Ir	0.39
Se	0.31	Pt	0.42
Br	4.11	Au	44.56
Sr	0.84	Hg	0.53

Due to contamination concerns the samples that were in the autoclave were removed and isolated. New samples were made to put into the autoclaves for testing. The autoclaves were also taken apart and cleaned using water, acetone, and then ethanol while being scrubbed with a scouring pad. Additionally a rotameter was installed on the outlet line from each of the condensate traps. This provided an easy visual check to ensure outlet flow. To test the system the autoclaves were brought up to temperature and run without any samples being loaded. The autoclaves were run for 1 week, at which time no plugging of the outlet lines was noticed. After the autoclaves were cleaned and tested the new samples were loaded and testing was restarted.

The system was watched closely during restart and the temperatures stabilized at their set points and gas flow was even on the inlet and outlet sides of the system. Upon inspection of the system 24 hours later it was noticed that the outlet flow had dropped to zero. The system was again shut down and the outlet lines were inspected. Visual inspection of the outlet lines revealed the presence of white deposits on the inside of the outlet line which had formed a solid plug in the line of both the 400°C and 570°C autoclaves. Samples of the deposits were collected for investigation by X-ray Diffraction (XRD).

XRD measure the angle of reflection of X-rays off of a sample. During XRD a sample and a detector are set in a fixed geometry. An X-ray generator fires a beam of X-rays at the sample at a glancing angle. Some of the X-rays are diffracted off the sample and strike the detector. The number of X-rays that strike the detector depends on the orientation of the beam to the sample and the crystal structure of the sample. The angle of the incident X-rays is varied over the course of investigation. For a given crystal lattice certain angles of incidence will cause the X-rays to be diffracted toward a detector. The combination of angles that produce a given set of peaks is unique to a crystal structure.

Although a specific diffraction pattern is specific to a single crystal the results of XRD can be difficult to interpret. Part of the problem comes from the number of diffraction planes that can produce a signal. A single compound can produce more than a dozen signal peaks. This problem is further compounded when the sample you are investigating contains multiple compounds. In order to determine the correct identity of an unknown spectrum requires knowledge of what elements are present. The combination of potential elements can then be fed into a database that will then produce a list of potential compounds. An XRD spectrum of each species is then compared against the unknown spectrum. The comparison can be assigned a

Figure of Merit (FOM) to numerically express how well the known spectrum matches the unknown; the lower the FOM the better the fit.

In performing the analysis a background fit was performed to allow for the subtraction of noise in the results. The Kα peaks were then subtracted out and the peak locations were identified. Identification of the peaks occurred through a compilation of three separate searches: line-based, profile-based, and chemistry-based.

Analysis of the spectrum generated by the deposits found in the autoclave outlet lines showed the strongest matches to boron oxide and boron hydroxide species, particularly sassolite compounds. Two other possible species that could be present include sodium and silicon. Though their presence cannot be discounted if they are present it is only trace amounts in minor secondary phases. The closest fits were to B_2O_3 with an FOM of 16 and $B(OH)_3$ with an FOM of 19. Two other forms of sassolite, $H_6B_2O_6$ matched with an FOM of 40 and H_3BO_3 which showed up in a line-based (non-FOM) search. The XRD results can be seen in Appendix A

The identification of the deposits as boron oxide and sassolite is significant. Since both of the compounds contain boron it means that boron is able leach out of the samples at a significant enough rate that the outlet lines can become completely plugged in one day. The loss of boron in the samples means reduced ability for the material to maintain criticality control during storage. Thus even if the material is not deteriorating away due to oxidation its functionality is still being reduced. Identifying the mechanism for boron loss is vital to being able to predict long-term performance of these materials.

To prevent further buildup and plugging of the outlet lines heat tape was wrapped around the lines leading from the head of the autoclave down to the condensate trap. Insulation was then placed over the tape to ensure that it would stay hot. Thermocouples were placed between the

tube and the heat tape to allow for temperature control. The temperature on the lines was set to 250°C.

The inlet line in the condensate trap was then increased from 0.25 inch tubing to 0.75 inch tubing. Since the heat tape could not be used inside the can due to the high moisture environment the larger tube size was used to prevent large scale deposition from plugging up the line. A drain valve was installed on the condensate trap to allow condensate to be periodically drained without having to disrupt the heat tape and insulation on the lines. It was originally hoped that the condensate could be analyzed to help identify the products being carried away in the outlet but the steel cans used for the condensate traps have significant corrosion and as such have interfered with any potential data.

Figure 23 Autoclave systems used for corrosion testing

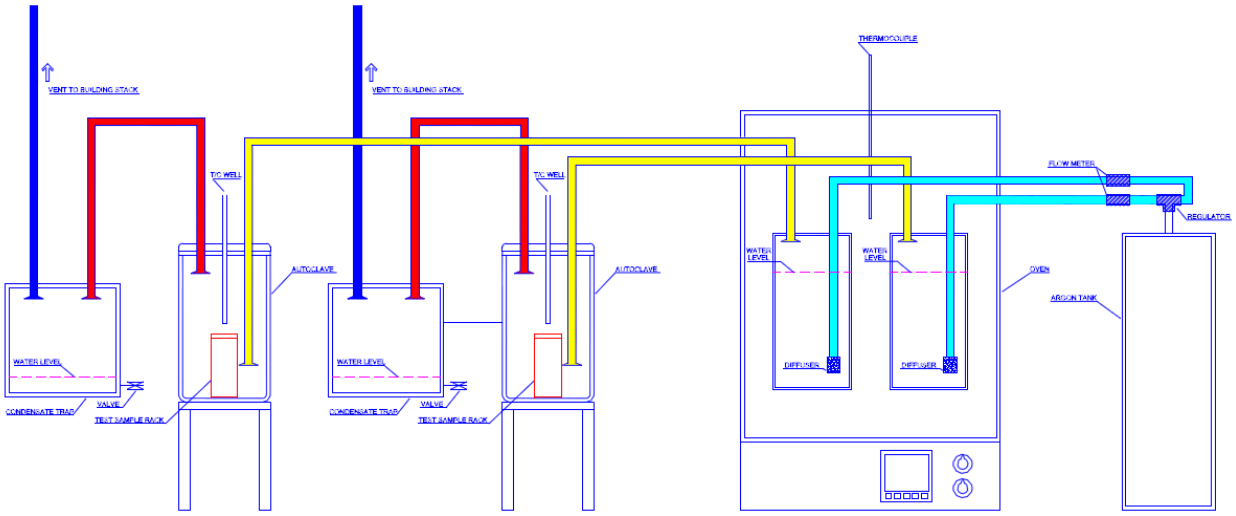

Figure 24 Schematic showing flow of autoclave systems used in corrosion testing

The sample rack used in the autoclave tests was made from titanium wire. The wire was formed and welded into a cylindrical shape. On the inside of the cylinder wire posts were placed to hang the samples on. Four wire posts were equispaced around the circumference of the cylinder at the bottom, in the middle, and at the top of the cylinder. To electrochemically insulate the samples from the rack alumina sleeves were placed on the wires. To insulate samples from each other alumina spacers were used between the rack and the sample and between samples that were hung on the same wire.

2.3 Microscopic Analysis

Much of the characterization work was performed on a Scanning Electron Microscope (SEM). SEMs are versatile instruments that allow a wide variety of investigative techniques to be applied to a single sample. Collecting data from and SEM is reliant on the capabilities of the instrument and the quality of sample preparation. In order to collect sufficient data to be able to characterize the samples multiple sample preparation techniques have been used in conjunction with multiple SEMs.

An SEM images a sample by scanning the surface using a focused electron beam. The beam is generated by the application of a current to a source material. There are two general categories of electron sources: thermionic and Field Emission Guns (FEG). Thermionic sources typically use a tungsten or LaB_6 filament that is heated to a high enough temperature to overcome the work function of the metal, allowing the electrons to escape. FEG sources a strong electric field forms on the tip of the gun and the electrons are drawn toward the anodes. A comparative list of electron sources is found in Table 13.

Table 13 Comparison of electron sources used in electron microscopes

	Units	Tungsten	LaB_6	Schottky FEG	Cold FEG
Work Function, Φ	eV	4.5	2.4	3.0	4.4
Richardson's constant	A/m^2K^2	$6x10^9$	$4x10^9$		
Operating Temperature	K	2700	1700	1700	300
Current Density (at 100 kV)	A/m^2	5	10^2	10^5	10^6
Crossover size	nm	$>10^5$	10^4	15	3
Brightness (at 100kv)	A/m^2sr	10^{10}	$5x10^{11}$	$5x10^{12}$	10^{13}
Energy spread (at 100kV)	eV	3	1.5	0.7	0.3
Emission current stability	%/hr	<1	<1	<1	5
Vacuum	Pa	10^{-2}	10^{-4}	10^{-6}	10^{-9}
Lifetime	Hr	100	1000	>5000	>5000

2.3.1 Sample Preparation Techniques

Proper sample preparation is a key parameter for obtaining quality results from SEM investigation. A number of techniques are available for preparing metallic samples including: cutting (with tools such as a wire saw), chemical and thermal etching, and mechanical polishing. The chemical differences between boron carbide and aluminum preclude the use of chemical means to polish the surface. This leaves mechanical polishing as the best method for sample preparation though the differing hardness between the boron carbide and aluminum creates its own challenges.

The extreme hardness of the boron carbide in the soft aluminum matrix can result in the aluminum being preferentially polished away. This prevents a smooth surface finish and creates imaging artifacts as the boron carbide particles have exposed edges and cast shadows across the sample. It can also lead to rounding of the edges of the boron carbide particles, resulting in the loss of information about the interface region. Close attention to the polishing is required to prevent this.

2.3.1.1 Sectioning and Mounting

The first step in preparation is sectioning the samples. The samples were cut with a Buehler IsoMet® Low Speed Saw equipped with a 4-inch diamond wafering blade and using de-ionized (DI) water as lubricant. Two cuts were made in each coupon. The first cut was to remove 3mm from the side opposite the hole. This is to help minimize any edge effects that may occur due to the exposed bottom surface. The second cut is to remove a section approximately 2mm thick that will be used for SEM imaging.

After sectioning the samples were then mounted in epoxy in preparation for polishing. Initial efforts had the sectioned piece placed in the bottom of a 1 inch Buehler SampleKup and covered with a quick curing resin. Samples were prepared using both Buehler VariDur® acrylic resin and Buehler SamplKwick™ acrylic resin. For as-received samples, the quick curing resins provided a sufficiently hard mount for the samples.

For samples that had undergone corrosion testing it was found that the quick curing resins weren't allowing for a good sample polish in the Boral®. One of the major issues with the corroded samples is that corrosion around the boron carbide particles allows the particles to become lose and to break away during polishing. Free boron carbide particles in the polish

create large scratches in the sample surface that prevent good SEM imaging. To get around this a slow-cure epoxy had to be used.

The use of a slow-cure epoxy has the advantage that it has time to seep into the pores in the sample, thus allowing the epoxy to help hold in the boron carbide particles. The seepage of the epoxy is aided by curing the resin under vacuum. To further aid in the adhesion of the boron carbide after the epoxy had cured the samples can be backfilled by pouring resin over the surface and then curing again. One of the disadvantages of the slow-curing epoxy is that it is softer than the quick cure. The softer epoxy can lead to rounding of sample edges while polishing. To help avoid the rounding of sample edges the sample was placed between two pieces of hardened glass to provide support.

To achieve the best results the sample is placed in the SampleKup and filled with Buehler EpoThin epoxy resin. The cup is then placed in a vacuum jar and the jar is evacuated. The sample then sits for at least 12 hours to allow the resin to harden. The sample is then ground down using Buehler grinding disks to a 15 micron finish. The sample is the rinsed and washed face down in an ultrasonic ethanol bath and then allowed to dry in a 40°C oven for 30 minutes. After being dried a small amount of resin is applied to the still warm sample. The sample is then placed back in the oven for about 1 minute to warm the epoxy and make it a little less viscous. The sample is then placed back in the vacuum jar and the jar is then evacuated. The sample is allowed to sit overnight to allow the epoxy to cure.

2.3.1.2 Polishing

After both the Boral® and Bortec® samples have been mounted in epoxy and the Boral® samples have been backfilled they can then be polished. The first step of polishing is grinding

off any surface epoxy. Grinding is accomplished using a powered multi-head automatic polisher and silicon carbide grinding paper to remove the epoxy.

Once the sample has been ground and all deep surface damage from sectioning has been removed the sample is polished by hand using 6 micron diamond slurry on a nylon cloth. The samples are hand polished for about 5 minutes and then they are sonicated in ethanol. After cleaning they are placed on a vibratory polisher with 1 micron diamond polish on a nylon cloth. The samples are loaded in a 2 pound weight and left on the polisher for 24 hours. After being removed from the vibratory polisher the samples are placed in an ultrasonic bath of soap and water. Once cleaned the samples are placed back on a vibratory polisher in a colloidal silica polish on a soft felt cloth. The samples were again loaded in a 2 pound weight and left on the polisher for 24 hours.

Rounding of the boron carbide particles was difficult to overcome. Grinding is the fastest way to polish the sample but the hardness difference between the aluminum and boron carbide results in the rapid removal of aluminum and the exposure of boron carbide particles. Short grinding times are insufficient to remove surface damage. Finding the best pads for polishing was also a challenge since pads with a thick nap can also cause sample rounding. The short grind time and long time on the vibratory polisher with a nylon pad was found to be the best combination to avoid the rounding of the edges of the boron carbide particles.

Bombardment of a sample with an electron beam can cause the accumulation of a static field on the surface of the sample if the sample is not conductive. To prevent this accumulation of charge, or charging as it is commonly called, the sample surface is coated with a conductive layer, typically carbon, gold, or platinum. Charging of the sample surface can cause an image to drift, resulting in a blurry image. If charging is sufficiently severe then it can cause the detector

to become saturated and prevent the accumulation of an image. The coating can also serve to reduce damage sustained by the sample due to the electron beam. The choice of which covering to use depends on the material and the investigation to be done. If a chemical profile is desired then it is important to pick a coating that will not result in peaks that may mask other peaks of interest.

2.3.2 Data Collection

The formation of an image or elemental profile in an electron microscope comes as a result of the interaction of electrons with the sample. When the electron strikes the sample a number of different particles are emitted. Some of the particles emitted are from the surface region while other particles come from deeper in the material. The volume of material from which signal can be generated due to an incident electron is called the interaction region. Figure 25 shows the interaction region due to electrons.

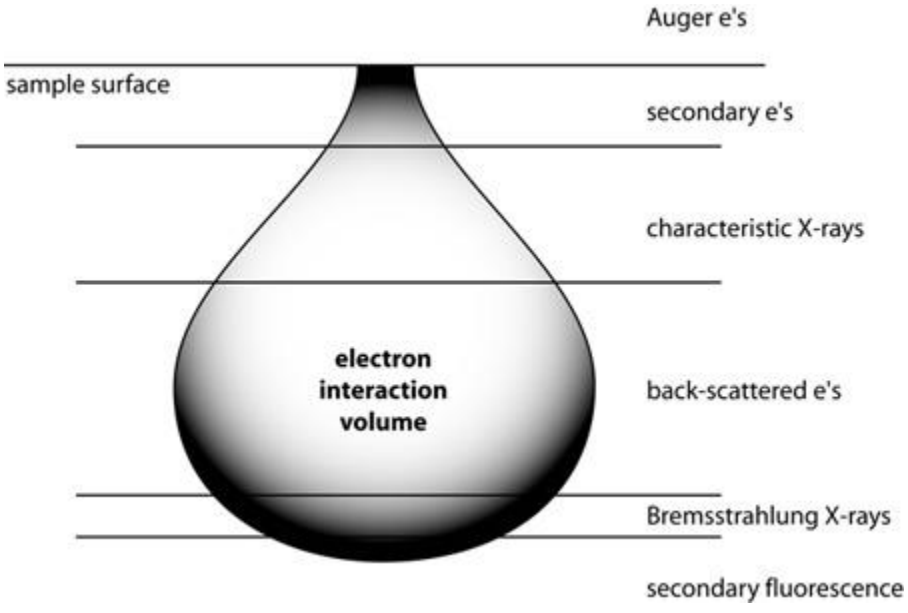

Figure 25 Electron interaction volume and associated signals generated through interaction of electrons with a sample. For an idea of scale, characteristic X-rays are usually generated at depths of up to 1µm [83]

One type of interaction is the removal of an inner-shell electron by an incident electron. When the inner shell electron is removed the atom is left in an excited state. The atom can then either have an outer shell electron drop into the inner shell, thereby releasing an X-ray. Sometimes that energy is instead imparted to another outer-shell electron which is then ejected. These electrons that are ejected are called Auger electrons.

Auger electrons are low energy and must be generated near the sample surface in order to escape. Since the energies of the Auger electrons are related to the energy bands in the atom Auger electrons can be used for chemical analysis. Use of Auger analysis is particularly useful in the detection of lighter elements since the generation of Auger electrons is most favorable in elements with smaller binding energies. However, due to the low energy nature of Auger electrons, detection requires special detectors and ultra-high vacuum and is generally not performed in conjunction with electron microscopy.

The X-rays generated due to the de-excitation of an atom are called characteristic X-rays since the energies with which they are released are characteristic of the element in which they are generated. The particular energy of a single X-ray is determined by the jump that an electron makes during de-excitation. Figure 26 shows the jumps that give rise to certain characteristic X-rays. Detection of characteristic X-rays allows for chemical analysis of the sample. Since X-rays are not as strongly absorbed as electrons they are able to be released from further in the sample. This allows for higher count-rates than Auger electrons but the larger interaction region makes it difficult to analyze chemical data from small inclusions.

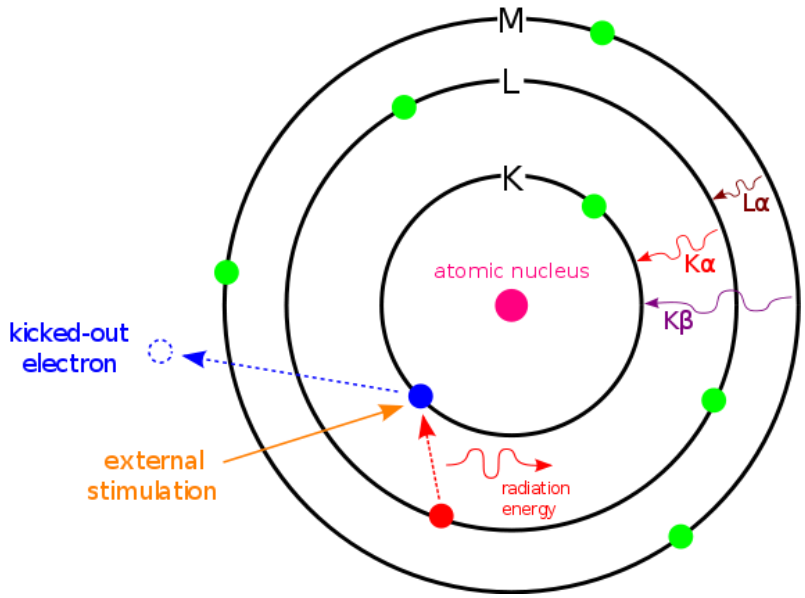

Figure 26 Production of characteristic X-rays used in EDS analysis [84]

Secondary electrons (SE) produce the primary signal used for imaging. Secondary electrons are generated when lightly bound outer shell electrons interact with the incident electrons. Secondary electrons are low energy and thus only escape when generated near the surface. This surface generation makes a SE signal sensitive to the topology of the sample surface. This sensitivity is what allows secondary electrons to be used for imaging the sample surface.

Backscattered electrons come from the elastic scattering of the incident electrons. Backscattered electrons penetrate into the sample and are then scattered back toward a detector that is placed above the sample. The fraction of electrons that are backscattered is largely dependent on the atomic number of the target, with higher Z elements producing more backscattered electrons. The result is that backscattered images have high Z contrast with heavier elements showing up brighter.

2.3.3 SEM Imaging

Scanning Electron Microscopes are versatile instruments. They can be equipped with a variety of detectors to provide a wealth of information about a sample. One of the principle uses of an SEM is for generating high-magnification images of a samples surface. Surface images are primarily obtained through collection of secondary electrons or backscattered electrons. The choice of which signal to use depends on the particular sample and what information is desired. Figure 27 shows a comparison of different SEM images taken from a Bortec® sample. Figure 27A shows a secondary electron image using 10 keV electrons. The bright edges of the boron carbide particles indicate that the particle is exposed and is lying above the aluminum surface. There is some evidence of different phases, though the boron carbide particles are about the only phase that stands out. The lack of topographical features minimizes the impact of the SE image. Figure 27B shows a Lower Secondary Electron Image (LEI). The LEI contains more backscattered electrons and hence has more compositional data while also containing information about surface structure. Note how the boron carbide particles in Figure 27A are lighter than the aluminum matrix whereas in Figure 27B the boron carbide particles are darker. This is due to the boron carbide particle having a lower Z than aluminum.

Figure 27C is a backscatter image. From this image we can confirm the existence of multiple phases. The contrast between the different phases is more pronounced than in the other images but the boron carbide particles appear to be more flush with the surface than is apparent in the SE images. Figure 27D is another backscatter image with increased contrast. Along with atomic mass backscattered electrons are also sensitive to grain orientation. Increasing the contrast has removed some of the sensitivity to different phases but has allowed the observation

of the grain structure. It is important to note that to observe grains the sample surface must be smooth.

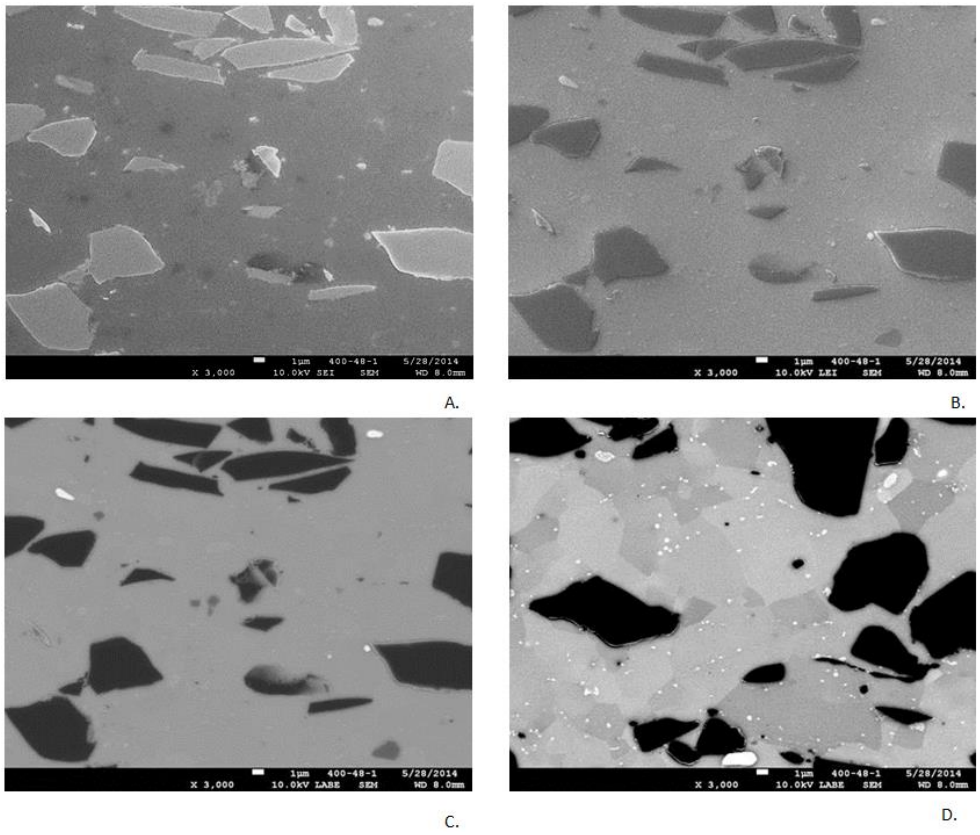

Figure 27 SEM images showing differences between signals. All images are taken at 3000x magnification. A – Secondary electron image. B – Lower secondary electron image. C – Low-angle backscatter image. D – Low-angle backscatter image with high contrast showing grains

The combination of all three images helps to give an accurate picture of the sample surface. By comparing the different images it is possible to determine what features that appear are real and what are artifacts. You can confirm the presence of holes and other surface phenomenon. It also allows you to discern alternate phases from surface deformation.

2.3.4 Energy Dispersive X-ray Spectroscopy

The ability to extract compositional information through EDS makes the SEM a very valuable tool. However, great care needs to be taken in collecting and interpreting EDS results.

Key parameters that need to be considered when collecting and interpreting an EDS spectrum are electron energy, interaction volume, and detector dead time.

The selection of beam energy depends on composition of the sample and desired resolution. The spread of the electron beam depends upon the electron energy. Lower energy electrons have a longer wavelength and thus have more spread. This can be problematic if you are trying to focus the beam on small particles. This problem is not as pronounced in FEG instruments since they are able to maintain small beam diameters at low energies [85].

High beam energies have the disadvantage of having a larger interaction volume. Since SEM imaging only looks at the surface it is not possible to know what particles might lay underneath the surface. A large interaction volume can result in collecting spectrum data from particles or matrix beneath the surface. Interpretation of results, particularly for samples containing small particles, must acknowledge the possibility of signal generated by particles that are within the interaction volume but not seen on the surface.

Using a low energy beam for EDS analysis is useful in decreasing the interaction volume, but the tradeoff is that low energy beams can only map out low-energy X-rays and there is greater peak overlap. A general rule of thumb is that, at a minimum, the beam energy needs to be two times the energy of the peak you want to see. However, if the beam energy is more than 10-20 times the energy of a peak the portion of the interaction volume from which the low-energy X-rays can escape becomes small, making the low energy peaks more difficult to see [85].

Besides beam energy, when mapping out lighter elements it is important to note that bonding can cause the peaks to shift. The bonding of an element can cause a “pull” on the element’s outer electrons. Depending on what the element is bonded to will affect the amount of

"pull". Since EDS signals are generated by the removal of inner electrons the effect of the "pull" on outer electrons typically has little effect. In small elements the closeness of inner and outer shell electrons causes the "pull" from bonding to shift the energy of the characteristic X-rays.

Another factor that can influence an EDS spectrum is excessive dead time in the detector. Dead time is caused by a pile-up of signals hitting the detector. Collecting spectrum from an area containing primarily a single element can cause the appearance of sum peaks; peaks that have an energy level that is the sum of two peaks of the primary element. The dead time can be reduced by reducing the beam intensity, but that also lowers the count rate. A low count rate increases the time that it takes to collect a spectrum, increasing the amount of beam damage and the deposition of carbon tracks.

The two key elements that were desirable to identify are boron and carbon. Boron has a Kα characteristic X-ray that appears at 0.185 keV and the Kα peak for carbon appears at 0.277 keV. Given the low energy of the characteristic X-rays it is desirable to use a low energy electron beam for analysis. Unfortunately the use of a low energy beam cuts off much of the higher energy Kα peaks that are useful for identification. This is important because many of the heavier elements have L and/or M peaks that appear down in the low energy range. Without the presence of the higher energy peaks it becomes difficult to identify the low-end peaks that appear. Table 14 lists the energies of characteristic X-rays for elements that appear in the studied samples and are of interest in this study.

Table 14 Characteristic X-ray energies (in keV) of selected elements

Element	Kα1	Kα2	Kβ1	Lα1	Lα2	Lβ1	Lβ2	Lγ1
Al	1.48670	1.48627	1.55745					
Ar	2.95770	2.95563	3.1905					
Fe	6.40384	6.39084	7.05798	0.7050	0.7050	0.7185		
Cu	8.04778	8.02783	8.90529	0.9297	0.9297	0.9498		
Ag	22.16292	21.9903	24.9424	2.98431	2.97821	3.15094	3.34781	3.51959

To strike a balance most of the imaging work done for this project was performed at 10keV. The energy is still low enough that by using a longer dwell time resolution between the boron and carbon peaks was still achieved. The lower energy also served to reduce the interaction volume. This is important since many of the EDS points were small phases and a large interaction volume could greatly increase the aluminum count or cause signal to come from other phases that existed just below the surface.

2.4 Neutron Depth Profiling

The effectiveness of any boron-containing neutron absorbing material is dependent on how much boron is present in the material and how it is distributed. The limitations of EDS and XRD analysis of these samples does not allow for measurement of the concentration of boron in the sample. One method of accurately measuring boron concentrations is through the use of Neutron Depth Profiling (NDP). NDP takes advantage of boron's large neutron cross section to detect concentrations.

In NDP the neutrons are not measured directly. When an incident neutron strikes a boron atom the boron undergoes an (n,α) reaction resulting in the production of energetic He and Li particles. For boron, the total energy released by the (n,α) reaction is 2790 keV. In 94% of the reactions 1472 keV goes to the He, 840 keV goes to the Li, and a 478 keV gamma ray is released. The remaining 6% of reactions result in a 1776 keV He particle and a 1013 keV Li particle.

Obtaining a concentration profile from the incident neutrons requires detection of the He and Li particles that escape from the surface of the sample. He and Li particles generated on the surface of the sample are able to escape with full energy. As the depth the neutron penetrates

into the sample increases the energy of the escaping particle decreases. The relationship between depth into the sample and the residual energy of the escape particle by be described by

$$x = \int_{E(x)}^{E_0} \frac{dE}{S(E)} \quad (1)$$

where x is the length of the particles path of travel, E_0 is the particles initial energy, E(x) is the energy of the particle as it emerges from the sample and S(E) is the stopping power of the target material.

Since the particles are fairly energetic electronic stopping dominates over elastic nuclear collisions. The electronic stopping power can be approximated using the Bethe-Bloch equation:

$$\frac{dE}{dx} = \frac{4\pi Z_2 Z_1 e^4}{mv^2} ln\left(\frac{mv^3}{Z_1 e^2 \omega}\right) \quad (2)$$

The Bethe-Bloch equation shows that the stopping power is a function of the mass of the ion, the matrix material and the velocity of the ion. It is important to notice that the stopping power is not linear with respect to energy [86]. The shape of the deconvoluted NDP spectra is affected by the shape of the stopping power curve and where the particles initial energy falls along that curve [87]. Figure 28 shows the stopping power curve for a helium ion in aluminum. The stopping power curve was calculated using the TRIM software package using a 1776 keV He^+ ion into a target of pure aluminum. Default values for aluminum were used.

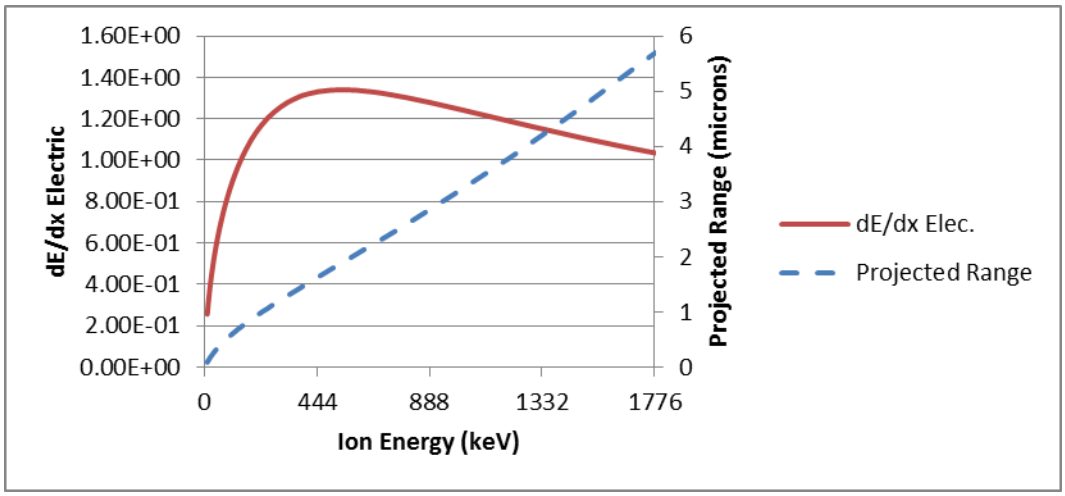

Figure 28 Stopping power and projected range of He^+ ions in aluminum

From Figure 28 we can see that the stopping power for a 1776 keV He^+ ion in Aluminum is on the high energy side of the peak stopping power. Thus as the particle loses energy the stopping power increases until it reaches around 550 keV. Once the particles energy drops below 500 keV the stopping power quickly decreases. Once the charged particles escape the surface of the sample any gasses present between the sample and the detector will further slow the particles down. To prevent loss of energy due to atmospheric interactions the sample and detector are housed in a vacuum chamber.

2.4.1 Beam Parameters

The neutron beam used for NDP analysis consists of low-energy, or cold, neutrons measuring 10^{-2} keV or less. Conditioning of the beam occurs through the use of a cryogenically cooled hydrogen moderator followed by Be-Bi crystals filters in the beam line. The filters are able to remove the high energy neutrons and significantly reduce the gamma ray component [88]. Collimators in the beam line are located in the biologic shield surrounding the reactor and in the external rotating shutter. The collimator in the shutter can be switched out to fit the needs of an experiment. With a 16mm diameter collimator in place the beam has a cold neutron

fluence rate of $1.1x10^9$ neutrons/cm^2/s. This is the fluence rate not the true numerical fluence but is used to express the equivalent thermal neutron reaction rate. The beam is well collimated to ensure that the sample surface is uniformly covered [89].

The ability of neutrons to penetrate through materials makes it difficult to mask off the sample and illuminate only small areas. However, the charged particles that recoil from the near-surface region of the sample have very limited range in solid materials. To control the area of the sample that generates signal an aperture is used to mask off all but a limited region of the sample and prevent all other recoil particles from striking the detector. The aperture can be cut to fit any desired geometry.

2.4.2 Target Chamber

The target chamber used to house the sample, aperture, and detector is a stainless steel vessel that was designed at NIST. The chamber is 610mm in diameter and is equipped with 100mm diameter beam ports that are sealed with thin aluminum windows. The chamber can handle samples up to 200mm in diameter and the entire sample is placed on a motorized platform that has 150mm of travel in the x, y, and z directions. There is also a secondary rotary base that allows for the sample to be rotated.

The chamber is set up to handle up to four different detectors that can be operated simultaneously. The aperture used to discriminately investigate the surface is placed in a fixed location relative to the detectors. The primary detector is located in line with the aperture and perpendicular to the sample surface. A secondary detector is placed to monitor the neutron beam to monitor for any anomalies that may arise due to a fluctuation in the beam.

2.4.3 NDP Procedure

Preparation of samples for NDP consisted of exposing a fresh cross-section surface. Concern of boron leaching in humid air raised questions about accuracy of results if measurements were taken on a surface that had long exposure to atmosphere. Cutting of samples occurred using a diamond rotary cutter on a mill with alcohol used for coolant. Both the Boral® and Bortec® resisted the efforts to be cut and, although cutting was successful, the rate that blades were worn out made it financially improbable to cut all samples using that method. In the end, all of the Bortec® samples used for NDP were cut using this method as were the Boral® standards.

To expose a fresh Boral® surface without the aid of a saw required the scoring of the aluminum clad layer on both sides and then the sharp application of force to break the sample along the score marks. Breaking the sample left the surface rough and this created problems with the sample dragging across the aperture during movement. To rectify this problem the rough surfaces were filed smooth.

Once the sample had been prepared it was placed on the sample holder. The sample holder consisted of a 150mm diameter aluminum disc with a hole in the center. On the back side of the disc at the base of the hole was a shelf that the sample would be placed on. The sample was place so that the edge of the sample was flush with the front of the disk. Strips of polyethylene were placed around the sample to prevent signal from being generated from other areas of the sample.

2.4.4 Energy Calibration

To be able to correctly interpret the NDP results it is important to know at which channel the different energy peaks appear. To do this a boron-containing standard is run and the

locations of the steps show where the different particles appear. The standard used for calibration is a borosilicate glass. The standard was let run overnight to allow for a high count rate in each channel. The resulting spectrum is seen in Figure 29.

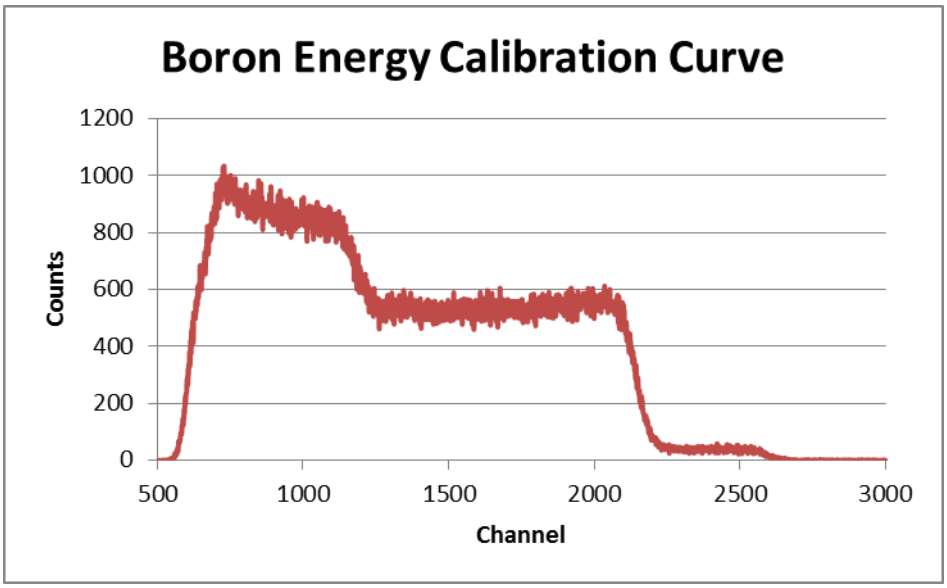

Figure 29 Energy calibration curve for NDP analysis

Since the leading edge of each step is not perfectly vertical the midpoint of the rise is used for the calibration. To determine the midpoint of each rise an average was taken of the number of counts at the lower end of the rise and at the upper end of the rise. Once the average of each end was established the difference was taken and a horizontal line was drawn at that point. Since the midpoint was crossed multiple times the central channel was picked by noting the first and last time the graph crossed the midpoint and the channel centered between the two was set to the corresponding energy.

The calibration curve used in Figure 29 lacks sharp, individual peaks due to the sample thickness being greater than the range of the reaction products. It would be possible to produce a spectrum with sharp peaks by depositing a monolayer of boron on a substrate such as silicon. Although this would allow for sharp peaks the sample would not be rugged and could easily be

destabilized. The use of a borosilicate glass as a standard is preferred because the glass is much more rugged. The borosilicate glass produces a spectrum with accurate results, and the spectrum can be easily fit mathematically.

Although there are four primary particle energies that are produce from the $^{10}B(n,\alpha)$ reaction only three are useable for the calibration. The 1472 keV alpha and the 840 keV Li are produce in approximately 94% of all reactions and so provide a nice large signal. The 1776 keV alpha, while only being produced 6% of the time is the highest energy particle and so shows up clearly on the graph. The 1013 keV Li signal is small enough to get lost in the sum of the 1776 and 1472 keV escape signals.

Having three points allows a linear regression of the points and the development of an equation to find the location of the 1013 keV peak and to assign an energy level to each channel. A linear regression of the three points shows a strong correlation with an R^2 value of 0.9999. Solving for the channel of the 1013 keV peak shows that it would be expected at channel 1447. Looking back, Figure 29 shows that there is a small bump below channel 1500 that is mostly lost in the sum of the other peaks.

Since the detector used is a silicon surface barrier detector a linear regression is applicable across the entire range of energies. To reduce the noise in the system the detector is transmission type and the voltage is set so that the detector is only partially depleted. The voltage is set low enough that the depletion depth excludes the excess volume beyond which incoming particles will penetrate.

2.4.5 Confidence of Results

The long dwell time for each location on a sample allows for a high total count. The reason for taking the time to get a high count is to obtain more accurate results. One way of

expressing the accuracy of the result is to calculate the margin of error. The margin of error is calculated on a confidence interval and expresses the confidence that the "true" value is located within some range, or margin of error, around your experimental value. The degree of confidence is described in terms of a probability and is set by the analyzer. There is a tradeoff between confidence and margin of error; the higher the confidence the larger the confidence interval. Typically the confidence interval used is 95%. The formula for calculating the margin of error for large sample sizes is defined by:

$$\bar{X} = \frac{0.98}{\sqrt{N}}$$

for the specified 95% confidence interval.

The large sample sizes enable the achievement of confidence intervals that are less than 0.1%. This confidence is satisfying, but misleading. While the instrument used is excellent and the statistics are solid enough to be completely confident that the measured value truly is the surface concentration of boron at that point there are other sources of error that can be introduced in the sample and in the procedure that can affect the results. Identifying these sources of error is important to be able to interpret the results from the NDP experiment.

For the Boral® the porosity of the core is a source of great error. The neutrons themselves and the charged He^+ or Li^+ ions ejected straight back to detector don't care if the surface is porous or not, they are going straight in and straight out. The complication arises from the deposition of boron or aluminum into the pores during the sectioning process. If the sample is cut the motion of the cutting blade naturally breaks the material into small particles and then drags them across the surface. Those particles have the chance of being trapped in the pores. Snapping the samples avoids the problem of using a saw but parts of the surface become too

rough to drag across the aperture, this necessitates filing the sample. The filing action creates the same deposition problems as the use of a saw.

In the Boral® the thick layer of aluminum cladding provides a ready source of aluminum that can be deposited into the pores. Deposition of aluminum covers up the boron and causes the count rate to decrease. Alternately, the small boron carbide particles that are loosely held in the core are free to get trapped in the pores, boosting the count rate. To minimize errors caused by boron and/or aluminum inclusions great care was taken to prepare the samples uniformly, thus any error is propagated across samples and canceled out by looking at the signal ratios. The use of a large aperture also helps to collect count rates across a larger area and hopefully obtaining a more average view of the sample. Even with the care taken there is still error.

Another source of error can come from physical deformation caused by the cutting process. Because NDP measures boron density any physical deformation that constricts the sample causing a density increase, or that relaxes the sample causing a density decrease will affect the measurement. While this density change is possible it is not likely to be a major source of error. Any change resulting in sufficient change in density is also doing to cause significant dimensional changes in the sample. These changes are easy to stop since dimensional measurement and even visual inspection can confirm density changes due to compression or swelling.

Chapter 3 Results

3.1 As-received Material

Samples of as-received Boral® and Bortec® were prepared for SEM investigation using the same sample preparation procedures that were used on the exposed samples. Characterization of the as-received material was undertaken to provide a standard reference measurement for corroded samples. Key areas of interest were the presence and location of secondary phases, interface between aluminum matrix and boron carbide particles, and the structure of the aluminum matrix.

The use of aluminum alloys in the manufacturing of Boral® and Bortec® introduces the possibility of secondary phase formation in the aluminum. Table 15 lists the solubility limits of some of the most prevalent species. The low solid solubility limits of the boron, iron, and nickel indicate that, if those species are present, they will likely appear as a precipitate. The solid solubility of copper is around two orders of magnitude higher than the other species and high enough that any copper present may be dissolved in the aluminum matrix.

Table 15 Solubility limits for various binary aluminum alloys[90]

	Temperature	Liquid Solubility		Solid Solubility	
Element	°C	wt. %	at. %	wt. %	at. %
B	660	0.022	0.054	<0.001	<0.002
Cu	550	33.15	17.39	5.67	2.48
Fe	655	1.87	0.91	0.052	0.025
Ni	640	6.12	2.91	0.05	0.023

Initial investigation of as-received Boral® shows that the core region is dominated by boron carbide and aluminum with sporadic porosity around the boron carbide. The porosity appears in the form of large voids that are typically either adjacent to larger boron carbide particles or in regions with high boron carbide density. Additionally, some porosity appears in the form of pits in individual boron carbide particles.

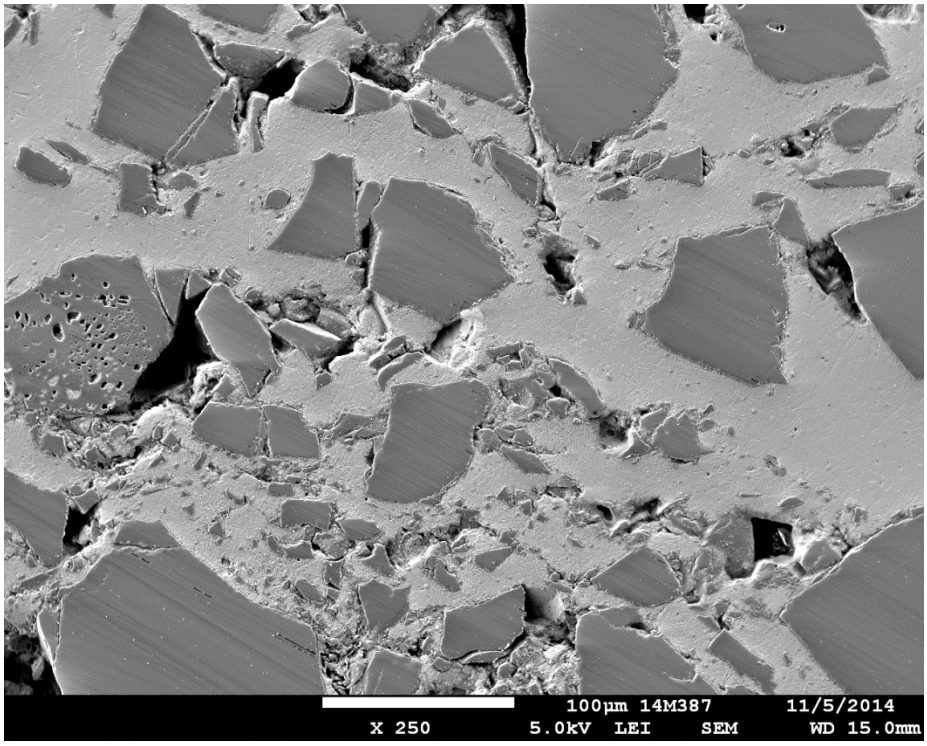

Figure 30 SEM LEI image of as-received Boral®

One of the issues with identifying secondary phases using SEM/EDS analysis is that subsurface particles can still produce signal. Additionally, small remnants of particles that existed above the surface may also remain behind. Both situations result in a mixed signal consisting of data from two particle types, this mixed signal can be misinterpreted as a new particle. In analyzing potential secondary phases in the Boral® or Bortec® one clue to identifying a secondary phase as opposed to a mixed signal is to look at the boron-to-carbon ratio. When performing EDS on a sample, analysis of known boron carbide pieces will establish a baseline

ratio. Ideally the ratio will be 4:1 however, both boron and carbon are approaching the limits of detectability for EDS and calibration and peak overlap make distinguishing and quantifying boron and carbon peaks difficult. If the boron-to-carbon ratio of an investigated spot falls outside variation found in baseline spectra than it is a reasonable assumption that the location is a secondary phase and not part of a boron carbide particle.

An EDS analysis of the sample showed iron, nickel, and copper as the primarily identifiable alloy elements. Silicon is also present, though it is difficult to determine if the silicon is part of the sample or if it is left over from polishing. The relationship between silicon content and oxygen content indicates that it is a silicon oxide and thus some is likely residual polishing compound. However, silicon is a common alloy element in aluminum and, accordingly, all silicon cannot be discounted as polishing residue. Analysis of the EDS results shown in Figure 31 and Figure 32 shows no boron outside of the boron carbide particles.

The spectrum in Figure 31 comes from a large boron carbide particle. The location of the species markers is positioned at a higher energy than where the center of the peak appears. This shift is due to the non-linearity of the detector at low energies. The boron and carbon peaks appear at as low of energy as the system can detect. Even though the peaks are shifted to lower energies the separation between the peaks is still sufficient to differentiate between the two. The differentiation is sufficient to determine the presence or absence of boron and carbon but a quantitative analysis of the data by the software will still produce errors for boron and carbon. While the values produced are not accurate for a particular location, comparing the ratios of boron to carbon at different locations will give an idea if two phases are similar.

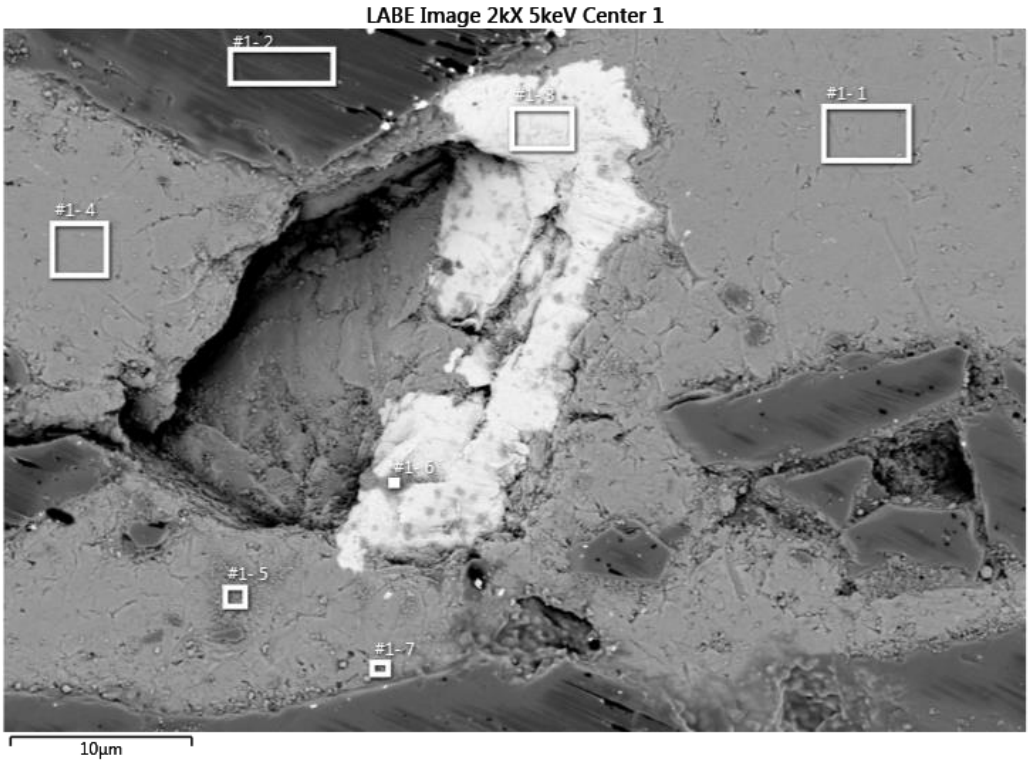

Result Type	Atomic %								
Spectrum Label	B	C	O	Al	Si	Fe	Ni	Cu	Total
#1- 1	0.00	8.84	3.55	87.45	0.16	0.00	0.00	0.00	100.00
#1- 2	59.30	39.91	0.79	0.00	0.00	0.00	0.00	0.00	100.00
#1- 3	0.00	23.33	6.28	2.64	2.44	55.32	8.37	1.61	100.00
#1- 4	0.00	9.64	3.84	86.31	0.20	0.00	0.00	0.00	100.00
#1- 5	0.00	17.82	27.15	42.35	12.52	0.16	0.00	0.00	100.00
#1- 6	0.00	29.48	31.82	0.63	15.94	19.31	2.25	0.57	100.00
#1- 7	0.00	17.19	11.75	67.61	3.45	0.00	0.00	0.00	100.00

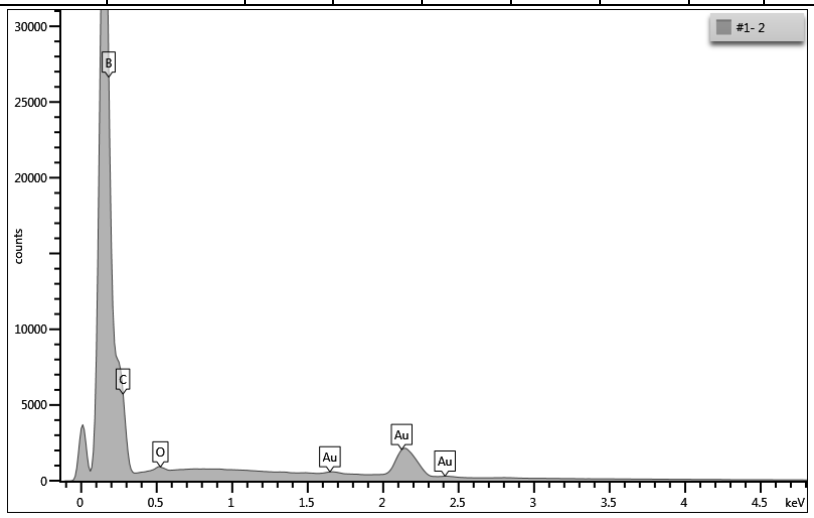

Figure 31 EDS of as-received Boral®. Spectrum is of location #1-2, a large boron carbide particle. Gold peaks in EDS spectra are from gold coating on the sample

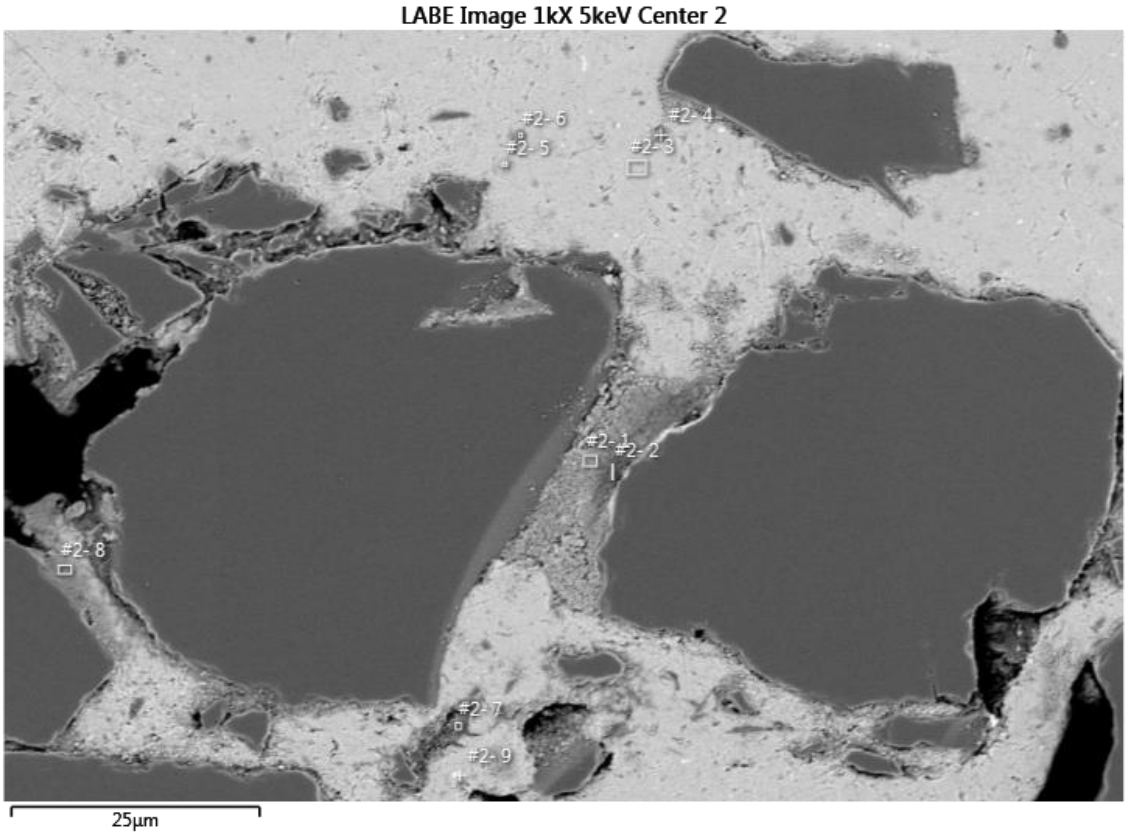

Result Type	Atomic %								
Spectrum Label	B	C	O	Al	Si	Fe	Ni	Cu	Total
#2- 1	0.00	38.20	37.79	0.00	23.53	0.48	0.00	0.00	100.00
#2- 2	0.00	40.59	39.40	0.00	20.01	0.00	0.00	0.00	100.00
#2- 3	0.00	7.51	2.96	89.52	0.00	0.00	0.00	0.00	100.00
#2- 4	0.00	82.47	2.84	14.48	0.21	0.00	0.00	0.00	100.00
#2- 5	0.00	11.54	25.40	50.18	12.71	0.17	0.00	0.00	100.00
#2- 6	0.00	79.17	3.94	16.28	0.61	0.00	0.00	0.00	100.00
#2- 7	0.00	85.45	13.87	0.46	0.22	0.00	0.00	0.00	100.00
#2- 8	0.00	37.69	21.28	32.24	8.79	0.00	0.00	0.00	100.00
#2- 9	0.00	6.14	13.11	74.90	0.63	4.73	0.50	0.00	100.00

Figure 32 EDS of as-received Boral®

Work has also been performed on a sample of Boral® from an older batch of material that was used in the EPRI work on Boral® performed at the University of Michigan. Microscopy work on the EPRI material was performed on a JEOL 7100F Schottky type SEM able to image using a Gentle Beam. JEOL's Gentle Beam applies a negative bias to the sample surface in order to decelerate the electrons. The result is a high resolution image formed using electrons with energies as low as 100 eV. This allows for imaging of small surface features.

Investigation of the sample using the SEM showed the presence of small precipitates that tended to collect around the edges and in the cracks of boron carbide particles. Analysis of the particles using EDS showed them to contain copper as seen in Figure 33. Note that the high carbon content reported at each location is artificial and is largely due to the carbon coating that was used on the sample.

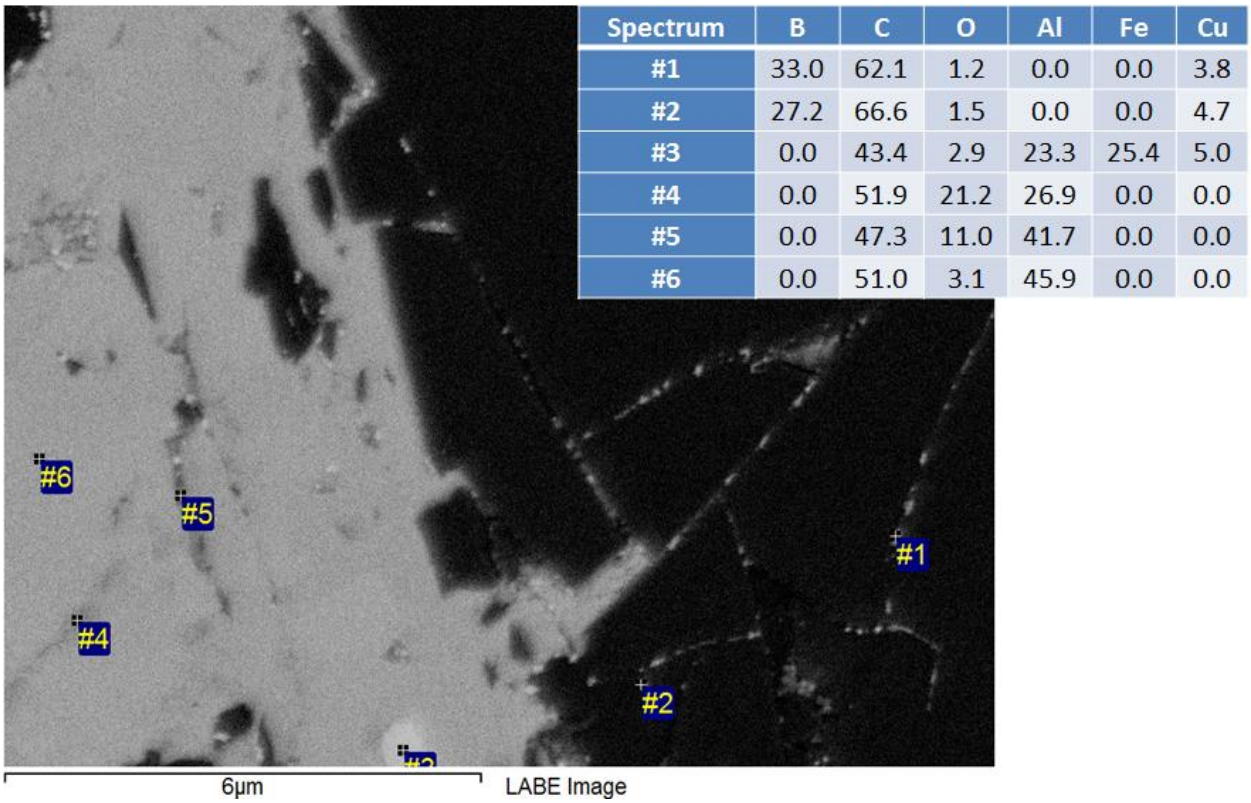

Spectrum	B	C	O	Al	Fe	Cu
#1	33.0	62.1	1.2	0.0	0.0	3.8
#2	27.2	66.6	1.5	0.0	0.0	4.7
#3	0.0	43.4	2.9	23.3	25.4	5.0
#4	0.0	51.9	21.2	26.9	0.0	0.0
#5	0.0	47.3	11.0	41.7	0.0	0.0
#6	0.0	51.0	3.1	45.9	0.0	0.0

Figure 33 Copper precipitates in as-received Boral®. Sample was carbon coated.

In Boral® the iron precipitates in the aluminum are most apparent in the cladding layer. Figure 34 shows the results of EDS analysis of the aluminum cladding layer in a piece of as-received Boral® from the EPRI project. It should be noted that copper does also appear in conjunction with the iron precipitates. Copper in contact with the boron carbide particles could lead to degradation of the boron carbide particle. Experiments involving copper droplets onto boron carbide show that the copper will cause a crater to form in the boron carbide. Upon

cooling, a cross section of the crater reveals the crater to be composed of graphite particles embedded in a copper-boron alloy[91].

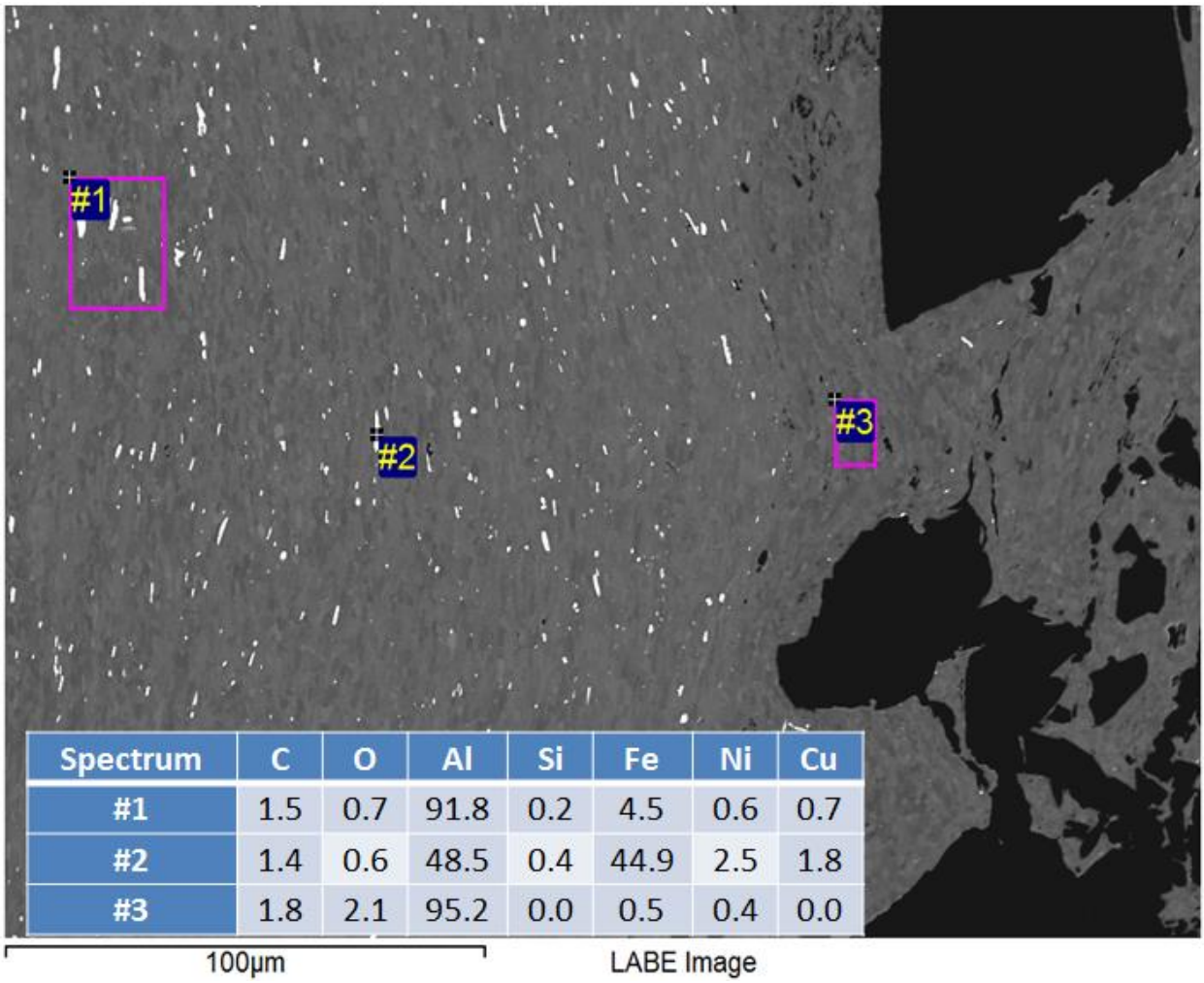

Spectrum	C	O	Al	Si	Fe	Ni	Cu
#1	1.5	0.7	91.8	0.2	4.5	0.6	0.7
#2	1.4	0.6	48.5	0.4	44.9	2.5	1.8
#3	1.8	2.1	95.2	0.0	0.5	0.4	0.0

Figure 34 EDS at cladding/core interface in as-received Boral®

Investigation of as-received Bortec® has shown much of the same characteristics as the as-received Boral®. One of the key differences is the reduced porosity of the Bortec®. Figure 35 shows as-received Bortec®. The texturing of the aluminum is due to the sample preparation.

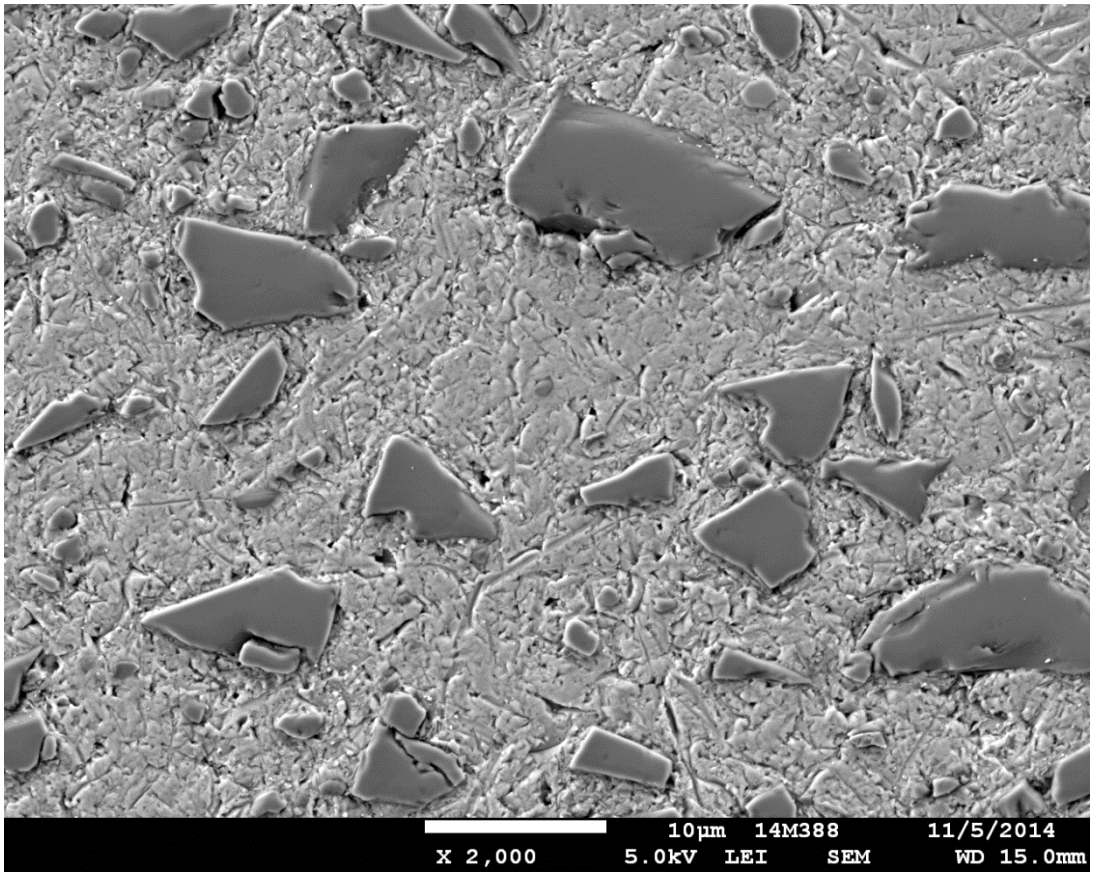

Figure 35 As-received Bortec®

Investigation of the as-received Bortec® sample using EDS reveals more than two distinct phases in the Bortec®. Figure 36 shows EDS results for 5 distinct phases in Bortec®. Spectrums #1 and #4 are particularly interesting since they have substantially more oxygen than any other location. It is also interesting to note the difference in the boron/carbon ratio between Spectrum #1 and Spectrum #2, the known boron carbide particle. Spectrum #1 shows a greatly reduced boron concentration. Spectrum #4 shows carbon without any boron.

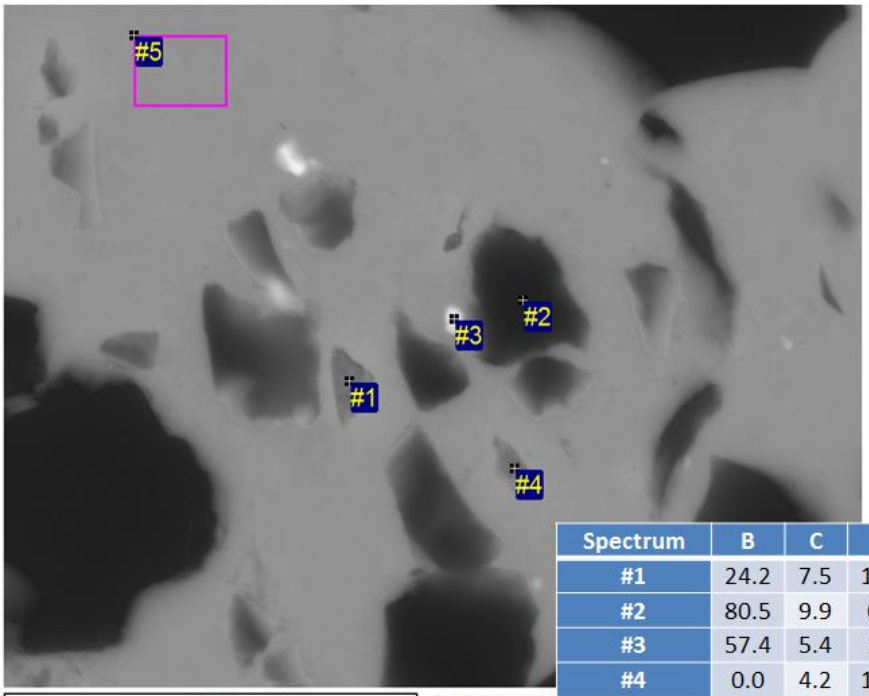

Processing option: All elements analyzed (Normalized)

All results in weight%

Spectrum	B	C	O	Al	Si	Fe	Ni	Cu
#1	24.2	7.5	11.2	53.8	3.0	0.2	0.1	0.0
#2	80.5	9.9	0.0	9.6	0.0	0.0	0.0	0.0
#3	57.4	5.4	1.1	30.1	0.1	5.7	0.2	0.0
#4	0.0	4.2	15.7	72.9	7.0	0.0	0.0	0.2
#5	13.0	1.8	0.9	84.0	0.0	0.0	0.3	0.0

Figure 36 EDS analysis of phases present in as-received Bortec®

3.2 Initial Corrosion Test

The initial corrosion test was carried out over a period of 155 days. The lack of any residual water at the conclusion of the test, combined with oxidation of the sample indicates that during the course of the test all of the water present reacted with the sample. The duration of time that humidity was present is unknown, but the results are still conclusive enough to cast doubt on the initial assumption that the samples would undergo corrosion of the aluminum.

Table 16 Results of initial corrosion test

			Difference (%)			
Sample ID	Material	Humidity	Length	Width	Thickness	Mass
33-01	Boral®	Low	0.043	0.023	0.037	0.042
33-01x	Boral®	Low	0.036	0.036	0.035	0.028
66-01	Boral®	Medium	0.025	0.030	0.019	0.101
66-01x	Boral®	Medium	0.071	0.056	0.120	0.118
100-01	Boral®	High	0.017	0.010	0.080	0.068
100-01x	Boral®	High	0.071	0.051	0.120	0.145
100-01T	Bortec®	High	0.020	0.012	0.105	0.013

Table 16 shows the changes in dimension and mass for samples in the initial corrosion test. The mass measured after exposure is the mass of the sample plus the mass of the oxide. No cleaning methods were employed to remove the oxide. Although oxide removal is typical for corrosion testing concern over degradation of the porous core in the Boral® samples caused the omission of this step. It was feared that if the oxide penetrated into the core then dissolving the oxide would destabilize the core material and result in loss of unoxidized core, greatly distorting the results. The slight mass increase observed in all of the samples is insignificant but the consistency of showing a positive mass increase does indicate oxidation.

Physical observation of the samples does confirm surface corrosion on all of the samples. Figure 37 shows the samples as they were removed from the pressure vessel. The Bortec® sample (Figure 37A) is uniformly covered in a black corrosion layer. The Boral® samples (Figure 37 B and C) have a flaky white corrosion layer that has formed. Figure 38 shows a secondary electron image of a Boral® surface that was exposed during the corrosion testing. The image was taken using 5 keV electrons. The underlying boron carbide particles are barely visible due to the inability of the electrons to penetrate through the surface layer.

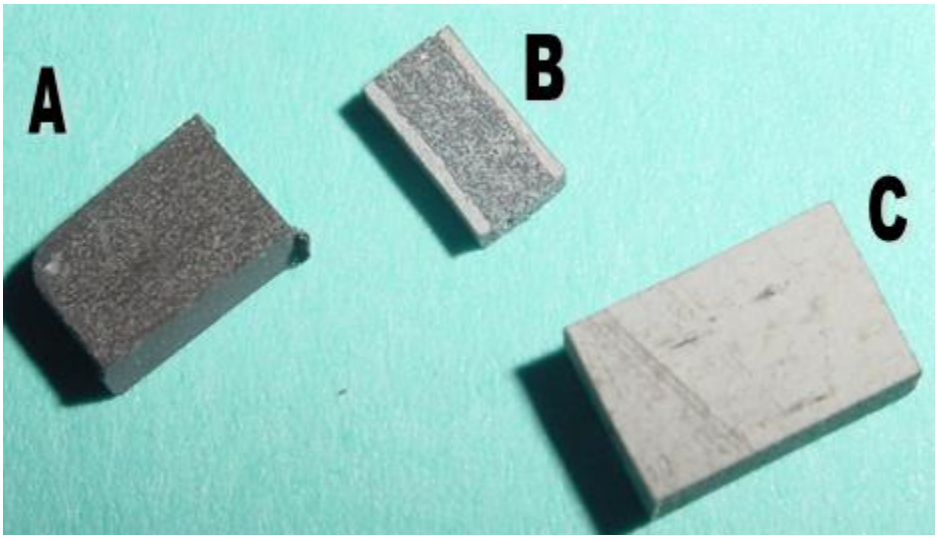

Figure 37 Samples from the high humidity initial corrosion experiment. A – Bortec® B – Boral® C- Boral®

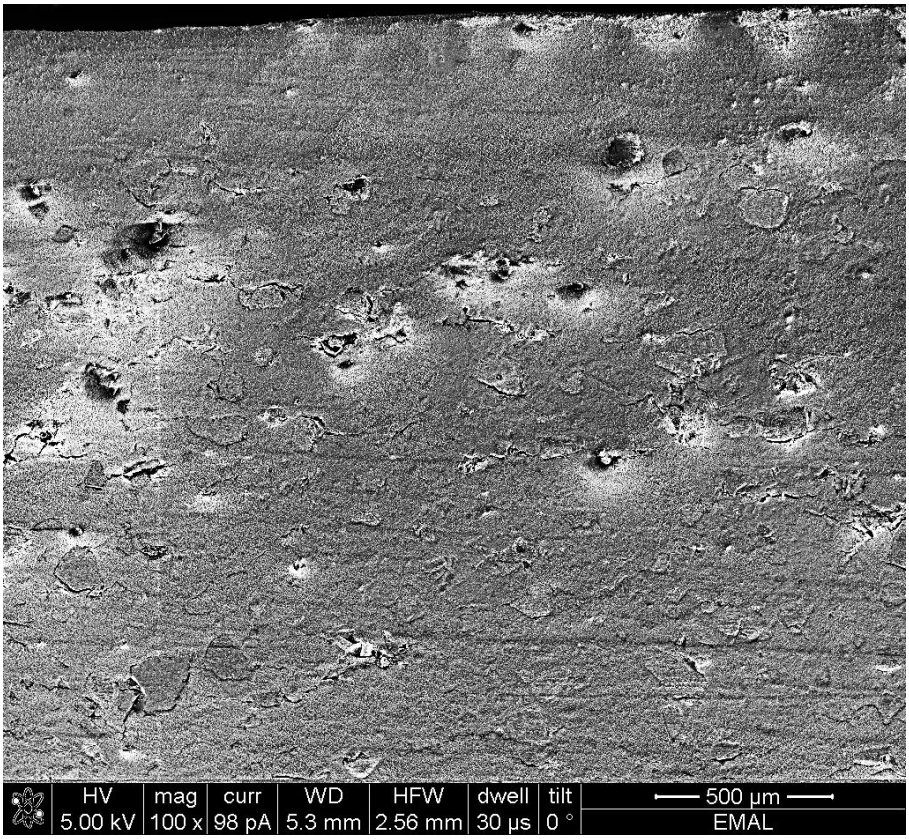

Figure 38 SEM image of Boral® surface exposed during initial corrosion test

The coloring on the samples can be compared to the coloring on as-received material shown in Figure 39.

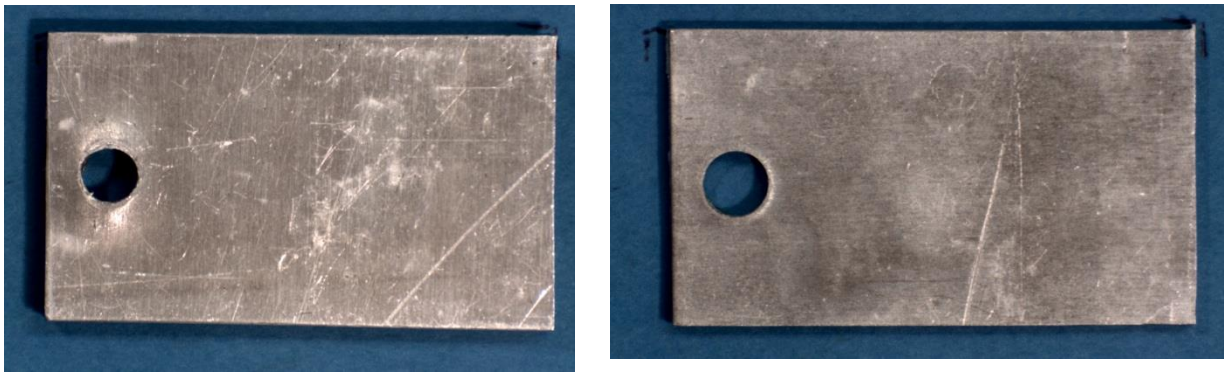

A. B.

Figure 39 As received samples of Boral® (A.) and Bortec® (B.)

Surface investigation was enough to show that corrosion did indeed take place but the lack of water in the vessels and the lack of weight gain raised questions about what really happened to the samples. SEM imaging of sample cross sections was used to help determine the extent of corrosion.

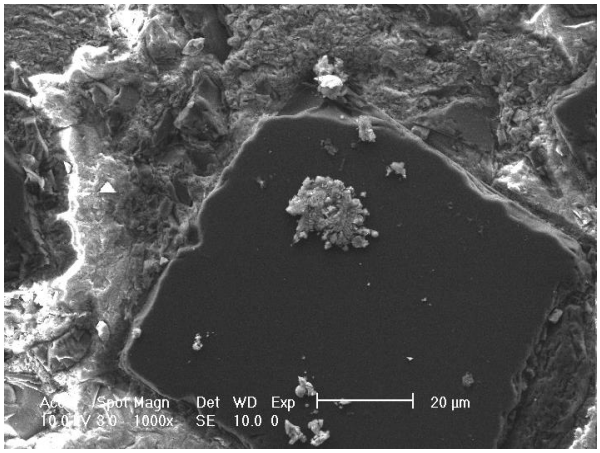

A.

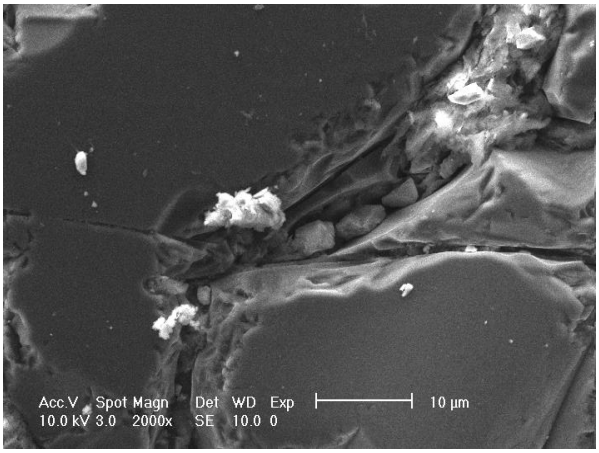

B.

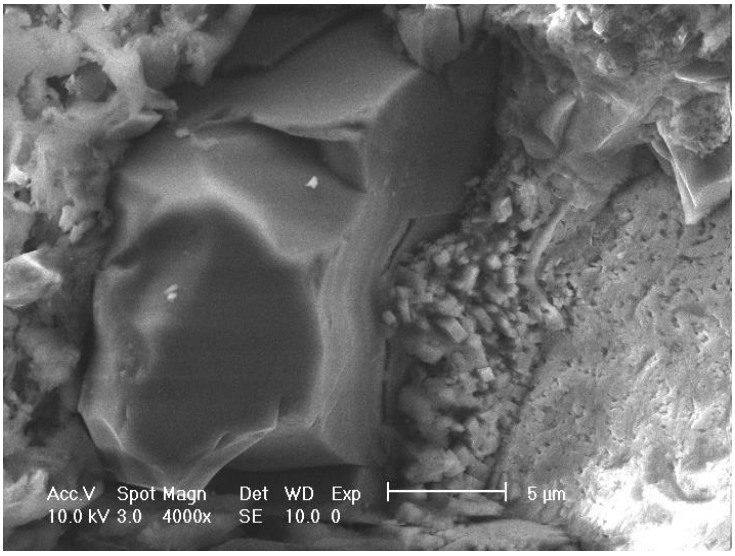

C.

Figure 40 Cross-sectional SEM image of Boral® sample after medium humidity initial corrosion test

Figure 40 shows the evidence of corrosion and new phase growth around boron carbide particles after 3700 hours of exposure in the medium humidity test. In Figure 40A there is corrosion all around the boron carbide particle. The contamination on the surface of the boron carbide particle is due to clumping as a result of trouble with the coater. Figure 40B shows new crystals growing in the gap region around a boron carbide particle. Figure 40C shows a gradient

of features leading up to the edge of a boron carbide particle. Figure 41 shows more of the extent of corrosion of boron carbide particles and the aluminum matrix in a Boral® sample from the high humidity corrosion test.

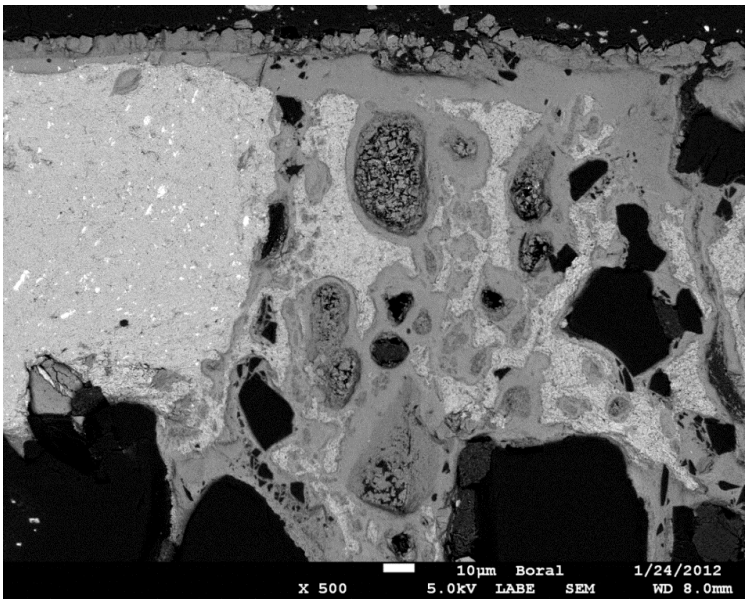

A.

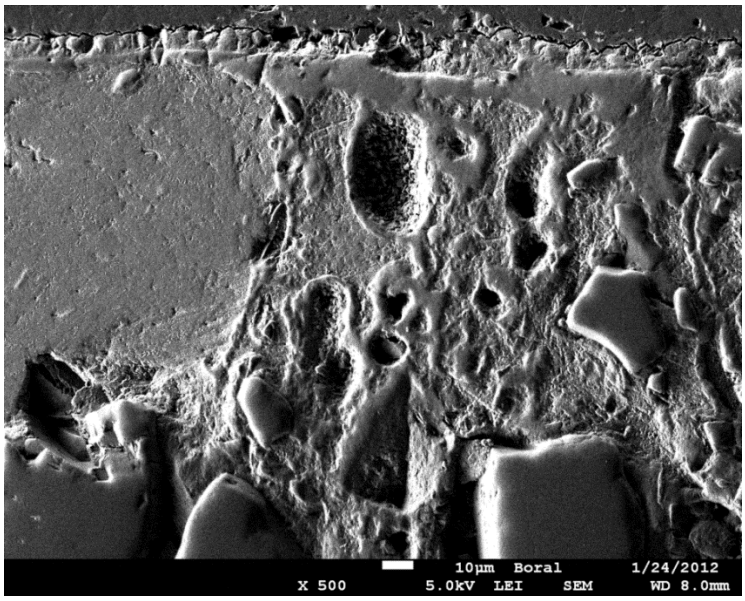

B.

Figure 41 SEM cross-section image of Boral® from high humidity initial corrosion test. A – Low-angle backscatter image. B – Lower secondary electron image

The top of Figure 41 is an edge of the core material that was exposed to water and steam during the initial corrosion test. The large smooth mass in the upper left is the aluminum cladding. The dark grey areas in Figure 41A are aluminum oxide. The backscatter electron image shows an oxide layer along the exposed and helps to highlight the flow path of the water as it penetrated into the sample from the exposed edge. The aluminum oxide surrounds pockets of new crystalline growth. Figure 41B confirms that these pockets of new growth are holes in the surface.

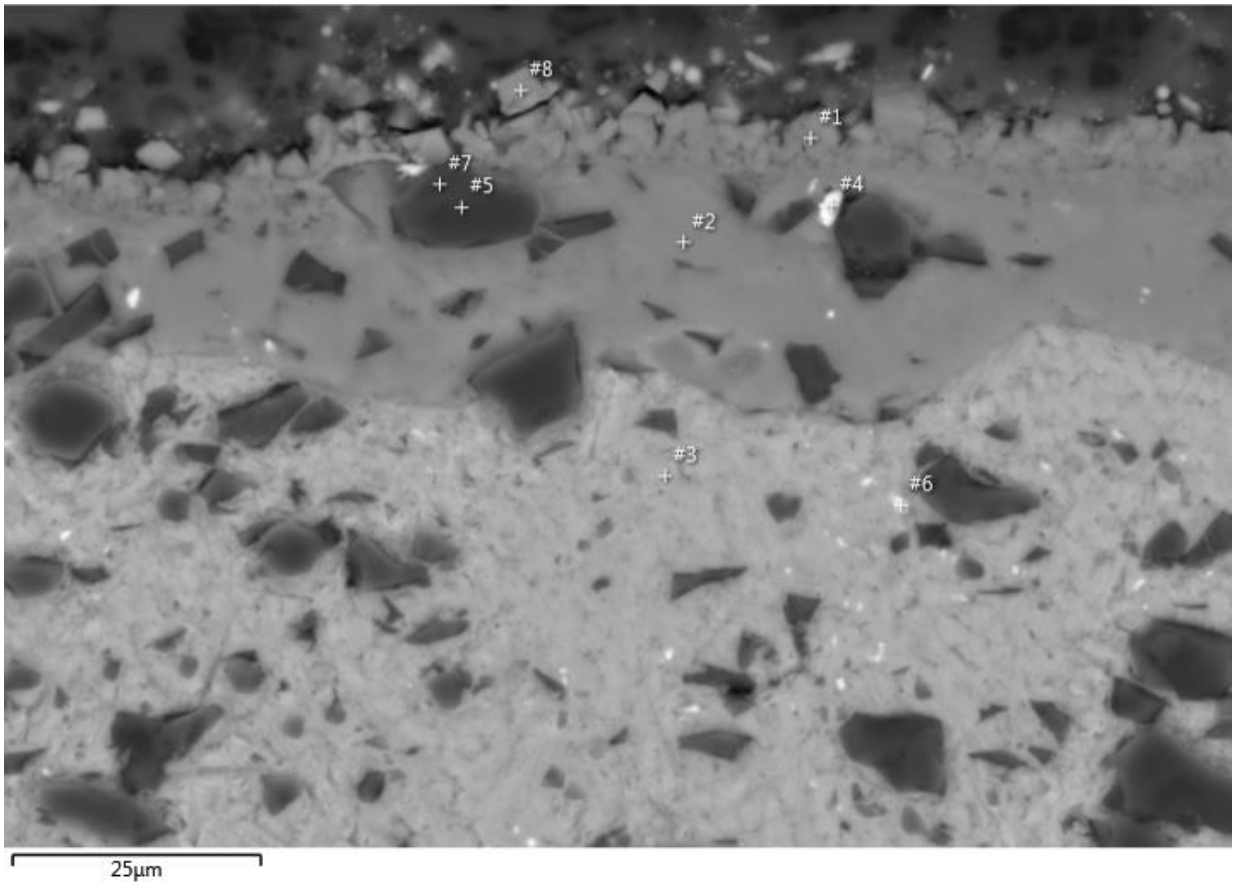

Spectrum Label	B	O	Al	Si	Ca	Fe	Total
#8	0.00	61.74	37.94	0.15	0.10	0.06	100.00
#7	97.02	2.60	0.33	0.01	0.02	0.01	100.00
#6	0.00	6.55	80.95	0.76	0.08	11.65	100.00
#5	99.41	0.56	0.03	0.00	0.00	0.00	100.00

#4	66.45	24.03	2.44	0.10	0.02	6.97	100.00
#3	0.00	3.55	96.21	0.17	0.06	0.00	100.00
#2	0.00	57.84	41.34	0.22	0.20	0.34	100.00
#1	0.00	63.03	36.82	0.00	0.08	0.06	100.00

Figure 42 EDS point results for oxide layer of high-humidity initial corrosion test Bortec® sample. 1,000X magnification, 20keV acceleration

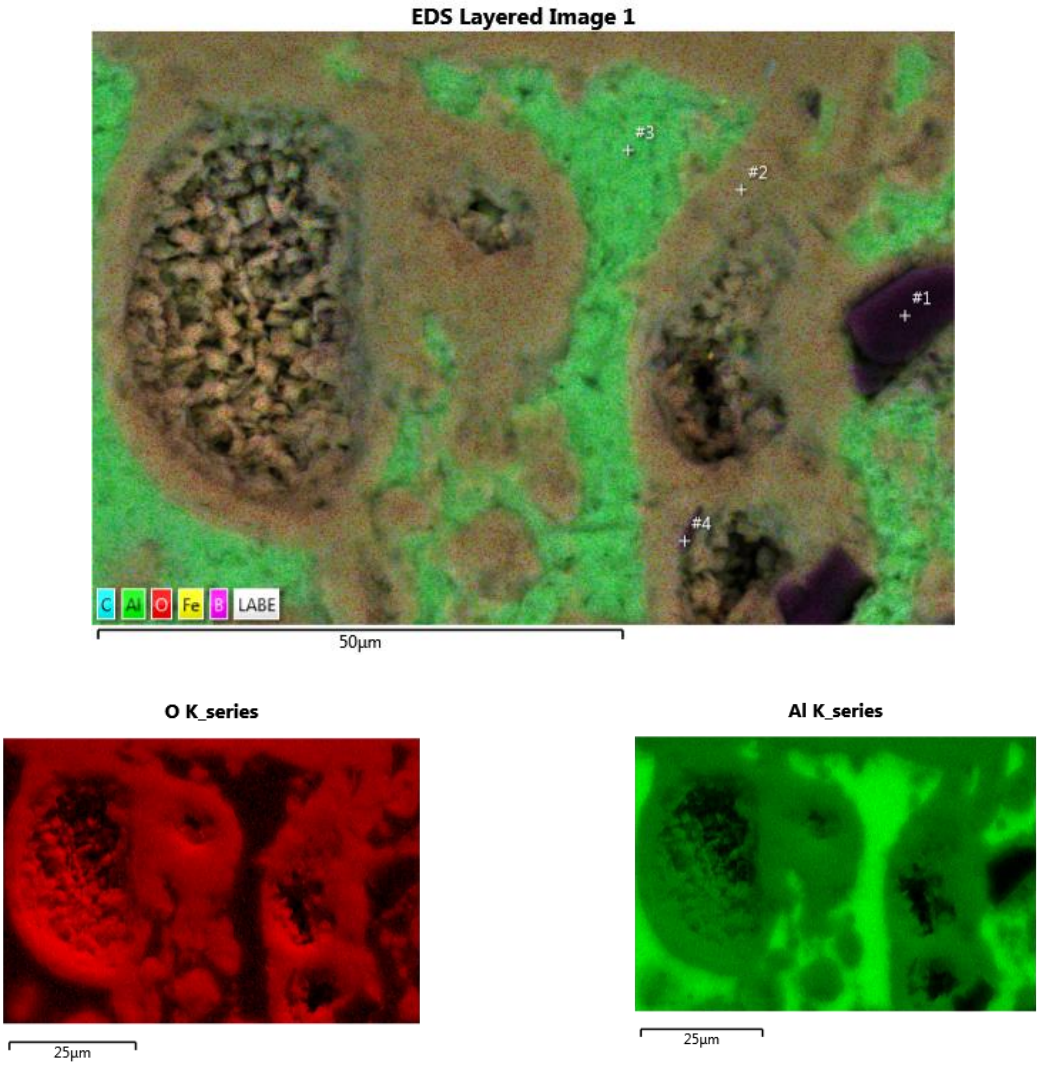

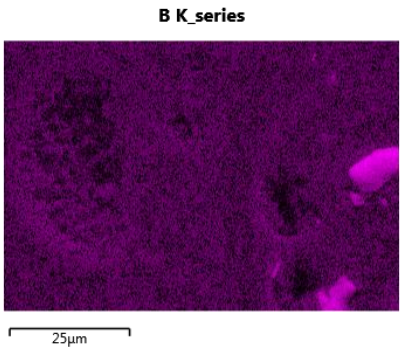

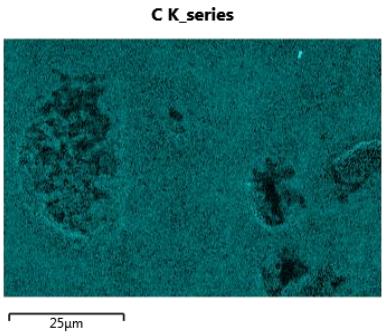

Spectrum Label	B	O	Al	Si	Total
#1	99.26	0.66	0.05	0.03	100.00
#2	0.00	56.15	43.85	0.00	100.00
#3	0.00	2.61	97.28	0.11	100.00
#4	78.58	15.17	6.23	0.01	100.00

Figure 43 EDS Map of Boral® from high humidity initial corrosion experiment

EDS mapping of the sample sheds light on the corrosion behavior of the Boral®. Limitations in the EDS system used do not allow for definitive results. One of the most significant limitations is the inability to differentiate between the boron and carbon. This prevents the identification of phases. Additionally, the topography of the holes creates shadowed regions that prevent full analysis of the new crystalline growth. One of the most significant points is Spectrum 4 in Figure 43. Spectrum 4 shows a sliver of a boron carbide particle left at the edge of one of the holes. This indicates that the holes are the remains of boron carbide particles.

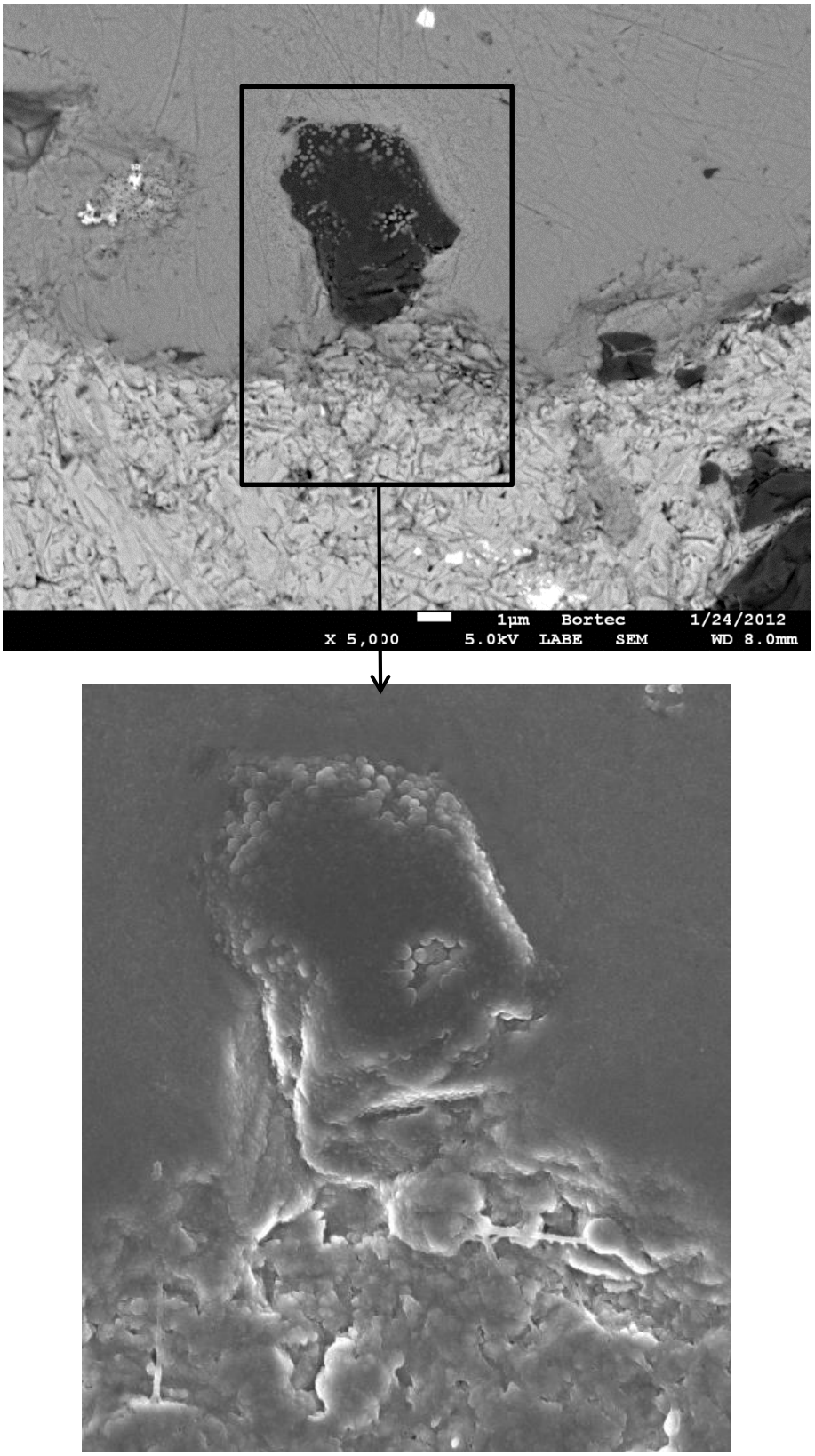

Figure 44 - Low-angle backscatter and secondary electron images of Bortec® from high humidity initial corrosion test

The Bortec® samples shows less evidence of corrosion than the Boral®. This is likely due to the lower porosity of Bortec® not allowing the water to penetrate into the sample. Figure 42 shows an EDS analysis of an exposed Bortec® edge (top of image) from the high humidity initial corrosion experiment. From that image there appears to be three distinct regions. On the outermost edge there appears to be a heavily oxidized layer that is breaking apart. Next to that is a more intact oxide layer. Beneath that is an aluminum layer that is not oxidized. Points 1, 2, and 3 from the EDS spectrum in Figure 42 do indicate that there are compositional differences between these three regions. Points 5 and 7 are both on the same boron carbide particle that lies along the line separating the two oxide regions. EDS analysis indicates that there is a compositional difference in that particle. However, the particle is thinner at point 7 and the large interaction volume could account for some of the difference. Figure 45 shows the boron carbide particle that was probed.

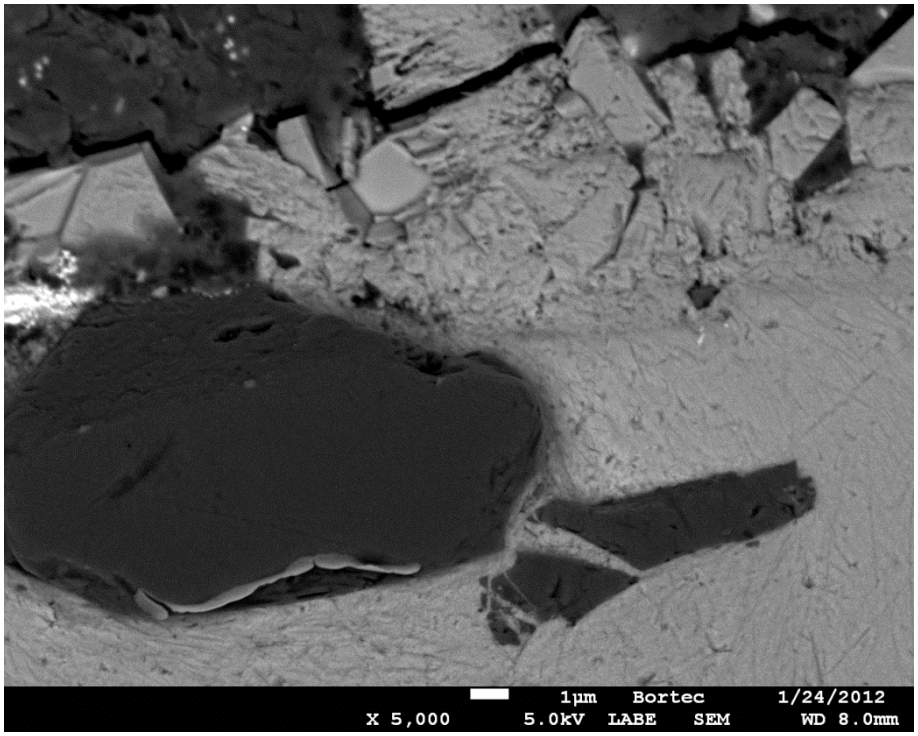

Figure 45 - Degraded boron carbide particle in Bortec® sample from high humidity initial corrosion experiment

Some of the boron carbide particles within the oxide layer appear to have developed nodular growths. Figure 44 shows one such boron carbide particle. The nodular growth on the boron carbide particle matches the structure of the surrounding aluminum oxide. It appears that most of the changes to the Bortec® occur in regions close in proximity to boron carbide particles. Corrosion testing began with tests at 400 and 570°C. The tests at 570°C were of the most interest to show the extents of corrosion that could potentially be expected. Although the conditions are well outside of anything that could be reasonable expected during deployment it is not expected that the corrosion mechanisms at work would be the same mechanisms that would affect the material at lower temperatures.

Prior trouble with the formation of solid deposits on the outlet lines from the autoclave showed that corrosion was taking place quickly at elevated temperatures. Since corrosion was

progressing at a fairly rapid rate and knowing that the conditions were outside of expected conditions only two sets of samples were loaded into the autoclave, each set consisting of one of each different sample material. After loading the autoclave the system was started and remained at temperature for 21 days. After 21 days the system was shut down and allowed to cool before opening. Upon opening the first set of samples was removed and the remaining set was replaced on the rack and returned to the autoclave. The system was then started back up and allowed to remain at temperature for an additional 29 days, resulting in 50 days of total exposure.

Soak Tests

Room temperature testing was performed through the submersion of samples in DI water or hydrogen peroxide for extended time. The results of the soak test cannot be directly used for predicting long-term behavior in a dry cask environment due to differences in corrosion mechanisms. However, the use of the soak tests does prove useful for helping to determine possible areas of concern.

3.3 Soak Tests

To gain an idea of the effect of hydrolysis on the samples soak tests were established. Although the material will not be submerged during dry cask storage the soak test provides an opportunity to observe the samples and determine if any effect is likely. Use of hydrogen peroxide in the autoclave system is not practical due to the temperatures involved. The hydrogen peroxide would be held at 90°C before uptake in the gas during which time it would undergo significant decomposition. Further heating to 250°C on the way to the autoclave would rapidly degrade any hydrogen peroxide left.

Soaking samples concurrently in DI water served as a base-line test to compare the effects of hydrogen peroxide against. Soaking samples in DI water followed by heating in an

inert environment was also useful to determine if the presence of water at temperature initiated the new phase formation or if the formation of surface oxide was sufficient to drive the changes.

3.3.1 Hydrogen Peroxide Soak Test

One of the concerns with the presence of water in a dry cask is the radiolysis of water. The radiolysis of water produces many different oxygen and hydrogen compounds that affect the chemistry of a system. Table 17 lists the reactions that are present in water undergoing radiolysis. The main oxidizing agent generated is hydrogen peroxide [92]. Since hydrogen peroxide is such a strong oxidizer it is important to understand how it will affect the material. It has been reported in literature that the additional of alumina powder to pure water undergoing γ-radiolysis resulted in a strong reduction of H_2O_2 and a high yield of hydrogen [93]. The strong reaction between the hydrogen peroxide and alumina could result in the deterioration of the protective oxide layer, furthering corrosion of the material.

To test the behavior of Boral® and Bortec® in hydrogen peroxide samples of each material were soaked in a sealed vial of an aqueous 30% hydrogen peroxide solution. The samples were left to soak for 12 months at room temperature. By the end of the soak all of the hydrogen peroxide and water had reacted with the samples and, although the vials were sealed, they were dry. As can be seen in Table 18 both samples experienced significant corrosion, especially when compared to the results from the DI water soak test.

Table 17 Water radiolysis reaction rate constants [94]

	Reaction	k_r		Reaction	k_r
1	$H^+ + OH^- \rightarrow H_2O$	1.4×10^{11}	40	$\cdot H + O_3 \rightarrow \cdot HO_3$	3.8×10^{10}
2	$H_2O \rightarrow H^+ + OH^-$	(13.999)	41	$2\cdot OH \rightarrow H_2O_2$	3.6×10^{9}
3	$H_2O_2 \rightarrow H^+ + \cdot HO_2^-$	(11.65)	42	$\cdot OH + \cdot HO_2 \rightarrow H_2O + O_2$	6.0×10^{9}
4	$H^+ + \cdot HO_2^- \rightarrow H_2O_2$	5.0×10^{10}	43	$\cdot OH + O_2^- \rightarrow OH^- + O_2$	8.2×10^{9}
5	$H_2O_2 + OH^- \rightarrow \cdot HO_2^- + H_2O$	1.3×10^{10}	44	$\cdot OH + H_2 \rightarrow \cdot H + H_2O$	4.3×10^{7}
6	$\cdot HO_2^- + H_2O \rightarrow H_2O_2 + OH^-$	(11.65)	45	$\cdot OH + H_2O_2 \rightarrow \cdot HO_2 + H_2O$	2.7×10^{7}
7	$e^- + H_2O \rightarrow \cdot H + OH^-$	1.9×10^{1}	46	$\cdot OH + \cdot O^- \rightarrow \cdot HO_2^-$	2.5×10^{10}
8	$\cdot H + OH^- \rightarrow e^- + H_2O$	2.2×10^{7}	47	$\cdot OH + \cdot HO_2^- \rightarrow \cdot HO_2 + OH^-$	7.5×10^{9}
9	$\cdot H \rightarrow e^- + H^+$	(9.77)	48	$\cdot OH + O_3^- \rightarrow O_3 + OH^-$	2.6×10^{9}
10	$e^- + H^+ \rightarrow H$	2.3×10^{10}	49	$\cdot OH + O_3^- \rightarrow O_2^- + O_2^- + H^+$	6.0×10^{9}
11	$\cdot OH + OH^- \rightarrow \cdot O^- + H_2O$	1.3×10^{10}	50	$\cdot OH + O_3 \rightarrow \cdot HO_2 + O_2$	1.1×10^{8}
12	$\cdot O^- + H_2O \rightarrow \cdot OH + OH^-$	(11.9)	51	$\cdot HO_2 + O_2^- \rightarrow \cdot HO_2^- + O_2$	8.0×10^{7}
13	$\cdot OH \rightarrow \cdot O^- + H^+$	(11.9)	52	$\cdot HO_2 + \cdot HO_2 \rightarrow H_2O_2 + O_2$	7.0×10^{5}
14	$\cdot O^- + H^+ \rightarrow \cdot OH$	1.0×10^{11}	53	$\cdot HO_2 + \cdot O^- \rightarrow O_2 + OH^-$	6.0×10^{9}
15	$\cdot HO_2 \rightarrow O_2^- + H^+$	(4.57)	54	$\cdot HO_2 + H_2O_2 \rightarrow \cdot OH + O_2 + H_2O$	5.0×10^{-1}
16	$O_2^- + H^+ \rightarrow \cdot HO_2$	5.0×10^{10}	55	$\cdot HO_2 + \cdot HO_2^- \rightarrow \cdot OH + O_2 + OH^-$	5.0×10^{-1}
17	$\cdot HO_2 + OH^- \rightarrow O_2^- + H_2O$	5.0×10^{10}	56	$\cdot HO_2 + O_3^- \rightarrow 2O_2 + OH^-$	6.0×10^{9}
18	$O_2^- + H_2O \rightarrow \cdot HO_2 + OH^-$	(4.57)	57	$\cdot HO_2 + O_3 \rightarrow \cdot HO_3 + O_2$	5.0×10^{8}
19	$e^- + \cdot OH \rightarrow OH^-$	3.0×10^{10}	58	$2O_2^- + 2H_2O \rightarrow H_2O_2 + O_2 + 2OH^-$	1.0×10^{2}
20	$e^- + H_2O_2 \rightarrow \cdot OH + OH^-$	1.1×10^{10}	59	$O_2^- + \cdot O^- + H_2O \rightarrow O_2 + 2OH^-$	6.0×10^{8}
21	$e^- + O_2^- + H_2O \rightarrow \cdot HO_2^- + OH^-$	1.3×10^{10}	60	$O_2^- + H_2O_2 \rightarrow \cdot OH + O_2 + OH^-$	1.3×10^{-1}
22	$e^- + \cdot HO_2 \rightarrow \cdot HO_2^-$	2.0×10^{10}	61	$O_2^- + \cdot HO_2^- \rightarrow \cdot O^- + O_2 + OH^-$	1.3×10^{-1}
23	$e^- + O_2 \rightarrow O_2^-$	1.9×10^{10}	62	$O_2^- + O_3^- + H_2O \rightarrow 2O_2 + 2OH^-$	1.0×10^{4}
24	$2e^- + H_2O + H_2O \rightarrow H_2 + 2OH^-$	5.5×10^{9}	63	$O_2^- + O_3 \rightarrow O_3^- + O_2$	1.5×10^{9}
25	$e^- + \cdot H + H_2O \rightarrow H_2 + OH^-$	2.5×10^{10}	64	$\cdot O^- + \cdot O^- + H_2O \rightarrow \cdot HO_2^- + OH^-$	1.0×10^{9}
26	$e^- + \cdot HO_2^- \rightarrow \cdot O^- + OH^-$	3.5×10^{9}	65	$\cdot O^- + O_2 \rightarrow O_3^-$	3.6×10^{9}
27	$e^- + \cdot O^- + H_2O \rightarrow OH^- + OH^-$	2.2×10^{10}	66	$\cdot O^- + H_2 \rightarrow \cdot H + OH^-$	8.0×10^{7}
28	$e^- + O_3^- + H_2O \rightarrow O_2 + 2OH^-$	1.6×10^{10}	67	$\cdot O^- + H_2O_2 \rightarrow O_2^- + H_2O$	5.0×10^{8}
29	$e^- + O_3 \rightarrow O_3^-$	3.6×10^{10}	68	$\cdot O^- + \cdot HO_2^- \rightarrow O_2^- + OH^-$	4.0×10^{8}
30	$\cdot H + H_2O \rightarrow H_2 + \cdot OH$	1.1×10^{1}	69	$\cdot O^- + O_3^- \rightarrow O_2^- + O_2^-$	7.0×10^{8}
31	$\cdot H + \cdot O^- \rightarrow OH^-$	1.0×10^{10}	70	$\cdot O^- + O_3 \rightarrow O_2^- + O_2$	5.0×10^{9}
32	$\cdot H + \cdot HO_2^- \rightarrow \cdot OH + OH^-$	9.0×10^{7}	71	$O_3^- \rightarrow O_2 + \cdot O^-$	3.3×10^{3}
33	$\cdot H + O_3^- \rightarrow OH^- + O_2$	1.0×10^{10}	72	$O_3^- + H^+ \rightarrow O_2 + \cdot OH$	9.0×10^{10}
34	$2\cdot H \rightarrow H_2$	7.8×10^{9}	73	$\cdot HO_3 \rightarrow O_2 + \cdot OH$	1.1×10^{5}
35	$\cdot H + \cdot OH \rightarrow H_2O$	7.0×10^{9}	74	$O_2 \rightarrow O_2D$	0
36	$\cdot H + H_2O_2 \rightarrow \cdot OH + H_2O$	9.0×10^{7}	75	$H_2 \rightarrow H_2D$	0
37	$\cdot H + O_2 \rightarrow \cdot HO_2$	2.1×10^{10}	76	$H_2O_2 \rightarrow H_2O + \cdot O$	1.0×10^{-3}
38	$\cdot H + \cdot HO_2 \rightarrow H_2O_2$	1.8×10^{10}	77	$\cdot O + \cdot O \rightarrow O_2$	1.0×10^{9}
39	$\cdot H + O_2^- \rightarrow \cdot HO_2^-$	1.8×10^{10}			

Table 18 Soak test results

Sample	Solution	Initial Mass (mg)	Final Mass (mg)	Change (%)
Bortec®	DI Water	986.4	988.37	0.200
Boral	DI Water	711.3	712.81	0.212
Bortec®	H_2O_2	980.0	914.27	-6.7
Boral®	H_2O_2	711.3	534.07	-24.9

The corrosion behavior of Boral® in the hydrogen peroxide soak test showed preferential corrosion of the aluminum cladding layer with minimal effect on the inner core material. Figure 46 shows an image of the Boral® sample taken with optical microscopy. Figure 46A shows the

remnant of cladding on the left of the sample and where the core material is now exposed. Figure 46B shows the exposed surface at the top of the image; note that the core is still mostly intact. Figure 47 shows corrosion of the Bortec® sample from the hydrogen peroxide soak test.

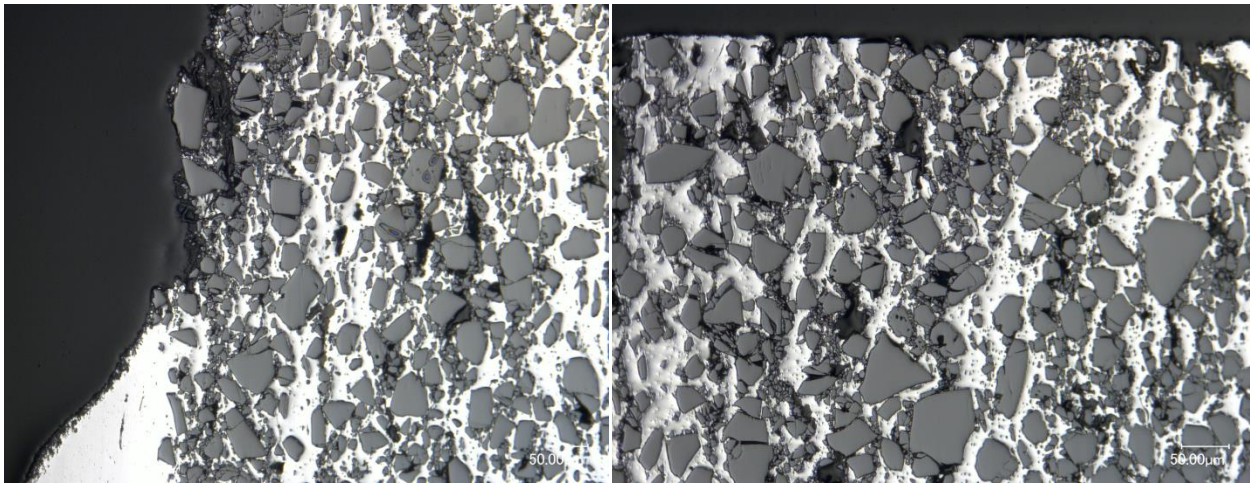

A. B.

Figure 46 Optical image of Boral® sample from the hydrogen peroxide soak test

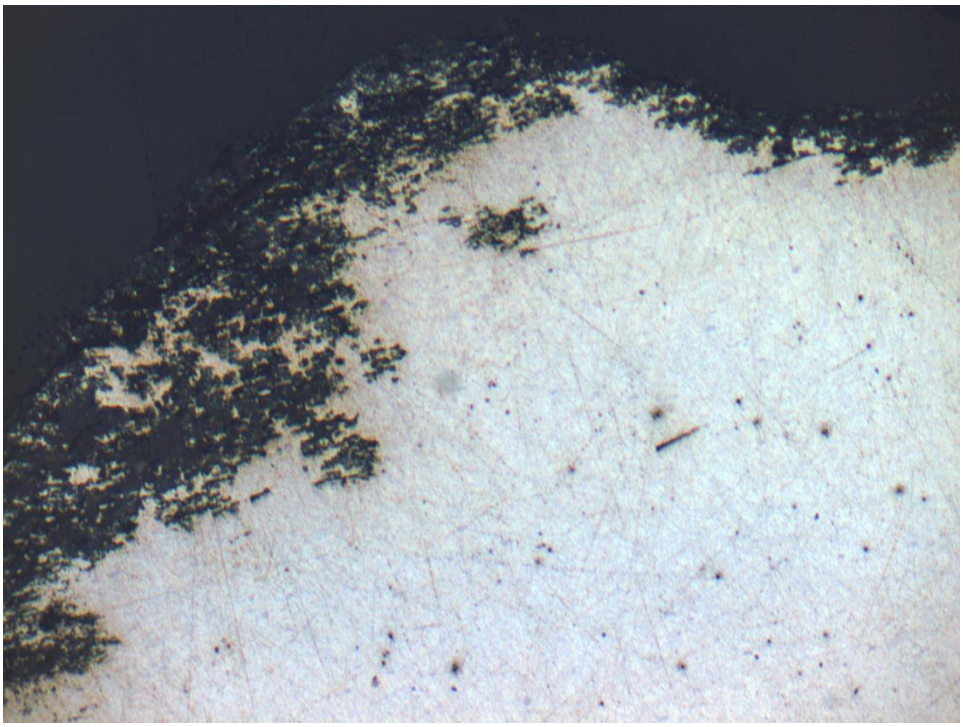

Figure 47 20X optical image of Bortec® sample from the hydrogen peroxide soak test

3.3.2 Water Soak Samples

For the soak tests carried out in DI water the samples were placed in a 24 mL glass vial with a PTFE closure to prevent any moisture from evaporating. On sample of Boral® and one sample of Bortec® was placed in the vial. The remainder of the volume was filled with 18 MΩ DI water. The samples were placed in a fume hood and left to sit at room temperature.

The samples were left to sit in the water for 15 months. At the end of 15 months the samples were still fully submerged. However, the samples did develop a white flakey layer that completely covered the outside of the sample. The samples also exhibited weight gain after being removed from the water and allowed to dry in air at room temperature for one week. The mass increases for both samples are slight, but the gain is consistent for both.

The samples were then loaded into a Thermogravimetric Analyzer (TGA). After loading the TGA argon was flowed through the system for 30 minutes to purge out any remaining air. Argon remained flowing through the system at 95 sccm for the duration of the test. The system was then ramped up to 540°C over a period of 2 hours. The system was held at temperature for 594 hours.

Optical microscopy of the sample post-TGA shows evidence of the formation of new secondary phases in the aluminum matrix. Preservation of the original oxide is also seen in the epoxy surrounding the sample. Figure 48 shows a cross section of a sample of Bortec®. Further analysis through an SEM and EDS reveals some oxidation and boron in the aluminum matrix. The EDS results in Figure 49 show boron at every location. Figure 49 also shows the presence of nickel and iron. Nickel and iron are of interest, especially near the surface, since nickel and iron oxides will react with boron carbide and consume it[95, 96].

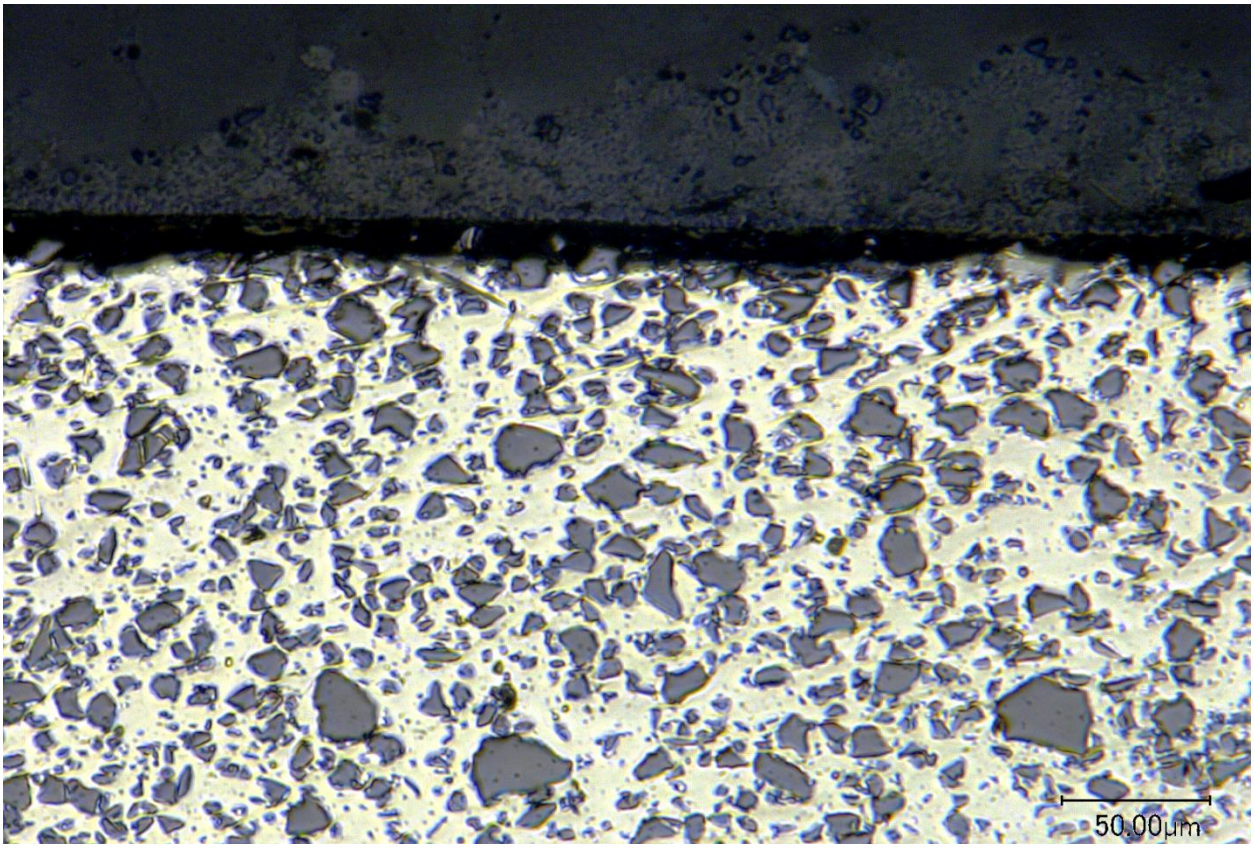

Figure 48 Bortec sample after soaking in DI water followed by heating in dry argon at 550°C

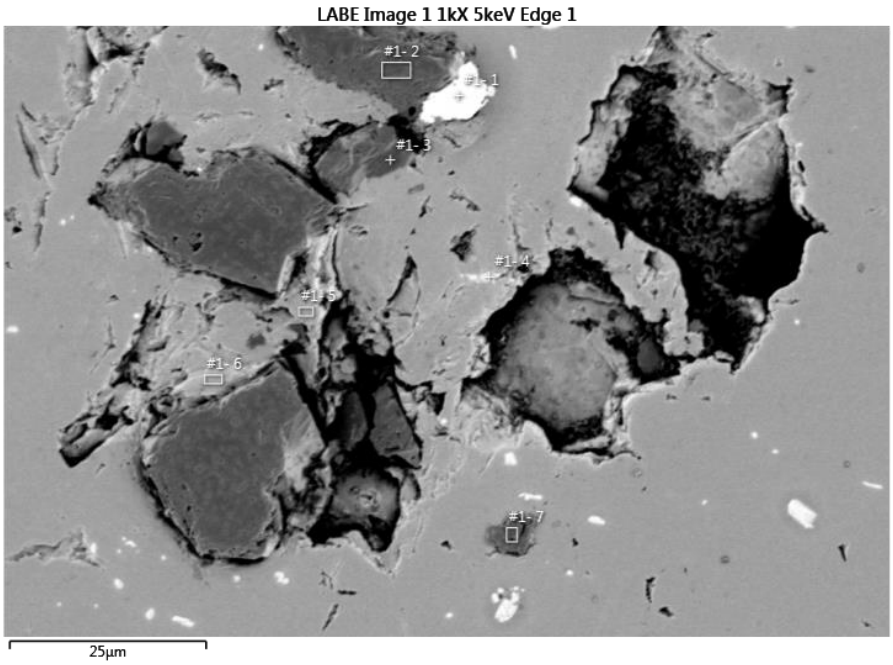

Result Type	Atomic %							
Spectrum Label	B	C	O	Al	Si	Fe	Ni	Cu
#1- 1	14.70	5.33	6.83	1.54	1.11	57.33	9.27	3.88
#1- 2	4.39	94.79	0.35	0.47	0.00	0.00	0.00	0.00
#1- 3	6.37	93.03	0.15	0.46	0.00	0.00	0.00	0.00
#1- 4	9.16	2.85	6.83	54.16	0.91	26.09	0.00	0.00
#1- 5	5.00	8.32	4.75	81.94	0.00	0.00	0.00	0.00
#1- 6	4.99	5.38	4.12	85.27	0.00	0.24	0.00	0.00
#1- 7	6.12	92.44	0.36	0.76	0.00	0.00	0.00	0.32

Figure 49 EDS analysis of Bortec® sample from soak test after heating in dry argon at 570°C

3.4 Autoclave Corrosion

Corrosion in the autoclaves was performed at three different temperatures: 300°C, 400°C, and 570°C. Testing at all three temperatures was conducted with humidified argon. The argon flow rate averaged around 1.5 scfh and water usage was approximated at 34 mL/hr. The argon flow rate can be converted to a mass flow rate using the ideal gas law. Since the argon temperature does not exceed 90°C when it is humidified and the system is at ambient pressure than the ideal gas law sufficiently models the system. The water flow rate is easily converted to a mass flow rate using the density of water at 90°C. From these values the humidity ratio for these tests is determined to be $0.58\frac{kg_{water}}{kg_{argon}}$.

Initial investigation of samples was conducted using SEM and EDS to locate and differentiate new phases present in the materials. Comparison of phase compositions can reveal the uniformity of mechanisms across the temperature range. Comparisons across time and temperature reveals information about the kinetics involved with the phase formation.

Corrosion testing was also performed in the autoclaves at 400°C with the humidity level of the inlet water lowered. For one test an intermediate humidity ratio of 0.082 $\frac{kg_{water}}{kg_{argon}}$ was used. A low humidity test was also conducted using a gas flow with a humidity ratio of 0.028$\frac{kg_{water}}{kg_{argon}}$. The goal of low humidity testing is to determine the effect of humidity on the formation of new phases and hopefully discover if there is a limit. Turbulent effects from gas flow were neglected since the linear flow rate is on the order of 0.1cm/s at the highest flow rate.

3.4.1 570°C Test

Only two sets of samples were loaded into the autoclave to be run at 570°C. Since 570°C is well above any temperature expected for the material to reach during deployment the high temperature serves as a useful mark to determine extents of damage to the samples. If no evidence of corrosion or new phase formation was shown at 570°C then it would be senseless to perform tests at lower temperatures.

The first samples were pulled from the autoclave after being at temperature for 21 days. Visually the samples showed no change signs of oxidation. Measurement of mass changes shows that the Boral® samples lost over 30% of their mass for both thicknesses. Mass of the Bortec® samples changed by less than 0.2% for both thicknesses, though both exhibited mass loss. Table 19 tabulates the mass changes to the samples. The Sample ID is express by the

material (L for Boral®, C for Bortec®) and by the thickness (in thousandths of an inch) followed by the exposure temperature (in degrees Celsius) and then by the exposure time (in days)

Table 19 Mass changes to samples exposed in autoclave for 21 days

Sample ID	Thickness (in)	Start Mass (g)	End Mass (g)	Change (%)
L75-570-21	0.0750	5.1381	3.5621	-30.678
L135-570-21	0.1360	9.2029	5.8520	-36.411
C75-570-21	0.0740	5.5563	5.5523	-0.0720
C101-570-21	0.1010	7.5992	7.5851	-0.1855

The last set of samples was pulled out of the autoclave after 50 days of exposure. After removal from the autoclave the samples mass and dimensions were measured. Table 20 shows the changes that occurred in the samples after 50 days. The dimensional changes to the sample were minimal with the greatest changes being in sample thickness. The greatest changes in length and width were noticed in the Bortec®. The change in height in the Boral® is due to expansion of the core. The crack runs the length of the sample as shown in Figure 50.

Table 20 Mass and dimension changes to samples exposed in autoclave for 50 days at 570°C

	Changes (%)			
Sample ID	Mass	Length	Width	Height
L75-570-50	-39.506	0.0783	-0.0355	1.000
L135-570-50	-41.539	0.1134	0.2675	9.259
C75-50-570	-0.0900	0.1847	0.3396	0.6472
C101-570-50	-0.1656	0.1749	0.1965	0.4975

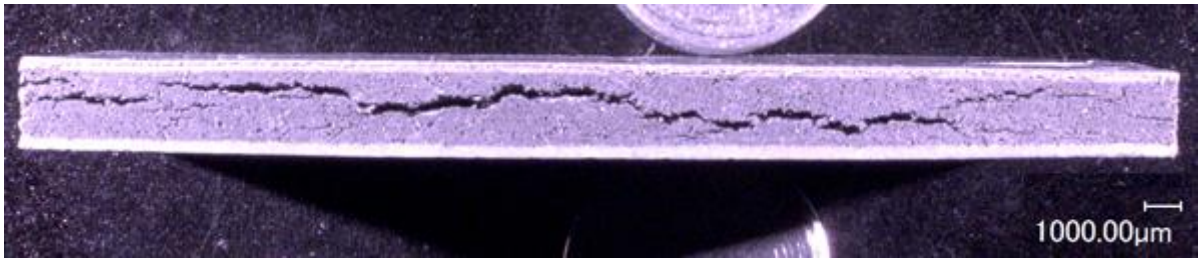

Figure 50 Cracking in Boral® sample L135-570-50 after exposure for 50 days at 570°C

The mass loss in the samples coupled with the dimensional increases results in an overall decrease in the density. This result is at odds with the typical oxidation behavior of aluminum. Oxidation of two moles of aluminum to one mole of Al_2O_3 results in the mass increasing from 54 grams to 102 grams and the total volume increasing from 20 cm^3 to 26 cm^3. Although oxidation of aluminum results in mass gain, degradation of oxide can result in mass loss. For a sample to exhibit mass sufficient oxide would have to be lost to offset the mass gain from the oxygen. The resulting oxide loss would result in a net volume loss to the sample, making the sample smaller. An oxidized aluminum sample that exhibits mass gain should typically exhibit mass gain. The mass loss exhibited by the samples must come from some other source.

Investigating the microstructure of the exposed samples has helped to provide insight into the corrosion behavior of these samples. After 21 days of exposure the samples were sectioned and polished in cross-section. Observation of the samples in an optical microscope revealed spots covering the entire area of the sample. The spots show up in colors ranging from yellow to grey and can be seen in Figure 51. The coloring of these new phases is reminiscent of the phases seen in Figure 48 though the phases formed in Figure 48 are in more of a ribbon shape than the coalescence seen in Figure 51.

New phase growth in aluminum boron carbide is not without precedent, but it has only been observed at temperatures above the melting point of aluminum (660°C) [78]. At these

elevated temperatures a number of different Al-B, Al-C, and Al-B-C phases have been observed including: Al_3BC, Al_4C_3, and $Al_3B_{48}C_2$.

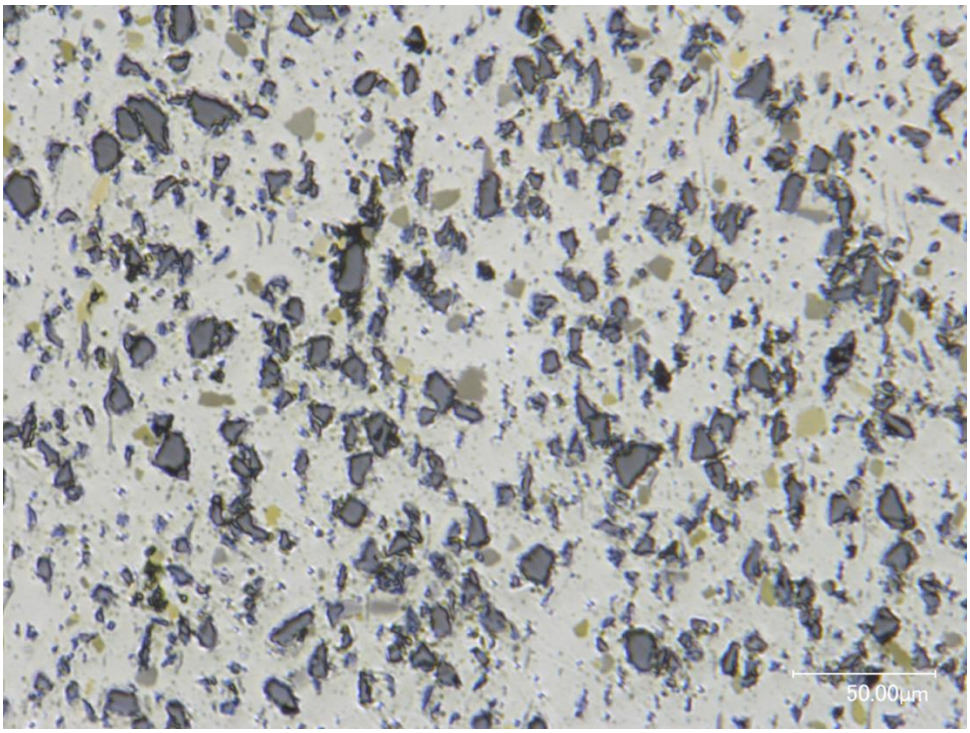

Figure 51 Cross section of Bortec® sample C75-570-21 after 21 days exposure at 570°C

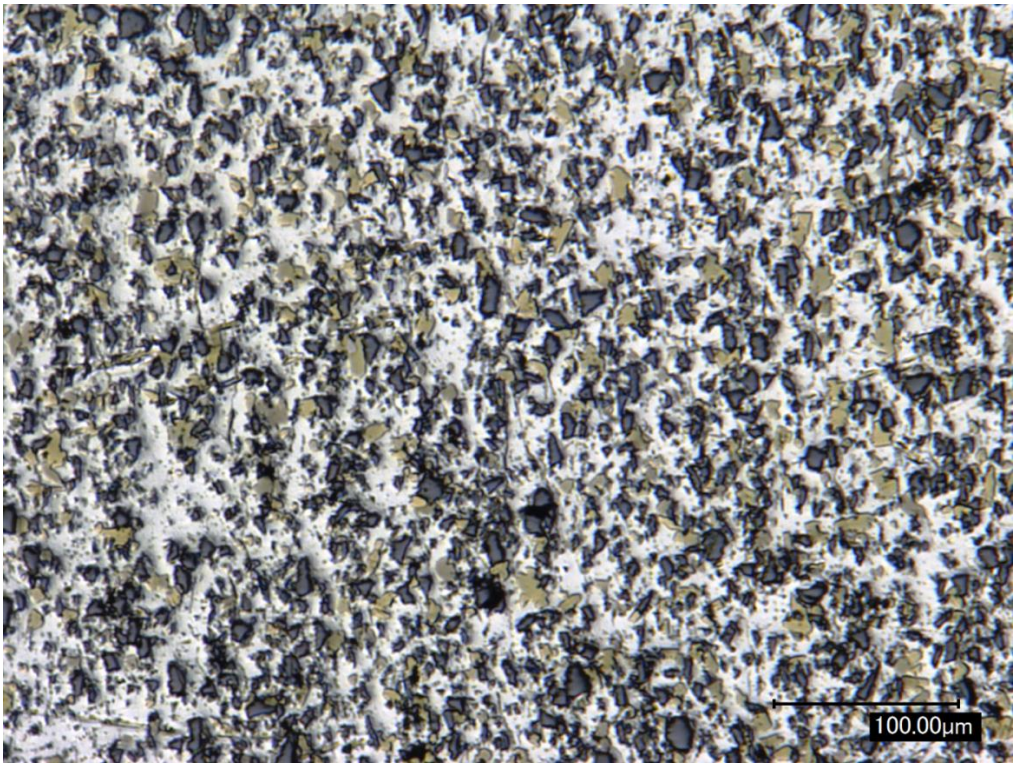

Figure 52 Sample C101-570-50 after 50 days exposure at 570°C

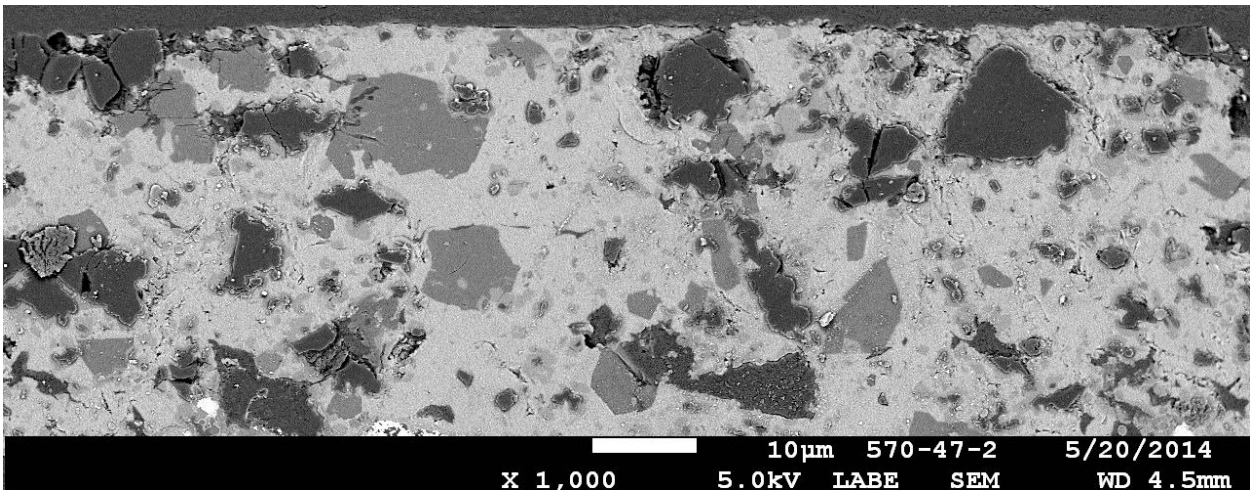

Figure 53 EDS of phases in Bortec® after 50 days at 570°C

A comparison of Figure 51 and Figure 52 shows the difference in phase growth between 21 and 50 days. After 50 days exposure sample C101-570-50 had two blisters formed on opposite surfaces. Blistering has been observed in Boral® but not in Bortec®. Figure 54 shows the blisters that formed on the Bortec®. A cross section was cut through the blister shown in Figure 54B that was subsequently polished and investigated on an SEM. Analysis of the blistered region showed oxidation and the formation of new crystalline growth.

The level of oxidation exceeds the oxygen penetration noticed in other samples. Aluminum is susceptible to pitting corrosion [97]. Blistering can occur as a result of the formation of a small pit that allows water ingress. Oxide growth then seals the pit with water inside. Water will oxidize the aluminum and boron carbide but the sealed pit will not allow the gasses produced to escape. Oxidation of aluminum and boron carbide both produce hydrogen as a byproduct, for boron carbide up to 8 moles of hydrogen can be produced for every mole of boron carbide oxidized. Hydrogen production from corrosion is significant enough that it has even been considered for use in fuel cells [98]. The oxidation seen in the blistered region provides a mechanism for the formation of the observed blisters.

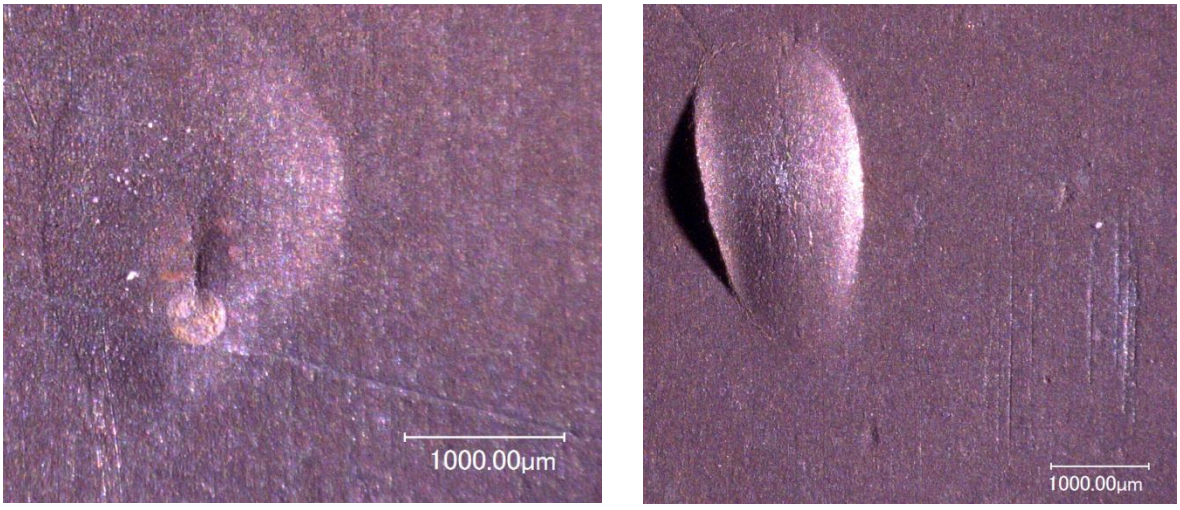

A. B.

Figure 54 Blisters formed in Bortec® sample C101-570-50 after 50 days exposure at 570°C.

The geode-like formations that appear in the blistered regions of the Bortec® are reminiscent of the formations that appeared in the initial corrosion testing of Boral® as seen in Figure 41. Comparison of Figure 55 with Figure 43 highlights the similarities. Both have high oxygen concentrations and have formed holes that served as locations for new crystalline growth. This size of the holes is also comparable to average boron carbide particle sizes for each respective material. Also of note in the EDS analysis are the boron-containing phases. Boron shows up in the boron carbide particle, as expected, but it also appears in a boron-carbon phase with nearly equal parts boron and carbon. There is also a boron rich phase that has very little carbon. Due to the potential distortion caused by the interaction volume little can be said about the boron/aluminum ratio.

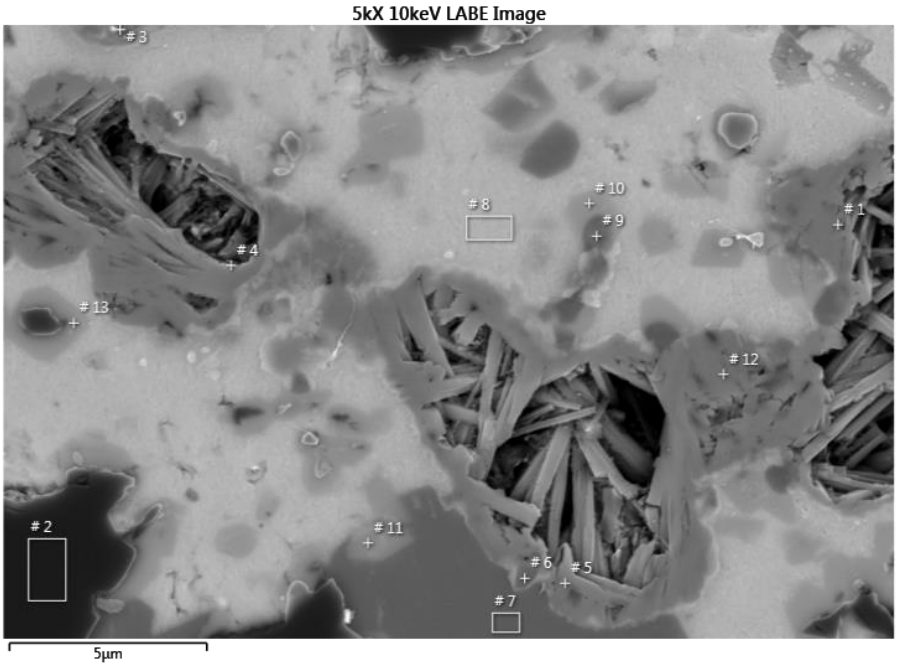

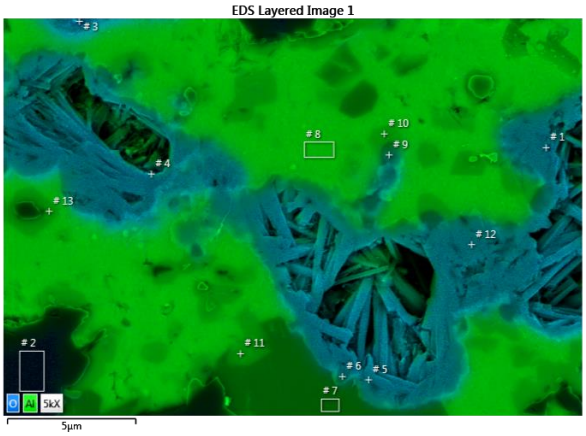

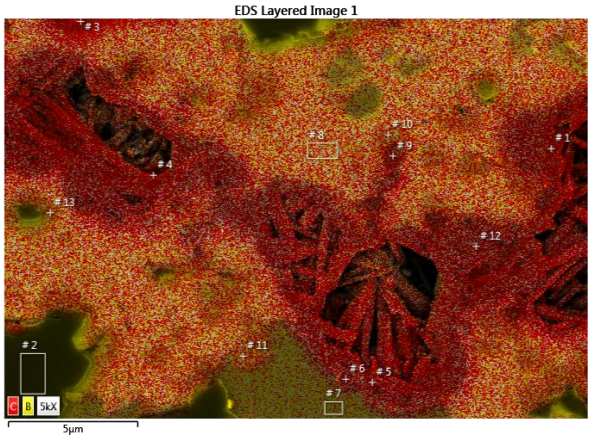

Result Type	Atomic %						
Spectrum Label	B	C	O	Al	Si	Fe	Total
# 1	0.00	12.79	56.48	22.57	8.16	0.00	100.00
# 2	69.19	30.41	0.25	0.15	0.00	0.00	100.00
# 3	0.00	51.40	32.57	7.32	0.16	8.56	100.00
# 4	0.00	27.27	35.57	28.10	9.06	0.00	100.00
# 5	0.00	8.57	62.08	29.18	0.17	0.00	100.00
# 6	0.00	4.36	58.62	36.91	0.12	0.00	100.00
# 7	54.41	3.96	0.77	40.86	0.00	0.00	100.00
# 8	0.00	2.36	1.63	95.90	0.11	0.00	100.00
# 9	0.00	10.87	25.15	63.78	0.19	0.00	100.00
# 10	0.00	3.93	1.81	94.02	0.24	0.00	100.00
# 11	0.00	4.90	2.72	92.37	0.00	0.00	100.00
# 12	0.00	4.35	61.61	33.89	0.15	0.00	100.00
# 13	13.50	15.15	1.47	69.79	0.09	0.00	100.00

Figure 55 SEM and EDS results of blistered region in sample C101-570-50

A TEM investigation of Sample C101-570-50 was undertaken in order to gain a closer look at the interface between boron carbide and the new phases that formed. Preparation of the TEM sample was made using the lift-out method on a FIB as part of an FEI NOVA SEM system. As part of the preparation a platinum layer was placed on the surface of the sample to protect it from ion damage during milling. After lift-out, the sample was mounted on a copper grid for transfer into the TEM.

Analysis of sample composition by EDS on a TEM provides a higher level of accuracy than on an SEM due to the thinness of the TEM sample. A TEM sample is, of necessity, electron transparent. Since the sample is so thin the interaction volume is decreased and does not experience the spread that is noticed in EDS on SEM samples. A glance back at Figure 25 shows that the majority of the interaction volume occurs at depths of greater than 1µm. Since TEM samples are thinner than 1µm all of the additional signals from that volume are not generated.

The images and data collected from the TEM work on Sample C101-570-50 are seen in Figure 56 and in Appendix B. Both Annular Dark Field (ADF) and Bright Field (BF) images were taken of the sample. ADF images collect the electrons scattered in an annular region around the probe location. This signal is Z sensitive, similar to a backscatter image on SEM. Since the ADF detector is annular it allows the primary beam to pass through and is therefore useful for its ability to work simultaneously with EDS and EELS analysis. Bright Field imaging is the standard operating mode in TEMs. Features are imaged in BF as electrons interact with a sample as they pass through. Contrast in a BF images comes from mass-thickness and diffraction.

Analysis of the locations indicated in Figure 56 by EDS indicates an absence of boron in any location but D, the boron carbide particle. This confirms the results obtained from EDS on the SEM that the secondary phases are aluminum carbides. The fate of the boron is unable to be determined from the TEM analysis.

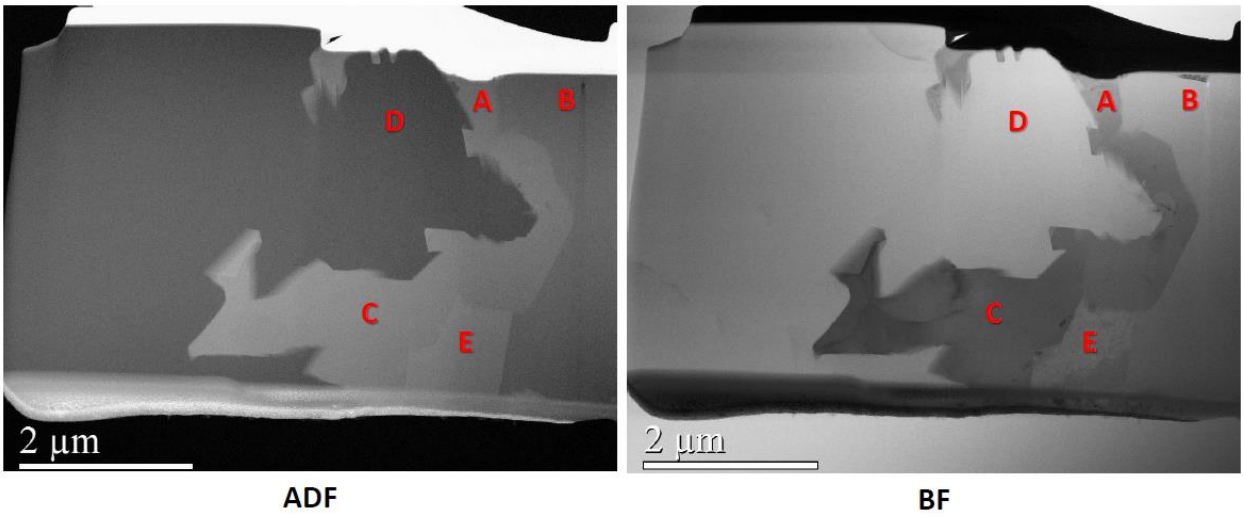

Figure 56 Overview of cross-sectional area on Sample C101-570-50 investigated by TEM

The secondary phases that formed in Bortec® are distributed throughout the sample. It is unclear if the phases formed during exposure or if they precipitated out during cooling. A segment of sample C101-570-50 was placed in a TGA under an argon atmosphere and heated to 570°C for 25 days. The system was ramped from room temperature to 570°C over 300 minutes. The system was cooled more rapidly at was returned to room temperature over a period of 100 minutes.

After heating in the TGA the sample was removed and polished for investigation on the SEM. A comparison of the sample before and after heating shows little difference in density or shape of the largest phases there appears to be a reduction in the density of the small phases. Figure 57 shows a comparison of the sample before and after heating in the TGA. Analysis of the

reheated sample was performed by EDS. Line scans were taken across the phases to gain an idea of the behavior of the elements.

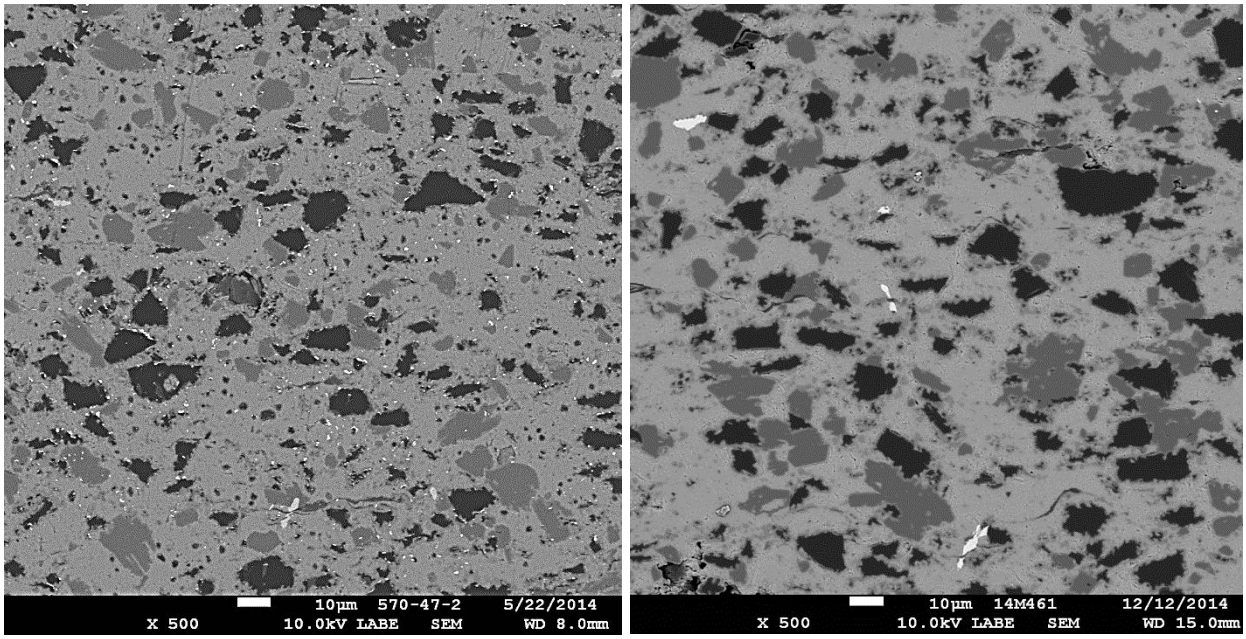

A B

Figure 57 SEM Backscatter images showing Bortec® sample after autoclave corrosion test at 570°C for 50 days (A) and the same sample after subsequent heating in Ar at 570°C for 25 days (B). The high density of metallic phases in Figure A is due to clumping of the gold coating that was put on the sample

The EDS line scan data shown in Figure 58 provides an interesting picture of what is occurring at the interface between a boron carbide particle and one of the new phases that has formed. One point of interest is the boron enrichment at the edges of the boron carbide particles. This enrichment can be seen at 1.5 and 6.5µm in Line Data 1 and at 9.5µm in Line Data 2. The region directly surrounding the boron carbide particles in both line scans is depleted in boron. Line Data 1 shows an area approximately 1µm wide that is depleted in boron and that exists between two different boron phases. The same depletion gap between phases is also seen in Line Data 2.

Conversely to the boron enrichment at the edge of the boron carbide particles Line Data 1 and Line Data 2 in Figure 58 show that the boron carbide particles are depleted in carbon at the

edges. The width of the boron enrichment region closely matches the width of the carbon depleted region. In addition, the secondary boron phases contain the lowest concentrations of carbon while the gap region in between appears to be carbon enriched in Line Data 1. The resolution of the line scan does not allow for good analysis of the narrow gap in Line Data 2 but the scan does show a slight increase in carbon concentration that corresponds to the boron decrease at the edge of the boron carbide particle. Line Data 1 and 2 both show very little oxygen content and that the oxygen appears to be correlated with the aluminum concentration.

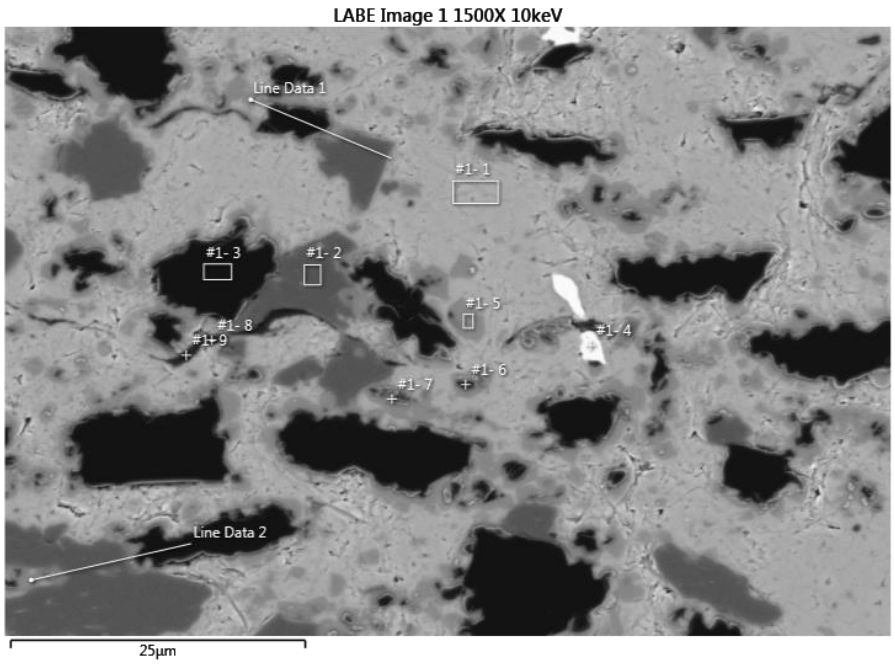

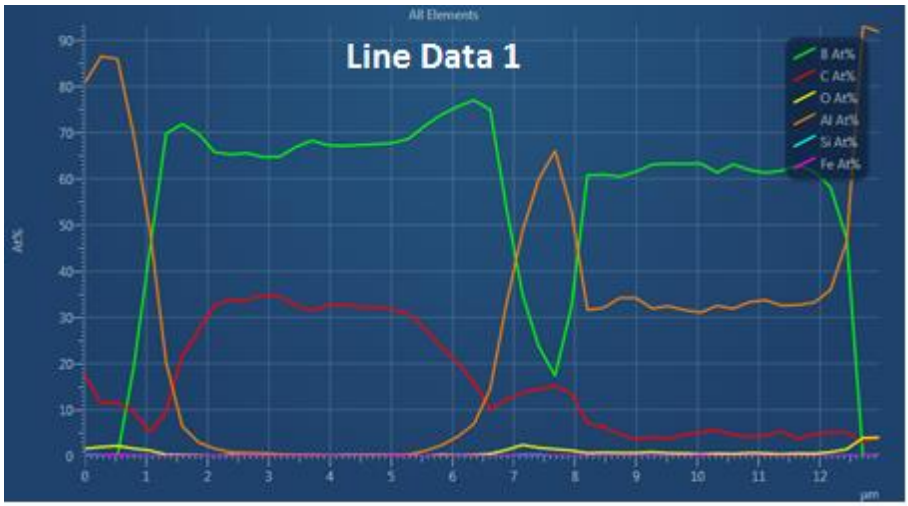

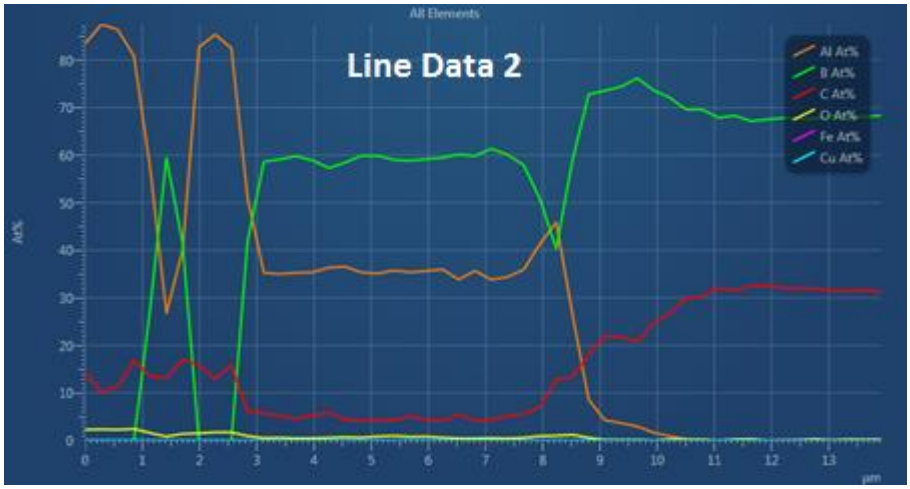

Figure 58 EDS line scan data for sample C101-570-50 after heating at 570°C in humidified Ar for 50 days followed by heating in dry Ar for 25 days

Two additional EDS line scans were taken of sample C101-570-50 after treatment in the TGA. Line Data 3 and Line Data 4 in Figure 59 both come from areas near the edge of the sample. Line Data 3 comes from the oxide layer that formed on the surface of the sample. One result from Line Data 3 that stands out is the inverse correlation between oxygen and aluminum concentrations. This may at first seem counterintuitive, but the stoichiometric ratio of aluminum to oxygen in aluminum oxide is 2:3. This ratio would result in a pure, perfect oxide being 40% aluminum and 60% oxygen, on an atomic basis. The results fall within this expectation.

Line Data 3 also shows a surprisingly high carbon concentration, with concentrations above 10 at% from 2.25µm until the edge at 8.1µ, peaking with a carbon concentration approaching 30 at%. Even though the carbon concentration is elevated the boron concentration is zero except for two locations where the concentration spikes to 7 at%. Iron is also present throughout the sample from 2.25µm to the edge at 8.1µm.

LEI Image 2 2kX 10keV

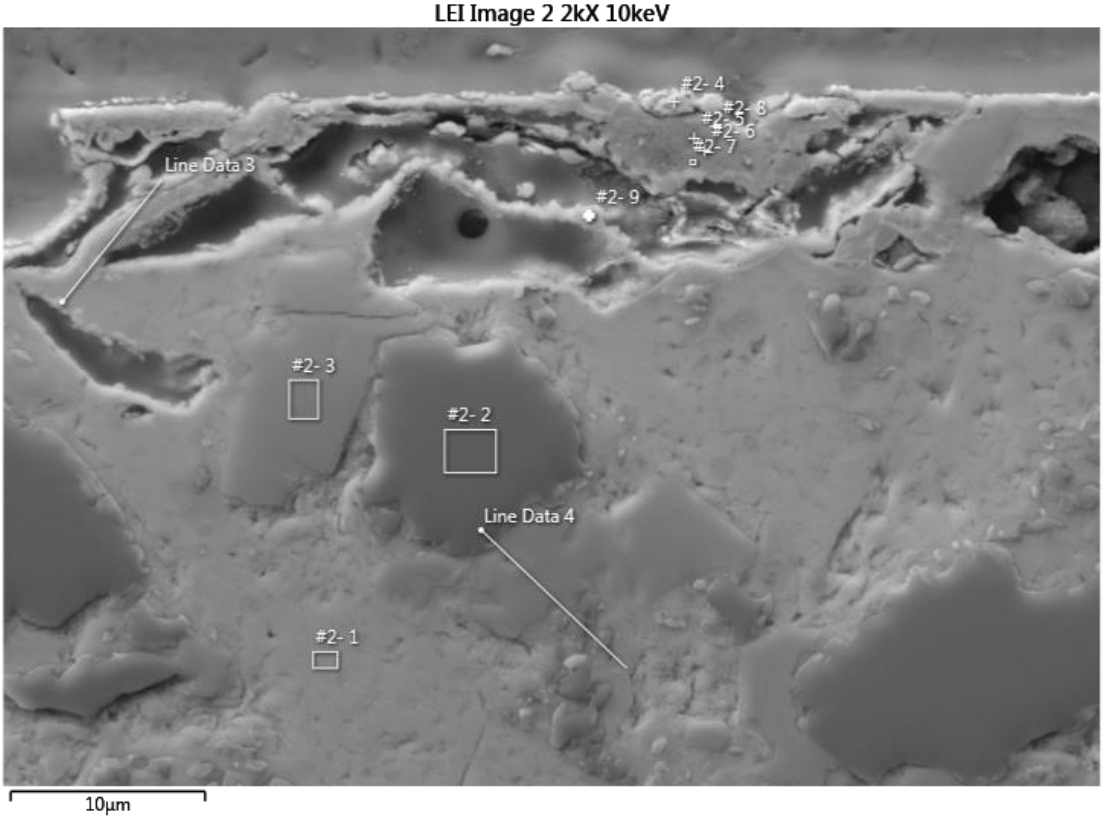

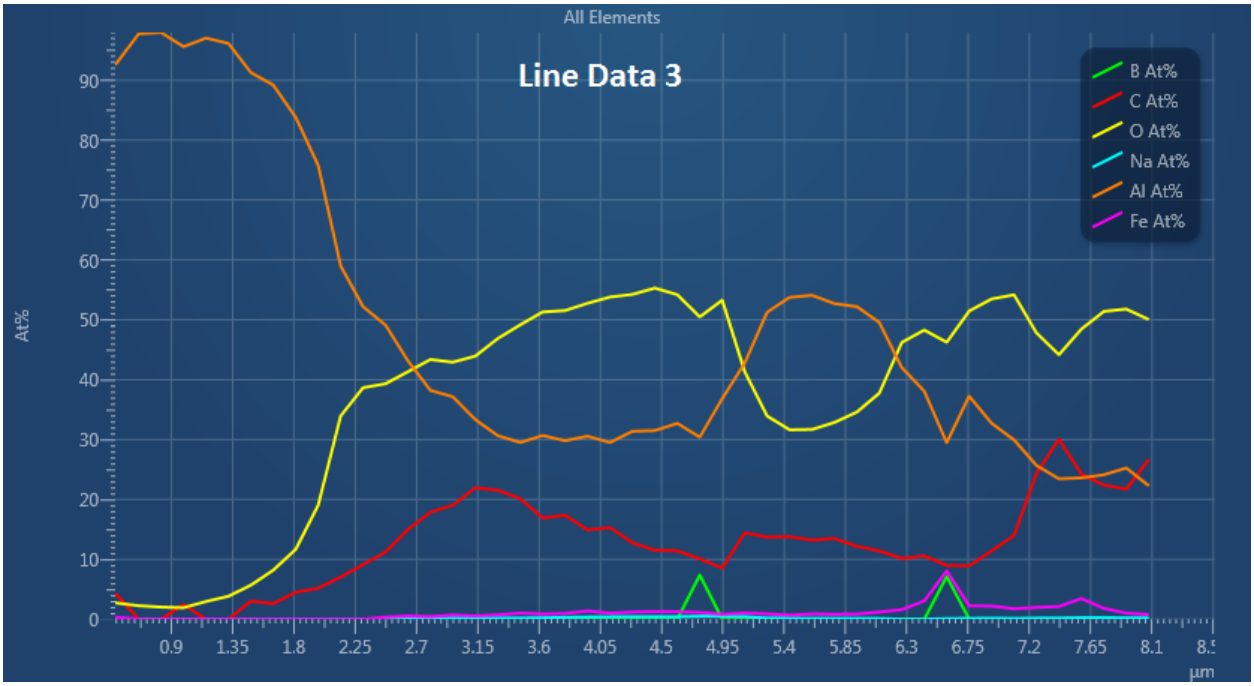

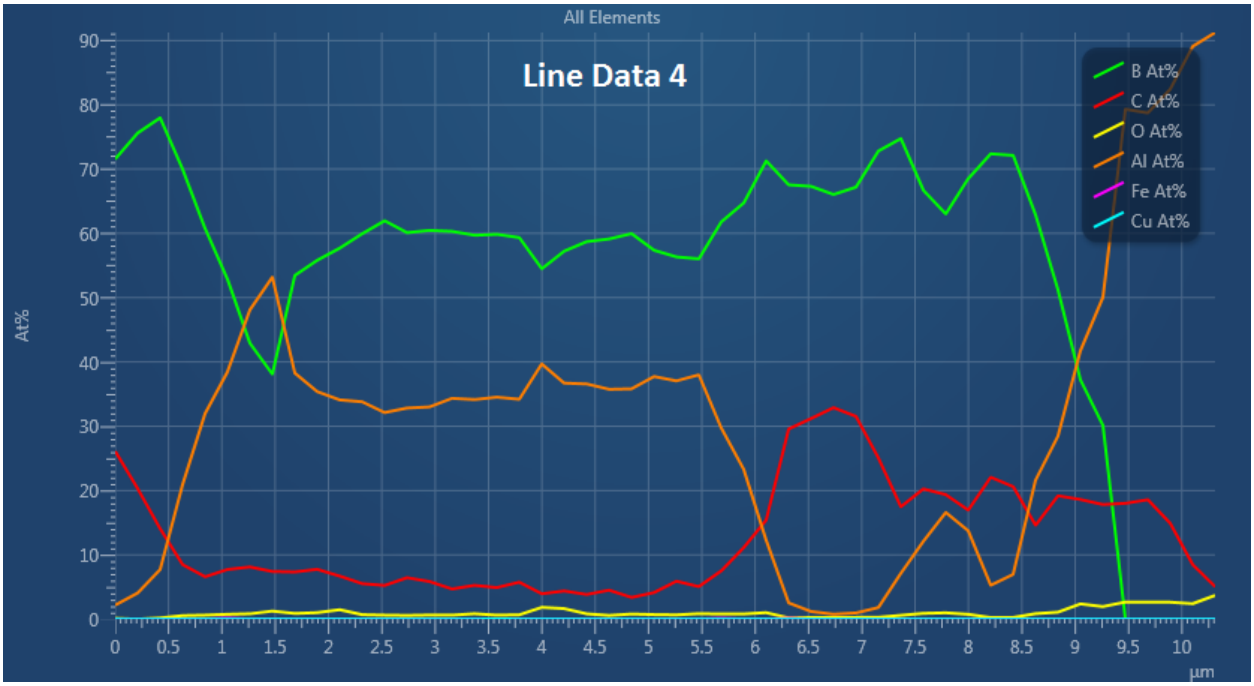

Figure 59 EDS line scan results from near an exposed edge in Sample C101-570-50 after heating in a dry argon environment

The results from Figure 59 Line Scan 4 show that very little oxygen has penetrated that far into the sample. Line Scan 4 does show that boron and aluminum concentrations are inversely related. Line Scan 4 continues to follow the trend of enriched boron concentration at the edge of a boron carbide particle with a depleted region next to the particle. The carbon concentration along the edge of the boron carbide particle is also reduced. The full results from the line scan are found in Appendix C.

Investigation of the Boral® samples showed almost total loss of boron carbide particles. The cross-sectional sample that was investigated came from a location approximately 1cm from the exposed end of the sample. EDS investigation did not show any evidence for remaining boron carbide particles in L135-570-50. It is unknown if the boron carbide particles were completely lost during exposure or if they fell out during cutting and polishing. Backfilling of the sample with epoxy could also mask the presence of any remaining boron carbide.

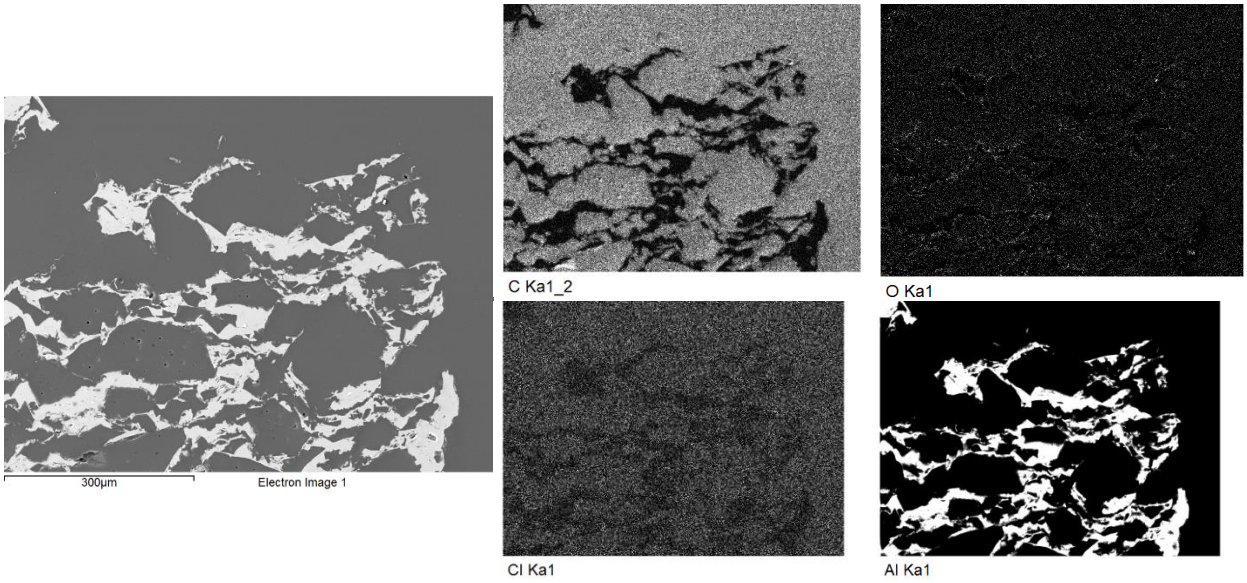

Figure 60 EDS map of sample L135-570-50 showing boron carbide loss

An EDS map of sample L135-570-50, shown in Figure 60**Error! Reference source not found.**, shows the loss of boron carbide. The heavy carbon presence is explained by the epoxy backfill. This is confirmed by the chlorine map as the epoxy does contain chlorine. It is particularly interesting to note that there is not a strong oxygen signal. There is some oxygen presence from the epoxy and some shows up on the edge of the aluminum, but it is not consistent nor as strong as the oxygen signal observed in the initial corrosion experiments. Aluminum observance is also observed. The voids remaining in the aluminum matrix are larger than boron carbide particles and are interconnected, a feature not observed in boron carbide particles.

3.4.2 400°C Testing

Three sets of samples were tested for periods of 31.5, 59.5, and 143.5 days. Mass loss in all samples followed much of the same trends that were observed in the 570°C tests. The thin and thick Boral® samples showed progressively increasing mass loss with time with total mass

loss over 21% after 143.5 days for both thin and thick samples. The Bortec® samples showed no consistent trend in mass change other than no samples showed any mass gain.

Dimensional changes showed no trend for length, width, or thickness for any of the Boral® or Bortec® samples. The one constant across all samples is that the total change in any direction is less than 1%. As with samples exposed at 570°C the largest changes were in the thickness. Changes in length and width were all less than 0.5%.

Table 21 Mass and dimension changes for samples exposed at 400°C

Sample ID	Change (%)			
	Length	Width	Thickness	Mass
L75-400-31	0.009	-0.036	0.000	-4.688
L75-400-89	-0.140	0.267	-0.333	-11.593
L75-400-143	-0.140	-0.142	-0.664	-21.637
L135-400-31	-0.043	0.373	-0.365	-3.1848
L135-400-89	-0.079	0.284	-0.912	-16.846
L135-400-143	-0.202	0.036	-0.184	-21.066
C75-400-31	0.062	-0.415	0.340	-0.0913
C75-400-89	-0.009	0.374	0.341	-0.0816
C75-400-143	-0.062	-0.108	-0.339	-0.1018
C101-400-31	-0.018	0.036	0.000	-0.1981
C101-400-89	-0.070	0.143	-0.750	-0.2391
C101-400-143	-0.139	0.108	0.491	-0.2140

The results shown in Table 21 are not surprising considering the limited corrosion observed in samples exposed at 570°C. Samples exposed at 400°C for 31.5 days showed little difference compared to the as-received samples. After 89.5 days the samples began to exhibit the formation of some new phases. After 143.5 days both the Boral® and Bortec® samples had shown new phase formation. New phase formation is typified by the presence of regions surrounding boron carbide that shows up darker than the main aluminum matrix in a backscatter image.

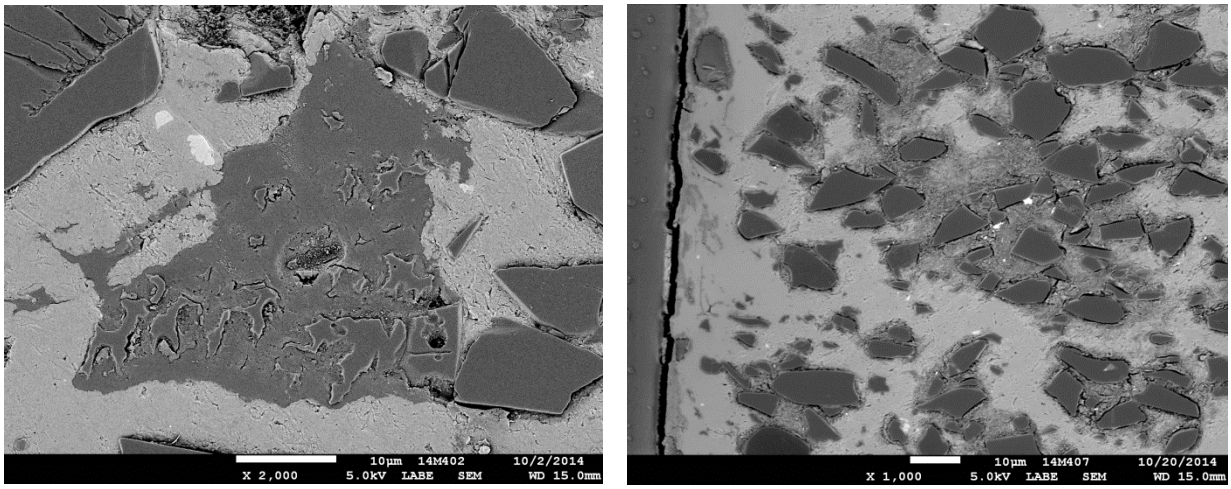

A B

Figure 61 Boral® (A) and Bortec® (B) after 143.5 days at 400°C

One unique result appeared in Boral® after 143.5 days. Figure 62 shows a backscatter image of an exposed edge in the Boral® sample. EDS analysis indicates that the edges of the sample are surrounded by a border that is predominately carbon and oxygen with lesser amounts of aluminum. Traces of iron and molybdenum are also present. The full results can be seen in Appendix B.2. These same structures were also observed along an exposed edge of Bortec® after exposure for 143.5 days and can be seen in Figure 63.

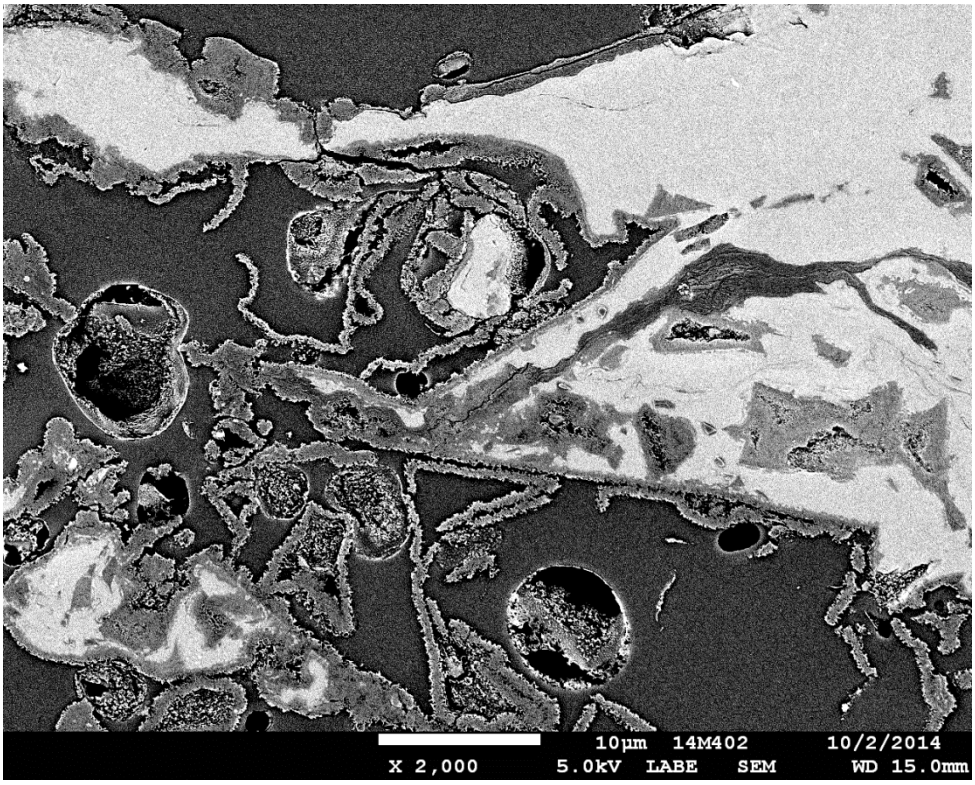

Figure 62 Rope-like phases in Boral® edge after 143.5 days at 400°C

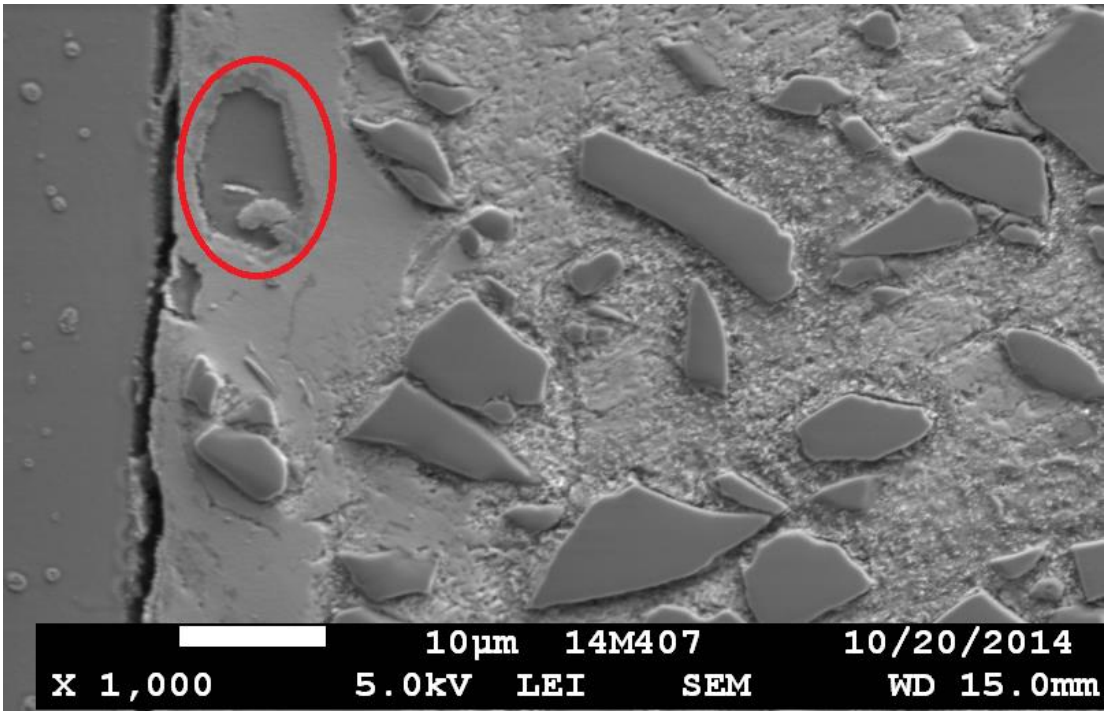

Figure 63 Edge corrosion, similar to metallic phases in Boral®, found in Bortec® after 143.5 days at 400°C

In addition to these unique metallic phases present, EDS has also confirmed that additional phases have formed. While EDS cannot definitively identify the stoichiometry of these small boron and/or carbon containing phases, looking at the ratio of boron to carbon can give an idea if we are seeing the natural boron carbide or if there is a new phase. Analysis of the EDS results from the Bortec® samples after 143.5 days reveals that most boron and carbon containing phases have approximately a 2:1 boron/carbon ratio on a per atom basis. The range of ratios extends from 1.86:1 to 8.08:1. Common to the sample are a number of phases that contain carbon, but no boron. Carbon concentrations in these phases range from around 3% to 26% carbon on a per atom basis. Also observed, though not as common, were phases that contained boron, but no carbon. Boron concentrations ranged from 20-60%.

In addition to the standard samples, some alternate samples were run at 400°C. The first set of alternate samples was comprised of samples that had been ion irradiated prior to exposure. All of the irradiated samples were Bortec® and consisted of a set of thin and thick specimens that were both irradiated under the same conditions. The first set of samples were irradiated by a 300 keV He^+ beam to a fluence of $2x10^{17}$per cm^2. The second set of samples were irradiated by a 50 keV He^+ beam to a fluence of $3.5x10^{16}$ per cm^2 and then by a 400 keV He^+ beam to a fluence of $1.5x10^{17}$ per cm^2.

The irradiated samples were placed in the 400°C autoclave for 112 days. After exposure the samples were removed and measured. The irradiated samples showed the same behavior as the non-irradiated samples with mass and dimension changes being on the same order of magnitude. As with the other samples, there is little correlation or consistency associated with the dimensional changes.

Sample ID	Material	Irradiation	% Change			
			Mass	Length	Width	Thickness
He-1	Thin	1	-0.1084	0.02659	-0.03764	0.6734
He-2	Thick	1	-0.2725	-0.1883	0.4674	0.9804
He-3	Thin	2	-0.1070	-0.03498	-0.07563	0.6711
He-4	Thick	2	-0.2694	-0.2445	0.1599	-0.2463

Table 22 Results of corrosion of ion irradiated samples. Irradiations: 1 – 300 keV He^+, $2x10^{17}cm^{-2}$. 2 – 50 keV He^+, $3.5x10^{16}cm^{-2}$; 400 keV He^+ $1.5x10^{17}cm^{-2}$

Mass changes are negative and of the same order of magnitude as observed for the Bortec® samples exposed at 400 and 570°C. Even though the change is on the same order of magnitude the actual change for each thickness is lower than at any other exposure. This result is unexpected given the small fraction of total area that has been irradiated. A cross-sectional view of the irradiated surface can be seen in Figure 64. The damage caused by the irradiation has led to an increased surface area on the sample. The greater surface area could account for the greater effect of exposure. Another possibility is void coarsening which would allow deeper water penetration and increase diffusivity in the matrix [39].

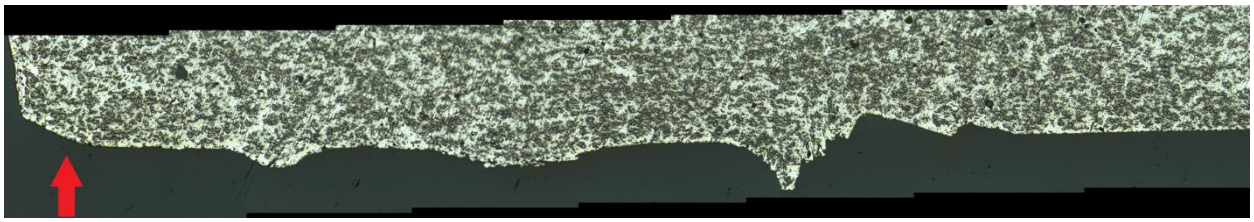

Figure 64 Cross sectional view of He-1 heavy ion irradiated sample. Arrow indicates direction of incident ions. Optical image was taken at 400x

Evidence for increased oxygen diffusion comes from an EDS map of the ion irradiated sample. In Figure 65 we can see that oxygen has penetrated over 10μm into the sample. We can also observe the buildup of iron along the exposed surface and the lack of boron in the range that has the heavy oxygen penetration.

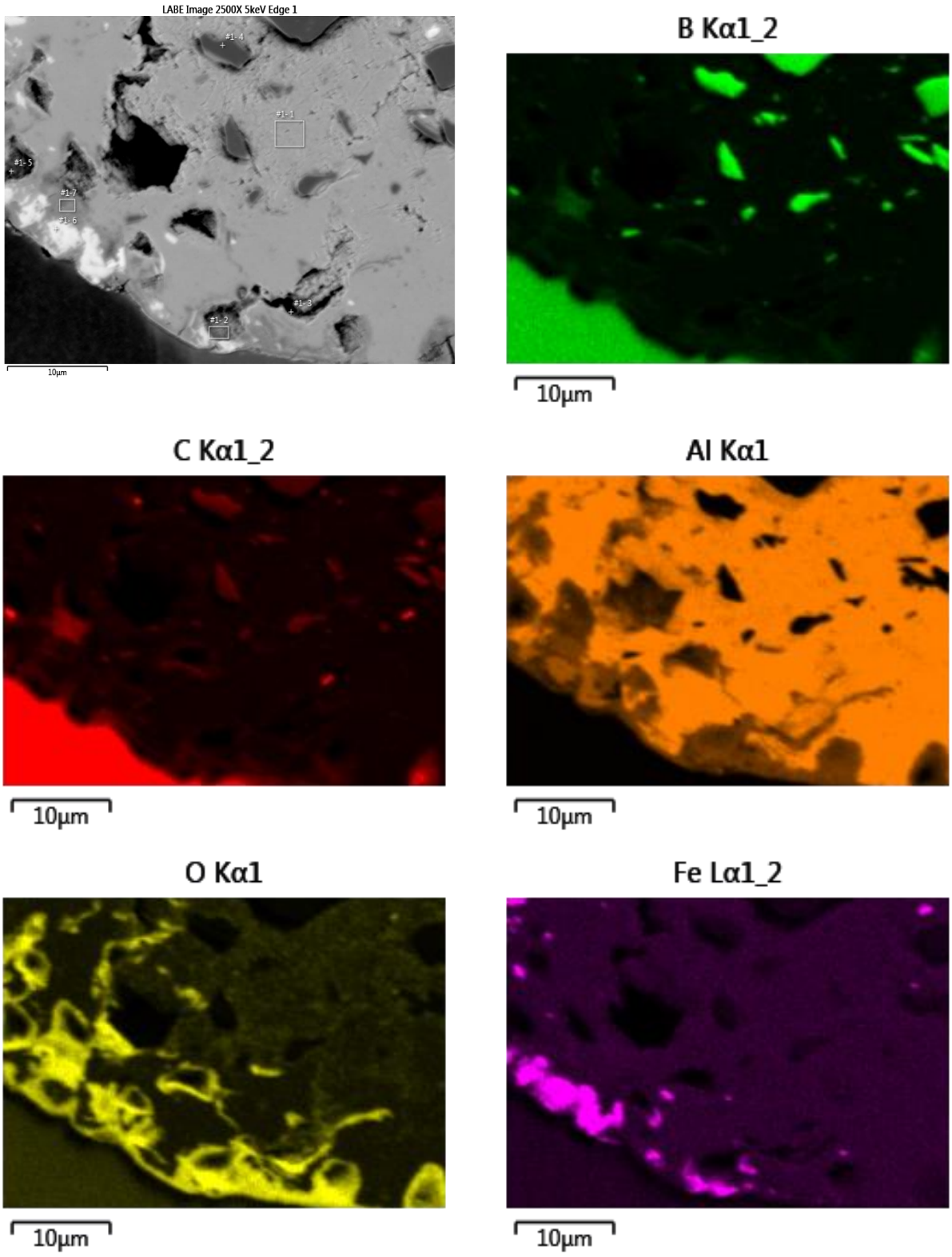

Figure 65 EDS map of He irradiated sample showing oxgen penetration

Oxygen penetration in Figure 65 can be compared to oxygen penetration in sample C101-400-31 as shown in Figure 66. The oxidation is generally limited to a layer less than 1μm thick along the exposed surface of the sample. The only exception is where defect surfaces allow further penetration. Penetrated oxide appears to surround boron carbide particles. This is likely due to pores that are often noticed around the particles, likely artifacts of manufacturing.

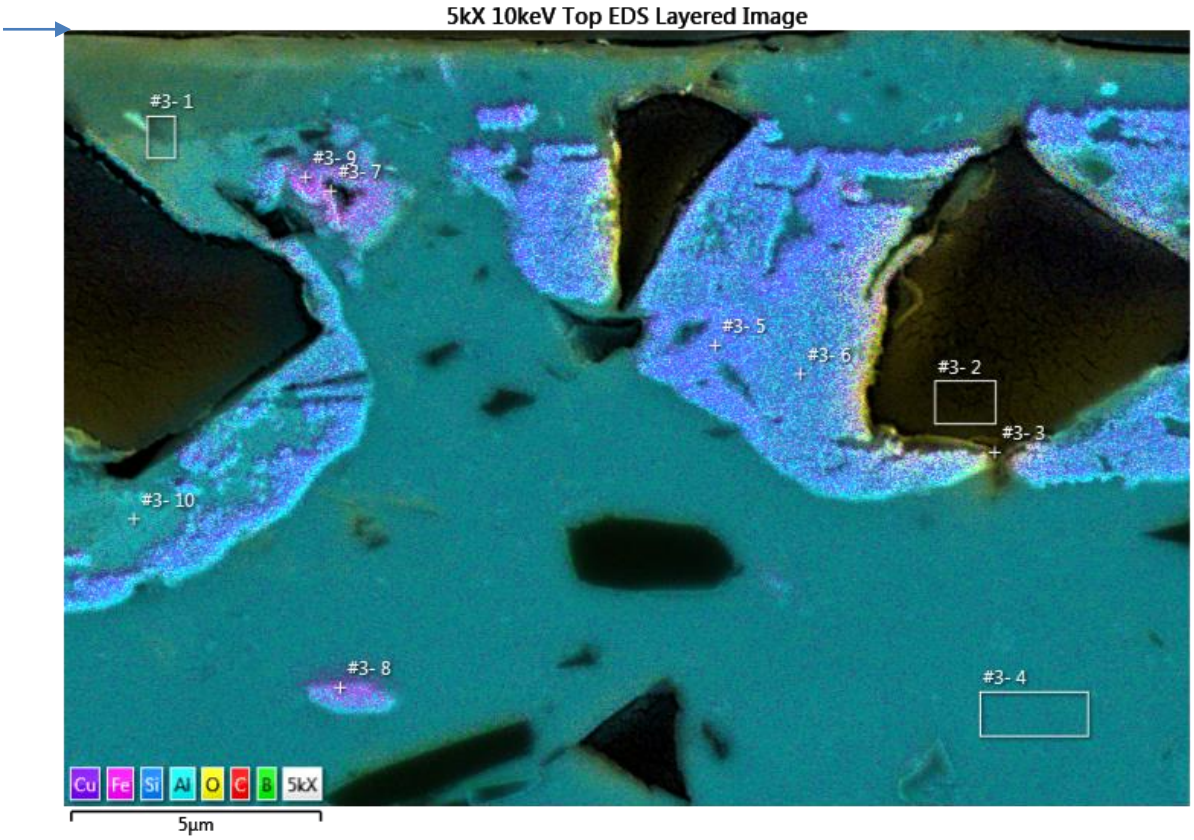

Figure 66 EDS map showing oxygen penetration in sample C101-400-31. Arrow points to exposed surface

The final tests performed at 400°C were at lower humidity. Two sets of samples were tested. To lower the humidity level of the inlet water the temperature of the bubbler was set to 50°C instead of the 90°C used in the other tests. Additionally, one sample set was loaded into an autoclave and the gas flow rate was set between 0.2-0.3 scfh. This translated into a water usage rate of approximately 0.3 mL/hr and a mass humidity ratio of 0.028. The second set of samples

was loaded into the other autoclave and the gas flow rate was set between 0.5-0.6 scfh. This corresponds to an approximate water usage rate of 1.6 mL/hr and a mass humidity ratio of 0.082. In comparison, the other tests were performed with an approximate mass humidity ratio of 0.576. In an attempt to get a better understanding of the moisture penetration the samples used were approximately 2" x 3". After 41 days of exposure the samples were removed and cross sectional samples were cut and mounted with the face of the cross section being cut normal to the exposed surface.

Table 23 Results for Low Humidity testing

Sample ID	Material	Humidity ratio	% Change			
			Mass	Length	Width	Thickness
LH-1	Thin Bortec	0.028	0.01188	-0.02865	0.02414	-0.6734
LH-2	Thin Boral	0.028	1.941	0.1308	-0.1085	0.3289
LH-3	Thin Bortec	0.082	-0.04084	0.02278	0.07229	-0.3378
LH-4	Thick Bortec	0.082	-0.05986	-0.03648	0.007262	-0.4975
LH-5	Thin Boral	0.082	-1.810	0.05470	0.02421	-1.003
LH-6	Thick Boral	0.082	-1.633	0.005462	0.03230	-0.1832
LH-7	Thick Boral	0.028	1.628	0.1964	-0.1435	0.5455
LH-8	Thick Bortec	0.028	0.02612	0.02659	-0.1243	-0.2469

The results for the low humidity test depart from the results of all previous tests. For both Boral® and Bortec® the dimensional changes are all consistent around +/- 1%. The mass change is a little more interesting. All samples in all tests at 400°C and 570°C showed mass loss. However, both the Boral® and Bortec® samples showed mass increase at the low gas flow rate. The samples at the higher gas flow rate showed a decrease in mass.

The increase in mass in the low flow samples follows along with the typical corrosion behavior of aluminum. The initial oxidation forms a protective oxide barrier that results in a mass increase. With time and exposure that oxide layer can decompose, resulting in a net mass

loss. Continued testing at low humidity would be recommended to determine if mass loss will eventually occur.

Plotting the change in mass in both Boral® and Bortec® after 41 days of exposure as a function of water use reveals a logarithmic relationship. Water use is the amount of water that flows into the autoclave and is measured in mL/day. The mass change for high humidity levels was calculated using a linear interpolation of the data collected at 400°C and high humidity.

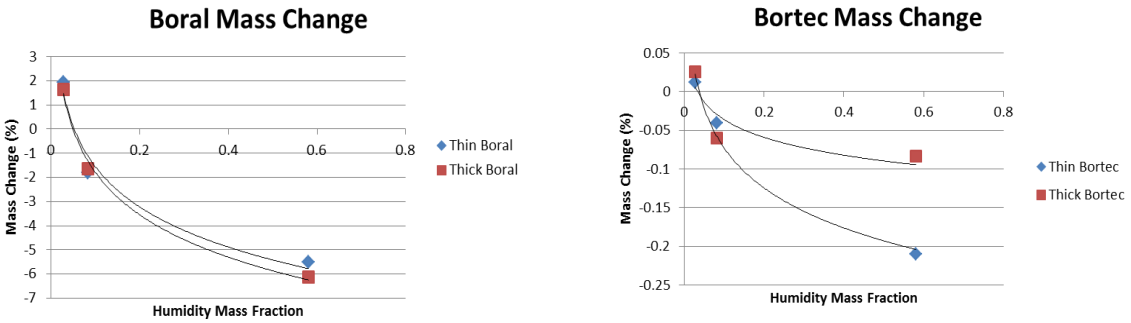

A B

Figure 67 Mass change in Boral® (A) and Bortec® (B) as a function of water use after 41 days at 400°C

3.4.3 300°C Tests

Tests at 300°C were carried out on three sets of samples over extended time. The sets were removed from the autoclave 21, 163, and 217 days. As with all other samples, dimensional changes don't follow any trend and are typically less than 1%. The exception is variation in Boral® thickness. The porous core in Boral® lends itself to greater variability in that dimension, but total change still less than 3%.

Table 24 Dimension and mass changes for samples exposed at 300°C

Sample ID	% Change			
	Mass	Length	Width	Thickness
L75-300-21	-2.328	-	-	-
L75-300-163	-4.1174	-0.0699	0.0533	0.6757
L75-300-217	-5.4811	0.1665	0.2130	0.6623
L135-300-217	-2.7694	0.1919	0.3719	-2.3050
L135-300-21	-1.4879	-	-	-

L135-300-136	-1.8891	-0.0087	0.1066	0.1821
C75-300-163	-0.0143	0.0703	0.0178	0.3401
C75-300-21	$-1.790*10^{-3}$	-	-	-
C75-300-163	-0.0178	0.0439	-0.0534	0.6826
C101-300-21	-0.01048	-	-	-
C101-300-217	-0.0197	-0.1049	0.0177	-0.4950
C101-300-217B	-0.0290	-0.0967	0.0536	0.2475

Mass changes at 300°C are negative for all sets of Boral® and Bortec® samples. Although the mass change is negative the magnitude of loss is smaller than those at 400 and 500°C with the high humidity gas flow. The magnitude of change in mass for the 300°C samples falls much closer in line with the samples exposed at 400°C with the lower humidity gas flow. Figure 77A shows the mass loss in Boral® as a function of exposure time. The mass loss at 570°C changes with the steepest slope and is of the greatest magnitude. The mass loss at 400°C has a shallower slope than 570° and at 300°C the slope is considerably less than at 400°C. The medium humidity tests fall in line with the testing at 300°C, while the low humidity tests show mass gain.

Figure 77B shows the mass changes in Bortec® as a function of exposure time. The tests at 570°C as well as the tests at 400°C and the He^+ irradiated samples show a distinct difference between the thin and thick samples, with the thick samples showing the largest mass loss. This separation is not able to be evaluated at 300°C due to two thin samples being removed after 163 days and two thick samples being removed after 217 days. The separation is surprising considering that the thickness difference between the samples averages only 32% while the difference in mass change falls between 80% and 200% for the 570°C and 400°C tests. The mass change from the medium humidity tests is greater than at 300°C but there is not the noticeable separation between the results for the thin and thick sample. Results for the low humidity test are the only results that show mass gain.

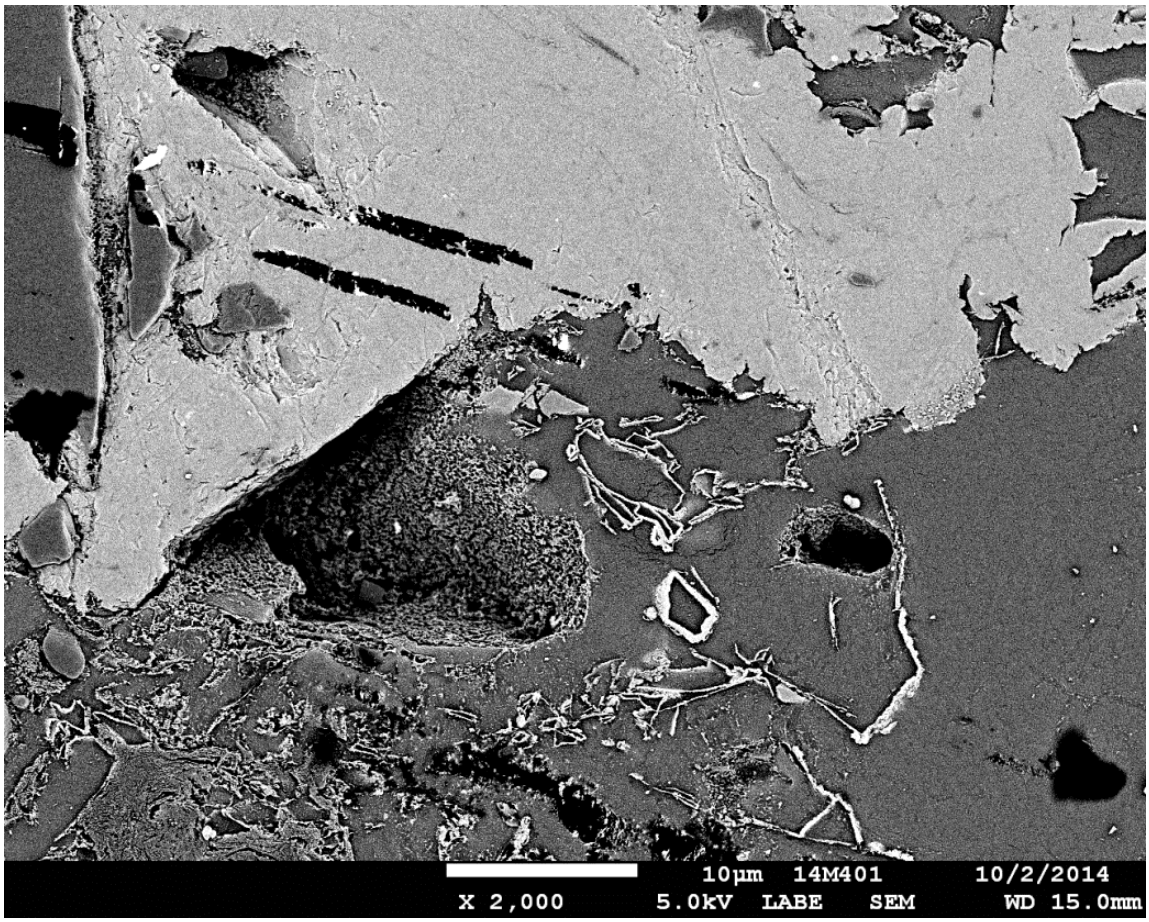

Figure 68 Boral® sample L75-300-217 after 217 days at 300°C

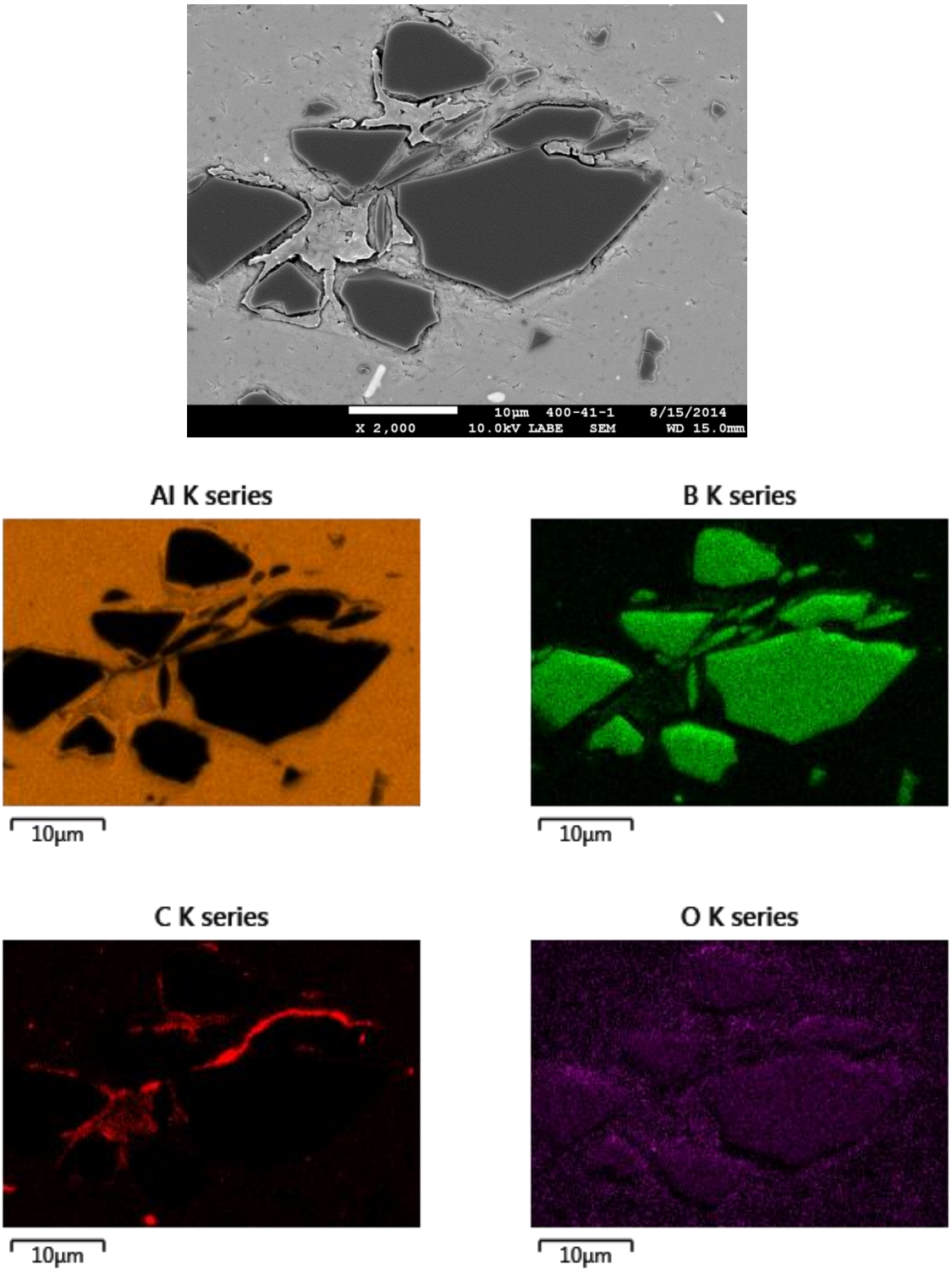

Figure 69 EDS map of Bortec® sample C75-300-163 after 163 days exposure at 300°C

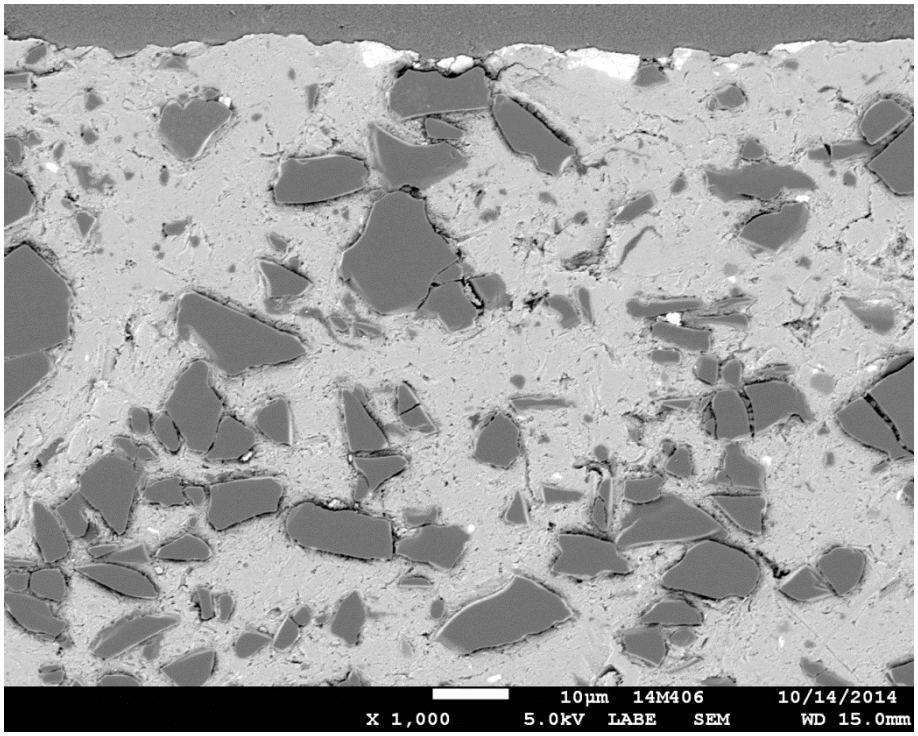

Figure 70 Bortec® sample C101-300-217 after 217 days at 300°C

Figure 68-Figure 70 show some of the more prominent features observed after exposure at 300°C. Although the mass loss in the samples is less than in the samples exposed at higher temperatures the SEM images do show that the material has been altered from the as-received form. Figure 68 shows structures similar to those found after exposure at 400°C and seen in Figure 62. The features observed in Figure 69 are rather unique but show the beginnings of change that seem to be focused around a group of boron carbide particles. In Figure 70 evidence of the carbon-rich ribbons is clearly seen in areas around the boron carbide particles. Although the magnitude of mass loss is not as great as at higher temperatures, the features evident in the sample are consistent with higher temperatures and indicate that the same decomposition mechanisms are applicable.

3.4.4 Neutron Depth Profiling

The initial corrosion testing, performed in a sealed autoclave, showed some aluminum oxidation and also revealed oxygen penetration into the Boral® samples. Subsequent corrosion testing showed little evidence of aluminum corrosion in the presence of humidified steam but the results indicated that the boron in the sample was mobile. The realization that the boron was becoming mobilized led to the realization that boron leaching was possible. Neutron Depth Profiling (NDP) was employed to measure a boron concentration profile across a cross section of select samples.

The Boral® and Bortec® standards that were used for NDP measurements came from the same batch of material as did the coupons for the corrosion testing. The samples that were used for NDP were cut from the material using a circular cutter on a mill and the cutting was cooled using alcohol. Since the samples were cut by the manufacturer using a water jet cutter care was taken to ensure to mark the factory cut edge. Four standards measurements were taken: Boral® Thin, Boral® Thick, Bortec® Thin, and Bortec® Thick. The Boral® Thin standard was the first measurement taken and was done with a 1mm aperture. All other standards measurements were performed with a 2mm aperture.

The diffusion of boron was assumed to occur through exposed edges. Since the Boral® has a cladding of aluminum alloy on the surface it was expected that all diffusion would occur through the peripheral edges. However, with no surface cladding on the Bortec® it was postulated that diffusion could occur through the surfaces as well as the peripheral edges. As such, the first sample that was investigated was one of the thick Bortec® samples. Instead of measuring the boron concentration across a series of points along the cross-sectioned edge of the sample two points were taken as shown in Figure 71.

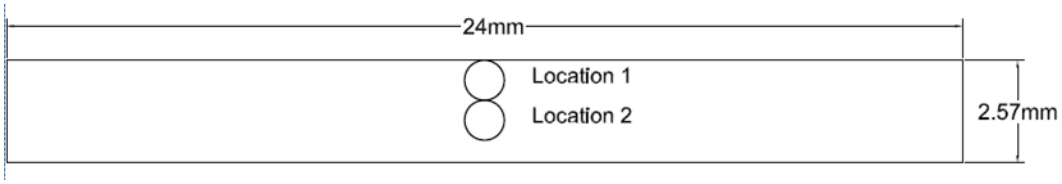

Figure 71 Bortec® edge diffusion profile

The results from the edge diffusion test showed that there was a 4.1% difference between the center point and the edge point. Each point had a total count of 13900 and 13863 counts respectively resulting in an error of 0.83%. Thus the difference, while small, is more than four times the error. Since there was a measured difference between the two points it was decided to use a 2 mm aperture. The use of a larger aperture would allow for an average over a larger area and would negate some of the edge effects. The use of a circular aperture also helps to reduce the edge effect. If the aperture is off the edge of the sample by 10% of the diameter (0.2 mm) the total area lost is only 5.2%. Given the size of the samples and the care taken to position them it is not expected that the concentrations of the endpoints reported will not be underestimated by more than 5% due to positioning.

One of the major sources of deviation in the data appears to be from local variation in boron loading. The use of the 2mm aperture helps reduce the error by sampling over a larger area, but the relatively small aperture size still leaves enough room for variable error. Since the samples were cut from larger plates there is expected to be no variation in boron loading between the edges of the sample and the center. That is, there is expected to be no manufacturing variability that would influence boron concentration along the edges.

The data collected comes in the form of a sum total of counts for each channel in the detector. Each channel represents a different energy of the particle striking the detector. A

representative plot is shown in Figure 72. Typically, deconvolution of an NDP spectra is accomplished through application of the Bethe formula:

$$-\frac{dE}{dx} = \frac{4\pi}{m_e c^2}\frac{nz^2}{\beta^2}\left(\frac{e^2}{4\pi\varepsilon_0}\right)^2\left[ln\left(\frac{2m_e c^2\beta^2}{I(1-\beta^2)}\right)-\beta^2\right]$$

where β has the relativistic definition of the ratio of the particles velocity to the speed of light and n is given by:

$$n = \frac{N_A Z\rho}{A\cdot M_u}$$

The use of a calibration curve allows one to correlate the channels of a collected spectra to discrete energy levels. Each point on the spectra represents either a lithium or helium particle that has been ejected from the sample. Any deviation from the maximum energy is caused by particles generated within the sample interacting with the sample before they escape the surface. By knowing the energy levels of the charged particles one can solve the Bethe formula to determine the depth at which the particle was generated.

This typical deconvolution of an NDP spectrum allows one to determine the boron concentration as a function of depth perpendicular to the sample surface. This approach will not work with our samples. The Bethe formula is dependent on the atomic number and density of the material through which the charged particle passes. Since neutrons are able to penetrate deep into a sample they will be able to interact with subsurface boron carbide particles. When analyzing the NDP data it is not possible to determine if the sample passed only through a boron carbide particle or if the particle was sub-surface and, if so, how thick of an aluminum layer covered the particle.

For this project we are primarily concerned with the ratio of boron carbide between two locations. Thus, by using a large aperture and probing points along a cross-sectional surface we are able to compare the ratio between points and determine if boron is lost.

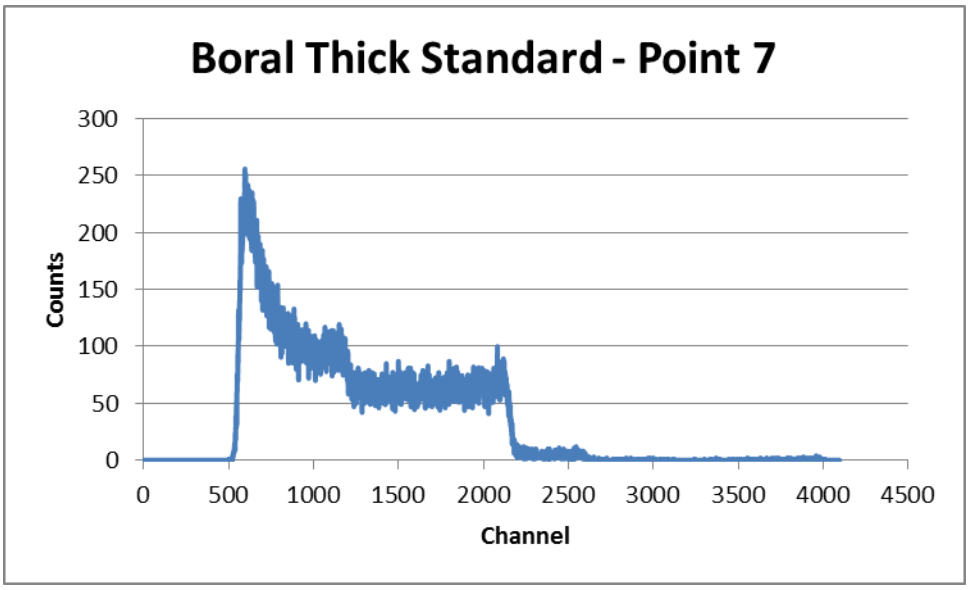

Figure 72 Plot of raw data from NDP experiment

To determine the count rate the integrated sum of counts from channel 1400 to channel 2000 was divided by the live time. The selection of that range of channels is to provide the highest total counts across a consistent region. Channel 1400 corresponds to an energy level of 982 keV and channel 2000 corresponds to an energy level of 1381 keV. This puts the region between the 840 keV and 1472 keV peaks. The 1013 keV peak is included in the range but is significantly small that the consistent inclusion of the peak will not affect results. It would be possible to include higher energies, closer to the 1472 keV peak but the presence of any surface contamination creates a spike on the leading edge of the peak. To avoid the inclusion of surface contamination in the integrated count rate those higher energy channels are excluded. The use of the live time instead of the real time is to factor in dead time from the detector.

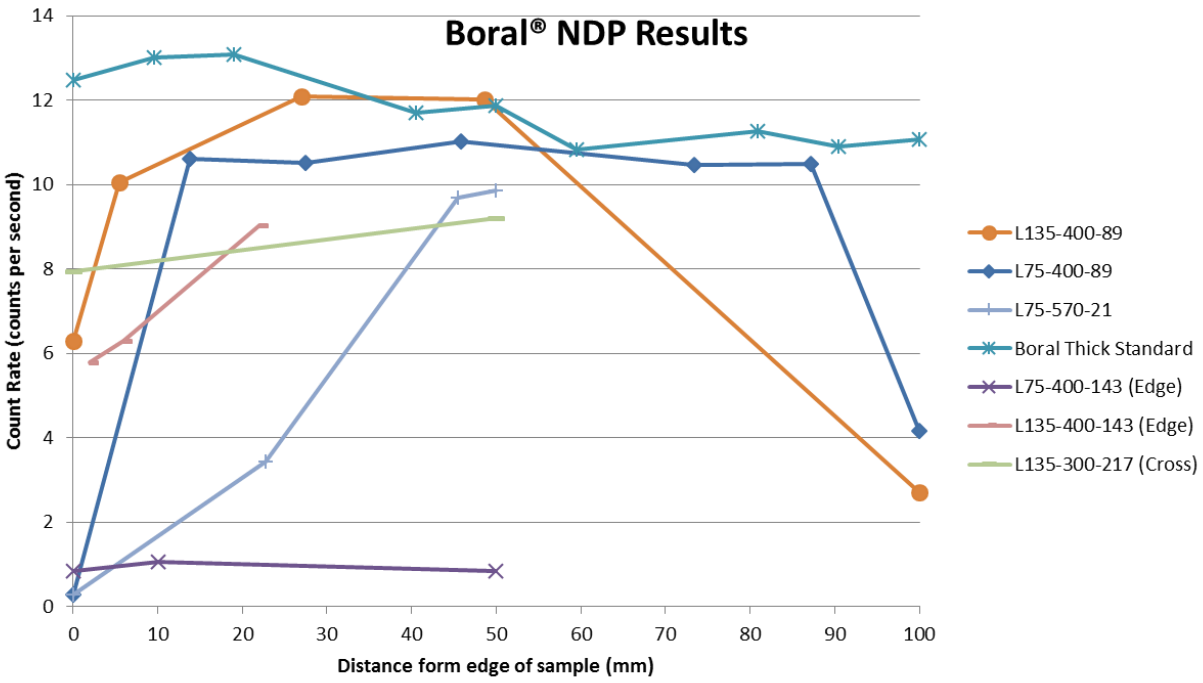

Figure 73 Boral® NDP results

The results of the Boral® samples, as seen in Figure 73, show that samples exposed in the autoclaves exhibit depletion of boron at the edges. The lone exception is sample L135-300-163 which exhibits the highest concentration and slight enrichment along the edge. This variation appears to be an artifact caused by damage to the porous core material and subsequent filing during sample preparation. The remainder of the corrosion coupons exhibit strong depletion behavior at the edges. The thin samples especially show a typical series of depletion curves. The concentration data for the thin standard was collected using a 1mm aperture but increasing the concentration by approximately four times to account for the larger area of the 2mm aperture puts the curve in its predicted place.

The small depletion on the origin edge of the Boral® Thin Standard is due to that edge being cut by water jet at the factory. The remainder of the sample appears to be fairly uniform in composition, as expected. The Boral® Thick Standard does not exhibit any edge depletion but

shows steady depletion from the origin edge to the opposite edge. The deviation is not large and is expected to be a result of boron particles being drug across the surface during cutting and becoming trapped in the pores.

The error induced by sample cutting and preparation reduces the value of the absolute results. However, the data is still incredibly valuable, especially when each point is plotted as a fraction of the maximum concentration observed in the sample. Figure 74 shows the Boral® results plotted as a percentage of the maximum concentration. The level of boron loss is quite surprising, especially given the use of a 2mm aperture. The large aperture means that 80% of the signal from the neutrons is generated more than 0.5mm away from the edge of the sample.

To help account for the size of the aperture and to determine the depletion along the outer edge a couple of points on the exposed edge were investigated. Sample L75-400-143 was exposed at 400°C for 143.5 days. Analysis of the boron concentration along the absorbed edges showed that it was greatly reduced compared to all other samples. The count rate along the exposed edge is about 10% of the count rate of other samples.

Sample L135-300-217 was exposed at 300°C for 217 days. Cross sectional investigation of the sample showed that the boron concentration was nearly 14% depleted at the edges. Profiling the exposed edge revealed the two-dimensional nature of depletion in Boral®. The edge points were furthest from the center showed the greatest depletion, nearly 60%. The edge point closer to the middle of the edge showed a concentration that was nearly as high as the center of the cross section.

The concentration profile of the points along the exposed edge indicates that the boron is readily leaching from all edges. The 1mm point on the exposed edge is also an edge point and has boron leaching from the probed surface and from the adjacent edge. The 11mm point on the

exposed edge is primarily diffusing perpendicular to the surface. The total boron concentration at all points in the sample is lower than the standard. In Boral®, long-range diffusion of boron is allowing boron to be diffused from the center of the sample to the edges.

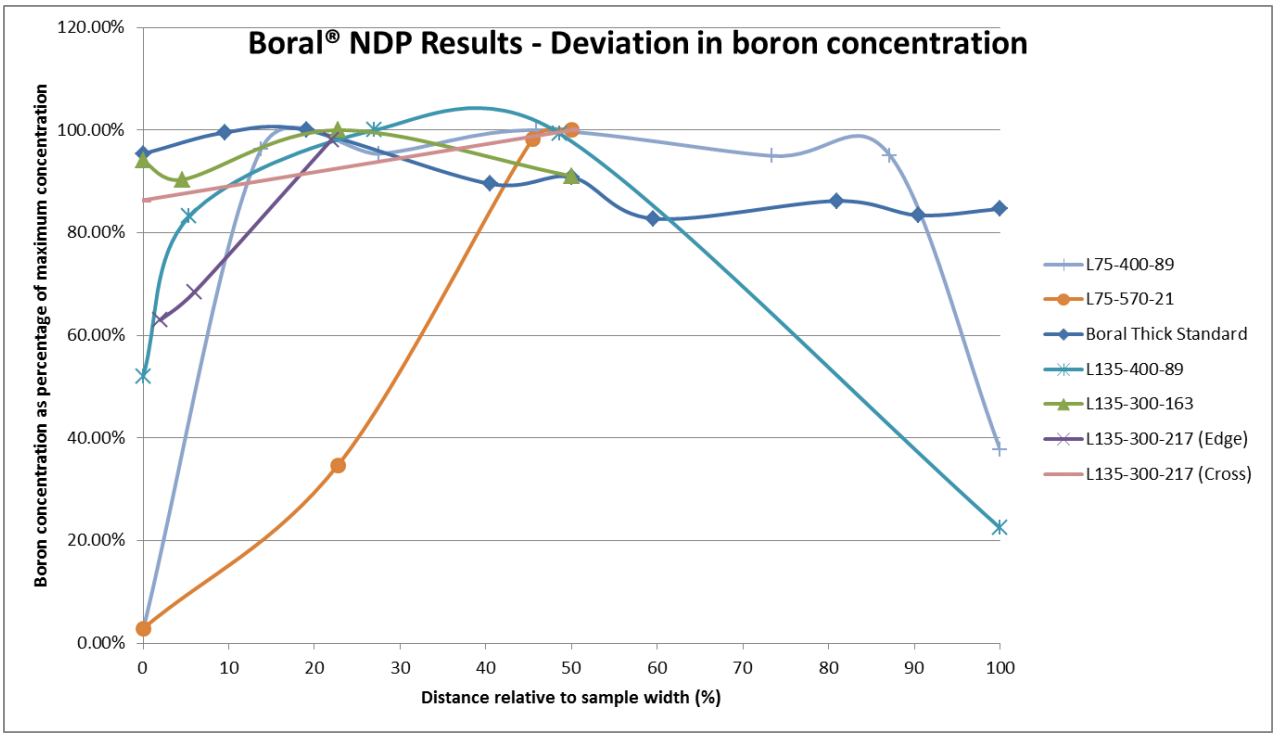

Figure 74 Boral® NDP results showing boron concentration as a percentage of maximum boron concentration

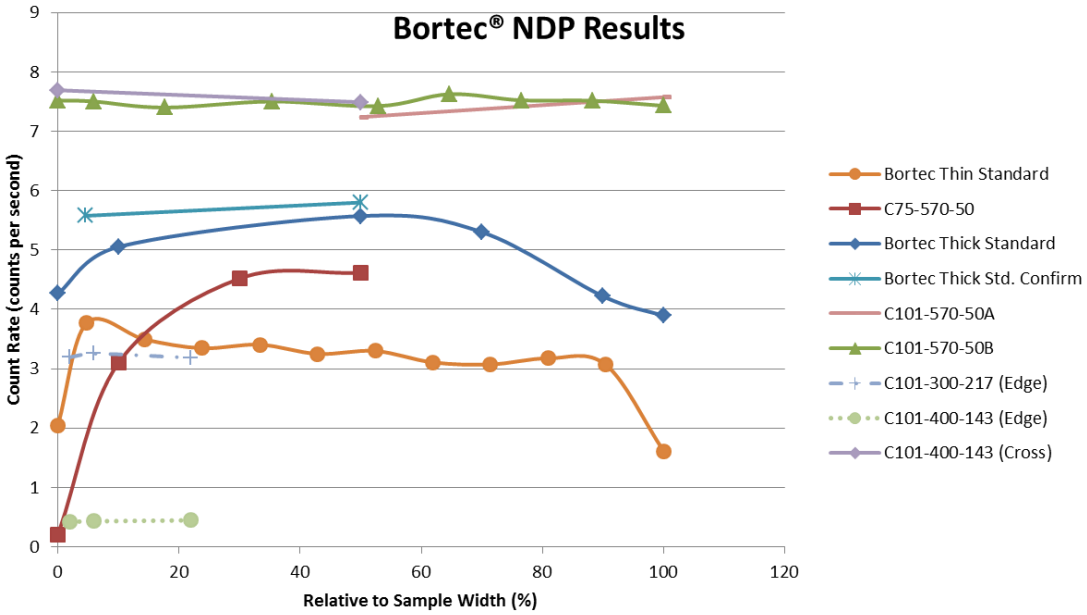

Figure 75 Bortec® NDP results

The results from the Bortec® samples are similar to those from the Boral® samples in that there is evidence of depletion along the edges. However, the Bortec® samples show more evidence of edge depletion in the standards than Boral® did and one of the Bortec® corrosion samples does not show signs of edge depletion and shows a higher boron concentration across the whole cross section than the corresponding standard.

These results are more surprising than the Boral® results. Boron concentrations in Boral® were expected to exhibit some deviation due to the porosity causing different localized densities and the ability of the pores to trap free boron carbide particles. In order to confirm the results Bortec® Thick Standard and sample C101-570-50 were run multiple times. The two data sets from C101-570-50 come from the same face of the same sample.

The depletion on both edges of the Bortec® Thin Standard is also quite surprising. Figure 75 shows that the boron concentrations in the edges of the sample depleted by more than 40%. Both edges of the Bortec® Thick standard also show the boron concentration to be depleted by

more than 20%. Sample C75-570-50 shows the expected depletion curve. Given the depletion exhibited by the standards and C75-570-50 it is concluded that depletion in Bortec® is real.

The investigation of the exposed edge of sample C101-400-143 shows that the depletion of boron in Bortec® is primarily along the edges. Sample C101-400-143 was exposed at 400°C for 143.5 days. Profiling of the cross section showed relative uniformity of the concentrations. A profile of the boron concentration along the exposed edge also revealed a uniformity of concentration. However, the concentration along the exposed surface showed that the boron concentration was 95% less than the concentration in the bulk. These results indicate that boron is depleted at the surface but diffusion of boron through the sample is limited.

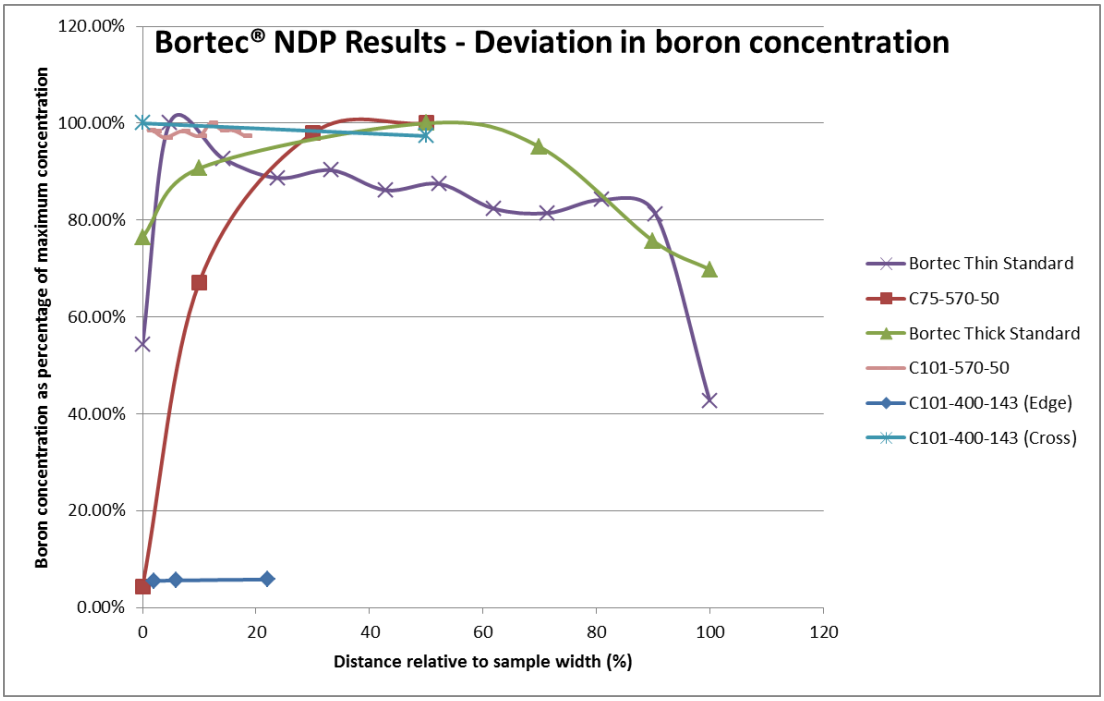

Figure 76 - Bortec® NDP Results - Deviation in boron concentration as a percentage of maximum concentration

Chapter 4 Discussion and Conclusions

4.1 Discussion

The results of the oxidation tests on the Boral® and Bortec® samples at 300, 400, and 570°C show little evidence of aluminum corrosion. Dimensional changes to the samples in the length and width averaged less than 1% and showed no trend in the direction of change, either increase or decrease. Changes in the thickness of the Bortec® samples were small and again averaged less than 1%. Changes in the thickness of the Boral® samples were greater and positive at 570°C but varied at lower temperatures. Much of large change at 570°C appears to be caused by expansion and cracking the core of the samples.

Mass changes in all samples show more consistent trends that can be observed in Figure 77. All samples exposed with high and medium humidity argon exhibited a mass loss. In Boral® samples the mass loss increased with exposure time and the changes was most rapid at 570°C and slowest at 300°C. The mass change was independent of sample thickness. The magnitude of change at 400 and 570°C ranges from 3% at 400°C for 31.5 days to 42% at 570°C for 50 days.

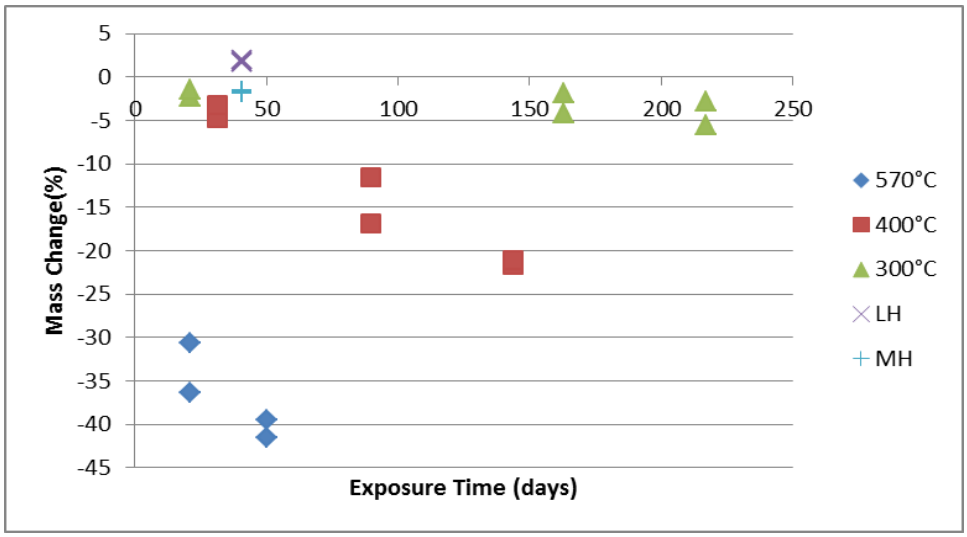

A

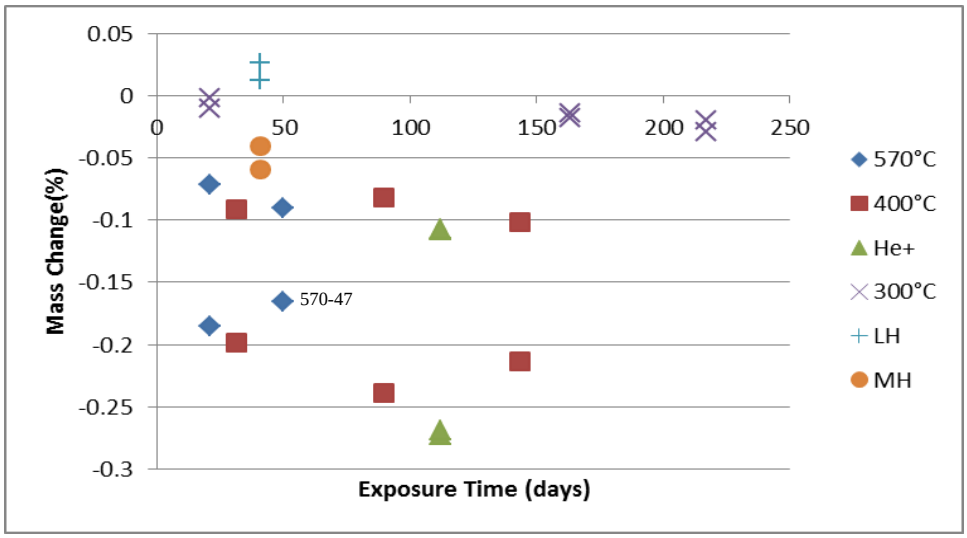

B

Figure 77 Mass changes in (A) Boral® and (B) Bortec® samples

The change at 300°C is less than at the higher temperatures and the rate of change is also an order of magnitude less. However, after 217 days the mass change in the thin Boral® sample still exceeds 5%. Changes in mass after exposure with the moderately humidified gas at 400°C shows results that falls right in line with the results from the 300°C test. Exposure to the low humidified gas at 400°C showed a mass increase in both thin and thick Boral® samples.

Mass changes in Bortec® samples are not as large as in the Boral® samples. Exposure at 570 and 400°C results in similar mass loss, though the results are based on sample thickness with thick samples exhibiting greater mass loss. At 300°C the mass loss in Bortec® is less than 0.03% for periods up to 217 days. Exposure to the moderately humidified gas for 41 days gave results that were between the tests at 300°C and the results for thin Bortec® at 400 and 570°C. Samples exposed to the low humidified gas showed a mass increase at 41 days.

The point that defies trends in Bortec® oxidation is the point labeled C101-570-50 in Figure 77 B. This is the only point in either Boral® or Bortec® tests that shows a decrease in mass loss with time. This deviation is explained by the presence of the blisters that formed. The oxidation of aluminum and boron carbide result in the formation of hydrogen. If hydrogen is generated, but unable to escape from the sample then the increase in pressure inside the sample can cause the formation of the blisters. The formation of oxides on a metal will result in mass gain.

Extrapolating the data for the thin Bortec® samples at 570°C and assuming the same change in the thick samples we can calculated an expected mass change. For the thick Bortec® samples we would expect the weight change to go from 7.6090g to 7.5935g instead of the observed 7.5964g. This difference would require 0.04454mm^3 of sample to be oxidized or about 1.740×10^{-3}% of the sample volume. From optical analysis of the sample we can approximate the area of the blisters. Looking that the SEM analysis of the blisters we can see that the thickness of the metal that has been pushed up is around 40 microns. By assuming that the oxidation extends as far down as above then, by multiplying the area of the blisters by 80 microns gives the affected volume. Carrying the calculation through gives a total blistered volume of 0.223mm^3.

This provides plenty of volume to provide the necessary 0.04454mm^3 of oxide required to account for the deviation in mass change.

The results for the ion irradiated samples showed the greatest mass loss of Bortec® samples. The irradiation can affect the sample in a couple of different ways. Irradiation will change the microstructure of the sample. Irradiation damage to the crystal structure of the sample can result in dislocations that provide diffusion pathways to the surface. Irradiation can also cause surface sputtering. Uneven sputtering of the surface can result in peaks and valleys forming on the sample surface resulting in an increase in total surface area.

An increase in total surface area on the Bortec® could result in an overall increase in mass due to the formation of surface oxides. Conversely, the larger surface area decreases the length of the diffusion path for surface boron, thus allowing more boron to leach and resulting in mass loss. The results from the corrosion experiment on the irradiated samples show that the samples have experienced overall mass loss and that the magnitude of the loss is greater than for other samples exposed at 400 and 570°C.

In typical corrosion experiments one would expect that mass loss, plotted as a function of time, would exhibit an Arrhenius trend. Figure 78 shows a plot of the change in mass of Boral® and Bortec® as a function of temperature after exposure for 50 days. From the graph we can see that the mass loss clearly does not follow an Arrhenius trend, but is consistent for both materials.

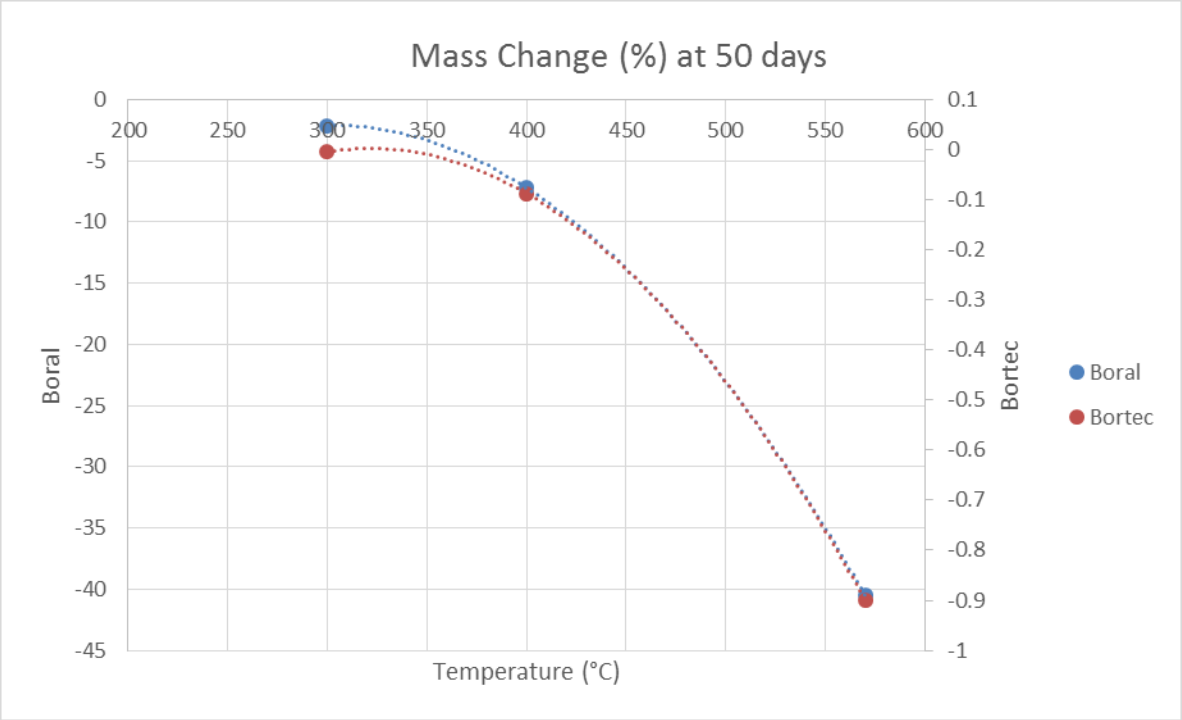

Figure 78 Mass change in Boral® and Bortec® as a function of temperature

The conclusion that the samples are losing boron is confirmed through the NDP results. The Boral® samples show the largest decrease in boron density near the edges. This is to be expected since the aluminum cladding will reduce boron diffusion through the surface as most diffusion will occur through the pores which lead to the edges. Coupling NDP analysis of an exposed edge to a cross section shows that boron loss is greatest in the corners where the boron can diffuse through two nearby surfaces. Boral® also shows an overall decrease of boron in the bulk. These results indicate that boron is diffusing through the sample to the edges where it is then able to be carried away in the steam.

Boron loss in Bortec® seems to be limited to the near surface region, though the results for Bortec® are few and mixed. What is clear is that the surface concentration of boron is depleted. The magnitude of loss of boron in the bulk will be limited by the diffusion of boron

through the sample. The diffusion limited nature of boron loss in Bortec® makes investigation of irradiation damage much more important.

The higher diffusion of boron in Boral® compared to Bortec® is enabled by the porous nature of the Boral®. The pores create diffusion pathways as well as increasing the total surface area available for reactions. The penetration through the pores is most clearly observed in the samples exposed at 570°C. Figure 79 shows a cross section of sample L135-570-50 taken at the sample edge (A) and in the middle (B). EDS analysis of both locations shows that the dark gray locations that make up the majority of the surface is the epoxy that the samples were mounted in.

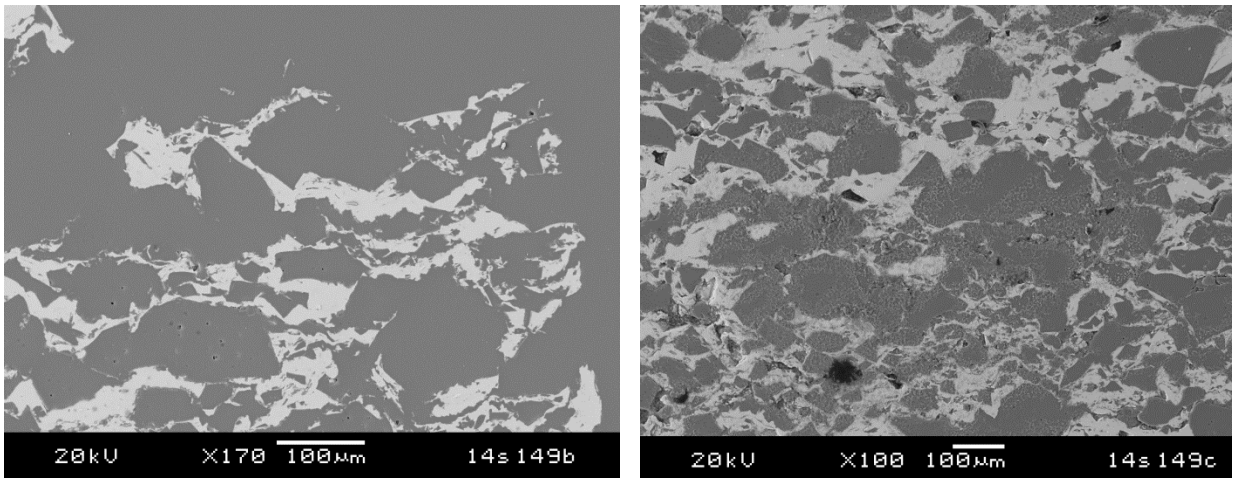

A B

Figure 79 Cross section SEM image of edge of L135-570-50, Boral® exposed at 570°C for 50 days

The loss of boron from the samples is corroborated with XRD data from the outlet lines of the autoclaves. Initial autoclave testing was hampered by the continuous plugging of outlet lines. XRD analysis of the deposits collected in the outlet lines showed that the particles contained boron. Both Boral® and Bortec® samples were loaded into each autoclave so the source of the boron cannot be determined but it does show that the boron is not contained in the samples.

Thus far our discussion has focused on diffusion. Creation of a model to predict projected corrosion behavior is difficult for complex systems as we have in this study. Typical diffusion analysis begins with Fick's Law

$$J = -D\frac{dC}{dX}$$

Fick's Law states that diffusion is driven by a concentration gradient and the rate of diffusion is determined by a diffusion coefficient. This diffusion coefficient, D, can be estimated by:

$$D \approx zR_0a^2exp\left(-{E_m}/{k_BT}\right)exp\left(-{Q_v}/{k_BT}\right)$$

The terms R_0, a, and E_m describe the attempt frequency of vibrational jumps, jump distance, and activation energy required for an atom to jump from one lattice site to another. The terms z and Q_v describe the number of lattice sites next to an atom that are occupied by vacancies and the energy to form a vacancy. Thus the diffusion is determined by how readily an atom is vibrating and how many vacancies are nearby. The number of thermally induced vacancies is also a function of Q_v and is calculated by

$$N_v = N_0e^{\frac{-Q_v}{k_BT}}$$

In a system where radiation is present we also need to account for radiation induced vacancies

$$R = N\int_{\check{E}}^{\hat{E}}\int_{\check{T}}^{\hat{T}}\phi(E_i)\sigma(E_i,T)\nu(T)dTdE_i$$

The radiation effect can greatly enhance diffusion and can help explain why the ion irradiated samples showed an increased magnitude of mass loss. However, concentrations and vacancies are not the only factors that will determine diffusion rates. Diffusion rates will also be affected by the microstructure and which species are diffusing. We also need to account for the differences in chemical potentials. These chemical potentials will exist between the boron carbide and aluminum and between the boron carbide, aluminum, and water.

To account for all of the different factors that will influence diffusion rates we need to use a more thorough equation. For this we will be better served by applying Onsager's diffusion equation. The theory behind the Onsager diffusion equation is that any flux of mass, heat, charge, or any other property, through a system is linearly correlated with the thermodynamic forces that are present in the system. Correlating the fluxes and forces are described by the Onsager reciprocal relations. Therefore we can write the general term as

$$\vec{J_\iota} = \sum_{j=1}^{n} L_{ij}\vec{X_J}$$

In our system we are not considering electrical charge forces, pressure gradients, temperature gradients, magnetic fields, or any other force besides the chemical force, μ. For a three component system we can set up our series of relations in the following matrix

$$\begin{pmatrix} J_A \\ J_B \\ J_B \end{pmatrix} = \begin{pmatrix} L_{AA} & L_{AB} & L_{AC} \\ L_{AB} & L_{BB} & L_{BC} \\ L_{AC} & L_{BC} & L_{CC} \end{pmatrix} \begin{pmatrix} -\nabla\mu_A \\ -\nabla\mu_B \\ -\nabla\mu_C \end{pmatrix}$$

Substituting in the term for chemical potential allows us to re-write this system as

$$\begin{pmatrix} J_A \\ J_B \\ J_C \end{pmatrix} = \begin{pmatrix} \frac{kTL_{AA}}{n_A} & \frac{kTL_{AB}}{n_B} & \frac{kTL_{AC}}{n_C} \\ \frac{kTL_{AB}}{n_A} & \frac{kTL_{BB}}{n_B} & \frac{kTL_{BC}}{n_C} \\ \frac{kTL_{AC}}{n_A} & \frac{kTL_{BC}}{n_B} & \frac{kTL_{CC}}{n_C} \end{pmatrix} \begin{pmatrix} -\nabla n_A \\ -\nabla n_A \\ -\nabla n_A \end{pmatrix}$$

The diagonal terms connect the generalized force with its conjugate flux (i.e. L_{AA} connects the chemical potential of species A with the flux of species A). The off-diagonal terms are what allow us to establish the influence of non-conjugate forces on the flux of a given species.

At this point we run into the problem of realizing that we do not have the experimental values for these transport coefficients. In addition, the true diffusion values will also depend on the microstructure of the sample. This microstructure includes the nature of the interface

between boron carbide particles and the aluminum matrix. Being able to understand the nature of this interface will allow the determination of the flux rate out of the boron carbide particle and hence the rate of degradation of the boron carbide particle. Even though diffusion is going to play a major part in determining the rate of degradation of these materials, diffusion is not the only phenomenon at work in this system, as evidenced by the mass-loss curves.

To determine the rate at which these materials will degrade requires the identification of the mechanisms at work on the system. The first mechanism that we propose is the diffusion of oxygen into the system. As oxygen is diffused into the system it can interact with the boron carbide and the resulting boron oxide is then able to diffuse back out through the system and escape. This mechanism is rejected on the basis of lack of evidence.

Oxygen does not diffuse through aluminum. Aluminum is too reactive and will immediately form aluminum oxide. If oxygen is diffusing in through pores then strong oxide signals should be able to be detected in the sample. If the pores are small there is also the chance that the oxidation will seal off the pores preventing further oxidation since the formation of aluminum oxide results in a 200% volume increase. The size of a B_2O_3 molecule will hinder diffusion and would be expected to become trapped within the sample.

The second mechanism considered is hydrogenation. The presence of oxides on the surface indicates that hydrogen is being generated. Further investigation of this possibility shows no evidence of hydrogen reacting with aluminum or boron carbide in the test conditions. The lack of reaction and the lack of a driving force to drive the hydrogen into the sample is sufficient to discount this mechanism.

The third mechanism considered is that the process is driven by surface oxidation. As the surface is oxidized and near surface boron carbide particles are oxidized it creates a

concentration gradient that induces the degradation of boron carbide particles further from the surface. This mechanism seems possible and could be determined by further testing, but it does not seem likely that loss of boron carbide on the surface is sufficient to cause long-range forces sufficient to break down boron carbide particles in the center of the sample. While this mechanism does not seem likely, it led us to the fourth, and most likely, mechanism.

Based upon the results seen it is believed that more than one mechanism is at work in these tests. The first mechanism is the direct reaction between boron carbide and aluminum. Although there is no work known to us that has looked at the interactions between aluminum and boron carbide at temperatures as low as considered in this test the interaction potential has been recorded. Figure 80 shows the phases that have been noted in the Al-B-C system for temperatures above the melt temperature of aluminum.

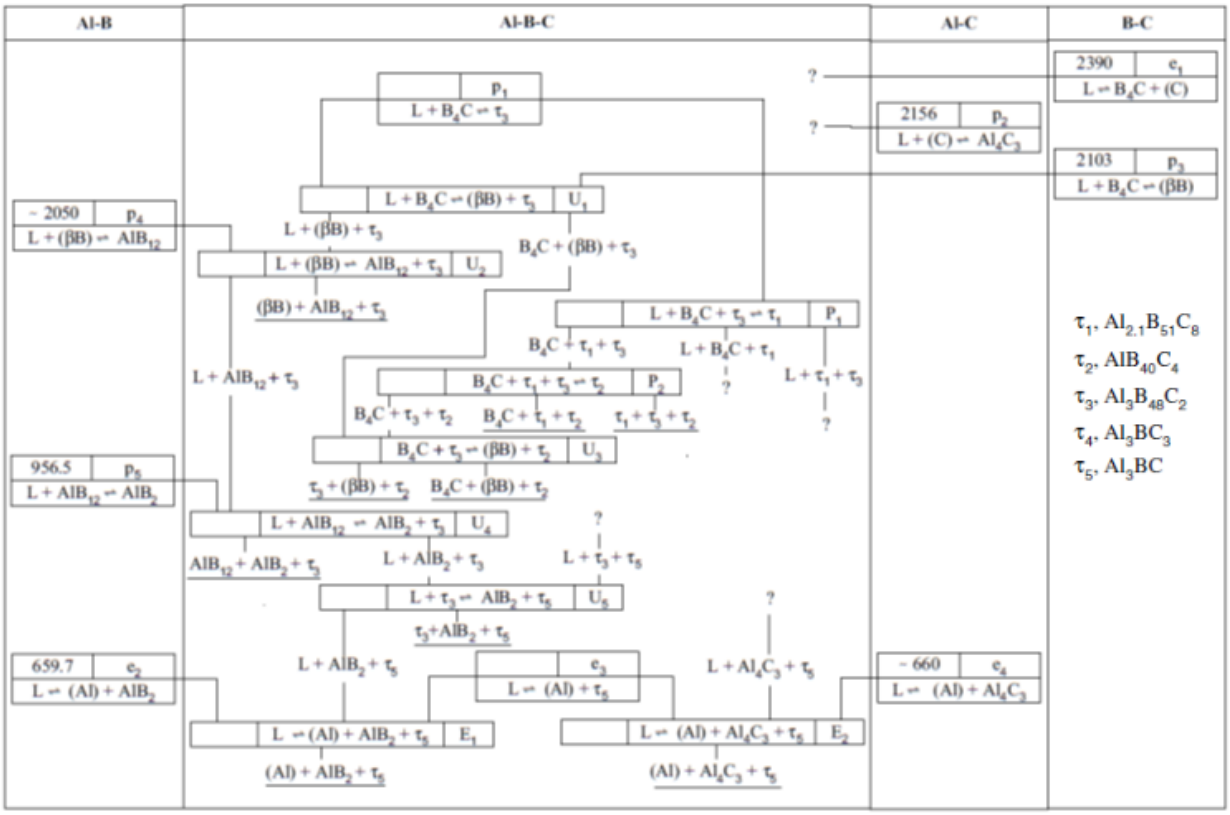

Figure 80 Phases formed in the Al-B-C system [82]

In addition to the phases formed above the aluminum melt temperature the reaction has also been observed at 627°C. Exposure of an aluminum/boron carbide material at 627°C in pure Ar for 160 hours has been shown to generate an aluminum boride phase and an aluminum oxide growth similar to what we observed in our initial corrosion experiment.

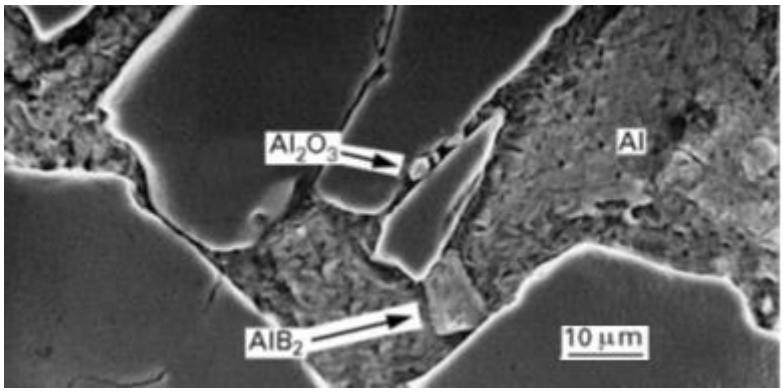

Figure 81 Phase formation in Al-B_4C system after 160 hours at 627°C in pure argon [78]

The breakdown of boron carbide as a result of interaction with the aluminum explains the presence of the various phases at the center of the sample without any strong oxygen signal from EDS analysis. The continued movement of phases at 570°C in dry argon shows that the species are mobile once out of the boron carbide.

In addition to the aluminum-boron carbide interaction we also have oxidation on the surface. Surface oxidation is sufficient to cause boron depletion in the near surface region. Once the boron is free of the boron carbide and mobile in the aluminum matrix then it is possible for the concentration gradient to drive diffusion toward the surface where more boron will be lost. Since the carbon is not oxidizing away it has no diffusion gradient and will stay in the local area.

Along with boron loss the water will oxidize the aluminum. The resulting oxide is more porous than an aluminum oxide formed in dry air. It is possible for this oxide to degrade and break off. This would indicate that the mass loss is a combination of oxide formation, which

results in mass gain, combined with the breakdown of the oxide and the loss of boron carbide. Modeling of this system would require the modeling of all four phenomenon.

4.2 Conclusions

The aim of this work was to determine the performance of Boral® and Bortec® after extended deployment in dry cask storage of used nuclear fuel. Experiments performed as part of this work focused on determining the corrosion behavior of the specified materials.

High steam flow tests (gas flow: 1.5scfh, humidity mass fraction: 0.58) were conducted at 300, 400, and 570°C. Test coupons exposed in these conditions showed no change in physical appearance. Dimensional changes for both Boral® and Bortec® were generally less than 1% and randomly varied between positive and negative. Mass changes in Boral® were all negative, indicating mass loss. The magnitude of mass loss extended up to 41.54%. Mass changes in Bortec® were also all negative, though not of the magnitude observed in Boral® with the largest mass loss being 0.239%. Testing on samples that had been irradiated with heavy ions showed increased mass loss, with a maximum mass loss of 0.273%

Reducing the flow rate of steam to (gas flow: 0.4-0.5scfh, humidity mass fraction: 0.082) resulted in less mass loss for all samples. Further reducing the flow rate of steam to (gas flow: 0.2-0.3scfh, humidity mass fraction: 0.028) resulted in an overall mass gain. Mass gain in the samples is expected due to the formation of aluminum oxide. The mass loss could result either from destruction of the oxide or leaching of boron. NDP results indicate that the concentration of boron is depleted in both Boral® and Bortec® suggesting that the mass loss did result from boron loss. In addition, XRD analysis shows that deposits formed on the outlet lines of the autoclaves did contain boron, lending further evidence that boron is leaching out of the samples.

Besides boron loss, the formation of new phases in the aluminum matrix has been noticed in both Boral® and Bortec®. These phases are most observable in Bortec®, particularly at higher temperatures. The high loss of boron in Boral® along with its porosity appears to reduce the concentration of these alternate phases but they are still evident. The phases appear across the temperatures investigated indicating uniformity in the corrosion mechanism in that temperature range. The majority of observed phases are carbides, this indicate a breakdown of the boron carbide particles and suggests free boron in the matrix that is able to diffuse.

It is proposed that the new phases observed and the mass loss (including boron loss) occurs through two different mechanisms. The phase changes occur due to the potential difference between boron carbide and aluminum. The mass loss occurs through interaction with water along exposed surfaces, either on the surface or in pores.

The amount of boron removed will relate to the amount of water available. A conservative estimate of water remaining in a cask after drying is approximately 1 L in a typical 4500L cask[99]. This estimate is not definitive. Additional work is ongoing to determine how much water is left in the cask. In comparison to these initial estimates, approximately 175L of water was used during the 217 day test at 300°C. Mass gain occurred during the lowest water use test where 0.3L of water was used on only 24in^2 of material. Material samples in an actual dry cask environment would be exposed to temperatures closer to 300°C and less water than the lowest test.

The results from this study conclude that humidity levels are important. Surface boron will leach away. Boral® is especially susceptible to the leaching due to the high surface area of the pores. The reaction between the aluminum and boron carbide will continue to allow the boron to diffuse to the surfaces where it can then be oxidized and depleted from the sample. In

the absence of water these materials should continue to act sufficiently as moderator materials. However, until the kinetics are determined and the total remaining water in a cask is known the ultimate long-term performance of these materials cannot be determined.

Chapter 5 Future Work

The discovery that the boron carbide particles were not as stable in the aluminum opens the door to many future research opportunities. To confirm the results of the work done here it is important to run the low humidity tests for longer durations. Additional testing also needs to be done in a dry environment to see if the microstructure changes with prolonged exposure at temperatures above 300°C.

Analysis of all samples using a FIB to prepare TEM specimens would be useful in understanding the phases that form. Identification of the phases provides a foundation for modeling work and it also helps confirm the continuity of the reaction mechanism across the temperature range. Analysis of the boundary layer between boron carbide and aluminum and between the various phases and the aluminum also needs to be performed. Understanding this boundary layer is imperative for simulation of the degradation of the boron carbide particles.

In situ microscopy would also be valuable. Observing the samples at high temperatures could reveal the dissolution of certain phases. Adjusting the cooling of the samples could also cause additional phases to form. Additional testing should also be performed on samples made from boron carbide in pure aluminum. The use of pure aluminum will help determine the effect of any of the aluminum alloy elements on the degradation of the boron carbide.

The results from the irradiation experiments indicate that irradiation does have an effect on the behavior of the material. To understand the effect of radiation on the material in dry cask environment corrosion testing should be performed on samples that have been neutron irradiated. Neutrons will be able to penetrate deeper into the material. The depth of damage will create

longer diffusion pathways to the surface, assisting the depletion of boron. Neutrons interacting with the boron will cause damage at the interface between the boron carbide and the aluminum, in addition to generating He and Li species. The damage and change in local chemistry will affect how the boron carbide and aluminum interact. This effect should be accounted for.

The formation of new phases in the microstructure will affect the mechanical properties of the materials. This is not such a big issue for the Boral® since it is not used as a structural material. In additional, most of the changes in Boral® occur in the core while the outer cladding provides structure and support for the material. Bortec® can be used as a structural material and as such it is important to understand how the microstructural changes affect the mechanical properties.

Predicting the behavior of Boral® and Bortec® after hundreds of years in a cask requires the creation of a model. Modeling the degradation of Boral® and Bortec® first requires an understanding of the transport of boron and carbon across the boron carbide/aluminum interface. Transport properties of boron carbide with group IV elements have been studied [100], but interface structure and geometry will greatly affect overall transport. Oxidation of boron carbide at the surface and transport into the gaseous phase is the second part of the model that needs to be investigated. This includes modeling transport to the gas inside the pores in Boral®. The third modeling component is the diffusion of boron through the sample.

Additionally, it is important to analyze these results with respect to storage and transportation. These materials have shown themselves to react quickly with water. Residual water is a concern in long-term storage as oxidation can degrade the fuel storage barriers and creates opportunities for release. These materials should be analyzed with regard to their functionality as a water getter in storage.

The cask environments also need to be re-analyzed with respect to increased hydrogen content. The reaction with water produces hydrogen, driving the cask toward reducing conditions. This is advantageous for the reduction of oxidation degradation during storage however, the hydrogen production should also be analyzed with regard to the hydriding of Ziracloy cladding. Zircaloy cladding readily absorbs hydrogen and the resulting hydrides cause embrittlement of the Zircaloy cladding, potentially leading to an increase in fuel rod failures.

Appendices

Appendix A

XRD results for deposits in autoclave outlet lines.

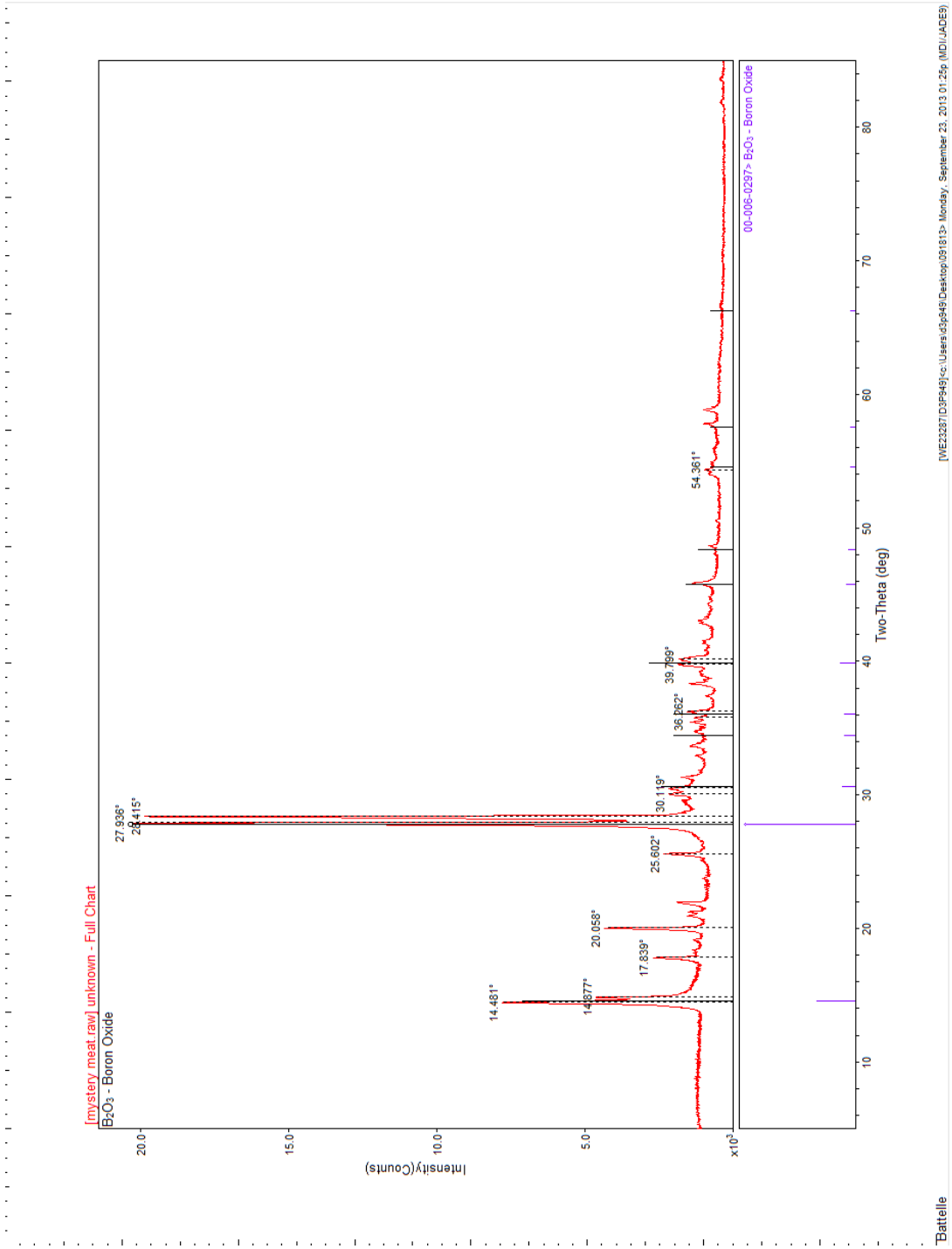
[mystery meat raw] unknown - Full Chart
B2O3 - Boron Oxide
00-006-0297> B2O3 - Boron Oxide
Intensity(Counts)
Two-Theta (deg)
x10^3
20.0
15.0
10.0
5.0
10
20
30
40
50
60
70
80
27.936°
28.415°
14.481°
14.877°
17.839°
20.058°
25.602°
30.119°
36.862°
39.799°
54.361°
[WE23287] [D3P949] <c:\Users\d3p949\Desktop\091813> Monday, September 23, 2013 01:25p (MDI/JADE9)
Battelle

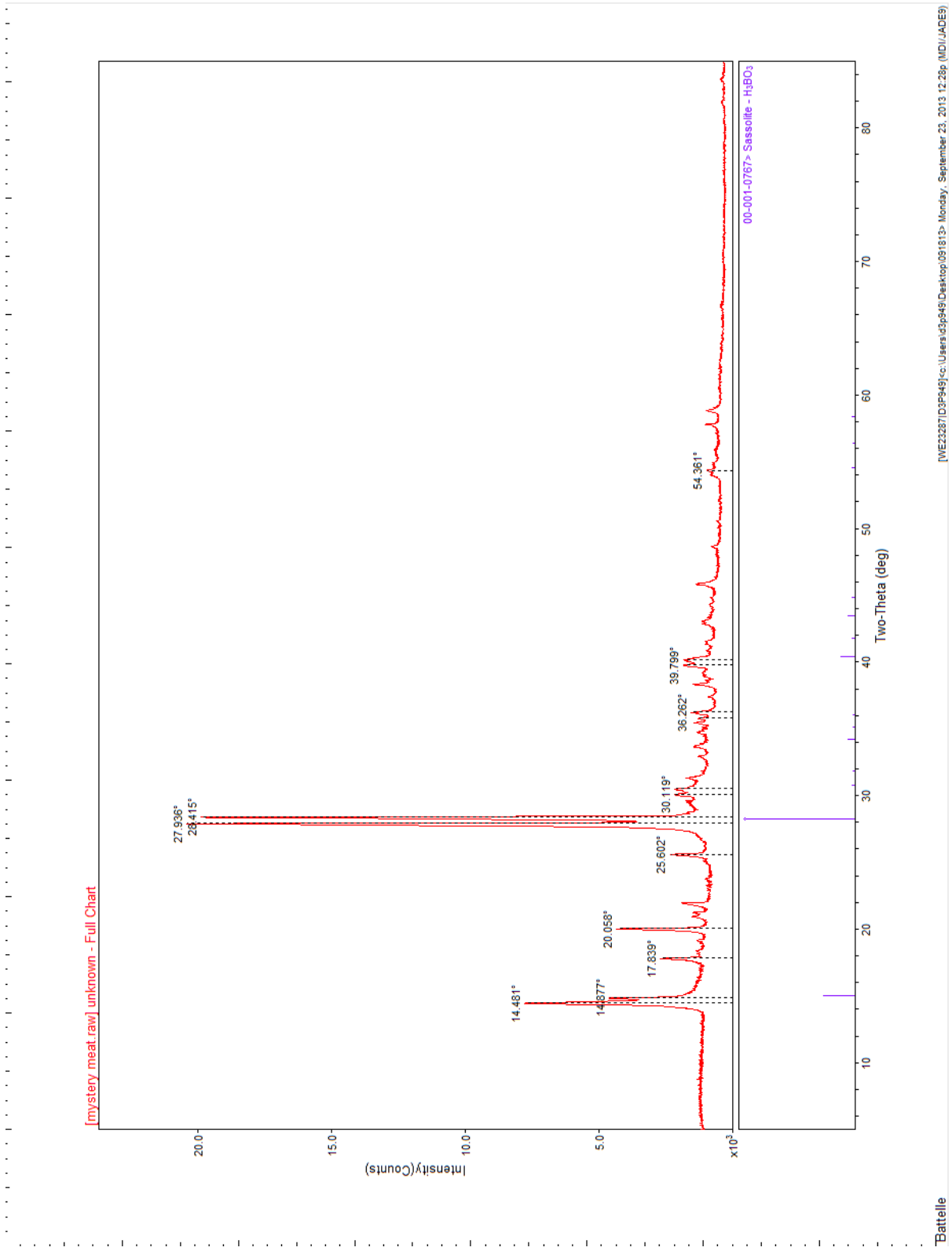
[mystery meat raw] unknown - Full Chart
Intensity(Counts)
x10³
20.0
15.0
10.0
5.0
27.936°
28.415°
14.481°
14.877°
17.839°
20.058°
25.602°
30.119°
36.262°
39.799°
54.361°
00-001-0767> Sassolite - H₃BO₃
10
20
30
40
50
60
70
80
Two-Theta (deg)
[WE23287(D3P949)<c:\Users\d3p949\Desktop\091813> Monday, September 23, 2013 12:28p (MDI/JADE9)
Battelle

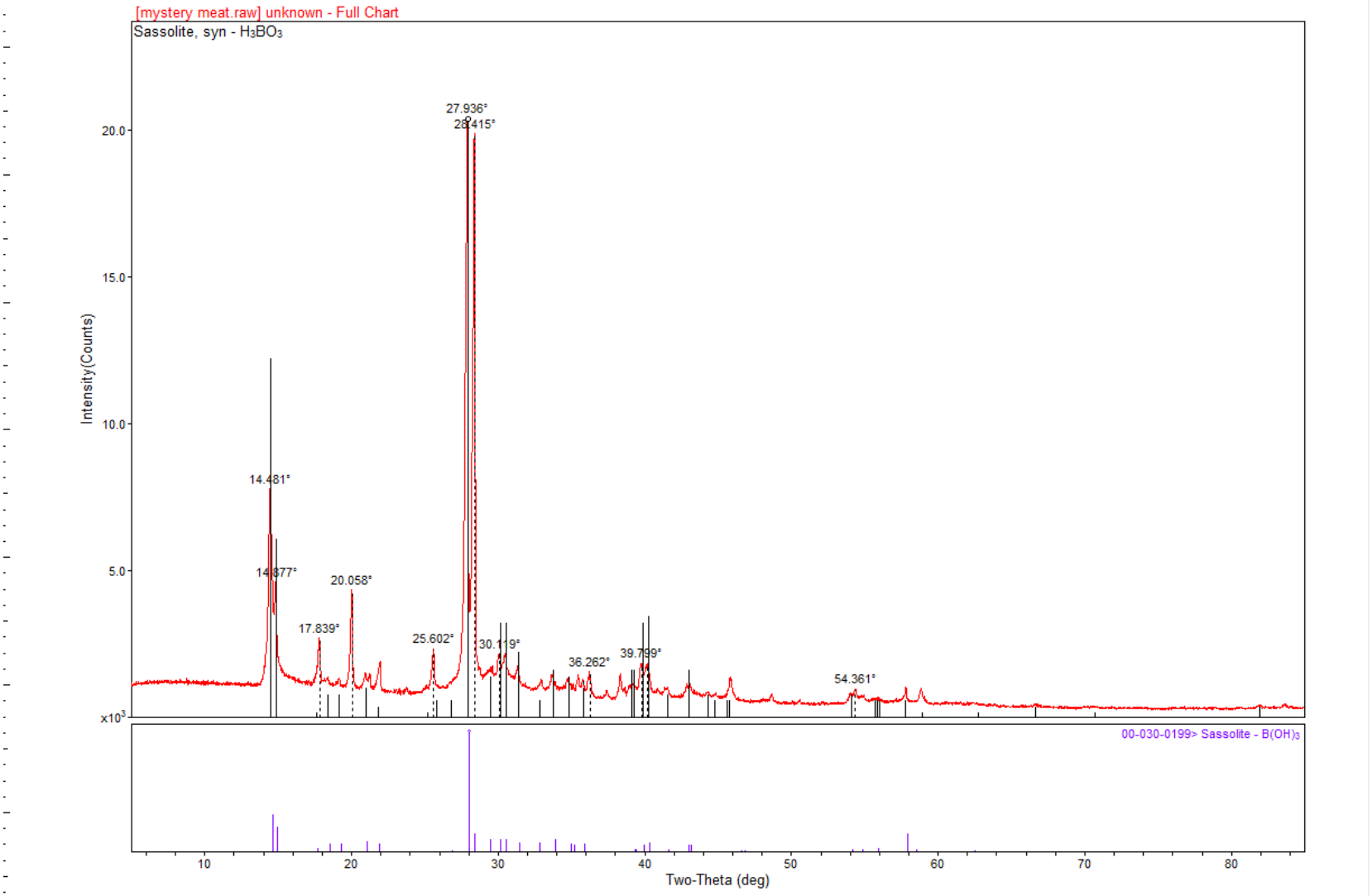
[mystery meat.raw] unknown - Full Chart
Sassolite, syn - H3BO3
27.936°
28.415°
14.481°
14.877°
20.058°
17.839°
25.602°
30.119°
36.262°
39.799°
54.361°
Intensity(Counts)
x10^3
20.0
15.0
10.0
5.0
00-030-0199> Sassolite - B(OH)3
10
20
30
40
50
60
70
80
Two-Theta (deg)
Battelle
[WE23287|D3P949]<c:\Users\d3p949\Desktop\091813> Monday, September 23, 2013 12:48p (MDI/JADE9)

Appendix B

TEM Results of Corrosion Samples

B.1 C101-570-50

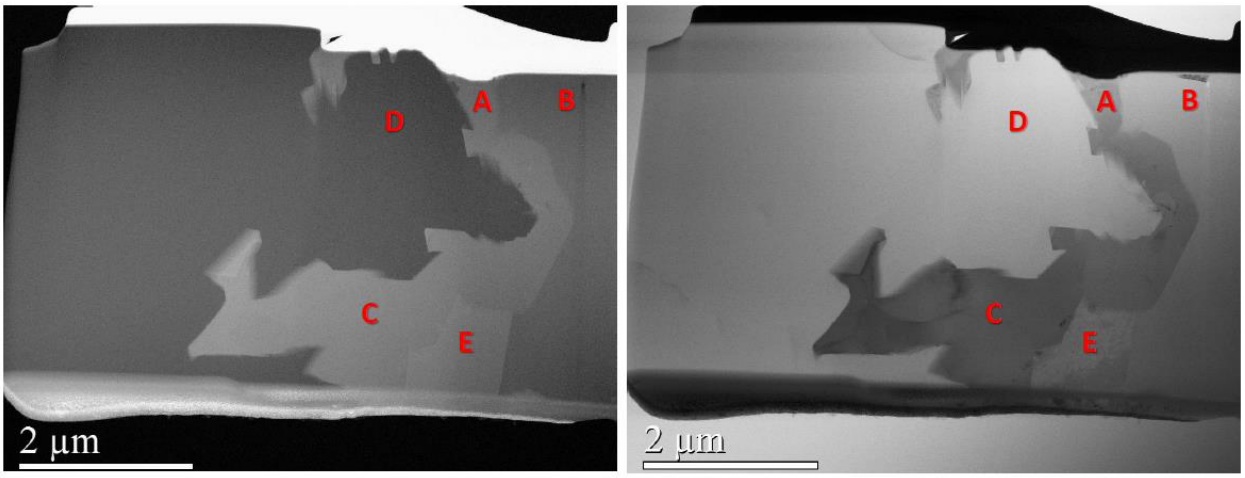

A

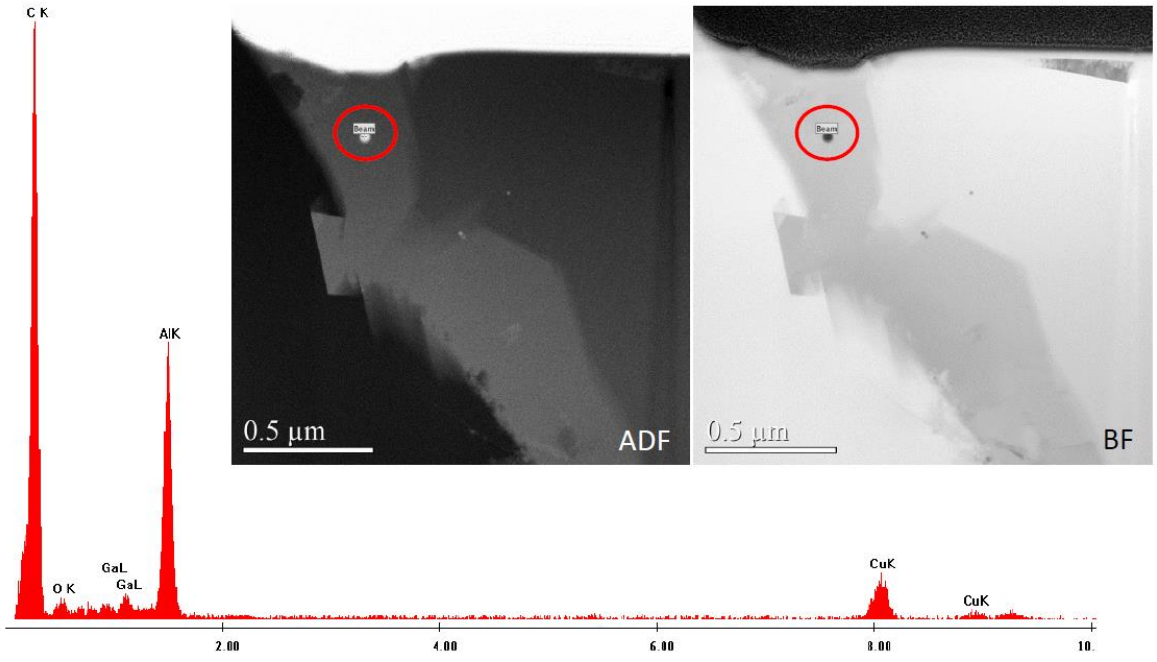

B

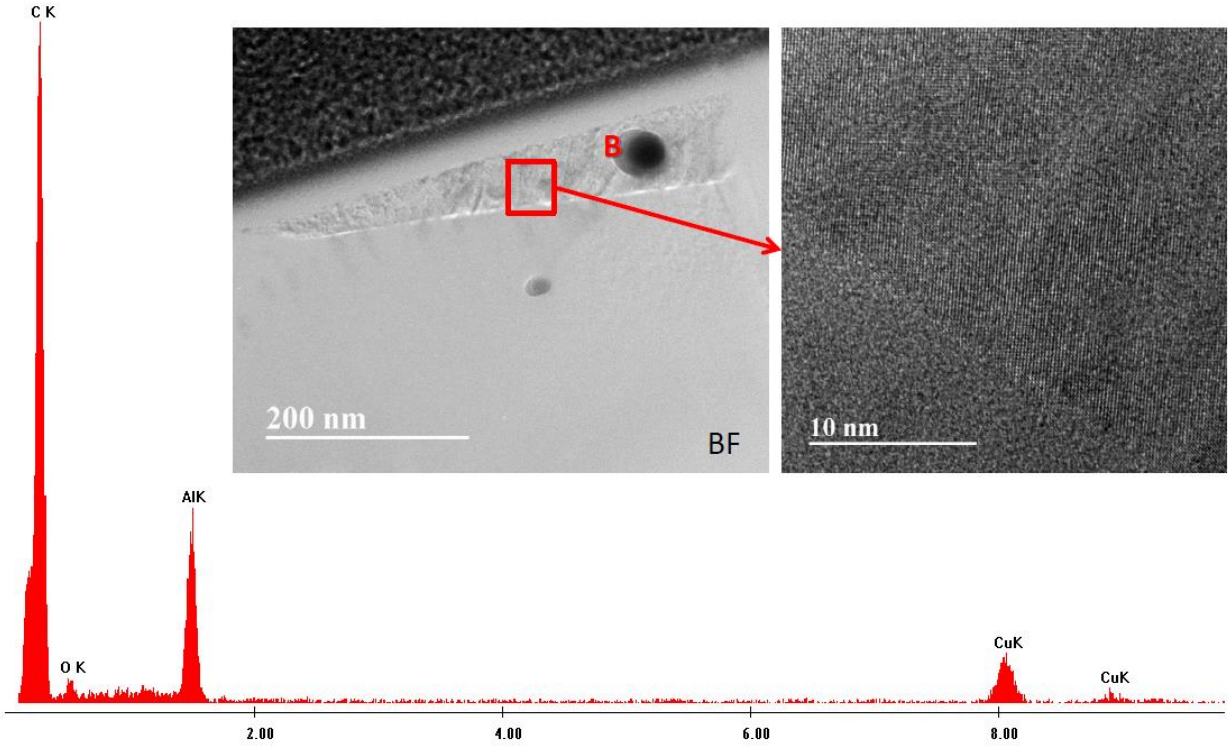
C K
B
200 nm
BF
10 nm
AlK
O K
CuK
CuK
2.00
4.00
6.00
8.00

C

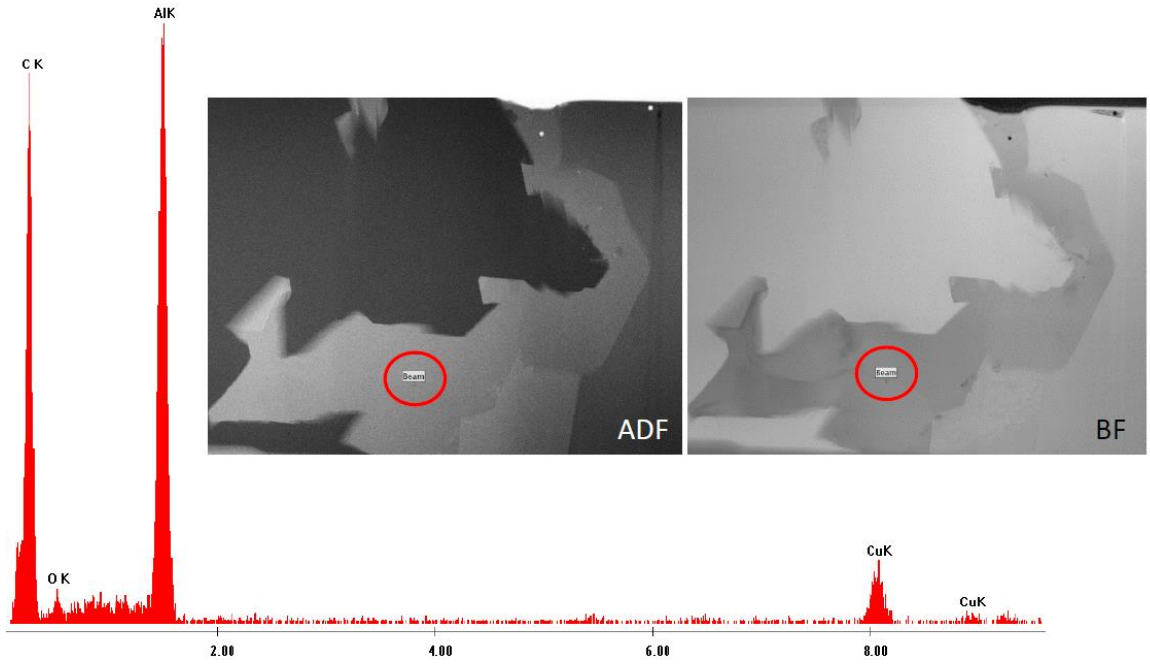
AlK
C K
ADF
BF
O K
CuK
CuK
2.00
4.00
6.00
8.00

D

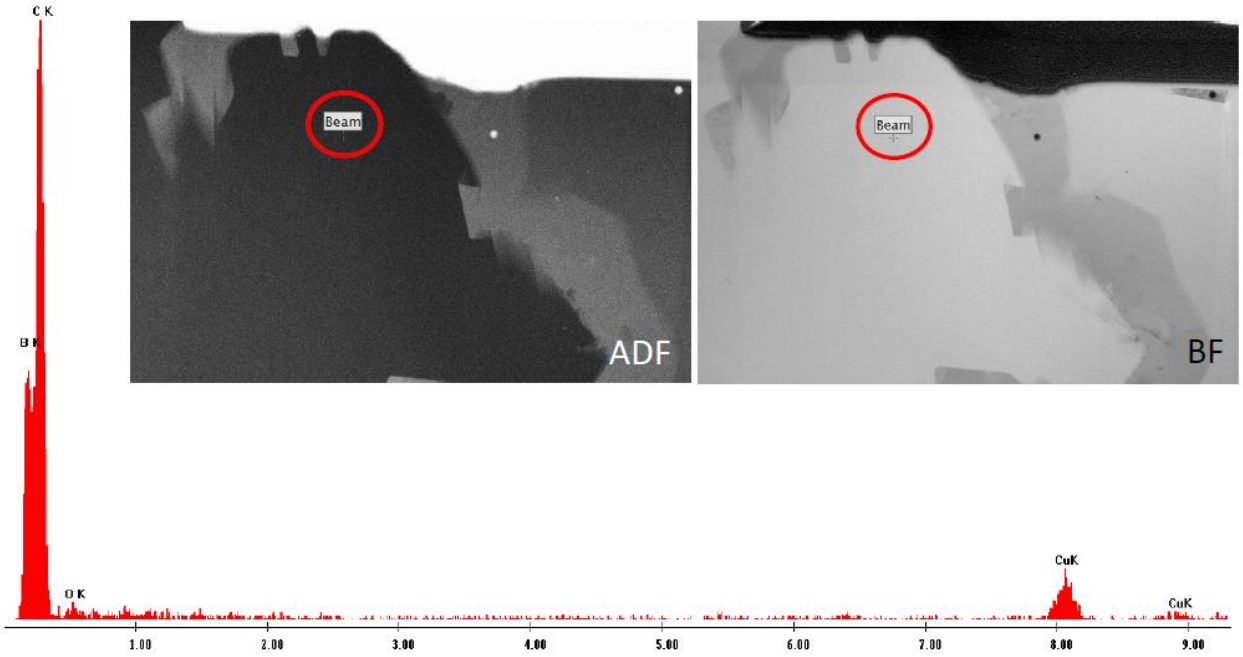
C K
O K
CuK
CuK
Beam
ADF
Beam
BF
1.00
2.00
3.00
4.00
5.00
6.00
7.00
8.00
9.00

E

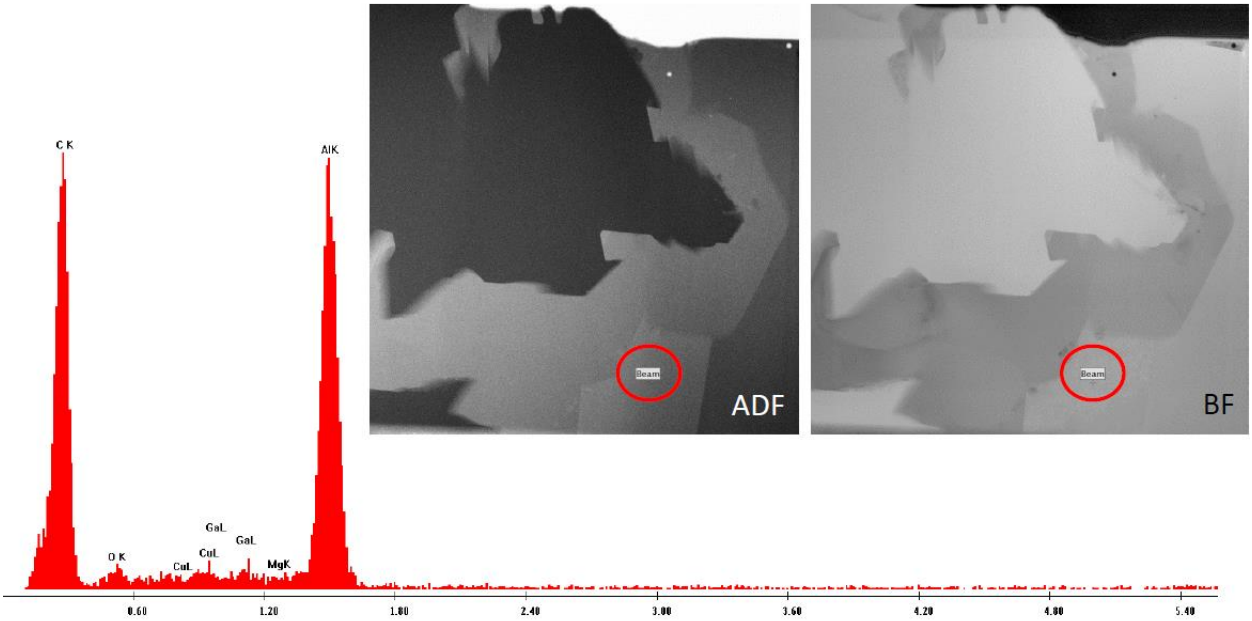
C K
O K
AlK
CuL
CuL
GaL
GaL
MgK
Beam
ADF
Beam
BF
0.60
1.20
1.80
2.40
3.00
3.60
4.20
4.80
5.40

B.2 He-4

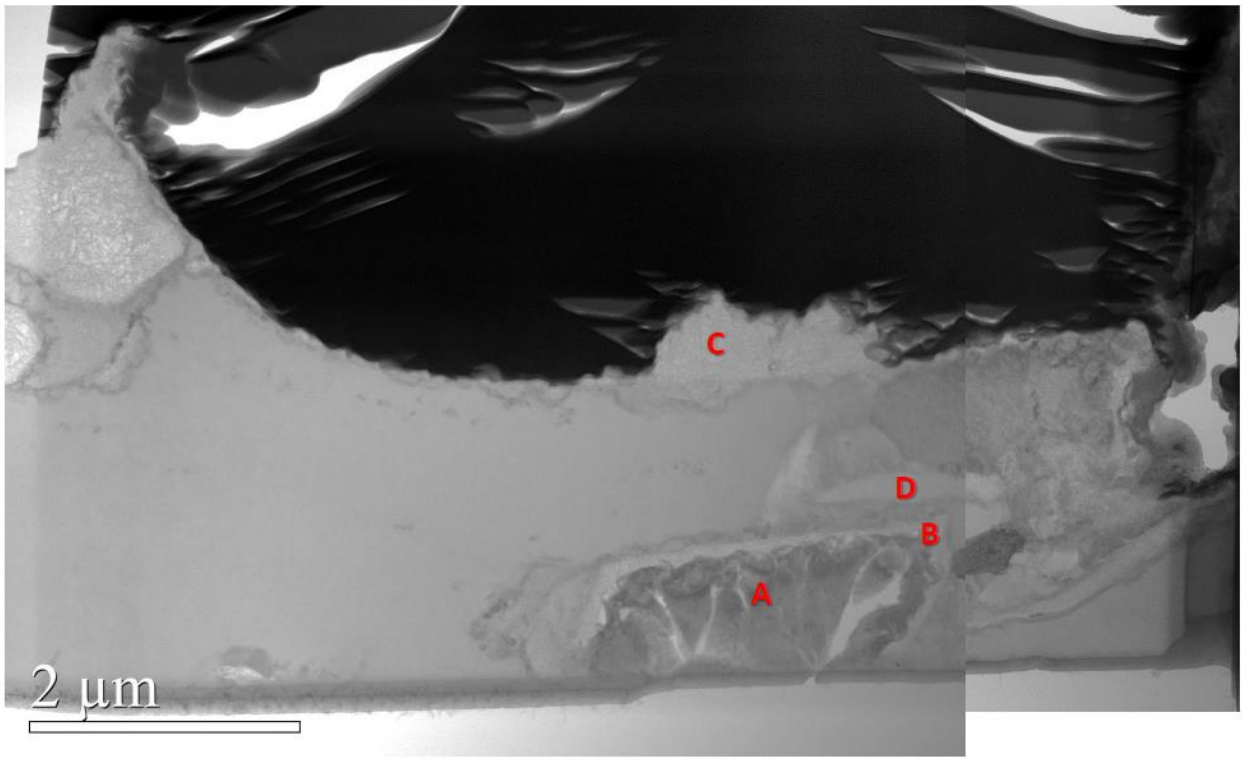
C
D
B
A
2 µm

BF

A

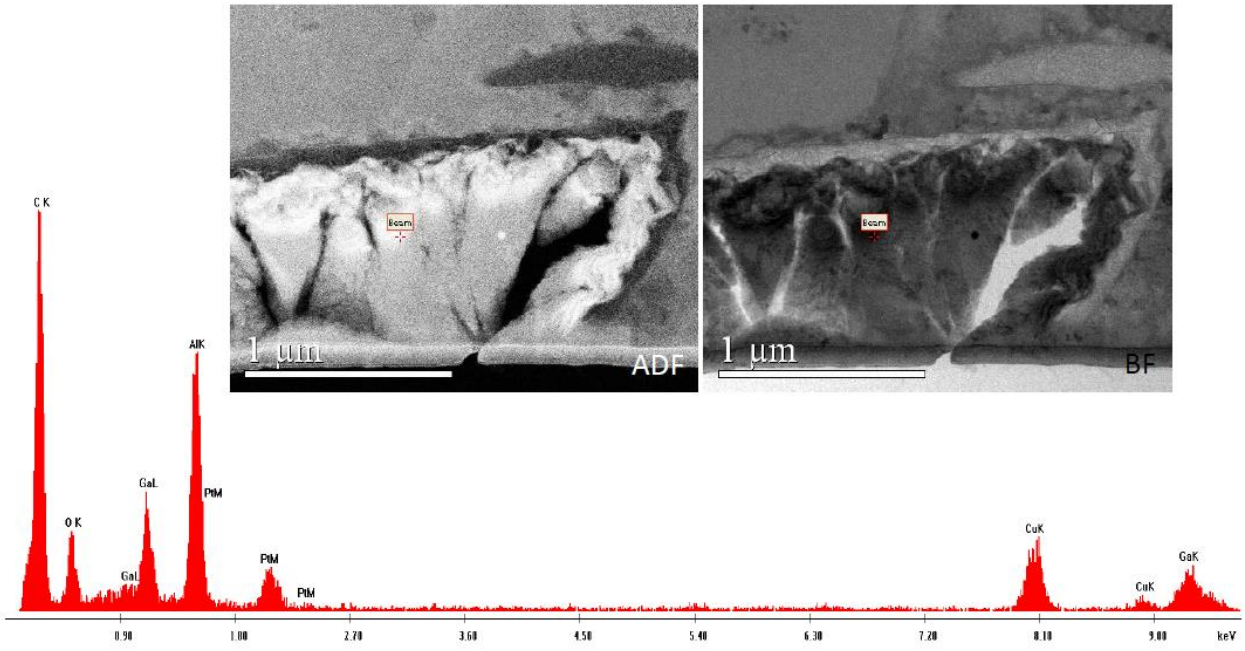
1 µm
ADF
Beam
1 µm
BF
Beam
C K
O K
GaL
GaL
AlK
PtM
PtM
PtM
CuK
CuK
GaK
0.90
1.80
2.70
3.60
4.50
5.40
6.30
7.20
8.10
9.00
keV

B

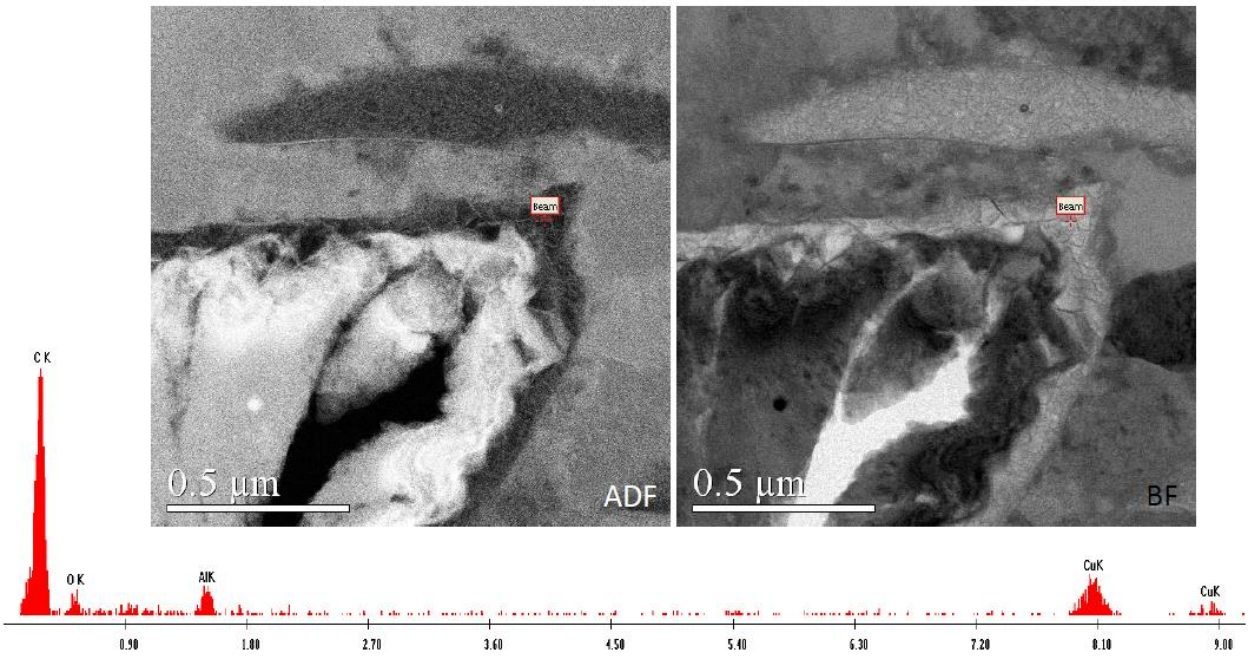
Beam
0.5 µm
ADF
Beam
0.5 µm
BF
C K
O K
Al K
Cu K
Cu K
0.90
1.80
2.70
3.60
4.50
5.40
6.30
7.20
8.10
9.00

C

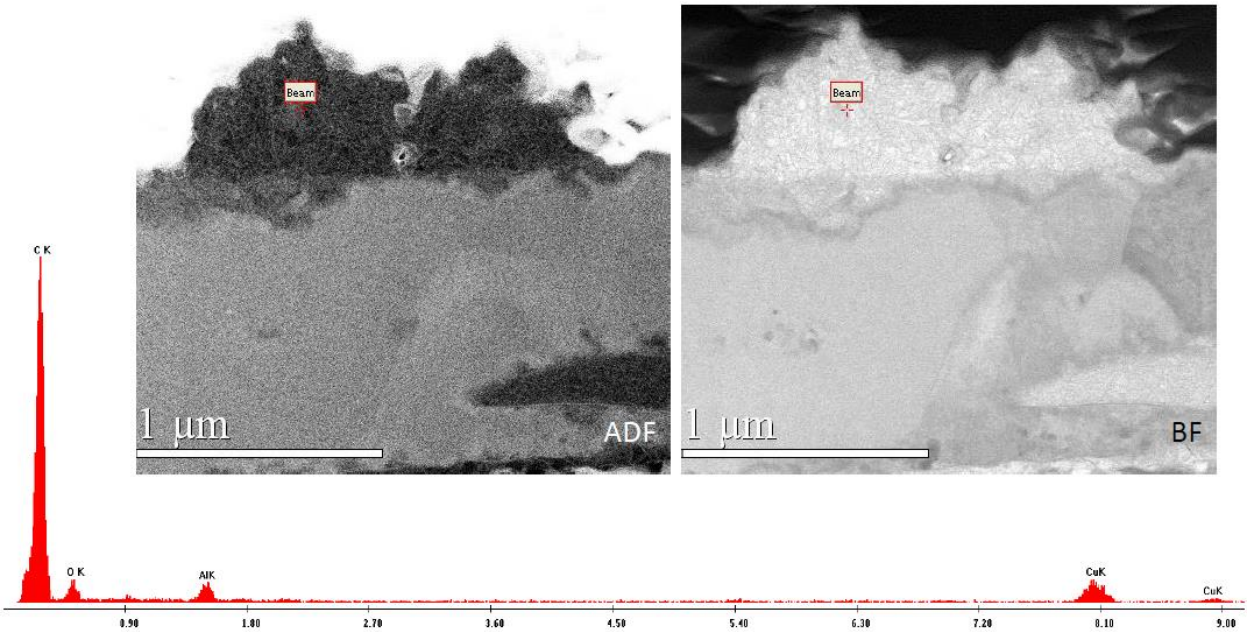
Beam
1 µm
ADF
Beam
1 µm
BF
C K
O K
Al K
Cu K
Cu K
0.90
1.80
2.70
3.60
4.50
5.40
6.30
7.20
8.10
9.00

D

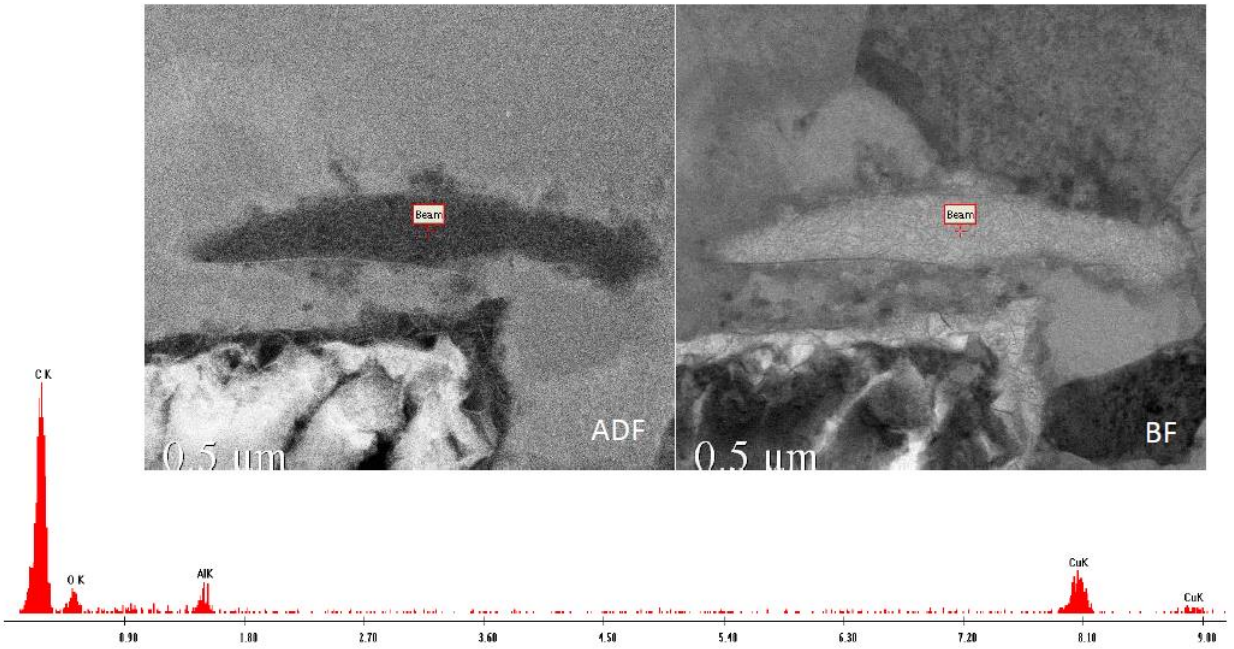
Beam
ADF
0.5 µm
Beam
BF
0.5 µm
C K
O K
Al K
Cu K
Cu K
0.90
1.80
2.70
3.60
4.50
5.40
6.30
7.20
8.10
9.00

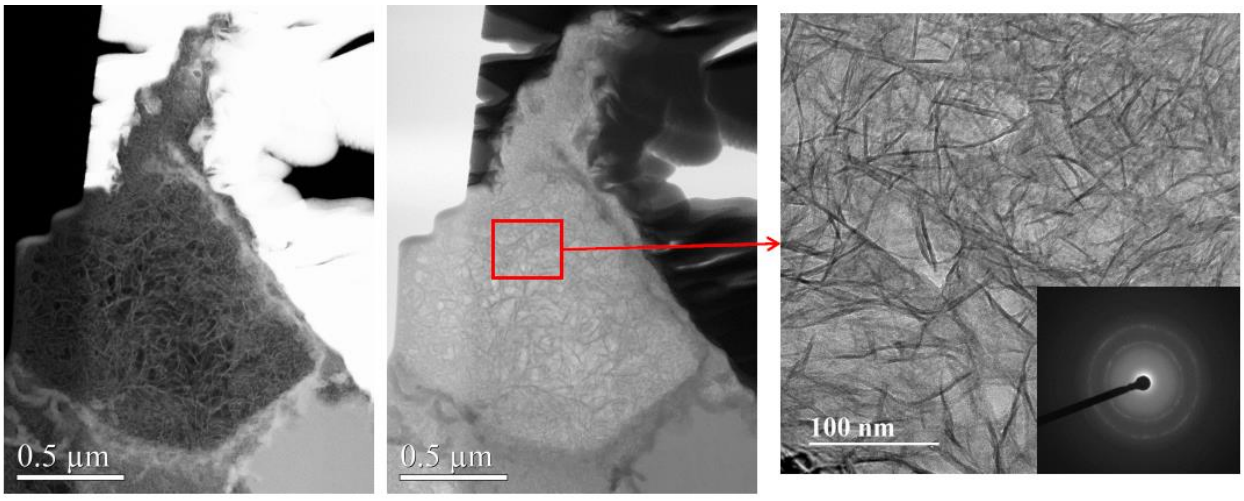
0.5 µm
0.5 µm
100 nm

ADF BF

Appendix C

EDS Results

C.1 C101-570-50

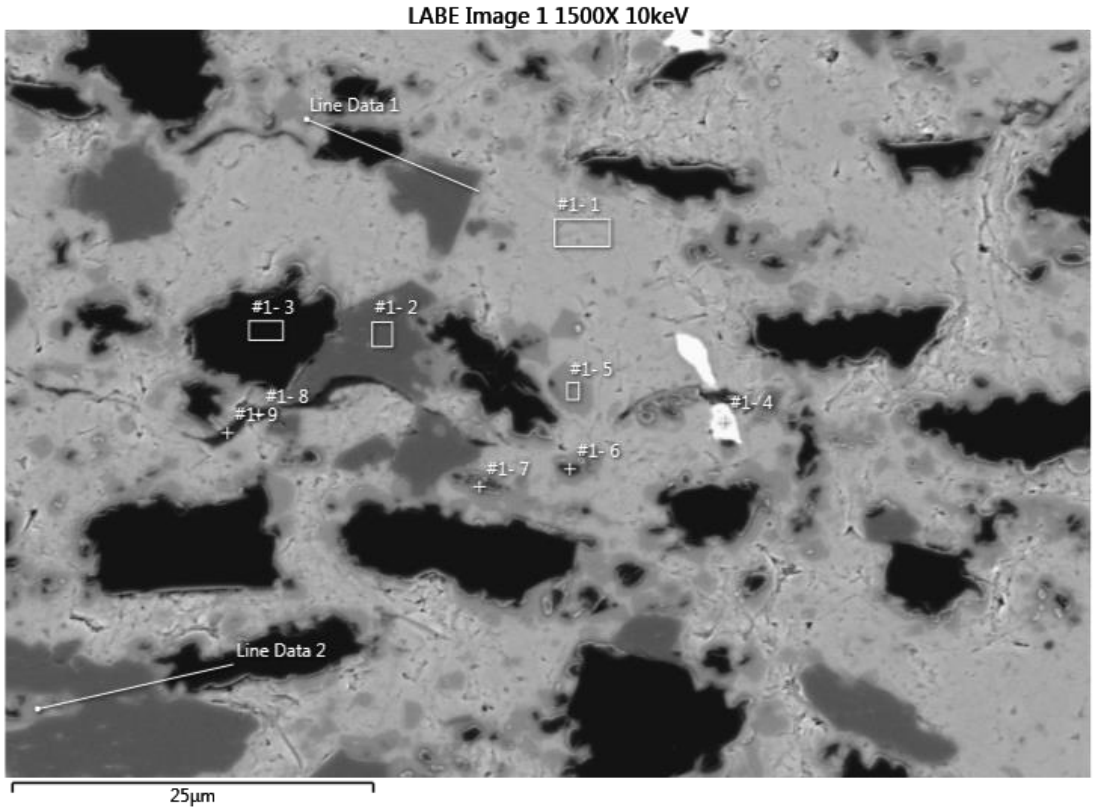

Result Type	Atomic %									
Spectrum Label	B	C	N	O	Mg	Al	Si	Fe	Ni	Total
#1- 1	0.00	0.00	0.00	2.23	0.09	97.60	0.07	0.00	0.00	100.00
#1- 2	61.09	4.17	0.00	0.62	0.03	34.10	0.00	0.00	0.00	100.00
#1- 3	68.64	31.05	0.00	0.13	0.00	0.10	0.02	0.04	0.02	100.00
#1- 4	0.00	0.00	0.00	4.18	0.11	68.18	0.21	26.11	1.20	100.00
#1- 5	0.00	17.57	0.00	1.56	0.07	80.66	0.14	0.00	0.00	100.00
#1- 6	69.40	17.61	0.00	0.58	0.00	12.34	0.07	0.00	0.00	100.00
#1- 7	67.62	15.88	0.00	0.47	0.01	15.97	0.05	0.00	0.00	100.00
#1- 8	53.93	0.00	25.25	0.94	0.03	19.82	0.03	0.00	0.00	100.00
#1- 9	55.95	0.00	23.97	0.63	0.00	19.44	0.01	0.00	0.00	100.00

Line Data 1

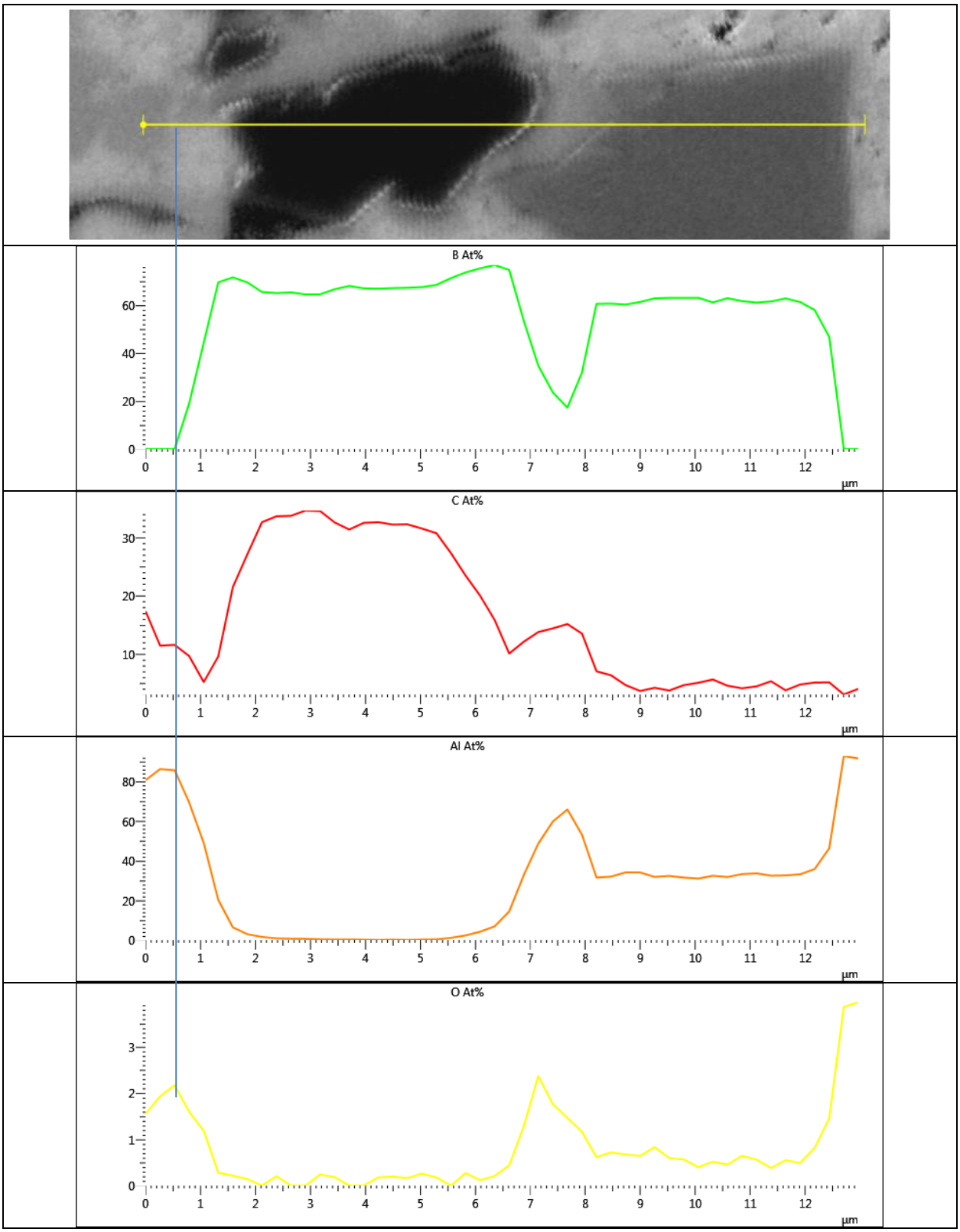
B At%
C At%
Al At%
O At%
µm

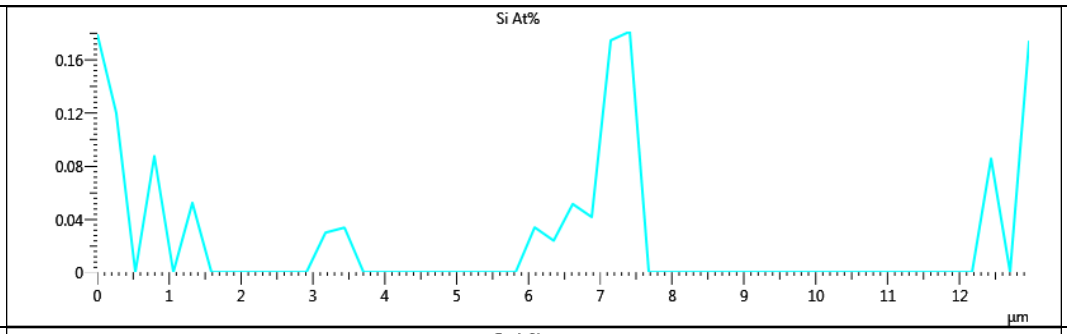
Si At%
0.16
0.12
0.08
0.04
0
0 1 2 3 4 5 6 7 8 9 10 11 12
µm

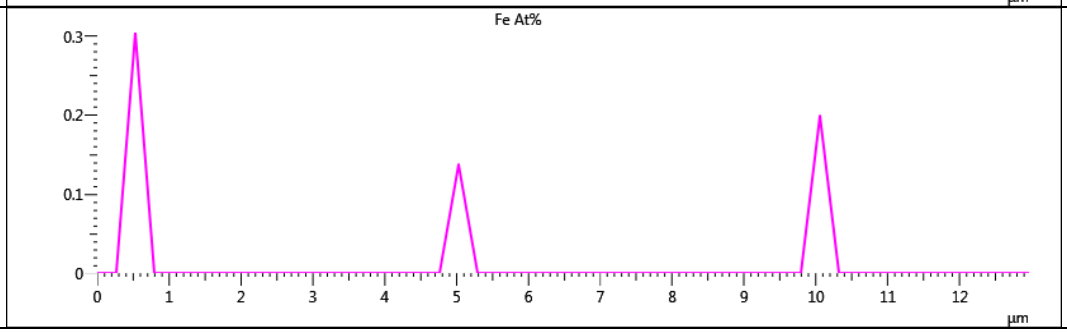
Fe At%
0.3
0.2
0.1
0
0 1 2 3 4 5 6 7 8 9 10 11 12
µm

Line Data 2

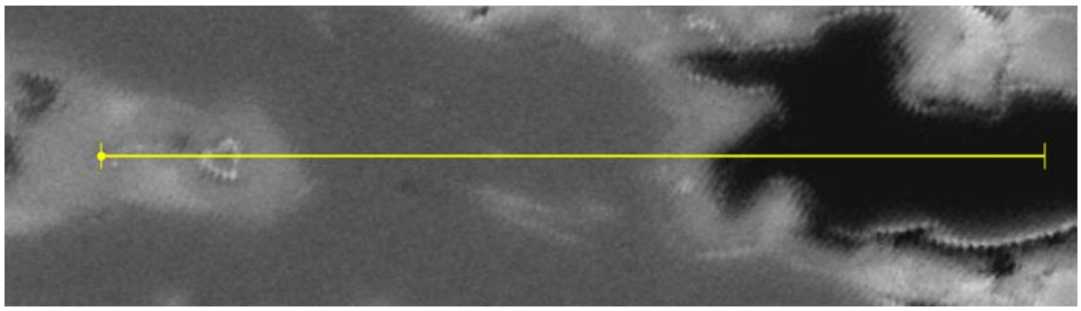

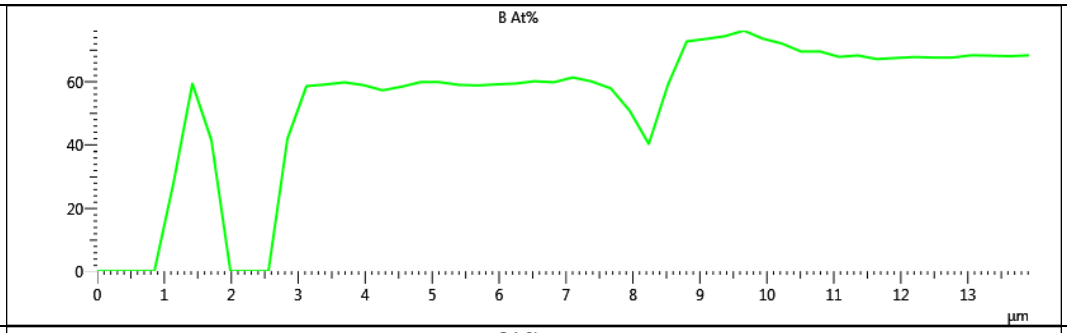
B At%
60
40
20
0
0 1 2 3 4 5 6 7 8 9 10 11 12 13
µm

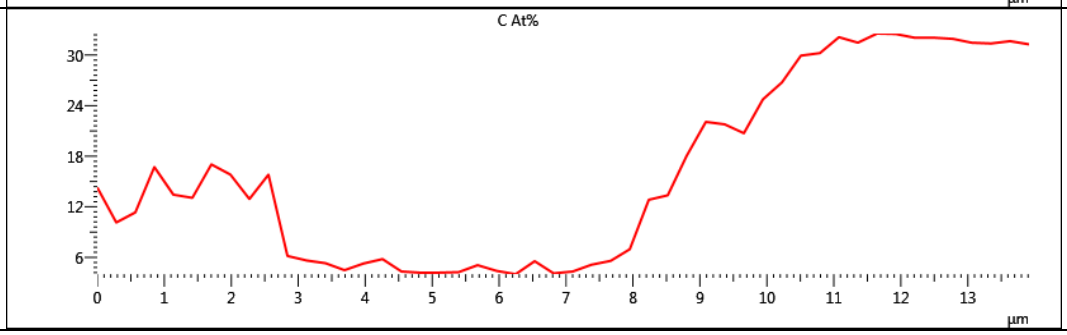
C At%
30
24
18
12
6
0 1 2 3 4 5 6 7 8 9 10 11 12 13
µm

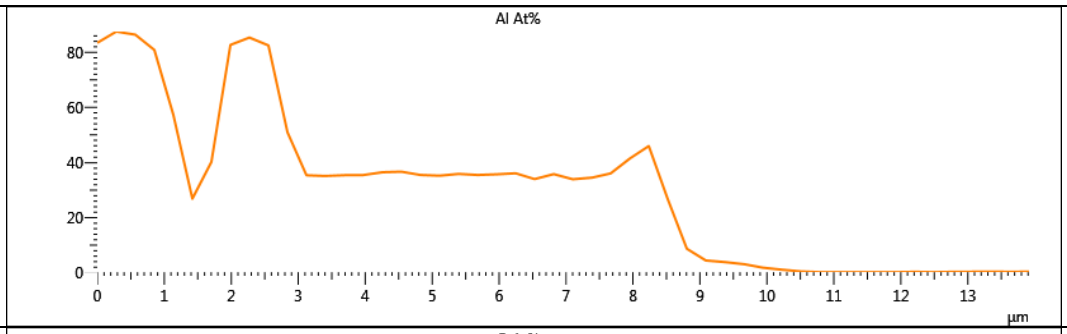
Al At%
80
60
40
20
0
0 1 2 3 4 5 6 7 8 9 10 11 12 13
µm

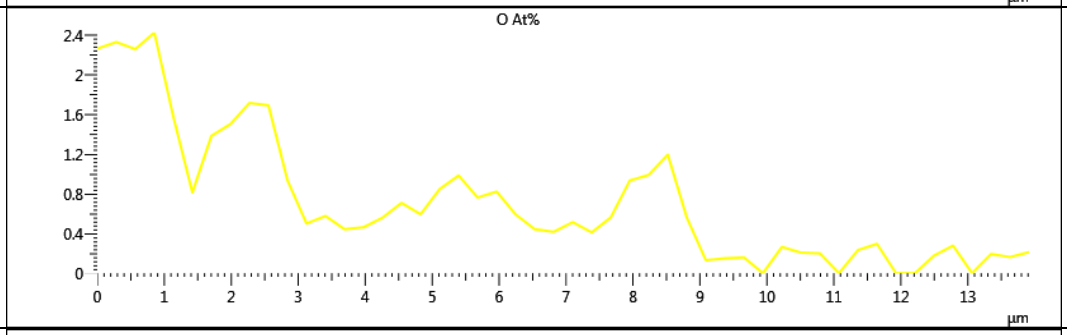
O At%
2.4
2
1.6
1.2
0.8
0.4
0
0 1 2 3 4 5 6 7 8 9 10 11 12 13
µm

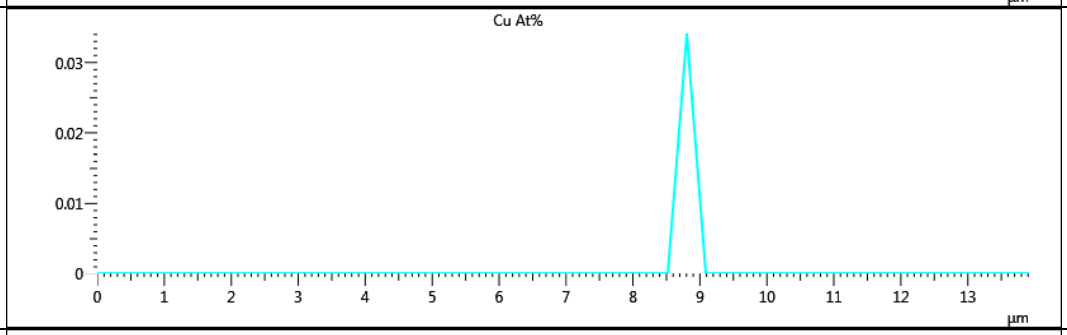
Cu At%
0.03
0.02
0.01
0
0 1 2 3 4 5 6 7 8 9 10 11 12 13
µm

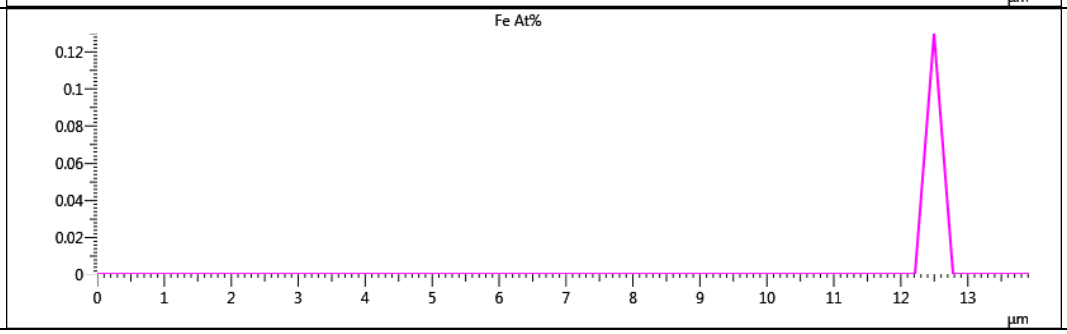
Fe At%
0.12
0.1
0.08
0.06
0.04
0.02
0
0 1 2 3 4 5 6 7 8 9 10 11 12 13
µm

LABE Image 2 2kX 10keV

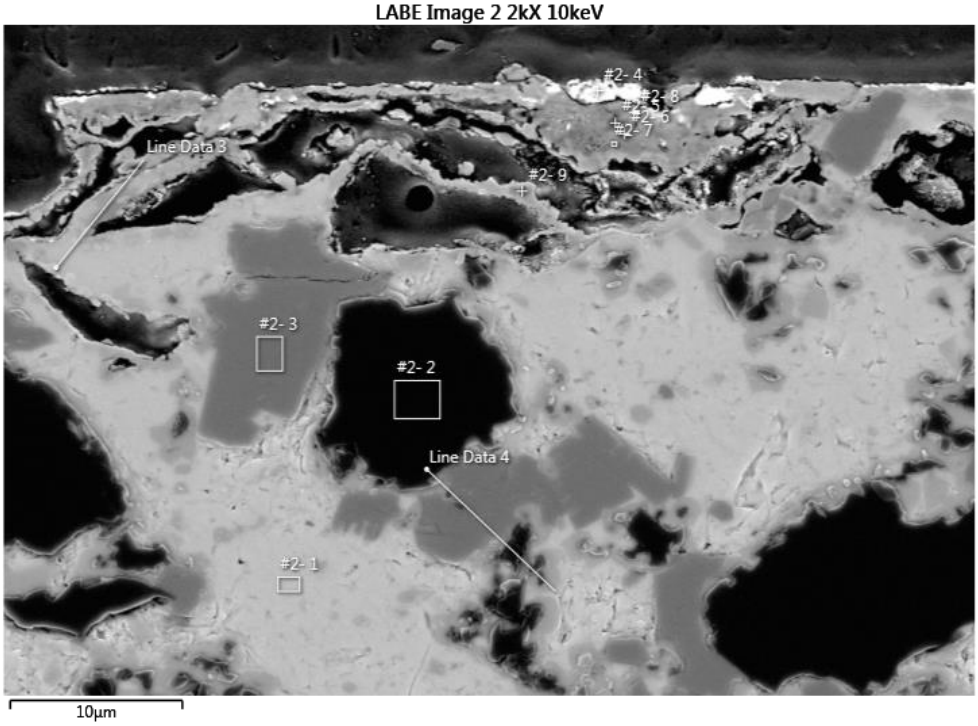

Result Type	Atomic %								
Spectrum Label	B	C	O	Al	Si	Cr	Fe	Mo	Total
#2- 1	0.00	0.00	1.85	98.15	0.00	0.00	0.00	0.00	100.00
#2- 2	68.01	31.92	0.00	0.07	0.00	0.00	0.00	0.00	100.00
#2- 3	62.65	4.68	0.46	32.21	0.00	0.00	0.00	0.00	100.00
#2- 4	0.00	9.10	52.03	3.45	0.25	1.72	33.44	0.00	100.00
#2- 5	0.00	41.57	37.74	20.24	0.00	0.00	0.00	0.46	100.00
#2- 6	0.00	18.04	48.42	32.87	0.00	0.00	0.66	0.00	100.00
#2- 7	0.00	16.56	50.07	32.18	0.40	0.00	0.79	0.00	100.00
#2- 8	0.00	17.39	47.95	32.28	0.00	0.00	2.39	0.00	100.00
#2- 9	0.00	36.17	42.25	21.19	0.39	0.00	0.00	0.00	100.00

Line Data 3

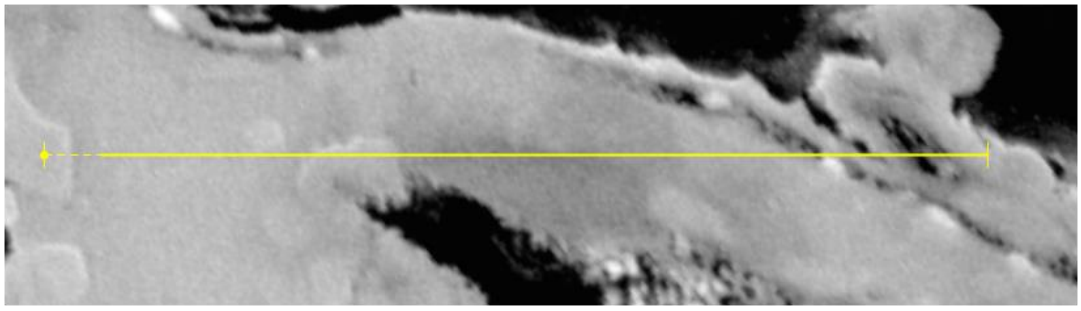

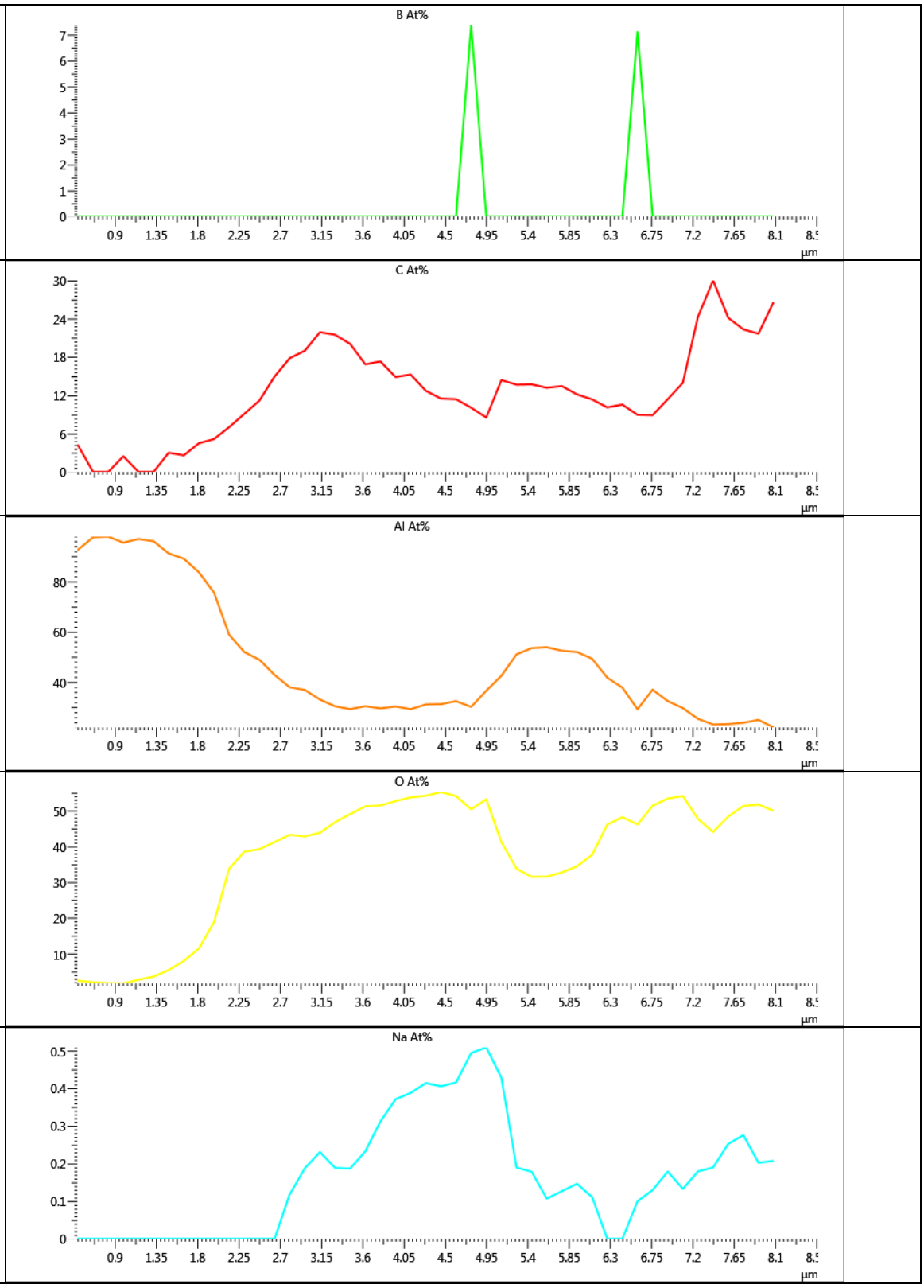
B At%
C At%
Al At%
O At%
Na At%
0.9 1.35 1.8 2.25 2.7 3.15 3.6 4.05 4.5 4.95 5.4 5.85 6.3 6.75 7.2 7.65 8.1
µm

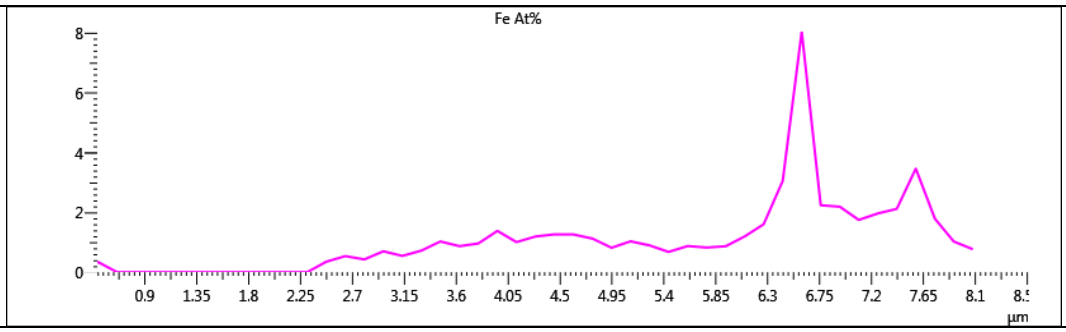
Fe At%
8
6
4
2
0
0.9
1.35
1.8
2.25
2.7
3.15
3.6
4.05
4.5
4.95
5.4
5.85
6.3
6.75
7.2
7.65
8.1
µm

Line Data 4

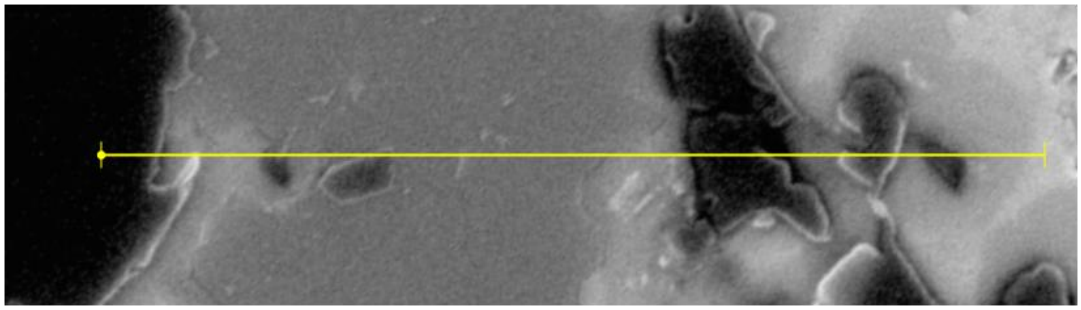

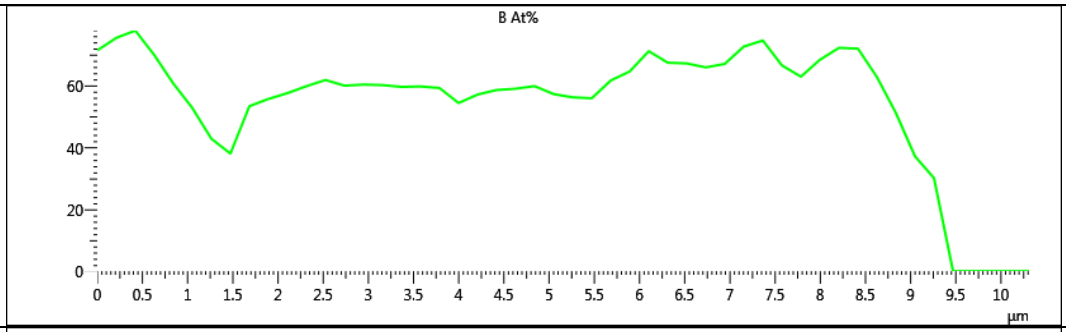
B At%
60
40
20
0
0
0.5
1
1.5
2
2.5
3
3.5
4
4.5
5
5.5
6
6.5
7
7.5
8
8.5
9
9.5
10
µm

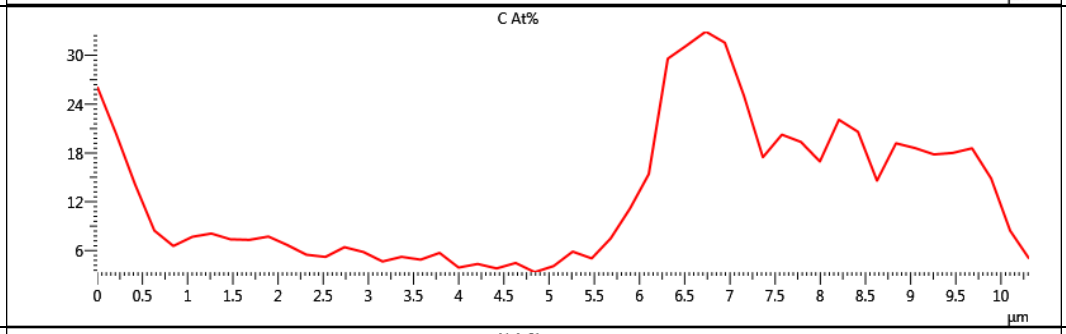
C At%
30
24
18
12
6
0
0.5
1
1.5
2
2.5
3
3.5
4
4.5
5
5.5
6
6.5
7
7.5
8
8.5
9
9.5
10
µm

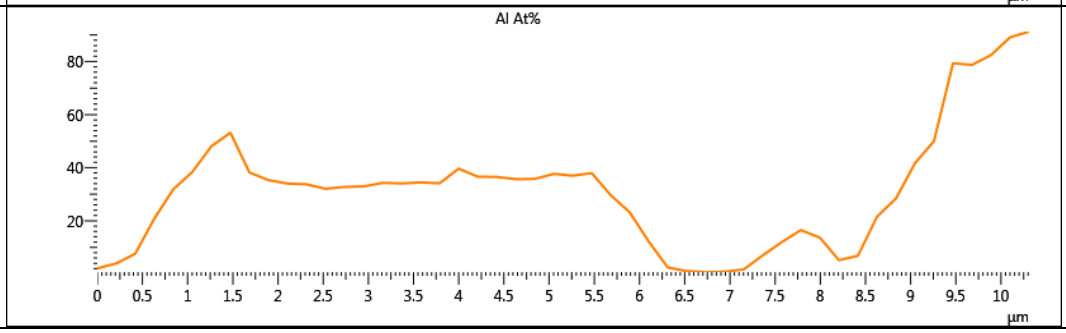
Al At%
80
60
40
20
0
0.5
1
1.5
2
2.5
3
3.5
4
4.5
5
5.5
6
6.5
7
7.5
8
8.5
9
9.5
10
µm

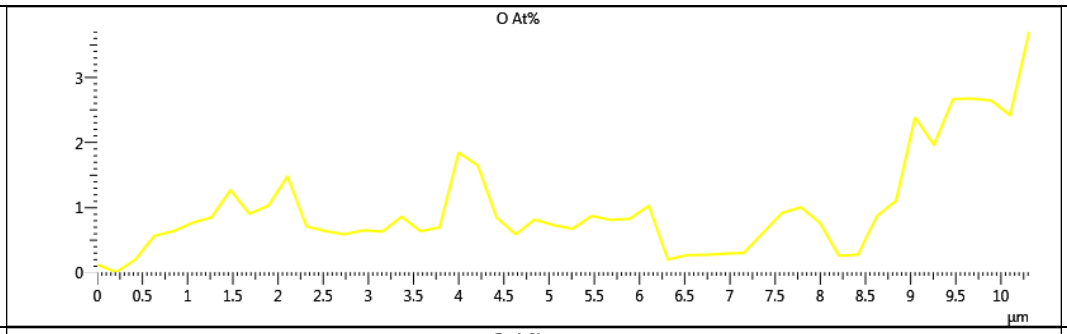
O At%
3
2
1
0
0 0.5 1 1.5 2 2.5 3 3.5 4 4.5 5 5.5 6 6.5 7 7.5 8 8.5 9 9.5 10
µm

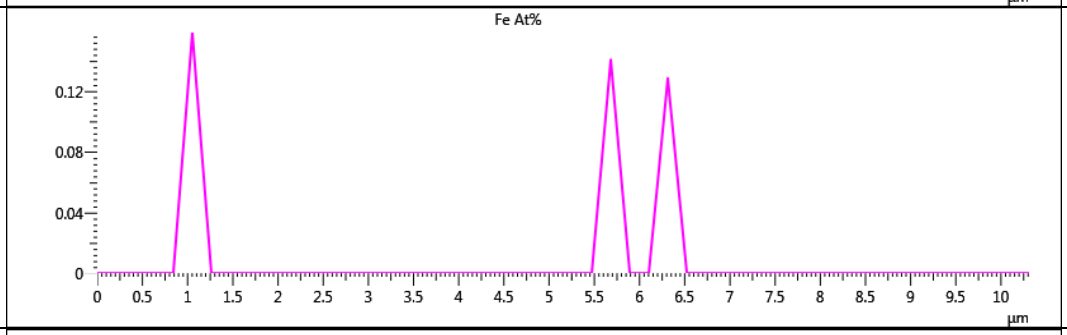
Fe At%
0.12
0.08
0.04
0
0 0.5 1 1.5 2 2.5 3 3.5 4 4.5 5 5.5 6 6.5 7 7.5 8 8.5 9 9.5 10
µm

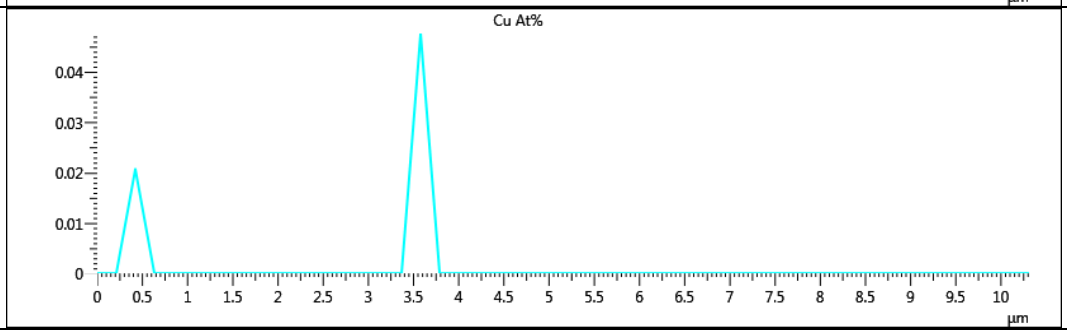
Cu At%
0.04
0.03
0.02
0.01
0
0 0.5 1 1.5 2 2.5 3 3.5 4 4.5 5 5.5 6 6.5 7 7.5 8 8.5 9 9.5 10
µm

C.2 L75-400-143

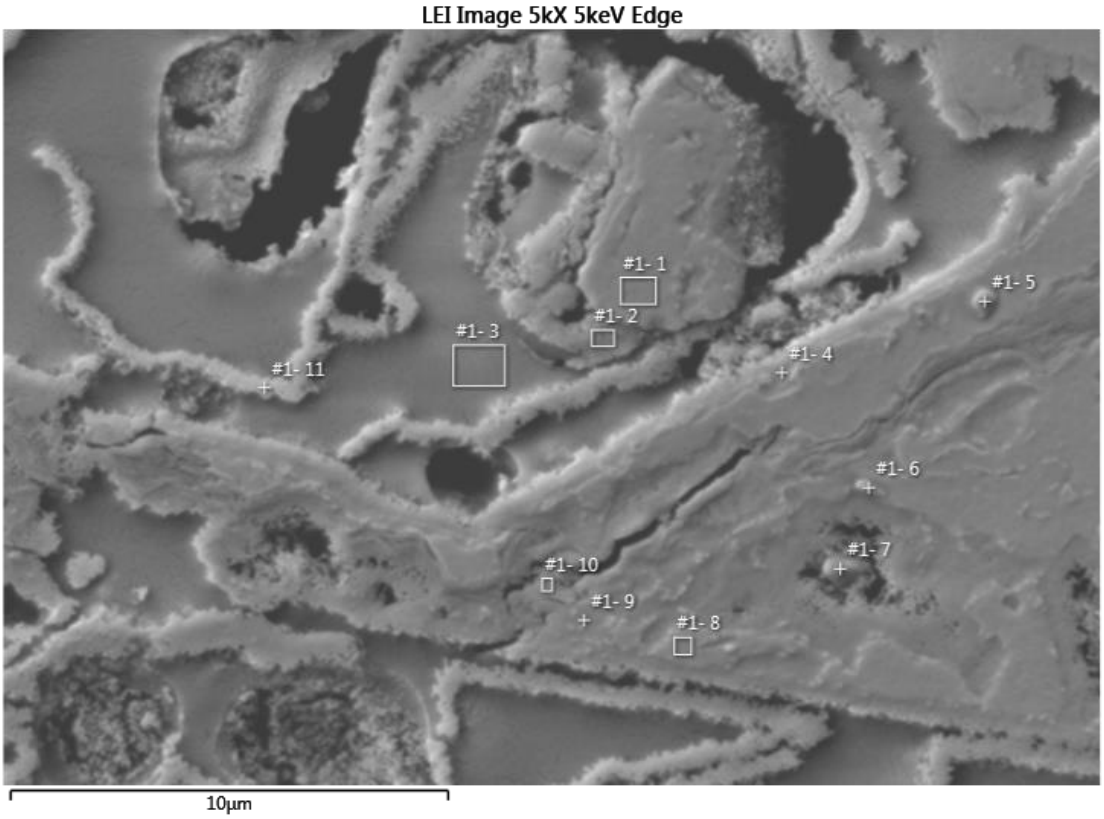

Result Type	Atomic %												
Spectrum Label	B	C	O	Na	Mg	Al	Si	Cl	Fe	Ni	Cu	Mo	Total
#1- 1	0.00	21.45	2.60	0.00	0.00	75.95	0.00	0.00	0.00	0.00	0.00	0.00	100.00
#1- 2	0.00	48.87	22.71	0.00	0.00	24.53	1.41	0.48	0.70	0.00	0.00	1.30	100.00
#1- 3	0.00	90.93	7.41	0.00	0.00	0.66	0.00	0.58	0.00	0.00	0.00	0.41	100.00
#1- 4	0.00	50.48	29.05	0.00	0.00	19.33	0.60	0.17	0.37	0.00	0.00	0.00	100.00
#1- 5	0.00	19.00	5.51	0.00	0.00	75.20	0.00	0.00	0.30	0.00	0.00	0.00	100.00
#1- 6	0.00	24.36	28.15	0.14	0.00	46.24	0.30	0.00	0.39	0.00	0.00	0.43	100.00
#1- 7	0.00	80.15	11.25	0.00	0.18	6.83	0.42	0.22	0.61	0.00	0.00	0.34	100.00
#1- 8	0.00	33.35	35.21	0.00	0.00	30.01	0.70	0.00	0.33	0.00	0.00	0.39	100.00
#1- 9	0.00	62.27	22.49	0.17	0.43	12.59	0.77	0.19	0.56	0.00	0.00	0.53	100.00
#1- 10	0.00	60.57	21.14	0.22	0.67	15.15	0.72	0.31	0.62	0.00	0.00	0.60	100.00
#1- 11	0.00	90.70	7.88	0.00	0.00	0.68	0.00	0.58	0.16	0.00	0.00	0.00	100.00

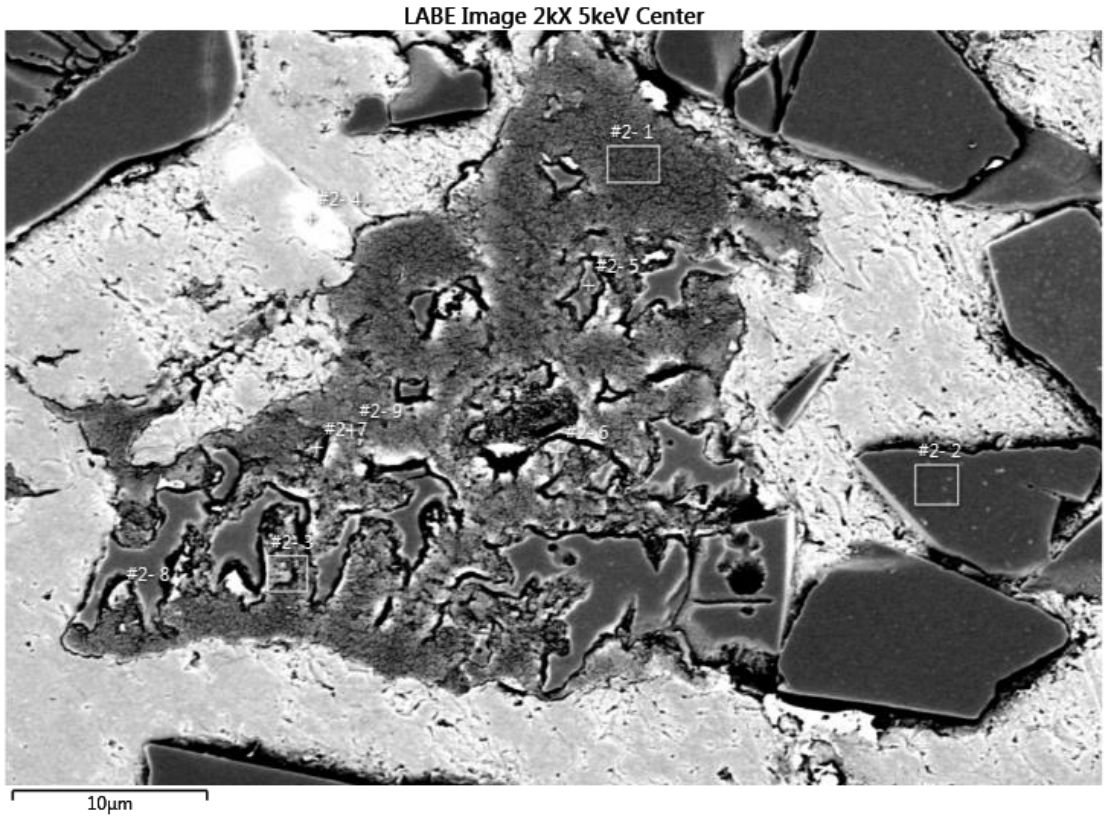

Result Type	Atomic %												
Spectrum Label	B	C	O	Na	Mg	Al	Si	Cl	Fe	Ni	Cu	Mo	Total
#2- 1	0.00	93.11	5.49	0.00	0.00	0.39	0.00	0.63	0.00	0.00	0.00	0.38	100.00
#2- 2	0.00	86.94	7.38	0.00	0.00	5.68	0.00	0.00	0.00	0.00	0.00	0.00	100.00
#2- 3	0.00	90.23	7.59	0.00	0.00	0.55	0.00	0.79	0.30	0.00	0.00	0.54	100.00
#2- 4	0.00	12.91	3.56	0.00	0.00	56.37	3.88	0.00	21.15	0.56	0.71	0.85	100.00
#2- 5	0.00	70.29	14.36	0.00	0.00	8.90	0.00	0.00	0.00	0.00	0.00	6.45	100.00
#2- 6	0.00	80.56	13.24	0.72	0.00	2.73	0.99	0.72	1.04	0.00	0.00	0.00	100.00
#2- 7	0.00	90.31	7.42	0.00	0.00	0.82	0.00	0.73	0.30	0.00	0.00	0.42	100.00
#2- 8	0.00	76.63	8.00	0.77	0.00	3.26	2.01	5.64	1.00	0.00	0.00	2.69	100.00
#2- 9	0.00	91.75	7.32	0.00	0.00	0.00	0.00	0.70	0.24	0.00	0.00	0.00	100.00

Appendix D

NDP Results

Material	Sample ID	Test Conditions	Distance from leading edge (mm)	Count Rate (cps)	Total Counts	Margin of Error at 95% confidence (%)
Boral	Boral Thin Std.	As - received	0.5	2.342	19598	0.700
			1.5	3.331	26497	0.602
			10	3.201	22784	0.649
			12	3.363	22550	0.653
			21.5	3.527	29518	0.570
	L75-400-89	400°C 89.5 days	1	0.289	847	3.367
			4	10.613	13342	0.848
			7	10.519	13196	0.853
			11	11.026	27666	0.589
			17	10.472	13157	0.854
			20	10.479	13172	0.854
			22.8	4.161	15255	0.873
	L75-570-21	570°C 21 days	1	0.285	1197	2.833
			6	3.422	10037	0.978
			11	9.683	32248	0.546
			12	9.859	33027	0.539
	Boral Thick Std.	As - received	1	12.467	36531	0.513
			3	13.01	43553	0.470
			5	13.072	38260	0.501
			9.5	11.704	39178	0.495
			11.5	11.876	34803	0.525
			13.5	10.818	36223	0.515
			18	11.268	37734	0.504
			20	10.901	31966	0.548
			22	11.068	69529	0.372
	L135-300-163	300°C 163 days	1	14.959	65725	0.382
			2	14.37	42093	0.478
			6	15.905	53255	0.425
			12	14.48	48473	0.445
	L135-400-89	400°C 89.5 days	1	6.288	18457	0.721
			2	10.064	33725	0.534
			6	12.096	35450	0.520
			10	12.011	40258	0.488
			19.5	2.716	9095	1.028
Bortec	Bortec Thin Std.	As - received	1	2.045	6852	1.184
			2	3.772	12628	0.872
			4	3.494	10245	0.968
			6	3.345	11212	0.926
			8	3.406	9977	0.981
			10	3.250	10895	0.939
			12	3.299	11055	0.932

			14	3.107	9106	1.027
			16	3.072	10301	0.966
			18	3.175	9293	1.017
			20	3.064	10269	0.967
			22	1.612	5458	1.327
	C75-570-50	570°C 50 days	1	0.202	929	3.215
			3	3.099	12966	0.861
			7	4.519	20808	0.679
			11	4.614	47695	0.449
	Bortec Thick Std.	As - received	1	4.263	24963	0.620
			3	5.053	27475	0.591
			11	5.573	30293	0.563
			15	5.300	31046	0.556
			19	4.220	22968	0.647
			21	3.891	30941	0.557
	Bortec Thick Std. Confirm	As - received	2	5.576	21019	0.676
			12	5.8	19425	0.703
	C101-570-50 (1mm aperture)	570°C 50 days	10	1.772	13836	0.833
			10	1.845	13900	0.831
	C101-570-50A	570°C 50 days	9	7.239	24227	0.630
			18	7.574	86052	0.334
	C101-570-50B	570°C 50 days	1	7.520	34693	0.527
			2	7.502	31402	0.553
			4	7.399	34079	0.531
			7	7.501	31394	0.553
			10	7.424	34184	0.530
			12	7.625	31905	0.549
			14	7.521	34620	0.527
			16	7.515	31478	0.552
			18	7.428	34194	0.530

References

References

1. *Good Practices for Water Quality Management in Research Reactors and Spent Fuel Storage Facilities*. 2011, IAEA.
2. Batra, I.P. and L. Kleinman, *Chemisorption of Oxygen on Aluminum Surfaces.* Journal of Electron SPectroscopy and Related Phenomena, 1984. 33: p. 175-241.
3. Hodgson, A. and S. Haq, *Water adsorption and the wetting of metal surfaces.* Surface Science Reports, 2009. 64: p. 381-451.
4. Ashar, H. and G. Degrassi. *Design and analysis of free-standing spent fuel racks in nuclear power plants: An overview*. in *10 International Conference on Structural Mechanics in Reactor Technology*. 1989. Anaheim, CA.
5. Andrews, A., *Nuclear Fuel reprocessing: U.S. Policy Development*. 2008, Congressional Research Service.
6. *Nuclear Waste Policy Act of 1982*, U.S. Congress, Editor. 1982.
7. *Department of Energy FY2011 Congressional Budget Request: Budget Highlights* D.o. Energy, Editor. 2010.
8. *Safety and Security of Commercial Spent Nuclear Fuel Storage: Public Report*. 2006, National Academy of Sciences: Washington D.C.
9. Wagner, J.C. and C.V. Parks, *A Critical Review of the Practice of Equating the Reactivity of Spent Fuel to Fresh Fuel in Burnup Credit Criticality Safety Analyses for PWR Spent Fuel Pool Storage*. 2000, Oak Ridge National Laboratory.
10. Kopp, L., *Memo to Timothy Collins: Guidance on the regulatory requirements for criticality analysis of fuel storage at Lighter-water Reactor Power Plants*. 1998, NRC.
11. Alvarez, R., et al., *Reducing the Hazards from Stored Spent Power-Reactor Fuel in the United States.* Science and Global Security, 2003. 11: p. 1-51.
12. Alvarez, R., et al., *Response by the Authors to the NRC Review of "Reducing the Hazards from Spent Power-Reactor Fuel in the United States".* Science and Global Security, 2003. 11: p. 213-223.
13. Wang, D., et al., *Study of Fukushima Daiichi Nuclear Power Station Unit 4 Spent-Fuel Pool.* Nuclear Technology, 2012. 180: p. 205-215.
14. Hughes, T.G. and T.P. Lin, *Thermal Cooling Limits of Sabotaged Spent Fuel Pools*. 2010, The Pennsylvania State University.
15. Alvarez, R., *What about the spent fuel.* Bulletin of the Atomic Scientists, 2002: p. 45-47.
16. Sailor, V.L., et al., *Severe Accidents in Spent Fuel Pools in Support of Generic Safety Issue 82*. 1987, Brookhaven National Laboratory.
17. Olander, D.R. and W. Wang, *Thermodynamics of the U-O and Zr systems and application to analysis of fuel liquefaction during severe accidents in light water reactors.* Journal of Nuclear Materials, 1997. 247: p. 258-264.

18. Rigby, D.B., *Evaluation of the Technical Basis for Extended Dry Storage and Transportaiton of Used Nuclear Fuel*. 2010, United States Nuclear Waste Technical Review Board.
19. Commission, U.S.N.R., *Cladding Considerations for the Transportation and Storage of Spent Fuel*. 2003, U.S. Nuclear Regulatory Commission.
20. *Overall Requirements*, in *10 CFR 72.122*, U.S.C.o.F. Regulations, Editor. 2001.
21. *Specific requirements for spent fuel storage cask approval and fabrication*, in *10CFR 72.236*, U.S.C.o.F. Regulations, Editor. 2011.
22. ASTM, *Standard Guide for Drying Behavior of Spent Nuclear Fuel*. 2008.
23. *Final Safety Analysis Report on the HI-STORM FW System*. 2011, Holtec International.
24. Kok, K.D., *Nuclear Engineering Handbook*. 2009, Boca Raton, FL: Taylor and Francis Group.
25. *Licensing Requirements for the Independent Storage of Spent Nuclear Fuel, High-Level Radioactive Waste, and Reactor-Related Greater Than Class C Waste*, in *10 CFR 72* 2012.
26. *Handbook on Neutron Absorber Materials for Spent Nuclear Fuel Applications*. 2005, EPRI: Palo Alto, CA.
27. *Bortec Qualification Program for Nuclear Fuel Storage Applications*. 2003, Northeast Technology Corp.
28. Rosenthal, J.E., *Memo to Carl J. Paperiello: Results of Initial Screening of Generic Issue 196, "Boral Degradation"*. 2004.
29. Balakrishnarajan, M.M., P.D. Pancharatna, and R. Hoffman, *Structure and bonding in boron carbide: The invincibility of imperfections.* New Journal of Chemistry, 2007. 31: p. 473-485.
30. Konovalikhin, S.V. and V.I. Ponomarev, *Carbon in boron carbide: The crystal structure of B11.4C3.6.* Russian Journal of Inorganic Chemistry, 2009. 54(2): p. 197-203.
31. Domnich, V., et al., *Boron Carbide: Structure, Properties, and Stability under Stress.* Journal of the American Ceramic Society, 2011. 94(11): p. 3605-3628.
32. Saal, J.E., S. Shang, and Z.-K. Liu, *The structural evolution of boron carbide via ab initio calculations.* Applied Physics Letters, 2007. 91(231915).
33. Vast, N., et al., *Atomic structure and vibrational properties of icosahedral alpha-boron and B4C boron carbide.* Computational Materials Science, 2000. 17: p. 127-132.
34. Thevenot, F., *Boron Carbide - A Comprehensive Review.* Journal of the European Ceramic Society, 1990. 6: p. 205-225.
35. Konings, J.M., ed. *Comprehensive Nuclear Materials*. 2012, Elsevier: Amsterdam, The Netherlands.
36. Singh, B.N. and T. Deffers, *Nucleation of helium bubbles on dislocations, dislocation networks, and dislocations in grain boundaries during 600 MeV proton irradiation of aluminum.* Journal of Nuclear Materials, 1984. 125: p. 287-297.
37. Victoria, M. and W.V. Green, *The Temperature Dependence of Void and Bubble Formation and Growth in Aluminum During 600 MeV Proton Irradiation.* Journal of Nuclear Materials, 1984. 122 & 123: p. 737-742.
38. Farrell, K. and J.T. Houston, *Suppression of Radiation Damage Microstructure in Aluminum by Trace Impurities.* Journal of Nuclear Materials, 1979. 83: p. 57-66.
39. Houston, J.T. and K. Farrell, *Void Coarsening in High Purity Aluminum During Postirradiation Annealing.* Journal of Nuclear Materials, 1971. 40: p. 225-229.
40. Golosov, O.A. *Corrosion of Aluminum Alloys in Water at Temperatures up to 100°C*. in *31st International Meeting on Reduced Enrichment for Research and Test Reactors*. 2009. Beijing, China.
41. Ismail, Z.H. and H.G. Mohammed, *Effect of prior history on the response of some commercial aluminum alloys to low dose neutron irradiation.* Scripta Metallurgica, 1989. 23: p. 2067-2072.

42. **Jostsons, A., et al., *Defect structure of neutron irradiated boron carbide.* Journal of Nuclear Materials, 1973. 49: p. 136-150.**
43. **Emin, D., *Unusual properties of icosahedral boron-rich solids.* Journal of Solid State Chemistry, 2006. 179: p. 2791-2798.**
44. **Simeone, D., et al., *Contribution of recoil atoms to irradiation damage in absorber materials.* Journal of Nuclear Materials, 1997. 246: p. 206-214.**
45. **Stoto, T., et al., *Swelling and microcracking of boron carbide subjected to fast neutron irradiations.* Journal of Applied Physics, 1990. 68(7): p. 3198-3206.**
46. **Okamoto, H., *Al-Li (Aluminum-Lithium).* Journal of Phase Equilibria and Diffusion, 2012. 33(6): p. 500-501.**
47. **Maruyama, T. and T. Iseki, *Irradiation response and tritium release behavior of boron carbide.* Journal of Nuclear Materials, 1985. 133&134: p. 727-731.**
48. **Inoue, T., T. Onchi, and H. Koyama, *Irradiation Effects of Boron Carbide Used as Control Rod Elements in Fast Breeder Reactors.* Journal of Nuclear Materials, 1978. 74: p. 114-122.**
49. **Hunter, M.S. and P. Fowle, *Natural and Thermally Formed Oxide Films on Aluminum.* Journal of The Electrochemical Society, 1956. 103(9): p. 482.**
50. **Jeurgens, L.P.H., et al., *Growth kinetics and mechanisms of aluminum-oxide films formed by thermal oxidation of aluminum.* Journal of Applied Physics, 2002. 92(3): p. 1649-1656.**
51. **Grove, C.A., J. Judd, and G.S. Ansell, *Investigation of the Aluminium-Aluminium Oxide Reversible Transformation as Observed by Hot Stage Electron Microscopy.* Journal of Materials Science, 1972. 7: p. 393-403.**
52. **Jeurgens, L.P.H., et al., *Structure and morphology of aluminium-oxide films formed by thermal oxidation of aluminium.* Thin Solid Films, 2002. 418: p. 89-101.**
53. **Levin, I. and D. Brandon, *Metastable Alumina Polymorphs: Crystal Structures and Transition Sequences.* Journal of the American Ceramic Society, 1998. 81(8): p. 1995-2012.**
54. **Shimizu, K., et al., *On the Nature of "Easy Paths" for the Diffusion of Oxygen in Thermal Oxide Films on Aluminum.* Oxidation of Metals, 1991. 35(5/6): p. 427-439.**
55. **Grimblot, J. and J.M. Eldridge, *Influence of the Growth Conditions of Al2O3 Passivating Layers on the Corrosion of Aluminum Films in Water.* Journal of The Electrochemical Society, 1981. 128(4): p. 729-731.**
56. **Chen, C., et al., *Measurement of oxide film growth on Mg and Al surfaces over extended periods using XPS.* Surface Science, 1997. 382: p. L652-L657.**
57. **Shreir, L.L. and R.A. Cottis, *Shreir's Corrosion*. Vol. 1. 2010, London: Elsevier.**
58. **Vargel, C., *Corrosion of Aluminium*. 2004, Kidlington, Oxford: Elsevier.**
59. **Birbilis, N., *Corrosion of Aluminum Alloys*. 3rd ed. Corrosion Mechanisms in Theory and Practice, ed. P. Marcus. 2012, Boca Raton, FL: CRC Press.**
60. **Vrublevsky, I., et al., *The study of the volume expansion of aluminum during porous oxide formation at galvanostatic regime.* Applied Surface Science, 2004. 222(1-4): p. 215-225.**
61. **Serebrennikova, I., P. Vanysek, and V.I. Birss, *Characterization of porous aluminum oxide films by metal electrodeposition.* Electrochimica Acta, 1996. 42(1): p. 145-151.**
62. **Palibroda, E., et al., *Aluminum porous oxide growth. On the electric conductivity of the barrier layer.* Thin Solid Films, 1995. 256: p. 101-105.**
63. **Diggle, J.W., T.C. Downie, and C.W. Goulding, *Anodic Oxide Films on Aluminum.* Chemical Reviews, 1969. 69(3): p. 365-405.**
64. **Curioni, M., et al., *Flow modulated ionic migration during porous oxide growth on aluminium.* Electrochimica Acta, 2010. 55: p. 7044-7049.**
65. **Li, Y.Q. and T. Qiu, *Oxidation behaviour of boron carbide powder.* Materials Science and Engineering: A, 2007. 444(1-2): p. 184-191.**

66. Seiler, N., et al., *Investigations on boron carbide oxidation for nuclear reactors safety—General modelling for ICARE/CATHARE code applications.* Nuclear Engineering and Design, 2008. 238(4): p. 820-836.
67. Steinbrück, M., et al., *Oxidation of B4C by steam at high temperatures: New experiments and modelling.* Nuclear Engineering and Design, 2007. 237(2): p. 161-181.
68. Litz, L.M. and R.A. Mercuri, *Oxidation of boron carbide by air, water, and air-water mixtures at elevated temperatures.* Journal of The Electrochemical Society, 1963. 110(8): p. 921-925.
69. Vishnevetsky, I., et al., *Boron Hydrolysis at Moderate Temperatures: First Step to Solar Fuel Cycle for Transportation.* Journal of Solar Energy Engineering, 2008. 130(1).
70. Wahbeh, B., T. Abu-Hamed, and R. Kasher, *Hydrogen and boric acid production via boron hydrolysis.* Renewable Energy, 2012. 48: p. 10-15.
71. Gurr, G.E., et al., *The Crystal Structure of Trigonal Diboron Trioxide.* Acta Crystallographica, 1970. B26: p. 906-915.
72. Sakowski, J. and G. Herms, *The structure of vitreous and molten B2O3.* Journal of Non-Crystalline Solids, 2001. 293-295: p. 304-311.
73. Kumar, A., S.B. Rai, and D.K. Rai, *Effect of thermal neutron irradiation on Gd3+ ions doped in oxyfluoroborate glass: an infra-red study.* Materials Research Bulletin, 2003. 38: p. 333-339.
74. Brazhkin, V.V. and A.G. Lyapin, *High-pressure phase transformations in liquids and amorphous solids.* Journal of Physics: Condensed Matter, 2003. 15: p. 6059-6084.
75. Misawa, M., *Structure of vitreous and molten B2O3 measured by pulsed neutron total scattering.* Journal of Non-Crystalline Solids, 1990. 122: p. 33-40.
76. Lavrenko, V.A. and Y.G. Gogotsi, *Influence of oxidation on the composition and structure of the surface layer of hot-pressed boron carbide.* Oxidation of Metals, 1988. 29(3/4): p. 193-202.
77. Steiner, H., *Modeling of boron carbide oxidation in steam.* Journal of Nuclear Materials, 2005. 345(1): p. 75-83.
78. Viala, J.C., et al., *Chemical reactivity of aluminium with boron carbide.* Journal of Materials Science, 1997. 32: p. 4559-4573.
79. Sedrick, A.J., J.A.S. Green, and D.L. Novak, *Corrosion behaviour of aluminium-boron composites in aqueous chloride solutions.* Metallurgical Transactions, 1971. 2(3): p. 871-875.
80. Katkar, V.A., et al., *Effect of the reinforced boron carbide particulate content of AA6061 alloy on formation of the passive film in seawater.* Corrosion Science, 2011. 53(9): p. 2700-2712.
81. Nagai, T., Y. Ogasawara, and M. Maeda, *Thermodynamic measurement of (Al2O3+B2O3) system by double Knudsen cell mass spectrometry.* J. Chem. Thermodynamics, 2009. 41: p. 1292-1296.
82. Grytsiv, A., P. Rogl, and M.S.I. Team, eds. *Al-B-C (Aluminium - Boron - Carbon)*. ed. G. Effenberg and S. Ilyenko. SpringerMaterials - The Landolt-Bornstein Database.
83. Henry, D. *Electron-Sample Interactions*. [cited 2014 13 June]; Available from: http://serc.carleton.edu/research_education/geochemsheets/electroninteractions.html.
84. Muso. *EDX_scheme*. 2007 [cited 2014 9 June]; Available from: http://en.wikipedia.org/wiki/Energy-dispersive_X-ray_spectroscopy#mediaviewer/File:EDX-scheme.svg.
85. Zhou, W. and Z.L. Wang, eds. *Scanning Microscopy for Nanotechnology: Techniques and Applications*. 2006, Springer: New York, NY.
86. Ziegler, J.F., *The Stopping of Energetic Light Ions in Elemental Matter.* J. Appl. Phys / Rev. Appl. Phys., 1999. 85: p. 1249-1272.
87. Maki, J.T., R.F. Fleming, and D.H. Vincent, *Deconvolution of Neutron Depth Profiling Spectra.* Nuclear Instruments and Methods in Physics Research, 1986. B17: p. 147-155.

88. Downing, R.G., *NIST Neutron Depth Profiling Facility: 2013, invited.* Transactions - American Nuclear Society, 2013. 109.
89. Downing, R.G., G.P. Lamaze, and J.K. Langland, *Neutron Depth Profiling: Overview and Description of NIST Facilities.* J. Res. Natl. Inst. Stand. Technol., 1993. 98(1): p. 109-126.
90. Davis, J.R., ed. *Aluminum and Aluminum Alloys: ASM specialty handbook*. 1993, ASM International, 1993.
91. Froumin, N., et al., *Ceramic-metal interaction and wetting phenomena in the B4C/Cu system.* Journal of the European Ceramic Society, 2003. 23: p. 2821-2828.
92. Hiroki, A., S.M. Pimblott, and J.A. LaVerne, *Hydrogen Peroxide Production in the Radiolysis of Water with High Radical Scavenger Concentrations.* Journal of Physical Chemistry, 2002. 106: p. 9352-9358.
93. Yamada, R., Y. Kumagai, and R. Nagaishi, *Effect of alumina on the enhancement of hydrogen production and the reduction of hydrogen peroxide in the gama-radiolysis of pure water and 0.4 M H2SO4 aqueous solutions.* International Journal of Hydrogen Energy, 2011. 36: p. 11646-11653.
94. Buck, E.C., et al., *Radiolysis Process Modeling Results for Scenarios*. 2012, PNNL.
95. Makarenko, G.N., et al., *Interaction of Boron Carbide with Nickel Oxide.* Powder Metallurgy and Metal Ceramics, 2001. 40(11-12): p. 601-605.
96. Makarenko, G.N., et al., *Characteristics features of boron carbide syntesis for iron triad borides.* Powder Metallurgy and Metal Ceramics, 2004. 43(3-4): p. 192-195.
97. Szklarska-Smialowska, Z., *Pitting and Crevice Corrosion*. 2005, Houston, Texas: NACE International.
98. Czech, E. and T. Troczynski, *Hydrogen generation through massive corrosion of deformed aluminum in water.* International Journal of Hydrogen Energy, 2010. 35: p. 1029-1037.
99. Ahn, T., et al., *Extended Dry Storage and Transportation: Model for Evaluating Vaccum Drying Adequacy*, in *International High-Level Radioactive Waste Management Conference*. 2013: Albuquerque, NM.
100. Collaboration, *Boron Compounds with group IV elements: boron carbide: transport properties*, O. Madelung, U. Rossler, and M. Schulz, Editors., SpringerMaterials - The Landolt-Bornstein Database.